# Numerical Simulation of Admiralty Inlet, WA, with Tidal Hydrokinetic Turbine Siting Application

Kristen M. Thyng

A dissertation submitted in partial fulfillment of the
requirements for the degree of

Doctor of Philosophy

University of Washington

2012

Reading Committee:

James J. Riley, Chair

Mitsuhiro Kawase

Brian Polagye

Program Authorized to Offer Degree:
Department of Mechanical Engineering

University of Washington

**Abstract**

Numerical Simulation of Admiralty Inlet, WA,
with Tidal Hydrokinetic Turbine Siting Application

Kristen M. Thyng

Chair of the Supervisory Committee:
Professor James J. Riley
Mechanical Engineering

Tidal hydrokinetic energy has been recognized as a potential source of sustainable, renewable energy. In order to properly site turbines for commercial-scale development, the complex flow conditions in a potential deployment region must be understood. Viable locations for turbines are limited by many factors, including underwater space that is above the bottom boundary layer, below shipping traffic, within areas of strong currents, and yet avoids additional fatiguing stresses. The primary area of interest in the Puget Sound for commercial tidal energy development is Admiralty Inlet, which includes potentially disruptive flow features such as vortices and strong turbulence. This dissertation seeks to increase the body of knowledge of these features both from an oceanographic perspective and as they pertain to turbine site characterization.

The primary means of studying Admiralty Inlet in this document is through numerical simulation of the region using the Regional Ocean Modeling System (ROMS). The model output is found to compare well with field data, capturing eddy fields, turbulence properties, relative tidal phases, and illuminating many flow features. Horizontal velocities in the simulation are, on average, approximately 75% the size of those found in the data. This speed deficiency is inherited from the forcing model in which the Admiralty Inlet simulation is nested. The model output also shows that the flow field of this fjord-like estuary is largely affected by a headland on the northeast side of the Inlet. Vortices generated by this

headland, Admiralty Head, are found to vary considerably depending on the tidal cycle. The eddies can persist beyond the half-cycle of generation to significantly affect the horizontal speed and other flow field properties in the subsequent half-cycle. Detailed analysis of the vertical vorticity governing equation shows that advection, tilting, stretching, and boundary generation are the most significant processes dictating the behavior of the vorticity.

Turbulence modeling in the simulation is carried out via a $k$-$\varepsilon$ turbulence closure scheme. Comparisons of model output with high resolution field data show the model to perform reasonably well: predicted Reynolds stress and turbulent dissipation rate values are usually within a factor of two of the field data. The turbulent kinetic energy from the simulation compares well with field data that is restricted to the frequency range of classical turbulence. The energy density spectrum of the data is found to follow Kolmogorov's theory beyond the inertial subrange. Using this fact and Taylor's frozen field approximation, an inferred calculation for the turbulent kinetic energy is derived that spans the full frequency range of the data set. The output from the inferred calculation compares well with the full turbulent kinetic energy from the field data.

Maps of metrics for tidal turbine siting are generated that address many considerations for turbine placement, and can be adjusted for the model's speed deficiency with a simple multiplication factor. Among the possible best locations for turbine deployment are north of Point Wilson on the west side of Admiralty Inlet and near the center of the channel between Point Wilson and Admiralty Head. These locations have a strong tidal resource available along with highly bi-directional tidal currents and low turbulence levels.

## TABLE OF CONTENTS

## LIST OF FIGURES

## LIST OF TABLES

## GLOSSARY

$\epsilon$: Truncation error

$\varepsilon$: Turbulent dissipation rate [$m^2/s^3$]

$\eta$: Turbine efficiency, taken nominally to be $\eta = 0.5$

$\kappa$: Horizontal wave number [1/m]

$\phi$: Dynamic pressure

$\psi$: Generic length scale in the turbulence closure scheme

$\rho$: Density - 1000 [$kg/m^3$]

$\theta$: Direction of horizontal velocity [degrees]

$\theta_{EBB}$: Direction of horizontal velocity on ebb tide [degrees]

$\theta_{FLOOD}$: Direction of horizontal velocity on flood tide [degrees]

$\theta_{M,EBB}$: Mean direction of horizontal velocity on ebb tide [degrees]

$\theta_{M,FLOOD}$: Mean direction of horizontal velocity on flood tide [degrees]

$\Theta$: Directional deviation

$a$: Bidirectionality or asymmetry parameter [degrees]

ADCP: Acoustic Doppler Current Profiler, measurement device used for gathering *in situ* data with depth at a given horizontal location for a given time.

ADV: Acoustic Doppler Velocimeter, measurement device used for gathering *in situ* data at a single location in space for a given time.

BATHYMETRY: Seabed topography

CUT-IN SPEED: The speed at which a tidal turbine will begin to produce electricity.

$D$: Kinetic power density, $D = \frac{1}{2}\rho s^3$ [kW/m$^2$]

$D_M$: Mean kinetic power density over an integer number of tidal cycles [kW/m$^2$]

$E$: Energy density spectrum [m$^2$/s$^2$/Hz]

DIURNAL INEQUALITY: Difference in tide height between two high and low tides in a day.

DIURNAL TIDE: A tide characterized by a single high and low tide per day.

EBB TIDE: Tidal flow out of an embayment, toward the open ocean. Opposite direction of flood tide.

FLOOD TIDE: Tidal flow into an embayment, away from the open ocean. Opposite direction of ebb tide.

HIGHER HIGH WATER: In a system with unequally-sized tides, this is the larger high tide, as compared with lower high water.

HIGHER LOW WATER: In a system with unequally-sized tides, because low tide is below mean sea level and often given a negative value, this is the smaller low tide, as compared with lower low water.

HUB HEIGHT: The height above seabed of the turbine hub, often taken as ten meters

HYDROSTATIC APPROXIMATION: Simplification often used in oceanographic and atmospheric models that the vertical pressure gradient is in equilibrium with gravity.

$K_M$: Vertical eddy viscosity [$m^2/s$]

$k$: Turbulent kinetic energy [$m^2/s^2$]

KPD: Kinetic power density

LEE: The lee side of a feature is the downstream side. Lee is the opposite of stoss.

MIXED TIDE: A combination of semdiurnal and diurnal tides with two high and two low tides in which one high and low tide is usually much larger than the other.

NEAP TIDE: Period of reduced magnitude tidal heights and currents due to the gravitational pull of the sun and moon being in quadrature; occurs every two weeks at opposite time as spring tide.

$\ell$: Turbulence length scale

LOWER HIGH WATER: In a system with unequally-sized tides, this is the smaller high tide, as compared with higher high water.

LOWER LOW WATER: In a system with unequally-sized tides, because low tide is below mean sea level and often given a negative value, this is the larger low tide, as compared with higher low water.

$P$: Power density, or the power divided by turbine cross-sectional area [$kW/m^4$]

$P_b$: Buoyancy production in the governing equations for $E$ and $\psi$

$P_b$: Power bias over an integer number of tidal cycles [dimensionless]

$P_M$: Mean power divided by turbine cross-sectional area over an tidal number of tidal cycles, [kW/m$^4$]

$P_s$: Shear production in the governing equations for $E$ and $\psi$

$p$: Total pressure

PRIMITIVE EQUATION: Navier-Stokes equations with the hydrostatic assumption

RATED SPEED: The speed at which a tidal turbine will stop increasing electricity production. Production will instead be made at the rated speed regardless of whether the actual speed of the flood is higher.

$s$: Speed or magnitude of horizontal currents, $s = \sqrt{u^2 + v^2}$ [m/s]

$S_b$: Speed bias over an integer number of tidal cycles [dimensionless]

$s_{cut-in}$: Cut-in speed, the speed at which a turbine begins producing power [m/s]

$s_{cut-out}$: Cut-out speed, the speed at which a turbine ceases producing power [m/s]

$s_m$: Mean speed over an integer number of tidal cycles [m/s]

$s_{rated}$: Rated speed [m/s]

$s_z$: Mean vertical shear over an integer number of tidal cycles [1/s]

SEMIDIURNAL TIDE: A tide characterized by two high tides and two low tides per day.

SPRING TIDE: Period of higher magnitude tidal heights and currents due to the alignment of the sun and moon's gravitational pull; occurs every two weeks at opposite time as neap tide.

STOSS: The stoss side of a feature is the upstream side. Stoss is the opposite of lee.

$t_{duri}$: Mean turbine idle duration during an integer number of tidal cycles [hours]

$t_{duro}$: Mean turbine operating duration during an integer number of tidal cycles [hours]

$t_{op}$: Fraction of tidal cycle a turbine would operate [dimensionless]

$T$: Tidal period

THALWEG: The deepest continuous path along a channel

$\underline{u}$: Horizontal velocity vector: $\underline{u} = (u, v, 0)$

$\underline{v}$: 3D velocity vector: $\underline{v} = (u, v, w)$

$u$: $u$-velocity, the horizontal component of velocity in the easterly direction [m/s]

$u'$: $u$-velocity fluctuation [m/s]

$v$: $v$-velocity, the horizontal component of velocity in the northerly direction [m/s]

$v'$: $v$-velocity fluctuation [m/s]

$w$: $w$-velocity, the vertical component of velocity [m/s]

$w_M$: Mean vertical speed over a tidal cycle [m/s]

## ACKNOWLEDGMENTS

I have very much enjoyed my time in graduate school learning and studying with my advisor Jim Riley. He often gave me the opportunity to figure things out on my own, yet provided expertise and guidance when most needed. He has been a caring, interesting, and interested overseer to this degree, as well as a friend along the journey.

My committee (Jim Riley, Mitsuhiro Kawase, Alberto Aliseda, Brian Polagye, and Dale Durran) and the NNMREC tidal energy group have been a good source of information and companionship at conferences over the years. In particular, I have had many rewarding conversations with Mitsuhiro Kawase, learning a lot from his many insights and thoughtful questions, and been grateful for his excitement for the research. Philip Malte was instrumental in my transfer to the mechanical engineering department, particularly through his kindness and attention to help me learn what I needed to pass the qualifying exams. The applied mathematics department at the University of Washington was an excellent community in which to have earned my masters degree. It was the source of much knowledge and many important relationships. The MUG group in oceanography has been key to begin my integration into the physical oceanography community, providing helpful experience and constructive criticism, particularly Parker MacCready and Sarah Giddings.

My graduate school friends from mechanical engineering and applied math, particularly in my office, have been important confidants and sources of sanity during a process that has at times been trying. The College Inn has, in particular, been a safe haven, taking in weary grad students and renewing their spirits and minds with beer and nachos.

My family has consistently been behind me throughout graduate school, whether or not they are really sure what I am working on. Thank you Mom, Dad, Elroy, Vince, Michell, Marc, Kristin, Grandma, Grandmother, and Grandfather. I learned that the quickest way to scare my mom away is to start talking about research, but that never caused her to waver

in her support. My weekly meet ups with my dad always cover updates on my progress, whether there was any or not. Special thanks to Dallas, who is always happy to see me.

Kyle Mandli has been a part of my graduate school experience longer than even my research. He has shared his incredible patience as well as his (seemingly) infinite knowledge with me, and for that and much more, I am so lucky.

Additional thanks to the US Department of Energy through the Northwest National Marine Renewable Energy Center at the University of Washington and the PACCAR Professorship for funding to do this research.

# Chapter 1

# BACKGROUND INFORMATION

## *1.1 Introduction*

The primary motivation for considering alternative energy sources has historically been due to an increase in the price of oil. While this motivation remains and has been extended by the desire to be free of dependence on foreign resources, the larger reason has arguably become global climate change. Additionally, it is imperative to move from burning fossil-fuels, of which there is a finite amount, to utilizing recurring resources. A peak in oil production is predicted to occur world-wide between 2020 and 2050, after which the amount of oil available for energy production will diminish continually (Greene et al., 2003). It is in our best interest to be prepared for this inevitability.

The key finding of the United States Global Change Research Program's (USGCRP) *State of the Knowledge Report of Global Climate Change Impacts in the U.S.* is that global warming is real and caused by humans (Karl et al., 2009). Additionally, it is stated that climate change effects are already noticeable and will continue to increase. A final key point is that future climate change depends on what is done today as a nation and as a planet. In response to this, many states and cities around the United States, as well as many countries, have begun to pass initiatives requiring the creation and integration of a fraction of their electricity to come from "green" sources. For example, the Secretary of State for Trade and Industry (2003) in United Kingdom set as a goal to have 20% of their electricity originate from renewable energy sources by 2020. The U.S. Department of Defense (2007) has similarly committed to renewable energy sources for 25% of their energy needs by 2025. Here in Washington State, Initiative I-937 has put forth an obligation on large utilities of 15% of energy production from new renewable sources by 2020 (Reed, 2006).

It is clear that new technologies must play an important role in the changes that are employed today in order to affect the future. Energy sources are renewable if they do not

consume a finite resource in the process of creating electricity, and thus may continue to be utilized as long as the hardware and resource remain.

Many renewable energy sources are presently being considered. Some draw on ideas and even technology that have been around for decades or longer, such as wind energy, solar energy, hydroeletric dams, and tidal barrages (dam-like barriers placed in an area with a high tidal range that trap the water upon entering and release it through turbines, creating electricity). Others are new applications of older ideas, like off-shore wind energy, which is similar to on-shore wind energy but is placed on deep enough water that a monopile structure may no longer be a feasible way to keep the turbine in place, necessitating innovative designs to harvest the vast amount of energy available in the winds farther away from land. There are many new ideas for creating energy, such as wave energy, biomass, ocean thermal, and hydrokinetic energy. Marine hydrokinetic (MHK) energy is a broad term encompassing wave, tidal, and river kinetic energy, whereas tidal hydrokinetic energy (THK) refers to turbines in a tidal environment, in which the gravitational influence of the moon and sun interact to cause the large body of water to move back and forth once or twice a day.

The decision of what renewable energy technology to consider is based on what resource is locally available to the population in need of electricity production. The Puget Sound is a deep, fjord-like estuary with several large cities, including Seattle and Tacoma, on its shoreline (Figure 1.1(a)). The Puget Sound metropolitan area supports about 3.5 million people (City of Seattle, 2010), a much higher population density than in the eastern half of the state, where much of the existing (conventional hydroelectric and wind) electricity is produced. One attraction of tidal hydrokinetic energy for this region is its proximity to a large population, which would require shorter transmission lines. Another attraction is that, unlike wind and wave energy, tidal hydrokinetic energy is a relatively predictable source of electricity and would be produced regardless of weather factors that may affect energy consumption and production of other sources of renewable energy.

One of the most promising locations for a commercial-scale tidal turbine array is in Admiralty Inlet, the main entrance to the Puget Sound (Figure 1.1(b)) (Polagye et al., 2007; Previsic et al., 2008; Haas et al., 2011). Admiralty Inlet has peak currents of over 3.5 m/s and depths between 50 and 180 meters, though at the northern sill, the area

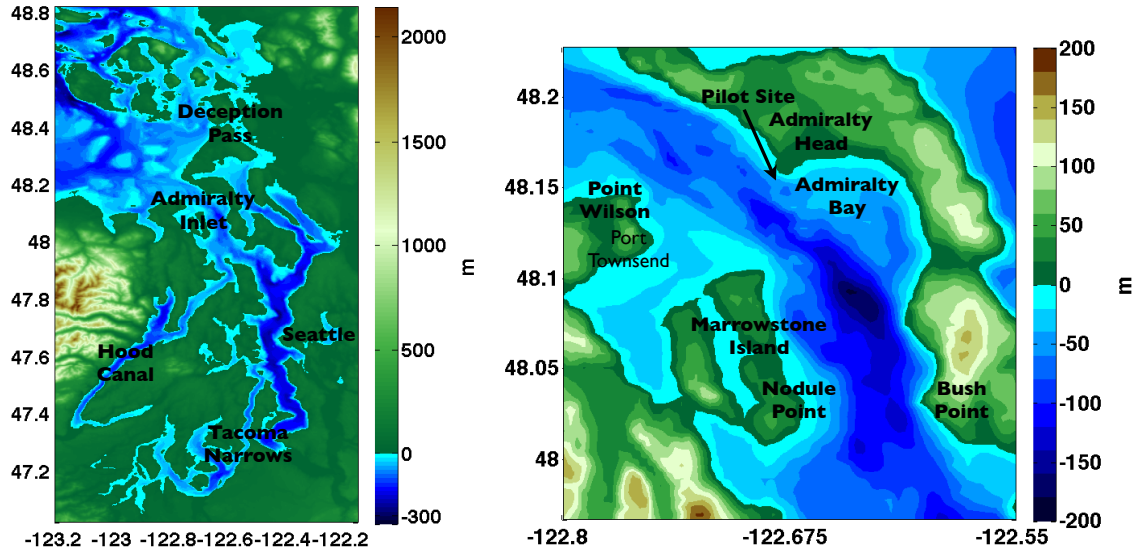


(a) Puget Sound

(b) Admiralty Inlet

Figure 1.1: Western Washington state's inland waters, the Puget Sound, where dense Pacific Ocean water mixes with fresh river water. Blue coloring indicates water depth and green indicates height of land above water, with both in units of meters.

of particular interest, depths are around 50 to 80 meters. These factors, along with the large underwater space available for potential development, make Admiralty Inlet a strong candidate for tidal hydrokinetic power development. Thus, there is a potential pilot-scale test site in Admiralty Inlet near Admiralty Head, as indicated in Figure 1.1(b), being developed by the Public Utility District No. 1 of Snohomish County (SnoPUD) in an effort to fulfill its obligation of 15% of its energy production from new renewable sources by 2020 (Reed, 2006). The SnoPUD pilot project will involve two tidal turbines in Admiralty Inlet and will enable the gathering of turbine flow data in a real environment (Public Utility District No. 1 of Snohomish County, 2012). This work, in conjunction with both field and numerical research being accomplished at the University of Washington, will enable science-based decisions to be made in the future about commercial-scale tidal energy development in the region, as well as aid in national and international decision-making.

### *1.2 Tidal Hydrokinetic Energy*

The basis of tidal hydrokinetic energy (THK) is the utilization of kinetic energy present in tidal currents. It is analogous to wind energy, with which many of us are familiar. A turbine is placed in the path of strong currents, the water rotates the turbine, and electricity is produced by a generator attached to the turbine. This electricity then needs to be exported from the turbine to land via transmission lines for utilization.

The main indicator of the intensity of the resource in a body of water at an $(x, y, z)$ location is the kinetic power density, or kinetic energy flux, which is defined as

$$D(x, y, z, t) = \frac{1}{2}\rho(x, y, z, t)s(x, y, z, t)^3, \tag{1.1}$$

where $\rho$ is the density of water and depends on location in space and time, though is often taken at the nominal value of 1024 kg/m$^3$ for salt water, and $s$ is the speed of the flow, or magnitude of the horizontal currents, which also changes in three-dimensional space and time. An important note is that a small increase in speed leads to a large increase in kinetic power density, due to the cubic relationship between the two. This suggests the importance of accurate knowledge of the tidal currents for turbine siting. Additionally, metrics for tidal turbine siting will often present properties at a water depth corresponding to "hub height," the nominal vertical location of the turbine hub, in order to examine the turbine properties at a single depth. The assumption is then that flow properties will not change significantly over the face of the turbine around the hub height, although Kawase and Beba (2010) specifically examines the effects of vertical changes of the currents with height. In the present work, a hub height of ten meters is assumed unless otherwise specified. This hub height is high enough above the seabed for a small- to medium-sized turbine, but close enough to the seabed for a reasonable-sized turbine support structure.

Tidal turbines come in many different designs and some are at various stages of development. The most familiar design is perhaps Verdant Power's design, as seen in Figure 1.2(a). This design is analogous to that of a typical wind turbine. A unit is installed on a monopile from the seabed and is completely submerged. The Marine Current Turbines (MCT) turbine design is similar but has a protruding monopile from the seabed to be-

yond the surface for easier maintenance, and additionally has two turbines attached to the monopile instead of one (see Figure 1.2(b)). The Open Hydro design, which is being used in SnoPUD's pilot project and is in Figure 1.2(c), is a ducted turbine design which sits on the seabed using a gravity base foundation. Ocean Renewable Power Company (ORPC) has a Gorlov cross-flow turbine design which may be gravity- or bottom-line mounted (see Figure 1.2(d)). The designs shown here are horizontal axis turbines, meaning that the axis of the turbine rotation is horizontal as opposed to vertical. The research presented in this document is largely independent of turbine design, but in some turbine siting analysis, a circular-face horizontal axis turbine will be assumed, instead of an ORPC-style design.

Typical tidal turbines start at around 5 meter diameter and may go up to as large as 20 meters. Turbine properties, such as cut-in speed, rated speed, diameter, and efficiency will all affect the power output of a turbine, which can range between 50 kW and over 2 MW. As an example, the Open Hydro pilot-scale turbine that may be placed in Admiralty Inlet by SnoPUD is expected to be 10 meters in diameter with a cut-in speed of 0.7 m/s and a rated speed of 4 m/s.

### *1.3 Local Area of Interest for Development*

The Puget Sound is a fjord estuary in western Washington State, in which fresh river water from the surrounding lowlands interacts with saltier, denser Pacific Ocean water that comes inland via the Strait of Juan de Fuca (see Figure 1.3). The main channel to the Puget Sound is Admiralty Inlet, though there is an additional small entrance channel, Deception Pass (Figure 1.1(a)). Underwater sills located at the entrance of each main channel affect the flow dynamics and density fields by increasing the current speeds and turbulent mixing.

The area of interest for this research is Admiralty Inlet, shown in Figure 1.1(b). This waterway has two sills: one northward between Point Wilson and Admiralty Head, and one southward, south of Bush Point. Depths at the sills are 50 to 60 meters in the north, closer to 75 meters in the south, and the Inlet is as deep as 180 meters between the two.

The tidal motions in the Puget Sound are those of a standing wave with some progression, since the tidal currents lead the free surface displacement by close to 90°. This is due to the geometry of the basins in relation to the wavelengths of the tides (Mofjeld and Larsen,

(a) Verdant Power (2010).

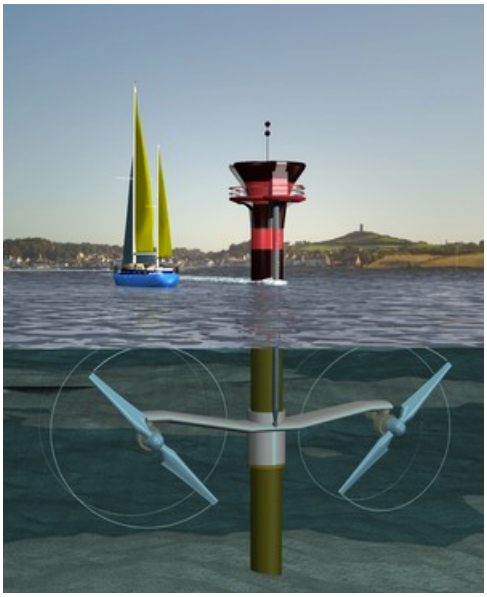

(b) Marine Current Turbines (2010).

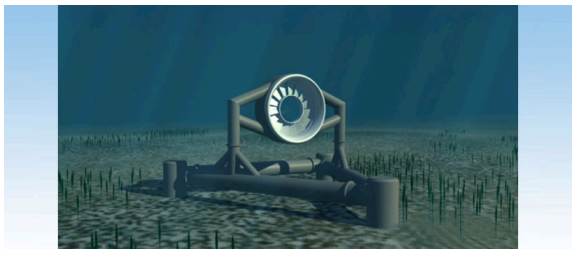

(c) Open Hydro (2010).

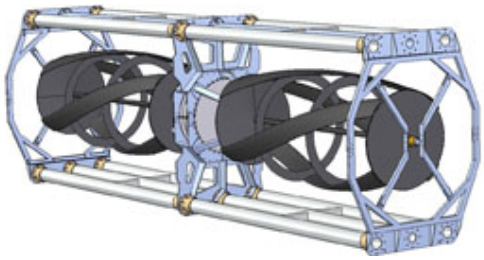

(d) Ocean Renewable Power Company (2010).

Figure 1.2: Various tidal turbine designs.

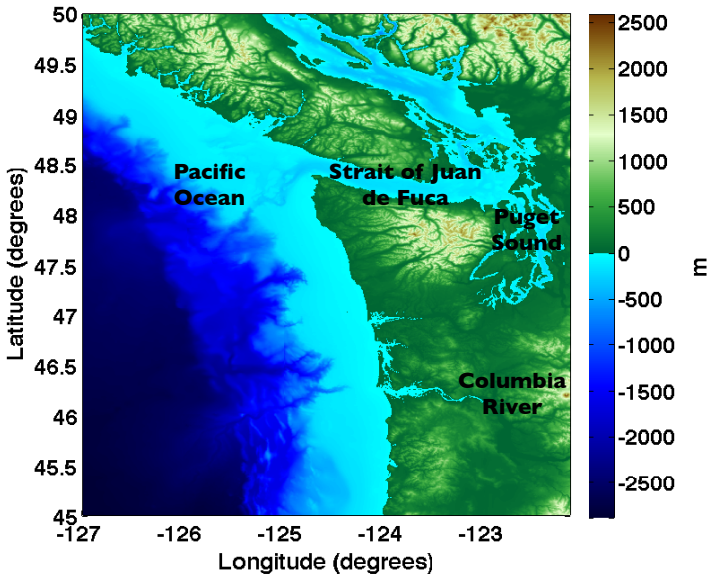


Figure 1.3: Western Washington state's inland waters the Puget Sound where dense Pacific Ocean water mixes with fresh river water

1984). Mean tidal ranges in the area are 1.6 meters at Port Townsend and double that in the southern reaches (Mofjeld and Larsen, 1984).

The best reference for the tides and tidal currents in Puget Sound remains Mofjeld and Larsen (1984), and more information on many of these topics can be found there. However, many other papers have added to the understanding of this complex waterway (Babson et al., 2006; Canals et al., 2009; Cannon, 1983; Geyer and Cannon, 1982; Lavelle et al., 1988; Leonov and Kawase, 2009; Warner and MacCready, 2009).

### *1.3.1 Tides*

The tides are caused by a combination of modulated gravitational effects between the moon and sun (see Figure 1.4). Despite the minuteness of the gravitational pull, water will move in reaction to the force and, with a large enough body of water, this small force can lead to large effects as seen in tidal motions. Water in one area will be slightly higher than in another from the force (as seen in high and low tides with free surface height changes), and

this potential energy difference leads to the water moving in reaction, causing potentially strong tidal currents.

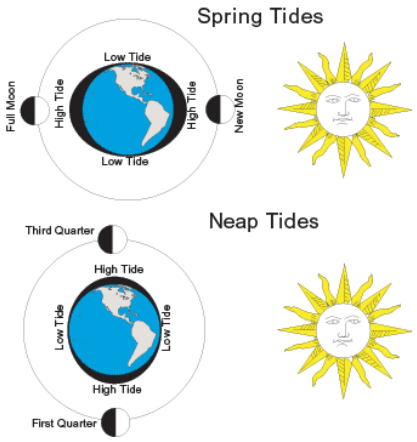


Figure 1.4: The gravitational force, mainly due to the moon, is shown as exaggerated bulges in water on the earth. The water that is closest to the moon is pulled the most, along with the water opposite the moon, while the water at a perpendicular angle is pulled least. The combination of gravitational pull between the moon and the sun causes a more complicated tidal signal and leads to twice monthly maximums and minimums in tidal strength. Figure from Atlantic Kayak Tours (2010).

A tidal period of one flood tide (water movement direction into embayments from the ocean) and one ebb tide (water movement toward the ocean from an embayment) can be approximately half a day (leading to two periods per days, called a *semidiurnal tide*) or approximately one day (called a *diurnal tide*). Many coastal areas have a mix of these two types when tidal frequencies from many different effects are combined together for the full tidal signal and is called a *mixed tide*. A mixed tide will generally have two high tides and two low tides per day, with one of each being more extreme than the other (*diurnal inequality*). More information on the tides can be found in Pugh (2004).

Tides in the Puget Sound are mixed, made up of both semi-diurnal and diurnal tides. They are characterized by periods of large inequalities between the lower low water and higher low water, for example, and periods of more equal, twice-daily tides. The tides are

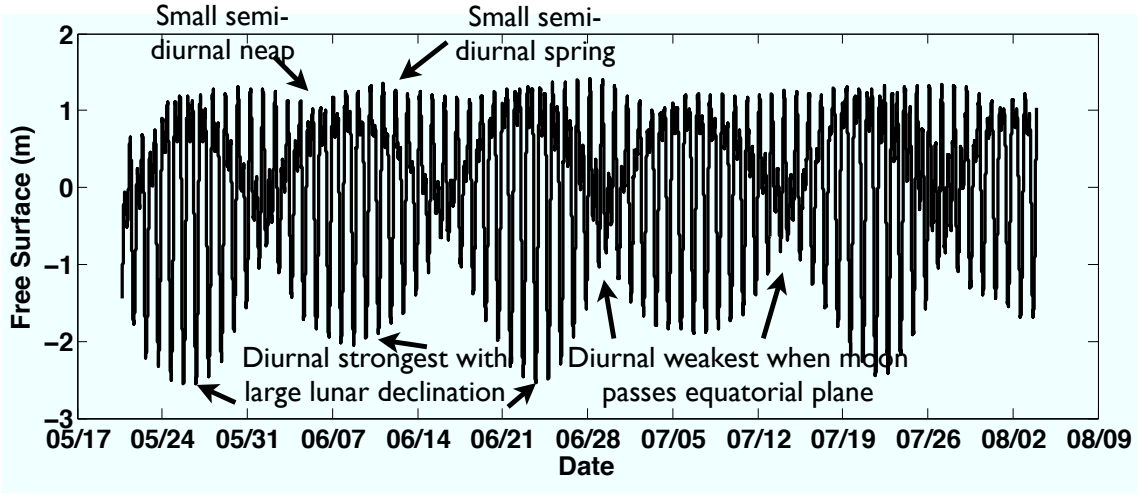


Figure 1.5: The mixed tides in Admiralty Inlet are mostly affected by the lunar declination cycle which dramatically changes the size of the diurnal tides. Small semi-diurnal changes happen due to the neap-spring cycle. Data from NNMREC, University of Washington (2010)

most dramatically affected by the lunar declination cycle, in which the diurnal tides are largest when the moon has the largest declination and smallest when the moon is passing the equatorial plane (Pugh, 2004). The tides have a relatively consistent high tides but widely varying low tides.

Another astronomical cycle that affects the tides is the spring-neap cycle. The strength of the tide changes at a period of two weeks when the moon and sun line up in relation to each other (see Figure 1.4). When the sun and moon are opposite or in line with each other, there is a peak in tidal strength called *spring tide*. When they are in quadrature, tidal strength is weakest and is called *neap tide*. The Puget Sound area shows only a small effect from the neap-spring cycle in the semi-diurnal tides, but since both the neap-spring and lunar declination cycles occur on an approximately fortnightly basis, they are easily confused. See Figure 1.5 for an example sea surface signal from Admiralty Inlet.

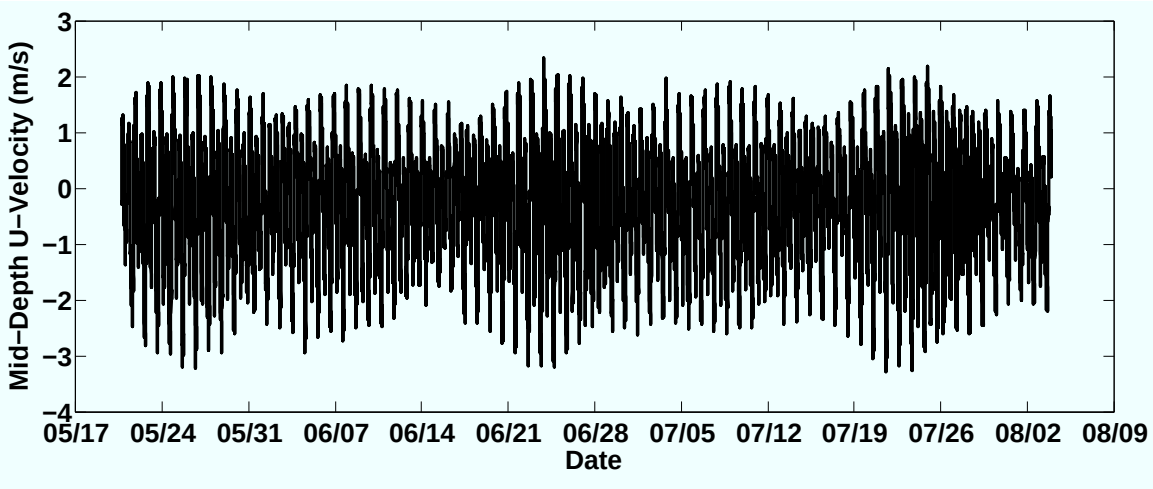


Figure 1.6: Tidal currents are more semi-diurnal than the free surface signal in the Puget Sound. Data from NNMREC, University of Washington (2010).

### *1.3.2 Tidal Currents*

The tidal currents in Puget Sound are large: in several places they can exceed 3 m/s, and in Deception Pass they can exceed 4 m/s. On the other hand, in the deep, wide main basin near Seattle, the water tends to move slowly. The tidal currents are strongly affected by local bathymetry and coastline changes, often abruptly, and in nonlinear ways.

The eastward velocity at a point in Admiralty Inlet is shown in Figure 1.6. The most distinguishing feature in the velocity in contrast to the sea surface signal in Figure 1.5 is that semi-diurnal tides are much more accentuated in current records than diurnal tides.

An additional level of complexity in tidal currents is depth variation. The currents are slowed near the seabed in different regions due to bottom friction and have different profiles over the water column. Most typical of the current variation with depth is a slowing to zero at the seabed, some possible slowing near the surface due to surface winds, and a peak in velocity in the middle or near the surface of the water column (Cushman-Roisin and Beckers, 2009). The profile typically is different on flood versus ebb, and can be drastically different when other effects come into play (eddies, unstable density, fronts, stratification, and other related phenomena).

### *1.3.3 Tidal Constituents*

The effects from various sources of influence of the sun and moon on the tides are taken into account through different tidal constituents, each of which has a distinct frequency. The strongest tidal constituent in the Puget Sound is the $M_2$ tide. The $M_2$ tide is due to the gravitational force from the moon and has a period of about half a day, making it a semidiurnal tidal constituent. The next largest constituent is due to a combination of the moon and sun and is a diurnal tide, $K_1$. The largest solar constituent is $S_2$, a semidiurnal tide. In the Puget Sound, the largest tidal constituents are $M_2$, $K_1$, $S_2$, $O_1$ (lunar declination diurnal), $P_1$ (solar diurnal), and $N_2$ (lunar elliptic semidiurnal). In general, tidal constituents are named such that the number attached to the name represents the numbers of occurrences of that constituent per day. Thus, any constituent with a "2" in the name is a semidiurnal tide and any constituent with a "1" is diurnal.

Harmonic analysis is a method of decomposing the tidal signal into separate constituents, each with a particular frequency. This method relies on the assumption that the full signal is a linear combination of distinct signals, which are defined by a constant amplitude and phase, along with their frequency, in a sinusoidal wave form, *i.e.*,

$$\zeta(x, y, t) = \sum_{i=1}^{N} A_i(x, y) \cos(\omega_i t - \phi_i(x, y)),$$

where $x$ and $y$ are horizontal Cartesian coordinates, $\zeta$ is the local free surface height, which changes with time and space, $N$ is the number of tidal constituents considered in the summation, and $A_i(x, y)$, $\omega_i$, and $\phi_i(x, y)$ are the harmonic amplitude, frequency, and phase, respectively, for constituent $i$. Note that $A$ and $\phi$ can and do change in space while the frequency is constant. Harmonic analysis is done in this research using the freely available Matlab toolbox `T_Tide` (Pawlowicz et al., 2002).

Harmonic analysis is used regularly to decompose free surface signals, and with good accuracy can be used for predictions of the tidal surface height well into the future. Harmonic analysis can also be used for tidal currents, with the additional complication of a third dimension in $z$ for $A$ and $\phi$ for each velocity component. However, while sea surface heights tend to vary smoothly over large length scales and tidal time scales, tidal currents can be

strongly nonlinearly affected by local coastlines, bathymetry, and even density variations. This decreases the accuracy of the linearity assumption in the decomposition for currents, but it is still used to summarize varied information in a region in space and time, and to compare model output and data (Godin, 1983).

### *1.3.4 Notable Features*

There are many notable dynamic features in the Puget Sound, including internal waves, fronts, vortices, and internal hydraulic jumps. While it is difficult to know with certainty, since times are not listed with the images, the satellite image in Figure 1.7(a) appears to show vorticity streaming from Admiralty Head on ebb tide, having separated and curled up into an eddy in the lee of the headland. The surface has been affected by the vortex, making it smooth with the recirculation zone visible in the image.

Figure 1.7(b) shows another satellite image of Admiralty Inlet. In this case, apparently seen is a front of water being pushed forward as the tide changes from flood to ebb. The remainder of flood tide is still pushing southeast-ward by the northeastern point of Marrowstone Island, possibly showing a strand of vorticity in the lee of the point.

Data possibly showing evidence of an internal hydraulic jump is shown in Figure 1.8. The density measurements upstream from Bush Point show a sharply stratified two-layer flow approaching the point, while measurements downstream show that the density field has become greatly mixed. This implies that a control point was crossed in which the flow underwent a jump in order to dissipate energy, and the likely location for that jump is the constriction created by Bush Point (Seim, 1993).

## ***1.4 Research Review and Motivation***

University of Washington researchers have been working to understand the complex issues surrounding the THK energy field as part of the Northwest National Marine Renewable Energy Center (NNMREC), a group funded by the Department of Energy to study tidal energy. NNMREC partner Oregon State University focuses its efforts on wave energy (NNMREC, University of Washington, 2010).


(a) The surface disruption due to a headland-generated eddy streaming off Admiralty Head on ebb tide.

(b) A front moves through the system as the tide changes from flood to ebb, near Admiralty Head. Near the northeast corner of Marrowstone Island, vorticity from flood tide is still visible.

Figure 1.7: Surface features are evident from Google Earth satellite images.

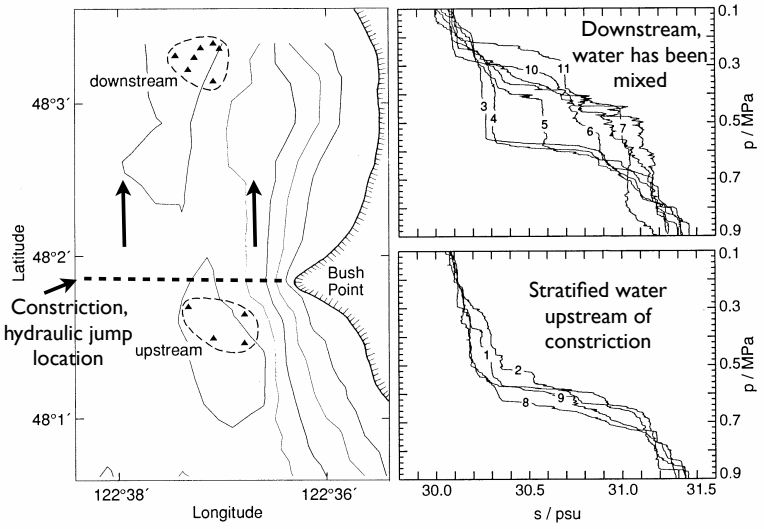


Figure 1.8: Measurements stoss and lee of Bush Point. Stoss of the point, the density field shows sharp stratification. Lee of the point, the density gradients have mixed across the water column. From Seim (1993), altered by author.

NNMREC's areas of research include: (1) turbine and array optimization; (2) materials; (3) environmental effects; and (4) site characterization. Site characterization is largely being addressed by gathering field data. This involves using acoustic Doppler current profilers (ADCPs) to investigate the velocities at specific areas of interest, such as near the pilot project site in Admiralty Inlet; conductivity, temperature, and depth casts to investigate the water density profiles; and hydrophones to record acoustic information. However, while this data is useful and necessary, it is limited in spatial and temporal resolution. To complement this work, numerical modeling is also being used for site characterization. Numerical modeling allows for the gathering of flow field and other parameter information anywhere in a numerical domain and at any time output from the simulation. In addition, a model allows for analysis of alternative turbine-siting scenarios without expenditure and potential environmental damage. This combination of complementary efforts enables a greater understanding of the tidal energy potential of the area.

### *1.4.1 Generalizability of Research*

Some common features can be found amongst THK sites around the world. Geographic features that generate vortices (and therefore turbulence), for example, can be found in many sites aside from Admiralty Inlet, making this research relevant to site characterization in other areas. Research by Baston (2012) in the Pentland Firth focuses on the generation of vortices by the islands in the channel, as shown in Figure 1.9. Recirculation areas due to vorticity detaching from headlands are clearly shown in Figure 1.10, in Minas Passage. Additionally, an ORPC development in Cook Inlet is near a headland (Figure 1.11). Furthering the understanding of vorticity mechanisms and features, accuracy of turbulence modeling, and methodologies for applying numerical simulation results to turbine siting will aid in turbine placement not only in Admiralty Inlet but in similar regions throughout the world.

### *1.4.2 Turbine Siting*

In order to facilitate the site characterization of tidal energy sites around the world with different bathymetry, coastline features, currents, and stratifications, a series of metrics


Figure 1.9: Map of the Pentland Firth (Kelisi, 2006)

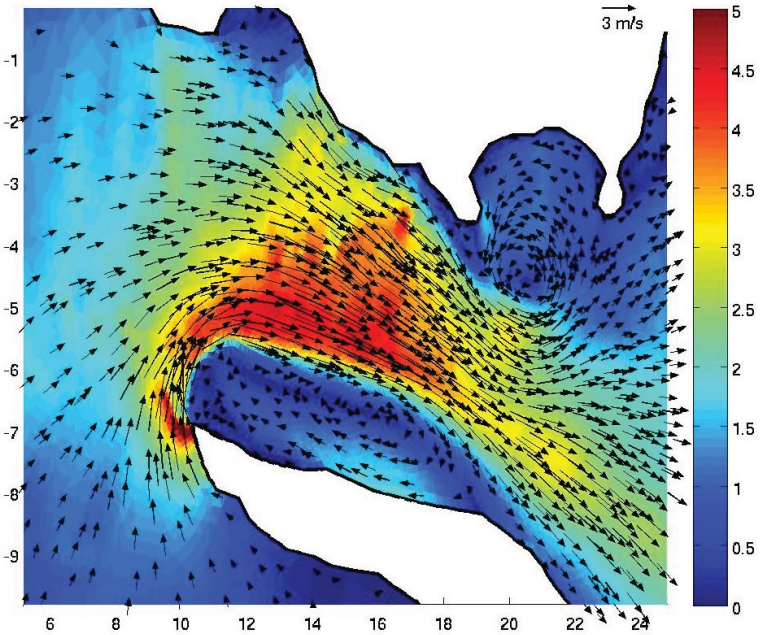


Figure 1.10: Evidence of eddies in the Minas Passage (Karsten et al., 2010)

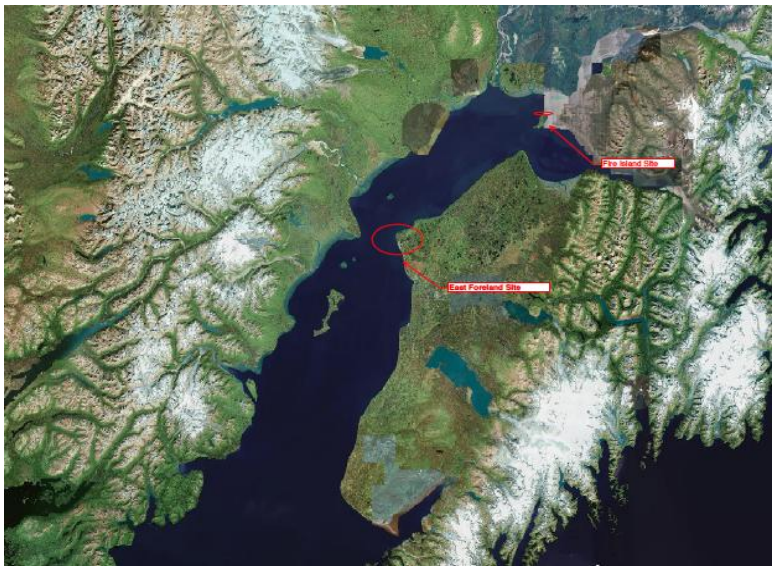


Figure 1.11: ORPC site in Cook Inlet is near a headland (Worthington, 2011)

were proposed by the European Marine Energy Centre (EMEC) (Legrand, 2009). These metrics quantify the influence that flow features would have on a turbine without the need for characterizing each feature individually. Metrics proposed by EMEC to scientifically and consistently evaluate potential tidal hydrokinetic energy sites include measures of vertical shear, turbulent eddy intensity, asymmetry of currents on ebb versus flood, peak sustained velocities, velocity distribution, and mean kinetic power density over a tidal cycle. Turbine developers may want to know existing conditions in sites that could support development in order to optimize turbine designs, and utilities will need to be able to locate and assess these potentially desirable locations.

The work presented here builds on previous work on site characterization in the Puget Sound (Epler, 2010; Gooch et al., 2009; Polagye et al., 2007, 2009, 2008; Polagye and Thomson, 2011; Previsic et al., 2008; Thomson et al., 2011). Some of this previous work identified areas of strong currents, leading to Admiralty Inlet's consideration for development (Polagye et al., 2007; Previsic et al., 2008). More recent studies used many of the metrics to analyze ADCP data that has been collected in Puget Sound (Gooch et al., 2009; Polagye and Thomson, 2011). Turbulence data have been gathered as well to calculate metrics such

as turbulence intensity (Thomson et al., 2011). Field data give temporal resolution, but it is more difficult to obtain spatial resolution (though there has been some work on this topic (Epler, 2010; Gooch et al., 2009)).

Metrics can be loosely separated into two categories: resource quantification, and resource qualification and turbine survivability. These categories each focus on a different aspect of tidal energy production. Resource quantification contains metrics that describe the amount of resource available for a turbine. This includes measures of mean speed and kinetic power density averaged in time and the percentage of time the turbines would spend producing power.

Resource qualification metrics primarily include asymmetry of the tidal flow. This asymmetry can affect the amount of resource that is actually accessible to the turbine. For example, some THK turbine designs, by having a fixed axis direction, assume the flow is bidirectional, *i.e.*, that there are 180° between flood and ebb. These designs may not be suitable for a location in which the currents significantly deviate from bidirectional due to the bathymetry or coastline, causing dynamical features such as eddies. Other turbine designs are able to yaw so that the face of the turbine can follow the flow. Such a design would be more appropriate for asymmetric flow locations.

Turbine survivability is another important and closely-linked consideration. Shear in the flow field can degrade a turbine more quickly and must be understood for turbine design and optimal placement. Flow asymmetry may be detrimental to turbine survivability in addition to decreasing the resource available, potentiality causing variable forces across a turbine blade. Another example of the overlap of resource qualification and turbine survivability metrics is turbulence, which can both negatively affect the efficiency of a turbine and increase fatigue on turbine blades. As part of this study, these metrics will be explained and used to create maps of siting metrics for Admiralty Inlet.

### *1.4.3 Local Features*

*Vortices*

Vortices are complicated flow features that significantly affect the local flow field. In Admiralty Inlet, they are tidally generated at the headlands and other topographic/bathymetric features and advect throughout the region. They are associated with mixing and changes in sediment transport, and they even can affect the bathymetry in their path of travel over time (Geyer and Signell, 1990). In terms of turbine siting, they affect the currents in the area with increases near headland tips, where vorticity is generated, decreases in currents in recirculation zones lee of headlands, and sharp velocity gradients between. The directionality in areas through which vortices may travel can quickly change, sometimes to even be opposite to the direction of the main channel flow. Chapter 4 demonstrates that vortices appear to be associated with significant vertical velocities, density changes, and increased turbulence.

These effects of vortices appear to be mainly detrimental to turbine siting, and imply avoidance of eddy fields in siting turbines. However, vortices may be collocated with increases in currents near headland tips due to the channel geometry. The larger resource could be harnessed by a well-placed turbine of the correct design. Regardless of whether eddy fields are to be avoided or utilized, it is currently unknown where eddies advect in space and time at different stages of the varied tidal cycles seen in Admiralty Inlet, the specific mechanisms of generation, and how the vortices locally interact with other flow feature effects. All of these considerations may be significant for turbine siting, and as such more understanding of this feature is required to maximize power production and lifespan of turbines that may be placed in Admiralty Inlet in the future.

Vortices have been studied in various regions around the world. A thorough understanding of the controlling parameters in tidally-generated headland eddies using an idealized numerical model is presented in Signell and Geyer (1991). Some measurements have been gathered from eddy fields. Multiple studies examined the structure of the eddies with a shipboard ADCP (Canals et al., 2009; Geyer and Signell, 1990). Details of the nature of flow within an eddy were investigated with both numerical modeling and field data in Black

and Gay (1987). A good review of the various studies of eddies as well as a study on the effect of the boundary on the interior in an oscillating flow in multiple flow regimes can be found in Pawlak and MacCready (2002).

It is well-known that headland-generated eddies propagate around the Sound with the tides (Mofjeld and Larsen, 1984). Studies in a slowly-moving area south of Admiralty Head in the Puget Sound have connected flow separation and form drag with vortex generation (Edwards et al., 2004; McCabe et al., 2006; Warner and MacCready, 2009). Another study has examined the behavior of tilted vortices generated at sloping underwater ridges (Canals et al., 2009). Multiple studies from within the NNMREC have found evidence of vortices in Admiralty Inlet from data collection and analysis (Epler, 2010; Gooch et al., 2009; Polagye and Thomson, 2011; Thomson et al., 2011). However, the details of where, with what strength, and when these eddies travel around an energetic and complex site like Admiralty Inlet, as well as a detailed understanding of generation details, are largely open questions. While the basics of vortex generation are well-known (Kundu and Cohen, 2004; Panton, 2005; Signell and Geyer, 1991), many questions remain about the details of generation and the complex interaction of competing mechanisms described in the vorticity equation (though some studies have addressed some questions (Dong et al., 2007)). This work addresses some of these open questions.

*Turbulence*

A high level of turbulence is expected in the areas around Admiralty Head due to strong mixing over the sills, density variations in the flow, and strong shear in the water column. In addition, vortices are suspected of being collocated with increased levels of turbulence, and in fact the energy in the headland region can be dominated by headland-generated eddies (Thomson et al., 2011). Because of this, a detailed study of turbulence in the area is a natural fit with a detailed study of vortices, particularly considering the application of turbine siting.

Turbulence is known to be a concern for turbine siting. In wind energy, many studies have examined turbulence as a cause of turbine failure (Frandsen, 2007; Madsen and Frand-

sen, 1984; Sheinman and Rosen, 1992; Thomsen and Sørensen, 1999; Wagner et al., 2010). Turbulence is known to decrease turbine efficiency as well as add additional stress onto the turbines (Sheinman and Rosen, 1992; Wagner et al., 2010). This has also been found to be the case with tidal turbines (Maganga et al., 2010).

Differences in the mixing predicted by the predictions of various turbulence closure schemes are shown in comparisons of slices of model-predicted salinity along an estuary in the literature (Warner et al., 2005b,a). However, fewer comparisons can be found between model predictions and turbulence data itself, partially due to the difficulty of obtaining the turbulence data. Two such studies, one of which was in a tidally-dominated flow, found reasonable comparisons for dissipation rate (Simpson et al., 2002; Stips et al., 2002). Another study in a shallow tidal estuary compared model predictions with data for Reynolds stresses (Wang et al., 2011). All of these studies found reasonable model-data comparisons, which is probably the best one can hope to find in comparing high resolution turbulence data with turbulence closure scheme output from an ocean modeling code. The authors seek to add another set of comparisons to the literature for this specific region and code in order to understand the performance of the turbulence closure scheme used. These comparisons show multiple parameters: turbulent kinetic energy, turbulent dissipation rate, and Reynolds stress. To our knowledge, this is among the most extensive set of comparisons between data and simulation results from the Regional Ocean Modeling System (ROMS). As the flow field is better understood, through numerical modeling and field data analysis, the knowledge may be applied to tidal siting and characterization.

### *1.5 Research Objectives and Organization*

The objective of the research discussed in this dissertation is to increase understanding about potential siting issues for tidal turbines in Admiralty Inlet, with clear application to similar areas of interest near headlands. The focus is on vortices and vortex generation, the ability of the numerical code to model turbulence accurately, and presentation and interpretation of metric maps for turbine siting. Additionally, the next logical step of modeling turbines in ROMS is discussed and a few simulations are analyzed in detail.

This document is organized as follows. Methodology for this work will be laid out

in Chapter 2. This will include a summary of relevant aspects of the numerical ocean solver, the Regional Ocean Modeling System (ROMS), used in this research, with additional extra information on the turbulence closure scheme used and the scheme for advection of momentum. Additionally, setup specifications will be given for the numerical simulations, which include an idealized headland simulation and a realistic simulation of Admiralty Inlet. The simulation results are described in Chapter 3, in order to give a general picture for the flow fields seen in the area and to understand how well the model is performing. An in-depth analysis of the generation and behavior of vorticity in Admiralty Inlet will be described in Chapter 4, along with a discussion of how this behavior will affect turbine siting. Model-output turbulent kinetic energy will be compared with data in Chapter 5, and insights into the best use of this information will be discussed. Chapter 6 describes the metrics that are used to analyze and characterize the flow field for turbine micrositing, and shows maps of these metrics in Admiralty Inlet. A method for including turbine modeling in the simulations is briefly described in Appendix C, and then applied to an idealized headland case in order to examine the effect of turbines on the flow field. Conclusions and future work are presented in Chapter 7.

# Chapter 2

# METHODOLOGY

## *2.1 Introduction*

The numerical simulations were accomplished using the Regional Ocean Modeling System (ROMS) (Shchepetkin and McWilliams, 2005). ROMS solves the primitive equations in three dimensions with a structured horizontal grid and terrain-following vertical coordinates. Details of this widely used code pertinent to the research objectives will be given in this chapter and references will be given for further information.

First, this chapter will give an overview of the equations of motion solved for in ROMS. Next, options used in these simulations for open boundary conditions will be covered, along with closed boundary conditions to be used at the sidewalls, seabed, and sea surface. Because they are focuses of this research, the turbulence closure scheme will be described, followed by details of the scheme for the advection of momentum. A careful analysis of the truncation error inherent in the scheme will be given, which is investigated because of its contribution to mixing in the simulations. Also, a form of modified horizontal momentum equations in ROMS that includes this implicit horizontal viscosity inherent in the momentum advection scheme will be presented.

In order to form a basis of understanding of the complicated physics occurring in the simulation of Admiralty Inlet, an idealized headland simulation is first examined. This headland simulation captures the main flow characteristics of a prominent headland in a baroclinic tidal channel. Headlands of this general type are seen at multiple locations in Admiralty Inlet, but this simplified model is addressed in order to focus on the underlying mechanisms. Building from this knowledge base, a simulation of the Admiralty Inlet region is then executed and analyzed. The realistic simulation allows for a highly resolved investigation and in-depth analysis of the complex, detailed flow in Admiralty Inlet.

## *2.2 Equations of Motion*

The equations of motion in ROMS are the set of primitive equations (Haidvogel et al., 2008; Shchepetkin and McWilliams, 2005). These are the Navier-Stokes equations with the hydrostatic and Boussinesq approximations, including the assumption that the fluid is incompressible. After decomposing the velocities, pressure, and scalar concentrations into a mean and fluctuation, *i.e.,* $u = \bar{u} + u'$, the equations are time-averaged in order to obtain a Reynolds-Averaged, Navier-Stokes (RANS) form. The following are the governing equations for ROMS, where, as throughout this document, the overbar is dropped from the mean properties:

$$\frac{\partial u}{\partial t} + \underline{v} \cdot \nabla u - fv = -\frac{\partial \phi}{\partial x} - \frac{\partial}{\partial z}\left(\overline{u'w'} - \nu \frac{\partial u}{\partial z}\right) + F_u + D_u \tag{2.1}$$

$$\frac{\partial v}{\partial t} + \underline{v} \cdot \nabla v + fu = -\frac{\partial \phi}{\partial y} - \frac{\partial}{\partial z}\left(\overline{v'w'} - \nu \frac{\partial v}{\partial z}\right) + F_v + D_v \tag{2.2}$$

$$\frac{\partial \phi}{\partial z} = -\frac{\rho g}{\rho_0} \tag{2.3}$$

$$\frac{\partial C}{\partial t} + \underline{v} \cdot \nabla C = -\frac{\partial}{\partial z}\left(\overline{C'w'} - \nu_\theta \frac{\partial C}{\partial z}\right) + F_C + D_C \tag{2.4}$$

$$\frac{\partial u}{\partial x} + \frac{\partial v}{\partial y} + \frac{\partial w}{\partial z} = 0. \tag{2.5}$$

Here, $\underline{v} = (u, v, w)$ is the Cartesian mean velocity vector such that $(x, y)$ gives the horizontal east-west and north-south position, and $z$ the vertical position; $D_u$, $D_v$, and $D_C$ are diffusion terms to solve for explicit horizontal eddy viscosities and horizontal eddy diffusivity; $F_u$, $F_v$, and $F_C$ are forcing terms; $f(x, y)$ is the Coriolis parameter; $\nu$ and $\nu_\theta$ are the molecular viscosity and diffusivity; $K_M$ and $K_C$ are the vertical eddy viscosity and diffusivity; $\rho$ is the density which is dependent on pressure, temperature, and salinity; $\rho_0$ is the background density; $\phi(x, y, z, t)$ is the dynamic pressure with $\phi = p/\rho_0$; $C(x, y, z, t)$ is a scalar concentration field; and $g$ is the gravitational constant. The Reynolds stresses and

turbulent tracer fluxes are parameterized as follows:

$$\overline{u'w'} = -K_M \frac{\partial u}{\partial z} \tag{2.6}$$

$$\overline{v'w'} = -K_M \frac{\partial v}{\partial z} \tag{2.7}$$

$$\overline{C'w'} = -K_C \frac{\partial C}{\partial z}, \tag{2.8}$$

$$K_M = c\ell\sqrt{2k}S_M + \nu \tag{2.9}$$

$$K_C = c\ell\sqrt{2k}S_C + \nu_\theta \tag{2.10}$$

where $u', v', w'$ are fluctuations about the mean, and $S_M$ and $S_H$ are stability functions describing shear and stratification, and are functions of the local buoyancy and shear. The overbar in the Reynolds stress terms represents a time average. These final terms are addressed in a turbulence closure scheme by determining the governing equations for the turbulent kinetic energy, $k$, and a turbulent length scale, $\ell$. Note that these equations only include turbulent momentum and mass fluxes in the vertical direction, since horizontal turbulent momentum fluxes are much weaker. Horizontal mixing can be explicitly defined in the terms $D_u$, $D_v$, and $D_C$, but are not used in this application because the inherent numerical mixing alone smoothes the solutions enough to keep the simulations stable. The turbulence closure scheme will be described in detail in Section 2.4. More information on these terms and others not pursued here can be found in Warner et al. (2005b).

### *2.3 Boundary Conditions*

The specific boundary conditions to be used in a particular simulation are to be chosen by the user. For open boundary conditions, there are options for the free surface, two- and three-dimensional velocity fields, and tracers. At closed side walls there are options for no-slip or free-slip conditions. For the seabed one can choose the functional relationship between velocity and the bottom stress and at the sea surface one can enforce a wind stress, in addition to the typical dynamic boundary condition. This and more information on boundary conditions can be found at the website for ROMS.

### *2.3.1 Open*

There are a handful of options for forcing the numerical model at the open boundaries. These are conditions on the free surface height, velocity fields, and tracers. Techniques include clamping, gradient conditions, nudging, and radiation, among others. Users on the ROMS forum have found that a good combination for forcing the physics uses the following conditions: the Chapman boundary condition for the free surface elevation height, the Flather boundary condition for barotropic velocity, and the radiation and nudging boundary conditions for baroclinic velocity, and, accordingly, these are used in the simulations presented in this research.

The Chapman boundary condition on the free surface assumes that outgoing waves leave the domain at the shallow water wave speed of $\sqrt{gH}$ (Chapman, 1985). To do this, the following is imposed:

$$\frac{\partial \zeta}{\partial t} = \pm\sqrt{gH}\frac{\partial \zeta}{\partial \xi}, \tag{2.11}$$

where $\zeta$ is the free surface elevation, $H$ is the local water depth, $\xi$ is the generalized coordinate normal to the open boundary, and this condition has been written here for simplicity in the one-dimensional case. The sign of the condition is chosen based on the direction of the waves. This condition is intended to be consistent with the Flather boundary condition for the barotropic velocity. A diagram illustrating $\zeta$ and $H$ is in Figure 2.1.

The Flather condition acts on barotropic velocities. Deviations in the velocity from the exterior value of the normal barotropic velocity, $\bar{u}_{ext}$, which is set with boundary forcing information, radiate out of the numerical domain at the speed of the external gravity wave (Flather, 1976):

$$u = u_{ext} - \sqrt{\frac{g}{H}}(\zeta - \zeta_{ext}) \tag{2.12}$$

The radiation condition allows outgoing parameters (baroclinic momentum and tracers) to exit the domain. With the two-dimensional condition set, this is accomplished for waves incoming at an angle. The two-dimensional radiation condition for a variable $\phi$ at a boundary point is:

$$\phi_t = -\left(\phi^x \phi_x + \phi^y \phi_y\right),$$

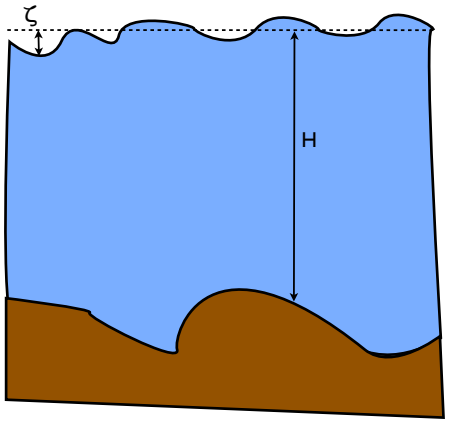


Figure 2.1: Notation illustration of the free surface, $\zeta$, as the fluctuation around mean sea level (dashed line), and the depth, $H$, as measured between mean sea level and the seabed.

where subscripts indicate partial derivatives, and

$$\phi^x = \frac{-\phi_t \phi_x}{\phi_x^2 + \phi_y^2} \tag{2.13}$$

$$\phi^y = \frac{-\phi_t \phi_y}{\phi_x^2 + \phi_y^2}. \tag{2.14}$$

Equations 2.13 and 2.14 are evaluated at the nearest interior point to the open boundary, and applied only to outgoing waves, as determined using a phase velocity check (Raymond and Kuo, 1984).

### *2.3.2 Closed*

*Vertical Boundary Conditions*

At the sea surface, $z = \zeta(x, y, t)$, are the following boundary conditions, from the continuity of stress:

$$K_M \frac{\partial u}{\partial z} = \tau_s^x(x, y, t)$$
$$K_M \frac{\partial v}{\partial z} = \tau_s^y(x, y, t),$$

and from the linearized kinematic boundary condition:

$$w = \frac{\partial \zeta}{\partial t},$$

where $\tau_s^x$ and $\tau_s^y$ are the applied surface stresses in the $x$ and $y$ directions, respectively.

At the seabed, $z = -h(x, y)$,

$$\begin{aligned} K_M \frac{\partial u}{\partial z} &= \tau_b^x(x, y, t) \\ K_M \frac{\partial v}{\partial z} &= \tau_b^y(x, y, t) \\ -w + \underline{v} \cdot \nabla h &= 0, \end{aligned}$$

where $\tau_b^x$ and $\tau_b^y$ are the bottom stresses in the $x$ and $y$ directions, respectively, and the final condition is the kinematic boundary condition.

The surface stresses are set using atmospheric information about the wind speeds from an atmospheric numerical model (see Section 2.7.2). Bottom stresses are set as a function of the bottom grid cell velocity. The function can be linear, quadratic, or logarithmic, and is chosen by the user along with the coefficient of friction, $C_D$. In these simulations, the quadratic relationship for the bottom stresses is chosen and is given as

$$(\tau_b^x, \tau_b^y) = \left( C_D u \sqrt{u^2 + v^2}, C_D v \sqrt{u^2 + v^2} \right), \tag{2.15}$$

where the bottommost output velocity is the velocity at the top of an assumed bottom boundary layer and $C_D = 3 \times 10^{-3}$.

*Sidewalls*

Vertical sidewalls in a ROMS simulation may generally have free- or no-slip conditions. The sidewalls are the vertical area above the seabed. In the case of variable bathymetry up to the coastline, the minimum height of the sidewall is set to the minimum depth in the simulation (see Figure 2.2). In the case of no bathymetry altering the simulation depth, the height of the sidewall is the maximum depth in the simulation. For a free-slip condition, the ghost cell value of tangential velocity on land is set to be equal to the closest interior value that is active, such that the gradient at the wall is zero. A no-slip condition requires

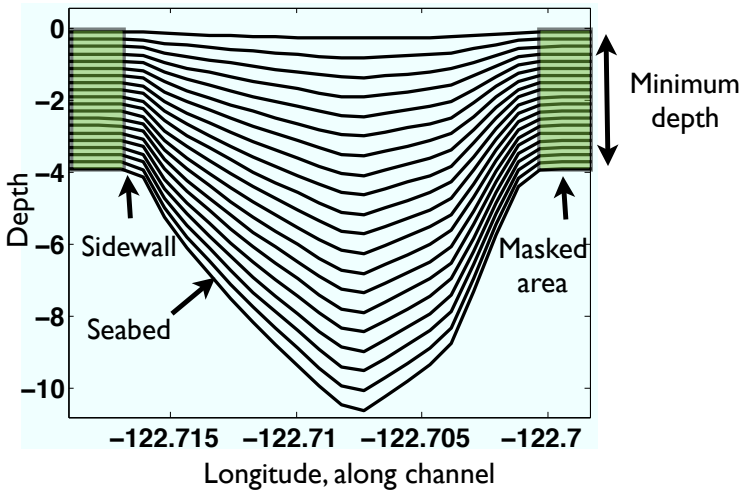


Figure 2.2: Illustration of sidewall versus seabed. The sidewall is vertical along the masked regions and is as deep as the minimum depth in the simulation. The seabed is the rest of the bottom boundary.

that the ghost cell value of tangential velocity be equal and opposite to the interior value so that the tangential velocity at the wall is zero.

Users are given the choice of no-slip or free-slip conditions at closed sidewalls, but only when there in no masking involved. Masking is the way to change active water cells into land cells using a switch in the grid generation. For example, in a simulation of a rectangular channel with no masking, the sidewalls can be set as no- or free-slip. However, if the channel has an area with masking, say, a headland protruding into the channel from the sidewall, that masked area has no-slip conditions hard-coded in.

### *2.4 Governing Equations in Turbulence Closure Scheme*

Since a focus of the research here is on the performance of the turbulence closure scheme in the realistic simulation and its ability to aid with turbine siting in terms of turbulence properties, the scheme is explained in detail here. Most of the turbulence closure schemes available in ROMS use the generic length-scale framework (Umlauf and Burchard, 2003;

Warner et al., 2005b). In this framework, well-known formulations are special cases of the generalized formulation and can be recovered using the appropriate constants. All of the formulations use a generic variable, $\psi$, to represent one variable (which may be turbulent dissipation rate, $\varepsilon$, turbulent frequency, $\omega$, or turbulent length scale, $\ell$), and the turbulent kinetic energy, $k$, for the other variable, which is equal to

$$k = \frac{1}{2}\left(\overline{u'^2} + \overline{v'^2} + \overline{w'^2}\right). \tag{2.16}$$

The governing equation for $k$ is

$$\frac{Dk}{Dt} = \frac{\partial}{\partial z}\left(\frac{K_M}{\sigma_k}\frac{\partial k}{\partial z}\right) + P_s + P_B - \varepsilon, \tag{2.17}$$

where $\sigma_k$ is the turbulence Schmidt number for $k$, $K_M$ is the vertical eddy viscosity presented in Equation 2.9, $P_s$ is the shear production, $P_B$ is the buoyancy production, and $\varepsilon$ is the turbulent dissipation rate. The shear and buoyancy production terms have been simplified to eliminate horizontal gradient terms that are expected to be small relative to vertical gradient terms, and have further been parameterized using the forms in Equations 2.6 to 2.8. Their forms are given as

$$P_s = -\overline{u'w'}\frac{\partial u}{\partial z} - \overline{v'w'}\frac{\partial v}{\partial z} = K_M M^2, \quad M^2 = \left(\frac{\partial u}{\partial z}\right)^2 + \left(\frac{\partial v}{\partial z}\right)^2$$
$$P_B = -\frac{g}{\rho_0}\overline{\rho'w'} = -K_H N^2, \quad N^2 = -\frac{g}{\rho_0}\frac{\partial \rho}{\partial z},$$

with $N$ as the buoyancy frequency. The turbulent dissipation rate is generally a function of $k$ and $\psi$.

In addition to the equation for $k$, a second equation is needed. ROMS uses a generic length scale (GLS) for its second variable, which can then be related to another variable depending on which constants the user chooses (*e.g.*, $\varepsilon$, $\ell$, or $\omega$). The governing equation for the GLS, $\psi$, is

$$\frac{D\psi}{Dt} = \frac{\partial}{\partial z}\left(\frac{K_M}{\sigma_\psi}\frac{\partial \psi}{\partial z}\right) + \frac{\psi}{k}(c_z P_s + c_s P_B - c_2 \varepsilon F_{wall}), \tag{2.18}$$

where $\sigma_\psi$ is the turbulence Schmidt number for $\psi$ and $F_{wall}$ is a wall function which is specific to each formulation.

For the $k-\varepsilon$ scheme, used in this work, with $\psi = \varepsilon$, the equations are

$$\frac{Dk}{Dt} = \frac{\partial}{\partial z}\left(\frac{K_M}{\sigma_k^\varepsilon}\frac{\partial k}{\partial z}\right) + P_s + P_B - \varepsilon \tag{2.19}$$

$$\frac{D\varepsilon}{Dt} = \frac{\partial}{\partial z}\left(\frac{K_M}{\sigma_\varepsilon}\frac{\partial \varepsilon}{\partial z}\right) + \frac{\varepsilon}{k}(c_{\varepsilon 1}P_s + c_{\varepsilon 3}P_B - c_{\varepsilon 2}\varepsilon), \tag{2.20}$$

where $\sigma_k^\varepsilon$ is the Schmidt number for the eddy diffusivity of turbulent kinetic energy and $\sigma_\varepsilon$ is the Schmidt number for the eddy diffusivity of the dissipation rate. The constant values are $\sigma_k^\varepsilon = 1.0$, $\sigma_\varepsilon = 1.3$, $c_{\varepsilon 1} = 1.44$, $c_{\varepsilon 2} = 1.92$, and $c_{\varepsilon 3} = \pm 1.0$.

## *2.5 Advection of Momentum*

The scheme for the advection of momentum used in these ROMS simulations is pertinent to energetics and mixing. Vorticity generated in the simulation depends on the level of mixing. In particular, the vortices seen in Admiralty Head have predominantly horizontal motions, and are generated by the friction along the sidewalls and seabed. Because horizontal mixing is not explicitly modeled in this simulation, frictional effects along the boundaries are at least partially due to truncation error, which stems from the scheme for the advection of momentum. Additionally, while the mixing in the simulation is expected to originate in the turbulence closure scheme, the truncation error due to momentum advection is another source of mixing that is occurring in the simulation, but due to the turbulence modeling scheme.

### *2.5.1 Description of Scheme*

ROMS by default uses a nominally third-order upstream advection scheme based on the UTOPIA scheme. Figure 2.3 shows a schematic of how the flux at the grid cell of interest is calculated. The value of the flux at the grid cell is approximated using a polynomial interpolation of field values from neighboring and upstream grid cells.

This advection scheme can be used for tracers as well as for velocity. More information about this scheme, including truncation error analysis, when used for advection of tracers, particularly in a constant velocity field, can be found in other sources (Haidvogel et al., 2008; Rasch, 1994; Shchepetkin and McWilliams, 1998). In this research, though, there

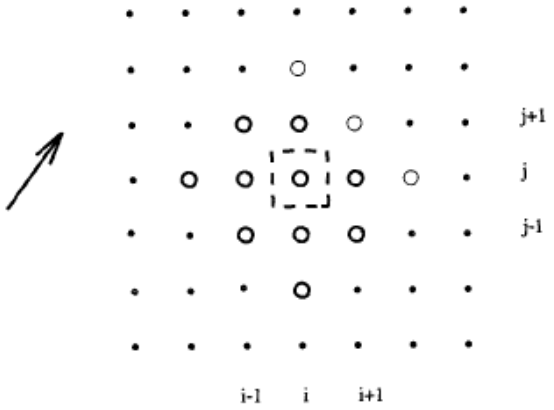


Figure 2.3: Diagram of UTOPIA scheme. Values at bold circles are used to approximate the flux into the grid cell indicated by the box. Utilized values are based on the direction of flow, as shown by the arrow. From Rasch (1994).

is a particular interest in the advection of momentum, and that is what is pursued here. The biggest difference between advection of momentum and advection of tracers is that the scheme is inherently nonlinear when advecting momentum. The case in which the velocity field is not constant is important. This spatial truncation error analysis is new as far as the authors can find in the literature, as others looking at these details have focused on the simpler case of advection of tracers in a uniform flow field.

### *2.5.2 Truncation Error*

Knowledge of the order and form of the truncation error may aid in understanding the performance of the momentum advection scheme and numerical mixing being generated in the system. When a physical equation $\mathcal{F}$ is numerically discretized as $F$, there is inherently a truncation error, $\epsilon$, introduced into the system:

$$\mathcal{F} = F + \epsilon. \tag{2.21}$$

The truncation error is solved for by subtracting off the discretized equation, expanded using Taylor series around the mean state, from the physical equation.

The conservation form of the horizontal advection of momentum is

$$\frac{\partial u}{\partial t} + \frac{\partial u^2}{\partial x} + \frac{\partial uv}{\partial y} = 0. \tag{2.22}$$

We have the following simplified form for the model of the spatial term in Equation 2.22:

$$u_{ijk}^{n+1} = u_{ijk}^{n} - \frac{\Delta t}{h^2}\left(F_{i+\frac{1}{2},j,k}^{n} - F_{i-\frac{1}{2},j,k}^{n} + G_{i,j+\frac{1}{2},k}^{n} - G_{i,j-\frac{1}{2},k}^{n}\right),$$

where $F$ is the flux in the $x$-direction and $G$ is the flux in the $y$-direction, superscript $n$ indicates the current time step and superscript $n+1$ the following time step, $\Delta t$ is the time increment, $h$ is the uniform grid spacing, and indices $i$, $j$, and $k$ indicate the $x$, $y$ and $z$ directions, respectively. Following analysis in Haidvogel et al. (2008), but without assuming the velocity field to be constant, the fluxes for momentum advection are rearranged and given from the ROMS code itself as follows:

$$F_{i+\frac{1}{2}} = h\left[\frac{1}{2}(u_i + u_{i+1}) - \frac{1}{8}(u_{i-1} - 2u_i + u_{i+1})\right] \times \left\{\frac{1}{2}(u_i + u_{i+1}) - \frac{1}{2}\left[\frac{1}{8}(u_{i-1} - 2u_i + u_{i+1}) + \frac{1}{8}(u_i - 2u_{i+1} + u_{i+2})\right]\right\},$$

$$G_{j+\frac{1}{2}} = h\left[\frac{1}{2}(u_j + u_{j-1}) - \frac{1}{8}(u_{j-1} - 2u_j + u_{j+1})\right] \times \left\{\frac{1}{2}(v_j + v_{j-1}) - \frac{1}{2}\left[\frac{1}{8}(v_{j-1} - 2v_j + v_{j+1}) + \frac{1}{8}(v_{j-2} - 2v_{j-1} + v_j)\right]\right\}.$$

Many indices are suppressed in this form, upstream direction assumptions $u_i + u_{i+1} > 0$ and $v_i + v_{i-1} \leq 0$ have been made, vertical fluxes have been ignored, and the terms have been rearranged to produce familiar forms.

The truncation errors for each part of these terms can be found by expanding in Taylor series around the value of the field at index $i$ or $j$. The Taylor series are analogous in $x$ and

$y$:

$$
\begin{aligned}
u_{i+1} &= u + hu_x + \frac{1}{2}h^2u_{xx} + \frac{1}{6}h^3u_{xxx} + \frac{1}{24}h^4u_{xxxx} + \mathcal{O}(h^5)\\
u_{i-1} &= u - hu_x + \frac{1}{2}h^2u_{xx} - \frac{1}{6}h^3u_{xxx} + \frac{1}{24}h^4u_{xxxx} + \mathcal{O}(h^5)\\
u_{i+2} &= u + 2hu_x + 2h^2u_{xx} + \frac{4}{3}h^3u_{xxx} + \frac{2}{3}h^4u_{xxxx} + \mathcal{O}(h^5)\\
u_{i-2} &= u - 2hu_x + 2h^2u_{xx} - \frac{4}{3}h^3u_{xxx} + \frac{2}{3}h^4u_{xxxx} + \mathcal{O}(h^5)\\
u_{i-3} &= u - 3hu_x + \frac{9}{2}h^2u_{xx} - \frac{9}{2}h^3u_{xxx} + \frac{27}{8}h^4u_{xxxx} + \mathcal{O}(h^5).
\end{aligned}
$$

Plugging these into the grouped terms above gives:

$$
\begin{aligned}
\frac{1}{2}(u_i + u_{i+1}) &= u + \frac{1}{2}hu_x + \frac{1}{4}h^2u_{xx} + \frac{1}{12}h^3u_{xxx} + \frac{1}{48}h^4u_{xxxx} + \mathcal{O}(h^5)\\
\frac{1}{2}(u_i + u_{i-1}) &= u - \frac{1}{2}hu_x + \frac{1}{4}h^2u_{xx} - \frac{1}{12}h^3u_{xxx} + \frac{1}{48}h^4u_{xxxx} + \mathcal{O}(h^5)\\
\frac{1}{8}(u_{i-2} - 2u_{i-1} + u_i) &= \frac{1}{8}h^2u_{xx} - \frac{1}{8}h^3u_{xxx} + \frac{7}{96}h^4u_{xxxx} + \mathcal{O}(h^5)\\
\frac{1}{8}(u_i - 2u_{i+1} + u_{i+2}) &= \frac{1}{8}h^2u_{xx} + \frac{1}{8}h^3u_{xxx} + \frac{7}{96}h^4u_{xxxx} + \mathcal{O}(h^5)\\
\frac{1}{8}(u_{i-1} - 2u_i + u_{i+1}) &= \frac{1}{8}h^2u_{xx} + \frac{1}{96}h^4u_{xxxx} + \mathcal{O}(h^6)\\
\frac{1}{2}(u_{i-1} + u_{i-2}) &= u - \frac{3}{2}hu_x + \frac{1}{2}h^2u_{xx} - \frac{3}{4}h^3u_{xxx} + \frac{17}{48}h^4u_{xxxx} + \mathcal{O}(h^5)\\
\frac{1}{8}(u_{i-3} - 2u_{i-2} + u_{i-1}) &= \frac{1}{8}h^2u_{xx} - \frac{1}{4}h^3u_{xxx} + \frac{25}{96}h^4u_{xxxx} + \mathcal{O}(h^5),
\end{aligned}
$$

all of which are again analogous for $v$ and in any direction.

Combining pieces and ignoring grid metrics for advection of $u$ momentum gives:

$$
\begin{aligned}
\frac{1}{h}\left(F_{i+\frac{1}{2}} - F_{i-\frac{1}{2}}\right) &= 2uu_x + h^2\left(\frac{1}{12}uu_{xxx} + \frac{1}{4}u_xu_{xx}\right) + \frac{1}{16}h^3\left(uu_{xxxx} + u_xu_{xxx}\right) + \mathcal{O}(h^4)\\
\frac{1}{h}\left(G_{j+\frac{1}{2}} - G_{j-\frac{1}{2}}\right) &= uv_y + u_yv + h\left(-\frac{1}{4}uv_{yy} - u_yv_y - \frac{1}{4}u_{yy}v\right) + \mathcal{O}(h^2)
\end{aligned}
$$

Since the first term in the $F$ equation and the second two terms in the $G$ equation are the spatial terms from the original equation, Equation 2.22, and can be subtracted off, the truncation error terms in $u$, and by analogy in $v$, are found as:

$$u:\ h\left(-\frac{1}{4}uv_{yy} - u_yv_y - \frac{1}{4}u_{yy}v\right) + \mathcal{O}(h^2) = h\left[-\frac{1}{4}(uv)_{yy} - \frac{1}{2}u_yv_y\right] + \mathcal{O}(h^2) \tag{2.23}$$

$$v:\ h\left(-\frac{1}{4}uv_{xx} - u_xv_x - \frac{1}{4}u_{xx}v\right) + \mathcal{O}(h^2) = h\left[-\frac{1}{4}(uv)_{xx} - \frac{1}{2}u_xv_x\right] + \mathcal{O}(h^2). \tag{2.24}$$

Note that the terms with the largest error for each momentum equation come from the cross terms (*i.e.*, terms involving both $u$ and $v$). This analysis shows that this scheme, when applied to advection of momentum, is first-order accurate in space for two dimensions. In one dimension, the scheme is second order accurate in space for advection of momentum, and when a tracer is being advected in a uniform velocity field, it is third order accurate in space. Future work will examine the spatial error in combination with the time discretization in order to determine the overall error for the advection of momentum.

An additional source of truncation error in the ROMS equations of motions that is not explored here is from the vertical grid. Terrain-following coordinates are known to create errors in the system when stratified flow moves over steep terrain, which could spuriously create vorticity in our system. There is some discussion of this and references in Burchard et al. (2004).

### *2.6 Modified Horizontal Momentum Equations*

Having derived the explicit forms for the lowest order truncation error terms, they can be added in to the equations of motion in ROMS to make explicit the effect of the truncation error. In this way, these modified governing equations are used in analysis done for vorticity and turbulence in Chapters 4 and 5, respectively, in order to directly find the effect of the error terms.

In ROMS, the horizontal momentum equations are given by

$$u_t + \underline{v} \cdot \nabla u - fv = -\frac{p_x}{\rho_0} + \frac{\partial}{\partial z}\left(K_M \frac{\partial u}{\partial z} + \nu \frac{\partial u}{\partial z}\right) \tag{2.25}$$

$$v_t + \underline{v} \cdot \nabla v + fu = -\frac{p_y}{\rho_0} + \frac{\partial}{\partial z}\left(K_M \frac{\partial v}{\partial z} + \nu \frac{\partial v}{\partial z}\right), \tag{2.26}$$

where $\underline{v} = (u, v, w)$, $\nu$ is the molecular viscosity, $K_M$ is the vertical eddy viscosity which parameterizes the Reynolds stress terms, and the diffusion and forcing terms have been left off. Because the flow is incompressible, the continuity equation is

$$u_x + v_y + w_z = 0.$$

Because ROMS is a hydrostatic code, the vertical momentum equation becomes a balance between gravity and the hydrostatic pressure.

We can find from scaling estimates that the molecular viscosity is smaller than the vertical eddy viscosity:

$$\frac{K_M}{\nu} \sim \frac{u'l}{\nu} = \mathrm{Re}_T \gg 1 \Rightarrow K_M \gg \nu,$$

where $\mathrm{Re}_T$ is the turbulent Reynolds number. In this case, $\mathrm{Re}_T$ is very large, and the molecular viscosity will be ignored for the rest of the analysis, although it is included in the ROMS equations themselves.

### *2.6.1 Implicit Numerical Viscosity*

Horizontal viscosity can be explicitly modeled in ROMS using one of several available flags. However, even without the explicitly-added viscosity, there is implicit numerical viscosity, $\nu_N$, inherent in a RANS simulation. This is a source of numerical error, but it can serve a purpose as well. The default momentum advection scheme is a nominally third-order upstream scheme. Previous analysis for the advection of tracers in a constant velocity field represent a velocity-dependent hyperviscosity brought into the simulation via the truncation error terms (Haidvogel et al., 2008). This smoothes out underresolved features and approximates the physics better than some explicit horizontal viscosity methods because it is a function of the flow field (Dong et al., 2007). It is also associated with enforcing the no-slip condition at the sidewalls through the advection operator. In Dong et al. (2007), it was found that vorticity plots from simulations of water flow around a tall cylinder with a decreasing level of explicit horizontal viscosity converged to the implicit-only (no explicit) horizontal eddy viscosity.

### *2.6.2 Added Terms from Truncation Error*

Since issues related to mixing and energetics occurring in a ROMS simulation are important in this study, it is critical to determine the size and effect of the horizontal numerical viscosity. To make explicit some of the implicit effects occurring because of the momentum advection truncation error, the form of the error terms are arranged for placement in the momentum equation.

The spatial truncation error terms from the momentum advection scheme are given in Equations 2.23 and 2.24. The typical form of a stress, $\tau$, in the Navier-Stokes equations is $\nabla \cdot \underline{\underline{\tau}}$. Some of the truncation error terms can be arranged into this form:

$$\underline{\underline{\tau}}_N = \frac{h}{4} \begin{bmatrix} 0 & (uv)_x & 0 \\ (uv)_y & 0 & 0 \\ 0 & 0 & 0 \end{bmatrix}.$$

Other truncation error terms cannot be fully put in this form. The leftover terms from the truncation error can be renamed into a vector:

$$\mathcal{T} = \frac{h}{2} \left( u_y v_y, u_x v_x, 0 \right).$$

We can do the same rearranging into stress form of the Reynolds stress terms from Equations 2.25 and 2.26:

$$\underline{\underline{\tau}}_R = \begin{bmatrix} 0 & 0 & 0 \\ 0 & 0 & 0 \\ K_M u_z & K_M v_z & 0 \end{bmatrix}.$$

### *2.6.3 Final Momentum Form*

With these rearranged and added terms, the effective ROMS momentum equations can be written as:

$$\underline{u}_t + (\underline{v} \cdot \nabla)\underline{u} + f\hat{k} \times \underline{u} = -\frac{1}{\rho_0}\nabla p + \nabla \cdot \underline{\underline{\tau}}_R + \nabla \cdot \underline{\underline{\tau}}_N + \mathcal{T}. \tag{2.27}$$

The second and third terms on the RHS are the stress terms resulting from the spatial numerical truncation error, and while the fourth term cannot be written in a convenient form it is expected to act as a force.

### *2.6.4 Effect of Spatial Truncation Error on Kinetic Energy in Simulation*

Energy dissipation in the system due to the truncation errors in the numerical advection is taken into account in this section. This erroneous dissipation could be accounting for a significant amount of mixing and playing a key role in the dynamics, without being specifically accounted for.

While horizontal mixing is not explicitly modeled in this simulation, there is effective horizontal mixing entering the system due to the truncation errors in the numerical scheme for the advection of momentum. This can supplement the vertical mixing from the turbulence closure scheme. The question is how large is the effect of truncation error. If it is large relative to the terms in the turbulent kinetic energy governing equation, this mixing should possibly be taken into account in the interpretation of turbulent kinetic energy.

The truncation error analysis is described in detail in Section 2.5.2. The expressions for the truncation error in the advection scheme are shown in Equations 2.23 and 2.24. We determine the effect of the truncation error terms in the kinetic energy equation by multiplying the terms in the $x$- and $y$-directions by $u$ and $v$, respectively:

$$u: \; h\left(-\frac{1}{4}u^2 v_{yy} - u u_y v_y - \frac{1}{4}u u_{yy} v\right) + \mathcal{O}(h^2)$$
$$v: \; h\left(-\frac{1}{4}u v v_{xx} - v u_x v_x - \frac{1}{4}u_{xx} v^2\right) + \mathcal{O}(h^2).$$

The terms resulting from the $u$ equation can be rewritten as

$$-h/4\left[(u^2 v_y)_y + (u u_y v)_y - (u_y)^2 v + u u_y v_y\right]. \tag{2.28}$$

The first two terms in Equation 2.28 are dispersive and conservative and can be ignored since they only result in energy transport. The second two terms cannot be put in a desirable form to ensure that they are dissipative; however they can still be calculated from the model output as source or sink terms. The numerical terms from the $u$ and $v$ momentum equations are given as:

$$\nu_{N,u} = -h/4\left[u u_y v_y - (u_y)^2 v\right] \tag{2.29}$$
$$\nu_{N,v} = -h/4\left[u_x v v_x - u(v_x)^2\right]. \tag{2.30}$$

These terms can be separated into components that are positive, adding energy to the flow, and negative, taking energy out of the system. This gives:

$$\text{Positive: } \nu_N^+ = \sqrt{\left(\nu_{N,u}^+\right)^2 + \left(\nu_{N,u}^+\right)^2} \text{ for } \nu_{N,u}^+, \nu_{N,v}^+ > 0$$
$$\text{Negative: } \nu_N^- = \sqrt{\left(\nu_{N,u}^-\right)^2 + \left(\nu_{N,u}^-\right)^2} \text{ for } \nu_{N,u}^-, \nu_{N,v}^- < 0.$$

Note that for an $(x, y)$ location at a particular time, both numerical dissipation rate components may be positive or negative, or one may be positive and one may be negative.

The size of these numerical terms compared with the modeled terms from the turbulent kinetic energy governing equation are shown in Figure 2.4. The turbulent dissipation rate and shear production are similar in size. The numerical sources and sinks are found to be significantly smaller than the other terms in the turbulence energy equation most of the time, but not always. At Nodule Point, the numerical terms are fairly consistently at least an order of magnitude smaller than the other terms. At Admiralty Head, the numerical effects are relatively larger at the higher energy comparisons, and may play a role in the dynamics there. Overall, though, from these results the truncation error is not expected to play a strong role in the energy dynamics.

## *2.7 Simulation Specifics*

### *2.7.1 Idealized Headland Simulation*

The flow in Admiralty Inlet is compressed due to multiple headlands along both sides of the channel. The largest is Admiralty Head on the east side of the channel. Eddies are known to be generated during each flow direction of the tidal cycle. The vortices may travel downstream or across the channel with varying speeds, and may persist for more than one tidal cycle. It is necessary to know the influence of large bathymetry and coastline features on the utility of any given location in Admiralty Inlet for tidal hydrokinetic energy before placing a significant number of turbines. It is desirable to quantify what flow conditions create the "best" turbine site. ROMS was first employed to examine the effects of a symmetric headland with a flat-bottomed rectangular channel on the tidal hydrokinetic siting characteristics (see Figure 2.5).

In this simulation, there are open boundaries at the west and east ends of the channel, and no-slip walls at the north and south ends. An $M_2$ tide is forced on both open boundaries with a phase difference between the two approximated using the shallow water wave speed, distance, and frequency of forcing. Both free surface and $u$-velocity are forced, using the ROMS open boundary forcing methods of Chapman for free surface and Flather for velocity

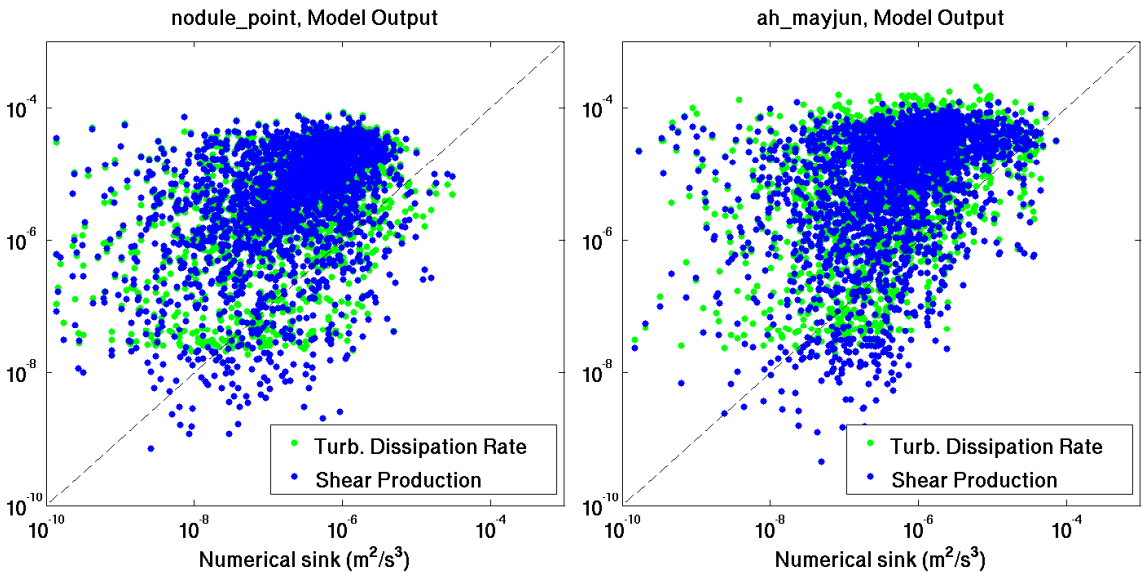


(a) Sink, Nodule Point




(b) Sink, Admiralty Head

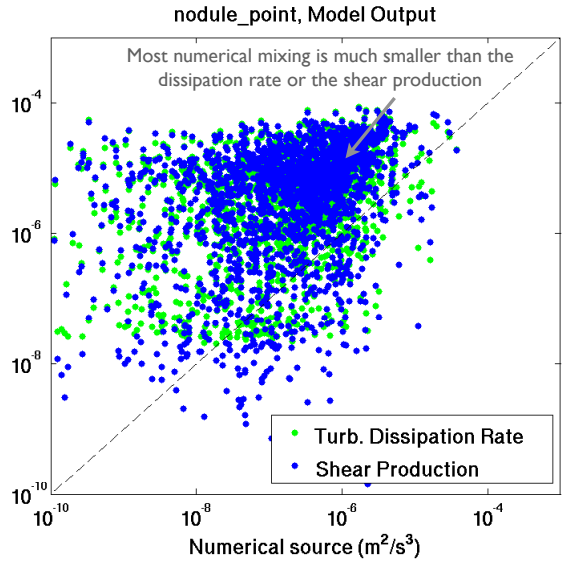


(c) Source, Nodule Point

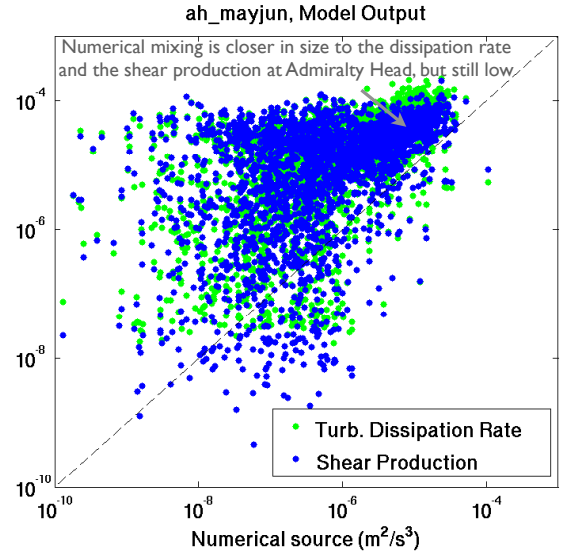


(d) Source, Admiralty Head

Figure 2.4: Numerical source and sink compared with other turbulence production terms.

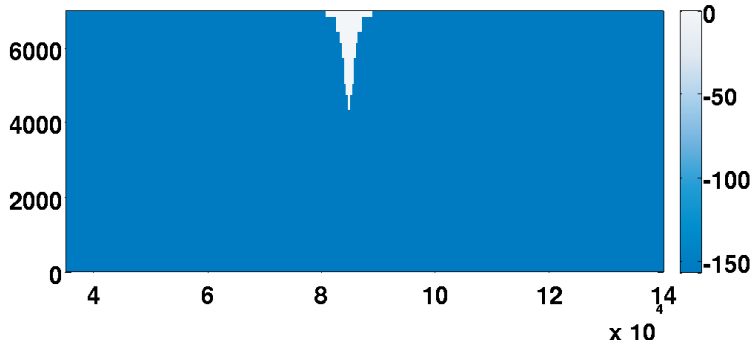


Figure 2.5: Idealized headland domain. This is a top-down view and units are meters. The coloring represents depth. The headland is close to the center of the channel and is symmetric.

(Section 2.3). The initial density is enforced at the east and west open boundaries, and outward-moving baroclinic momentum is radiated out of the system. Maximum speed reaches about 2.5 m/s and the density field is initialized using a linear stratification from 1025 kg/m$^3$ at the bottom to 1023 kg/m$^3$ at the surface, giving a buoyancy frequency of $N = 0.01$ 1/s. The Coriolis force is included. The dimensionless friction parameter $C_D = 3 \times 10^{-3}$ and was used in conjunction with quadratic bottom friction. This model was run for six tidal cycles and was ramped up over part of the first cycle. Averages and asymmetries were calculated over four tidal cycles.

The headland model domain is 105 km long and 7 km wide with a flat bottom of depth 157 meters, as seen in Figure 2.5. The headland is symmetric and about 5 km across and extends just over 2 km into the channel. The phase difference, $\phi$, between the two open boundaries is found using an approximation of a gravity wave moving across the length, $L$, of the channel. That is

$$\phi = \frac{L\omega}{\sqrt{gH}} = \frac{(105000 \text{ m})(1.4053 \times 10^{-4} \text{ rad/s})}{\sqrt{(9.81 \text{ m/s}^2)(157 \text{ m})}} = 0.3760 \text{ radians}, \tag{2.31}$$

where $\omega = 1.4053 \times 10^{-4}$ rad/s is the frequency of the $M_2$ tidal constituent and $H$ is the depth of the channel. This simulation is run in three dimensions. The horizontal resolution

is 100 meters and the vertical resolution is about 4 meters (in 40 layers).

### *2.7.2 Admiralty Inlet Simulation*

The high resolution simulation of Admiralty Inlet is one-way nested inside a larger, regional model of the neighboring waterways, called the Salish Sea, and part of the Pacific Ocean. The domain of this model is shown in Figure 2.6 and is described in detail in Sutherland et al. (2011). This regional model ranges in horizontal resolution from 280 meters in the Puget Sound to 3.1 km in the Pacific Ocean, and has 20 vertical layers with stretching such that the upper water column is more resolved than the bottom. It is one-way nested in the global Navy Coastal Ocean Model (NCOM) (Barron et al., 2006). Tidal forcing constituents were gathered from the $1/4^\circ$ TPXO7.1 inverse global tidal model (Egbert and Erofeeva, 2002) and imposed at the open boundaries, rivers were forced using daily river discharge data from U.S. Geological Survey gauge stations, and meteorological fields were forced using model output from the Northwest Modeling Consortium fifth-generation Pennsylvania State University-National Center for Atmospheric Research Mesoscale Model (MM5) regional forecast model (Mass et al., 2003). Both the regional model and the nested simulation include the Coriolis force. This regional model performs well in many skill assessments, though is known to have a deficiency in $M_2$ tidal amplitude.

The regional model was run for all of 2006. The nested Admiralty Inlet simulation was run for September 2006 for 30 days.

The horizontal grid in this simulation is uniform: the resolution in both the $x$ and $y$ directions is 65 meters. There are 20 vertical layers that are evenly spaced for every $(x, y)$ point. That is, the depth may change at every location horizontally, and for each $(x, y)$ point the depth is divided uniformly (see Figure 2.7). In this way, neighboring $(x, y, z)$ points in the domain may be in different vertical layers. The minimum vertical layer thickness is 0.2 meters, occurring at points that have the minimum depth allowed in the simulation of 4 meters, and the maximum thickness is about 9.3 meters and occurs where the domain is deepest. The bathymetry data was taken from the same set described in Sutherland et al.

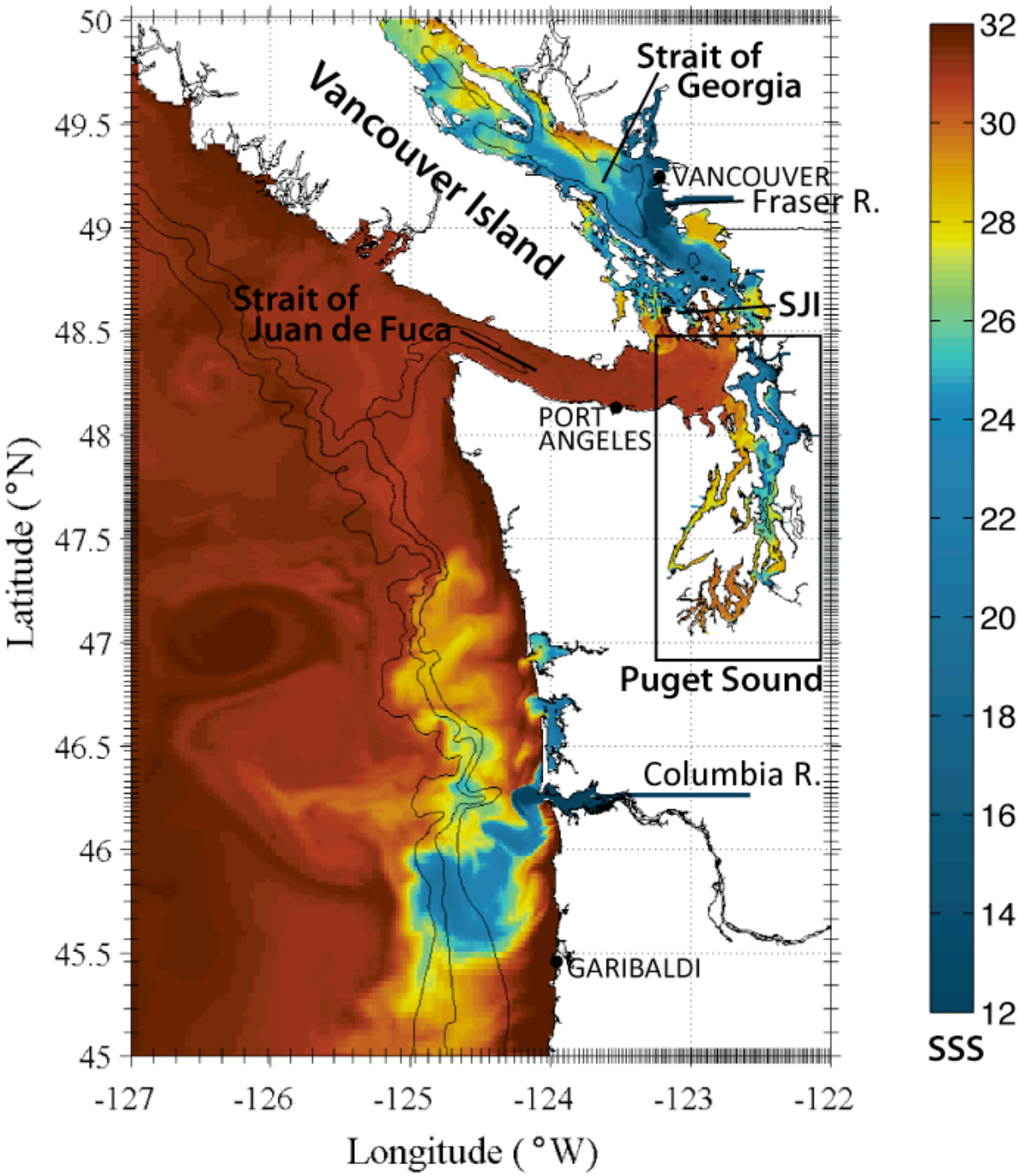


Figure 2.6: Surface salinity in a snapshot from the larger regional model whose output is used to force the nested simulation of Admiralty Inlet.

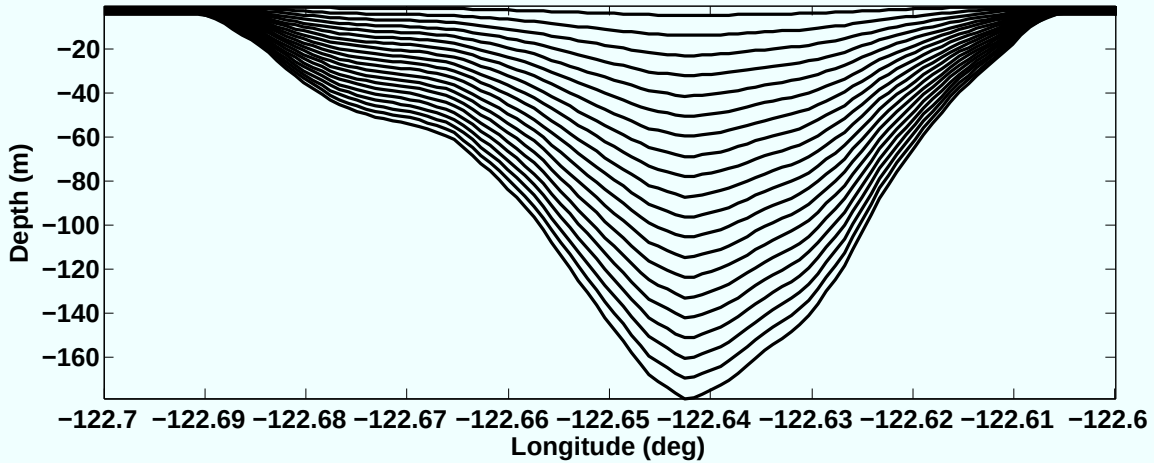


Figure 2.7: Example of vertical grid. Taken at a fixed latitude through deepest point in domain.

(2011) and is smoothed such that

$$r_0 = \max\left(\frac{H_i - H_{i-1}}{H_i + H_{i-1}}\right) \approx 0.2$$

for neighboring cells of full water column depth $H_i$ and $H_{i-1}$ (Beckmann and Haidvogel, 1993), and

$$r_1 = \max\left(\frac{z_{i,k} - z_{i-1,k} + z_{i,k-1} - z_{i-1,k-1}}{z_{i,k} + z_{i-1,k} - z_{i,k-1} - z_{i-1,k-1}}\right) \approx 7.6$$

for the vertical location $z$ for neighboring points $i$ and $i-1$ and vertical levels $k$ and $k-1$ (Haney, 1991).

The domain bathymetry is shown in Figure 2.8. The pilot site where a few turbines may be placed is just off Admiralty Head, so that the area of interest for turbine siting is near Admiralty Head. Point Wilson and the northeast corner of Marrowstone Island, along with Admiralty Head, strongly affect the flow field. Admiralty Bay is a large shallow region that can harbor eddies. Nodule Point on Marrowstone Island is a proposed testing area for tidal turbines and is thus also being studied.

The nested Admiralty Inlet simulation uses the same atmospheric forcing as the MoSSea model, interpolated down to the grid size, and all other forcing information comes into the

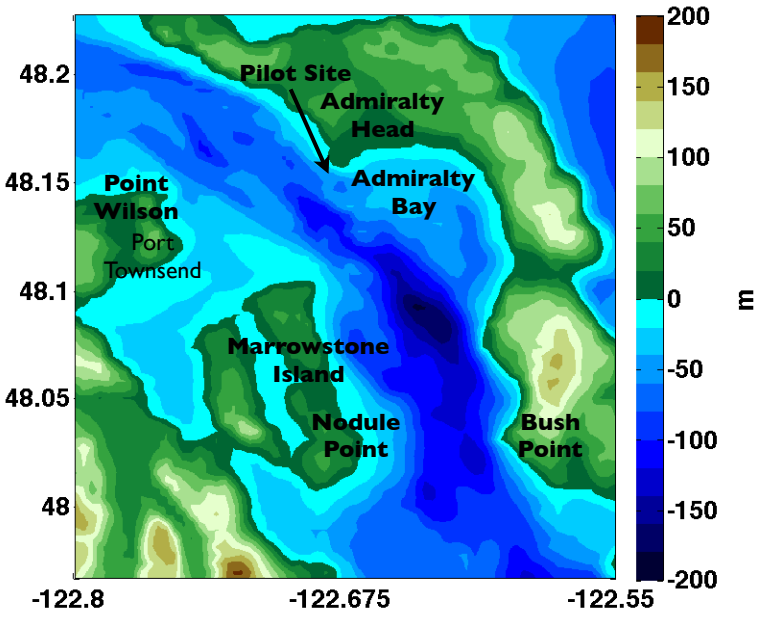


Figure 2.8: Simulation domain bathymetry of Admiralty Inlet, with significant locations marked for future reference.

model through the forcing from the MoSSea model. The open boundary conditions used for physical forcing are the Flather boundary condition for depth-averaged (barotropic) velocity, the Chapman boundary condition for free surface, radiation and nudging for the 3D (baroclinic) velocity, and for radiation with nudging for the tracer condition (Section 2.3). The seabed employs the quadratic friction relationship with velocity, with the dimensionless friction parameter $C_D = 3 \times 10^{-3}$, a typical value that was also used in the regional forcing model and was found to not significantly affect model results when varied by orders of magnitude Sutherland et al. (2011). The no-slip condition is imposed at every vertical wall.

# Chapter 3

# GENERAL SIMULATION RESULTS

## *3.1 Introduction*

In this chapter some results from simulations are presented, both for an idealized case and also for the realistic Admiralty Inlet case. The idealized case allows for the study of the effects of a headland in isolation, without the effects of complex bathymetry. The Admiralty Inlet case is examined in detail to note flow features in the system, some of which are seen in the idealized case and some of which are due to the complexity of the realistic situation.

An idealized simulation is examined in Section 3.2. With it, it is possible to investigate important flow features to increase understanding of the model for Admiralty Inlet. Section 3.3 describes the behavior of the realistic Admiralty Inlet simulation. Summary and discussion of this chapter can be found in Section 3.4. In particular, flow fields are examined in time to establish a general physical understanding of the typical behavior of the velocity, turbulent kinetic energy, free surface, vorticity, density, and vertical velocity. In the Admiralty Inlet simulation, comparisons are also made between the simulation output and data in order to understand model performance.

## *3.2 Idealized Headland Simulation Results*

The most notable features of the idealized headland simulation are the eddies formed at the headland with each tidal direction. The setup for the baroclinic, tidal channel simulation with a symmetric headland was described in Section 2.7.1. Evidence of these unsteady vortices are seen in all field variables. Since vorticity is one of the foci of this research, shown here is a set of snapshots of the model output showing effects of the vortices over flood tide. Flow field quantities are shown at a nominal hub height of 10 meters above the seabed, which in this flat-bottomed simulation is at a depth of 147 meters.

Flood begins with a packet of fast flow pushing past the headland to the right, as seen

in Figure 3.1(a), along with a circular dip in speed. This corresponds to the rollup of new vorticity right off the headland tip, that curls up into an eddy and is advected downstream, and the advection alongside of a persistent old vortex of the opposite sign (Figure 3.1(b)). The newly-forming vortex is associated with a dip in the free surface, as seen in Figure 3.1(c). This dip is expected as the free surface is adjusting to lower pressure in the center of the eddy and higher pressure along the outside of the eddy. Figure 3.1(d) shows the density field, in which there is a downwelling of the fresher water which is then pushed forward with the tide moving past the headland. The vorticity and density front generate turbulent kinetic energy (Figure 3.1(e)) and shear (Figure 3.1(f)), with shear magnitude calculated as

$$s_z = \sqrt{u_z^2 + v_z^2},$$

where the $z$ subscript denotes the partial derivative with respect to $z$. The turbulent kinetic energy and the shear both show the shape of the front, but with emphasis at different locations. All of the fields shown in Figure 3.1 demonstrate the jetting effect as the tide pushes around the headland.

Close to peak flood tide, multiple vortices are seen streaming from the headland tip downstream. Evidence of them can be seen in all of the flow fields: dips in the speed, free surface, and shear (Figures 3.2(a), 3.2(c), and 3.2(f)); patches of vorticity (Figure 3.2(b)); and density and turbulent kinetic energy wrapping around the outside of vortices (Figures 3.2(d) and 3.2(e)). Older persistent negative vorticity is still visible alongside the positive vortices being generated this half-cycle. The density field also shows that the horizontal gradients of density have advected downstream with the tide, but have retained much of the sharpness in the gradients. Turbulent kinetic energy and shear continue to accompany the vorticity field as well as the density front moving through the system.

Toward the end of flood tide, as ebb tide begins to ramp up, the speed increases alongside the headland first, a remnant from the large flood eddy that occupied most of the channel lee of the headland (Figure 3.3(a)). This eddy has a larger patch of vorticity that is weaker than earlier in the cycle (Figures 3.1 and 3.2), approximately consistent with conservation of potential vorticity (Figure 3.3(b)). In Figure 3.3(c), the effect of the large eddy can be seen as it causes a large dip in the free surface. The effect of ebb tide ramping up can be

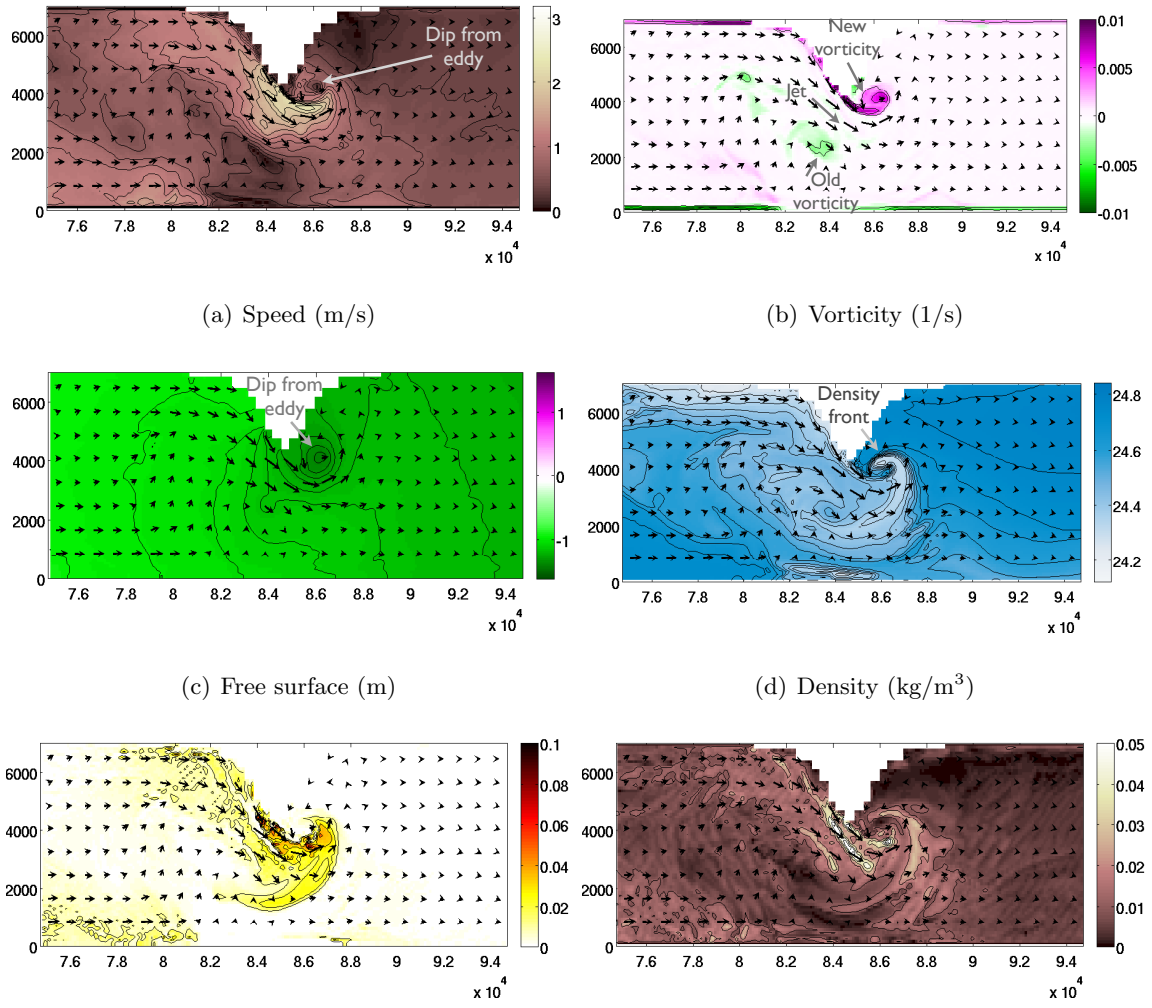


(a) Speed (m/s)

(b) Vorticity (1/s)

(c) Free surface (m)

(d) Density (kg/m$^3$)

(e) Turbulent kinetic energy (m$^2$/s$^2$)

(f) Shear (1/s)

Figure 3.1: Multiple snapshots are shown in shading and contours in $x$-$y$ (m) at hub height with horizontal velocity overlaid as arrows, just as the tide changes from ebb to flood. Fields shown are speed, vorticity, free surface, density, turbulent kinetic energy, and shear. The vorticity and tidal front can be seen in all fields.

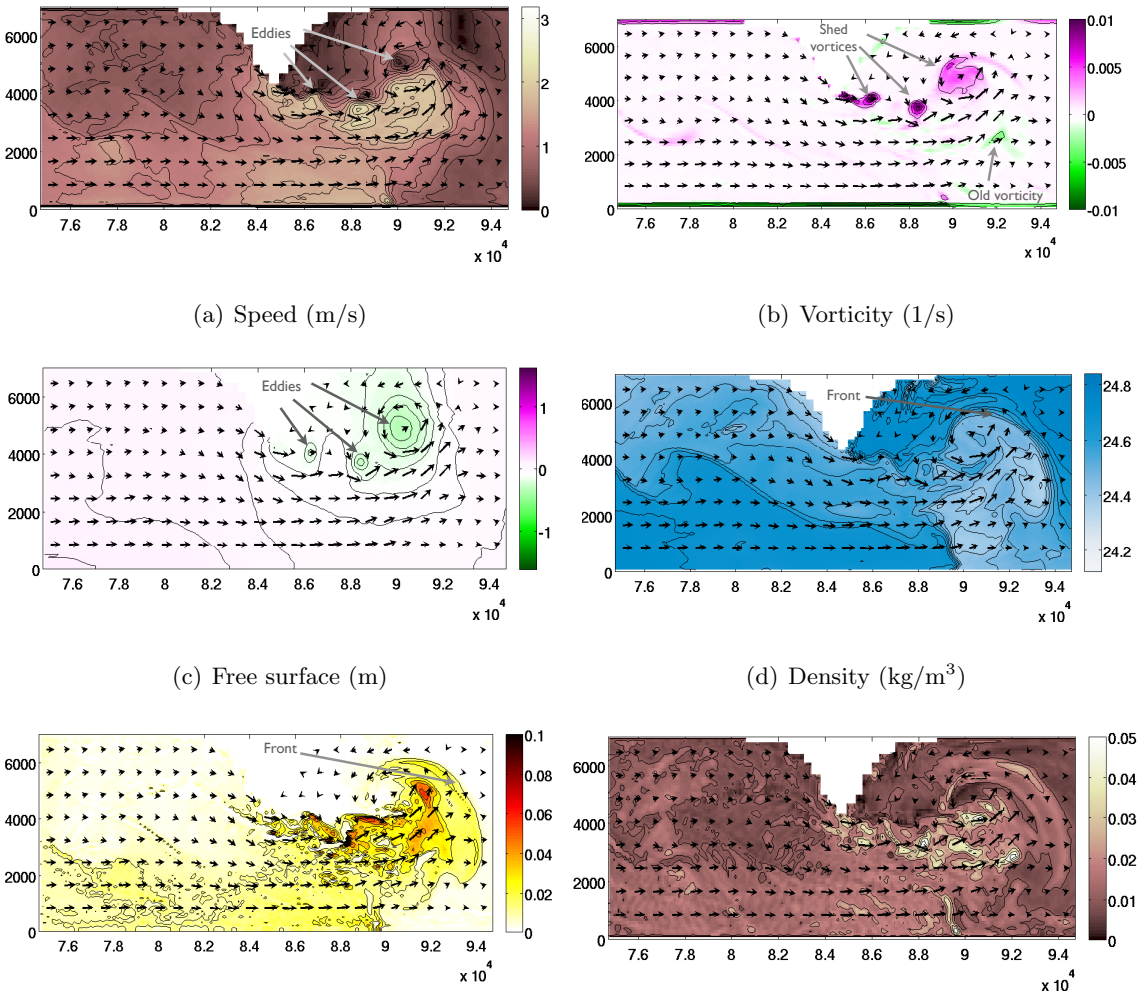


(a) Speed (m/s)

(b) Vorticity (1/s)

(c) Free surface (m)

(d) Density (kg/m$^3$)

(e) Turbulent kinetic energy (m$^2$/s$^2$)

(f) Shear (1/s)

Figure 3.2: Multiple snapshots are shown in shading and contours in $x$-$y$ (m) at hub height with horizontal velocity overlaid as arrows, at peak flood tide. Fields shown are speed, vorticity, free surface, density, turbulent kinetic energy, and shear. As the tide has progressed, more vorticity have shed from the headland tip and continued to affect the flow fields.

seen in the density, turbulent kinetic energy, and shear fields as well (Figures 3.3(d), 3.3(e), and 3.3(f)), where the density field prepares for another front on the next tidal cycle, and the other fields continue to accompany the vorticity field and areas of higher speeds.

These patterns of the various flow field characteristics around the regions with vortices, and the tidal fronts moving throughout the system, can be seen in the Admiralty Inlet simulation, along with more complicated details.

## *3.3 Admiralty Inlet Simulation*

### *3.3.1 Examination of Model Flow*

Many details of the flow field that we find in the Admiralty Inlet simulation can be traced back to and understood further from the simpler idealized headland case. The vorticity generated in this simulation behaves similarly to the idealized case: it advects downstream and persists before advecting back with the new tide. The speed and free surface both show effects from the eddies. The density field has fronts that move with the tide, as before, and turbulent kinetic energy is collocated with the vortices and fast tidal speeds.

Snapshots from a variety of flows field are shown in this section at three different times for a sample tidal cycle. Plots are shown at the surface when possible, and at 10 meters below mean sea level when more appropriate (for vertical velocity, shear, and turbulent kinetic energy). There is little variation from the surface to 10 meters down so that the surface and near-surface fields are nearly coincident in the spatial features shown. Plots show each field in color and sometimes in black contours for emphasis. Arrows indicate the size and directions of the tidal currents at the same vertical height as the plotted field. The signal in the upper right corner of the plots shows the free surface elevation at a point near Port Townsend on the western side of the channel, with a red dot indicating the time of that particular snapshot in the cycle.

Figure 3.4 shows flow properties after peak ebb tide. At this point, the free surface is mostly on the low end of its cycle (hence the all-green coloring) since it is ebb tide. The free surface also shows a few dips corresponding to vortex locations as well as along-channel contours showing the minor effect of the Coriolis force. The vorticity field shows that many

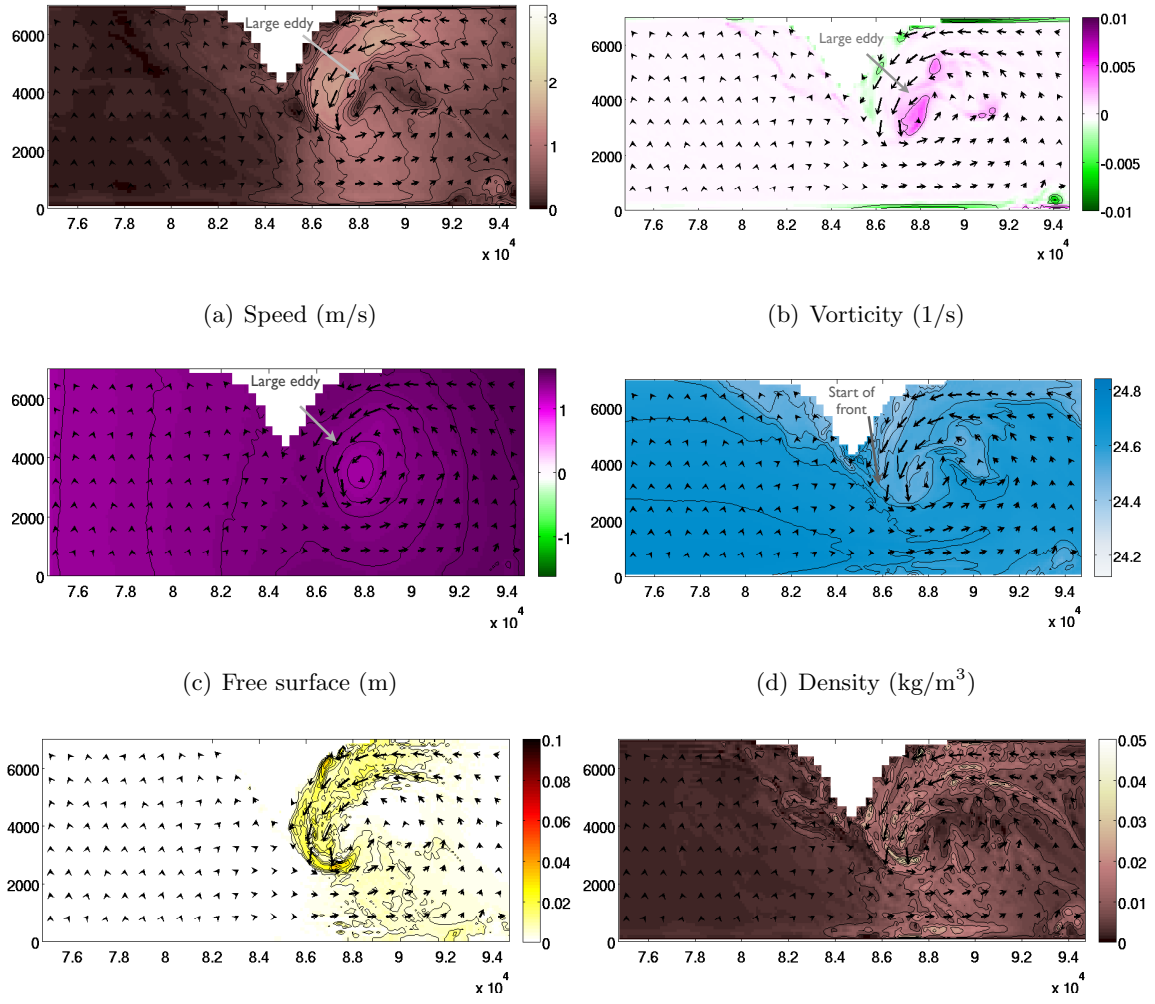


(a) Speed (m/s)

(b) Vorticity (1/s)

(c) Free surface (m)

(d) Density (kg/m$^3$)

(e) Turbulent kinetic energy (m$^2$/s$^2$)

(f) Shear (1/s)

Figure 3.3: Multiple snapshots are shown in shading and contours in $x$-$y$ (m) at hub height with horizontal velocity overlaid as arrows, just as the tide changes from flood to ebb. Fields shown are speed, vorticity, free surface, density, turbulent kinetic energy, and shear. A large eddy occupies the channel toward the end of the tide.

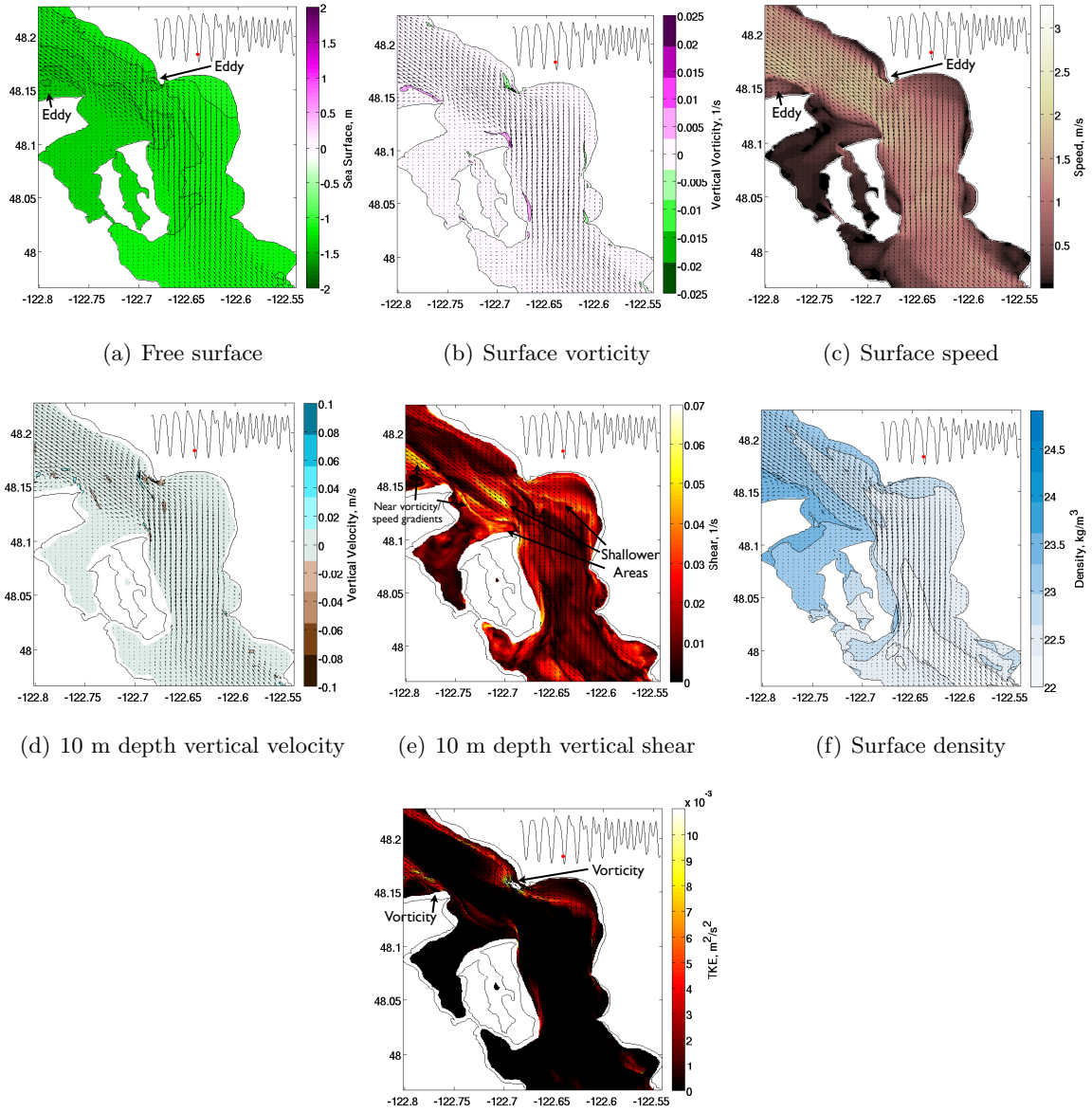


(a) Free surface

(b) Surface vorticity

(c) Surface speed

(d) 10 m depth vertical velocity

(e) 10 m depth vertical shear

(f) Surface density

(g) 10 m depth turbulent kinetic energy

Figure 3.4: Properties on ebb tide in Admiralty Inlet, at 1:15PM on 9/4/06.

of the points in the channel have tendrils of vorticity streaming from them as ebb tide pushes past. The plot of surface speed shows that most of the channel has a uniform speed, and the overlaid arrows show the same for direction, except lee of points where there is recirculation with vorticity. Intensification due to flow past the headlands in the channel is strongest earlier in the tidal phase. The vertical velocity field is not particularly active at this point, but does take on significant values near Admiralty Head, associated with the vorticity field.

It is interesting to compare shear and turbulent kinetic energy fields since they both can negatively impact turbines and are both associated with velocity fields (shear with the vertical derivative of the horizontal velocity fields and turbulence with increased velocity fluctuations), yet they have distinct behavior. The turbulent kinetic energy is produced by current shear, as seen from the production term in the kinetic energy equation (Equation 2.17). The turbulent kinetic energy is also affected by buoyancy (Equation 2.17), however, which usually acts to extract kinetic energy from the flow field in regions of significant stable stratification. Therefore, regions of high shear and high turbulence do not always correspond. In addition, current shear is lower frequency and associated which larger horizontal length scales, whereas turbulence is of much higher frequencies and has much smaller horizontal length scales. The shear is focused in particular in shallower areas, as the speed decreases near the seabed, whereas the turbulent kinetic energy is more focused in areas with high vorticity generation. The surface density shows that a considerable amount of river water has entered the domain from the south end and is headed northward with the tide. The river water enters at the boundaries at a rate that is prescribed by the boundary information of the forcing model.

The flow fields at the start of flood tide are shown in Figure 3.5. The mid-range color of the free surface plot shows that the tide is close to mean sea level. There is a persistent dip in free surface alongside Point Wilson as vortices are beginning to be spun off. This location of the vortex, just north of Point Wilson, is the area that first shows flood tide, with strong eastward velocities along the shore. A streak of vorticity from the previous ebb has been advected with the flow, now stretching with the flood tide. There is new vorticity being generated and streaming from each of the prominent points in North Admiralty Inlet:

Point Wilson, Admiralty Head, and northeast Marrowstone Island. The speed shows the front of the tide moving through the channel and being affected along the way by Point Wilson, Admiralty Head, and the corner of Marrowstone Island, with speed up at the points and recirculation behind. There is also a thin, long patch of increased speed coming into the estuary past Point Wilson that carries along with it old vorticity. There are notable negative vertical velocity strips in the field due to convergence (White and Wolanski, 2008) (discussed further in Section 4.2.6) and possibly from denser water meeting lighter water and pushing underneath. These strong negative vertical velocity regions can be aligned with a density gradient, suggesting a connection between the fields. An example of when a front often develops is when flow builds up behind a headland before the tidal direction changes, and then pushes past with the change in tide. These horizontal density gradients can then advect with the tide before being broken up by other currents over time. Shear again seems to be concentrated in shallower areas and TKE in vorticity-affected areas. It is expected that the vertical shear nearer the seabed would be largest, when it is in the bottom boundary layer. However, the shear is also largest in regions in which strong currents are moving from deeper to shallower areas, with strong speeds and shear as the flow adjusts to the change in bathymetry. This is shown in a plot of mean shear throughout Admiralty Inlet at ten meters above the seabed in Figure 6.24.

A view of what happens later in the flood tide is given in Figure 3.6. The surface elevation in the domain is above mean sea level but, despite flood being finished according to the velocity field, the surface has not yet reached maximum flood tide. The free surface elevation and velocity field are close to 90° out of phase but, in addition to this, flood tide as defined by the velocity field clearly starts at different times in different parts of the domain. The free surface shows a large dip in Admiralty Bay south of Admiralty Head, where an eddy has expanded over the entire bay toward the end of flood tide, and another dip, implying lower pressure in the center of the eddy, from the vortex off Marrowstone Island. Vortices extend leeward from Admiralty Head and from the NE point of Marrowstone Island, mirroring each other and creating a strong jet region between them. Additionally, the recirculation areas from these eddies are extensive, even as strong currents continue to push in the area between the eddies. This jetting is clearly seen in Figure 3.6(c). In

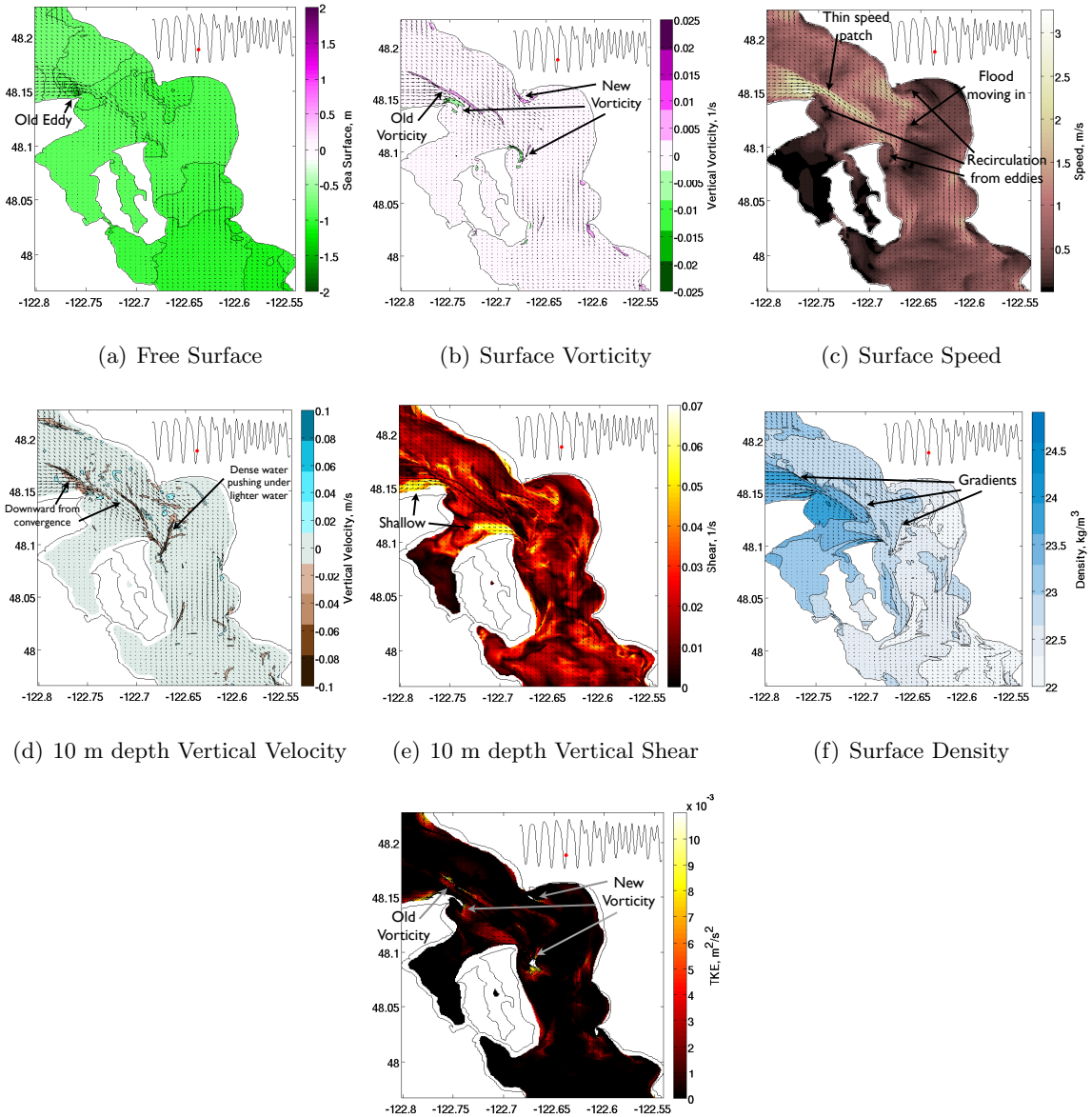


(a) Free Surface

(b) Surface Vorticity

(c) Surface Speed

(d) 10 m depth Vertical Velocity

(e) 10 m depth Vertical Shear

(f) Surface Density

(g) 10 m depth Turbulent Kinetic Energy

Figure 3.5: Properties on flood tide in Admiralty Inlet, at 6:45PM on 9/4/06

the figure, speeds are increased between the eddies and velocity vectors have significantly different directions in neighboring areas due to the eddies and jet. Negative vertical velocity is again apparent in areas of convergence, of which there are many at this time in the tidal cycle. The vertical velocity also corresponds to some of the sharp density gradients. The density field traces out the flow features in the system. Flood tide brings denser water southward through the channel, while the eddies on the sides of the jet contain fresher water. The freshest area in North Admiralty Inlet, just southeast of Admiralty Head, will shortly move with the start of ebb tide as the water there pushes past Admiralty Head as a front in density and speed, along with associated negative vertical velocity. Shear is spread throughout the channel but is concentrated in shallower areas like Admiralty Bay and north of Marrowstone Island. Meanwhile, the turbulent kinetic energy highlights the jet/vortex/front area.

The model output was harmonically analyzed to create a map of the harmonic constants in the area. Harmonic analysis was described in Section 1.3.3. Because the less-dominant tidal constituents maintain a constant phase and size relative to the dominant tidal constituent for each type of tide, we examine only $M_2$ and $K_1$ here to understand the behavior of the diurnal and semi-diurnal constituents (Mofjeld and Larsen, 1984). Inference was used to approximately separate the $P_1$ constituent from the $K_1$ free surface constituent using a known local relationship from two nearby 6-month data sets (the $P_1$ amplitude and phase are approximately offset by a factor of 0.33 and -2 degrees, respectively, from the reference constituent $K_1$) (NNMREC, University of Washington, 2010; Polagye, 2010), since a half year-long period is required to separate the two similar frequencies otherwise (Pawlowicz et al., 2002). This relationship did not seem to improve behavior with the tidal current decomposition and so was not used in the tidal current decomposition. Thus, we expect the $K_1$ velocities to be inaccurate for this reason, as well as because harmonic analysis does not work as well with tidal currents as with the tides themselves (which would also apply to the $M_2$ tide) (Godin, 1983).

The amplitude and phase for the $M_2$ constituent are shown in Figure 3.7 for the free surface. Harmonic constant maps for $K_1$ are shown in Figure 3.8. Admiralty Bay has the most noticeable impact on these maps. The $M_2$ amplitude plot shows deviation in the

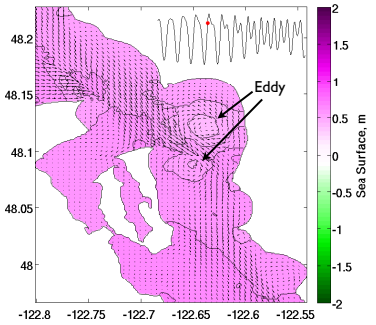


(a) Free Surface

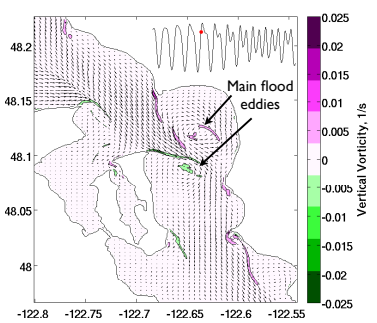


(b) Surface Vorticity

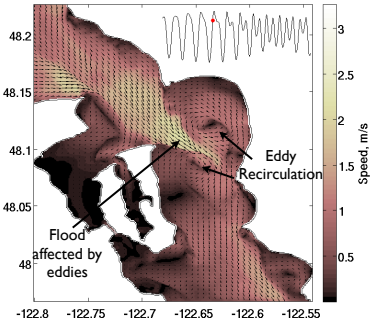


(c) Surface Speed

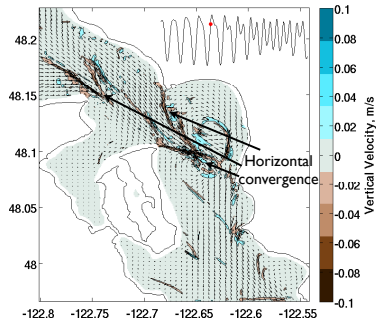


(d) 10 m depth Vertical Velocity

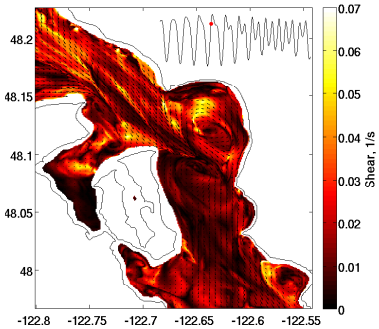


(e) 10 m depth Vertical Shear

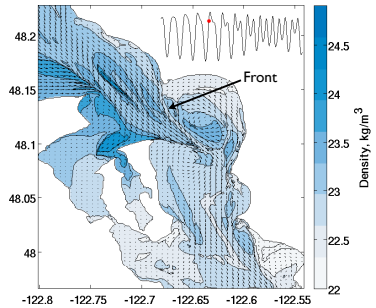


(f) Surface Density

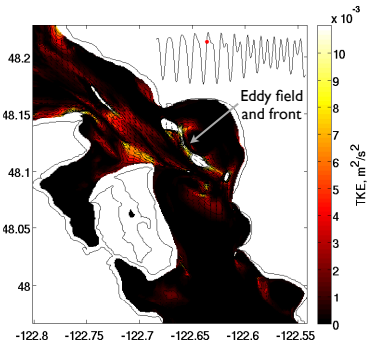


(g) 10 m depth Turbulent Kinetic Energy

Figure 3.6: Properties toward end of flood tide in Admiralty Inlet, at 9:45PM on 9/4/06

bay, but $K_1$ amplitude and phase plots both show changes in behavior right where the large eddy sits in Admiralty Bay on flood tide, implying that the Admiralty Bay eddy is more associated with the diurnal rather than semi-diurnal tide. Phases in both $M_2$ and $K_1$ progress through the channel, but the $M_2$ tide has a much larger range of phase than the $K_1$ tide, as expected (Mofjeld and Larsen, 1984).

Figure 3.9 shows the $M_2$ constants for velocity at hub height and Figure 3.10 shows them for $K_1$. Both amplitude maps show increased values in the areas of the channel that showed faster speeds in the snapshots examined earlier in this section. The highest values are in similar, but not identical, areas. For example, the strongest amplitudes for the $M_2$ tide is just north of Point Wilson, with smaller peaks near each of the other headland tips, and some down the main channel constriction. The $K_1$ amplitudes show a peak just north of Point Wilson and in the main channel, but the areas of larger values tend to be in the middle of the channel rather than focused at the headland tips. Also, whereas the $M_2$ and $K_1$ amplitudes are about the same size for the free surface elevation, the $M_2$ velocity amplitudes are much larger than those of $K_1$. The phase maps for the velocities are not smooth like those for the free surface; instead, they have sharp variation over short length scales in areas behind headlands where the flow can behave nonlinearly and the direction rapidly changes.

### *3.3.2 Model-Data Comparisons*

#### *Satellite Images*

Satellite images of the area can sometimes catch interesting events occurring near the water surface. Flow features can have surface signatures by changing the wavelength of the surface wave patterns, and the differences can then be visible due to differences in light reflection. Figure 3.11(a) shows a Google Earth image of the water immediately surrounding Admiralty Head. The surface appears to show the effect of the ebb tidal flow ripping past the headland, and the vorticity in the flow wrapping into an eddy with recirculation lee of the headland, seen as a smoother water surface. Figure 3.11(b) shows a somewhat typical moderately-sized ebb vortex in model output surface vorticity off Admiralty Head with a very similar

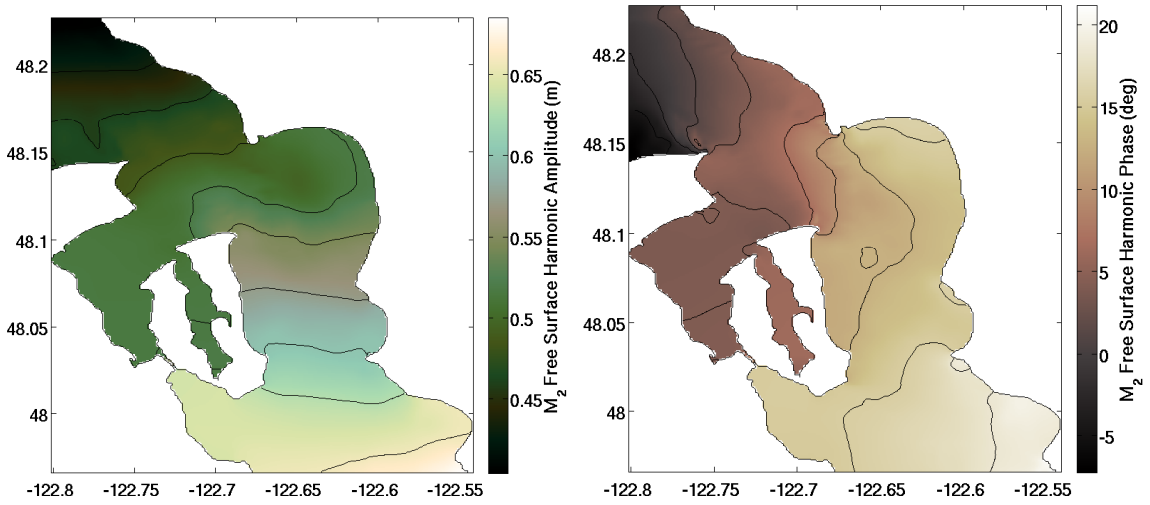


(a) Amplitude (b) Phase

Figure 3.7: $M_2$ free surface harmonic constants

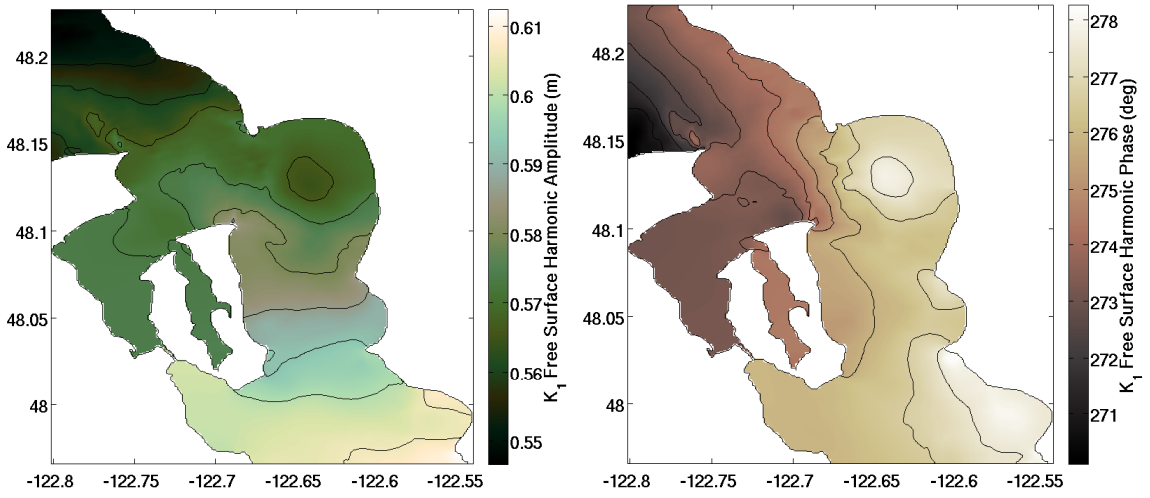


(a) Amplitude (b) Phase

Figure 3.8: $K_1$ free surface harmonic constants

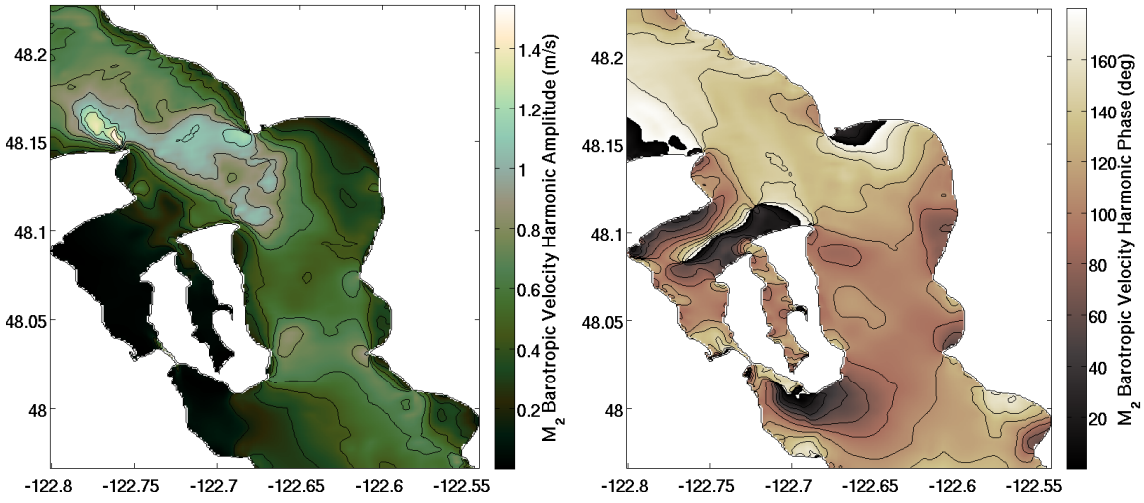


(a) Amplitude (b) Phase

Figure 3.9: $M_2$ hub height velocity harmonic constants

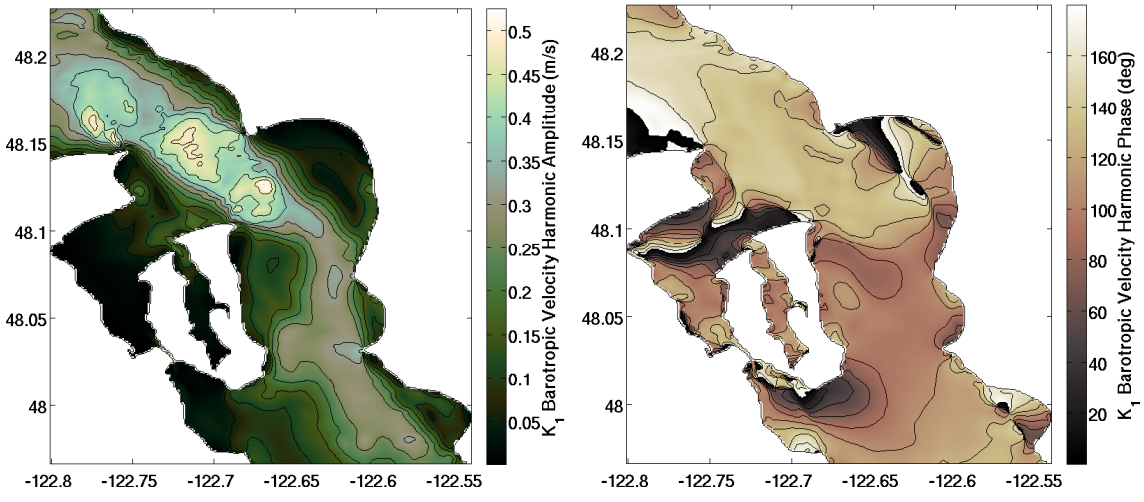


(a) Amplitude (b) Phase

Figure 3.10: $K_1$ hub height velocity harmonic constants

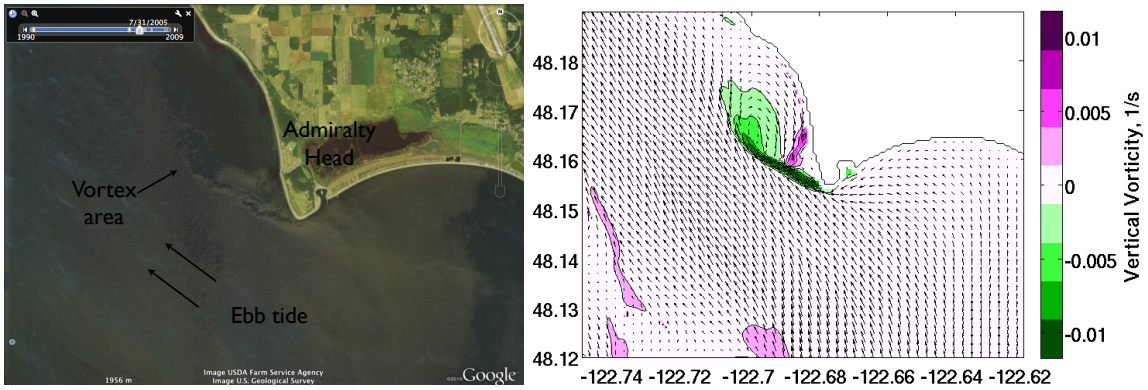


(a) Google Earth (b) Surface vorticity

Figure 3.11: Comparison between typical ebb vortex in model with Google Earth image.

appearance to the satellite image. Without a time stamp on the satellite image, however, an exact comparison cannot be made.

It is somewhat difficult to tell what is happening in the satellite image in Figure 3.12(a) until compared with a surface density plot from the simulation in Figure 3.12(b). With this extra information, we can better interpret what is seen in the satellite image. Between flood and ebb tides, there is time when flood tide is still ending, near Marrowstone Island, and ebb tide is just starting with a frontal push past Admiralty Head. This is most easily seen in the density field since the front brings fresher water with it. The density field also helps explain the front pattern further south, and the streak east of Marrowstone Island, since that is where flood tide, with dense water, continues flooding. The flooding brings with it vorticity streaming off Marrowstone Island, as apparent in the satellite image, and as can be seen in the vorticity field (not shown).

*Time Series Data*

A direct time series comparison between data from a NOAA tide gauge station at Port Townsend and simulation output from the same location is shown in Figure 3.13. The model phase lines up well with the data. Times when the diurnal tide dominates, such as at the beginning, middle, and end of the month, line up well, though some of the small tides

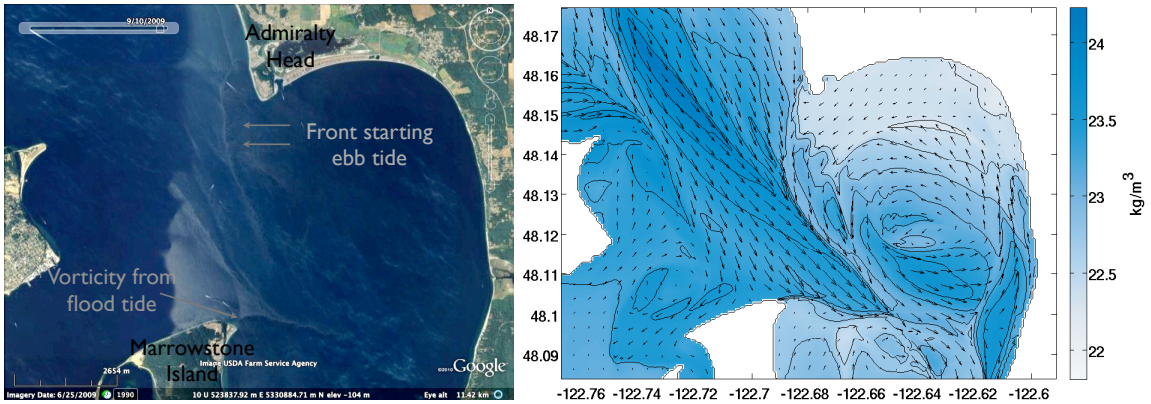


(a) Google Earth (b) Surface density

Figure 3.12: Comparison between transition from flood to ebb tide with Google Earth image.

are missed. The timing of the minimum in tides due to the lunar declination cycle (near 9/10/06 and 9/24/06) is good, but the extremums in the tides are not large enough at these times. There is a known deficiency in the dominant semi-diurnal $M_2$ tide in the regional forcing model that has been inherited into this nested model. It is logical that at a time of minimum effect of the diurnal tides, the model would perform worst.

*Time Series Comparison Method*

Only a few sets of data are available during the actual time period of the simulation run, September 2006. However, detailed examination of the simulation output shows that many of the features in the system occur periodically under similar circumstances. For example, medium-sized eddies tend to be generated and shed from Admiralty Head during tides with a larger free surface range (diurnally-dominated tides), and smaller eddies are shed on smaller, shorter tides (the small tide during a time of strong diurnal inequality). The largest eddies are produced during dominantly semi-diurnal tides, which during this simulation period are also approximately aligned with the strongest tidal currents. It follows that there may be a way to group occurrences of similar behavior and, using this technique, align non-

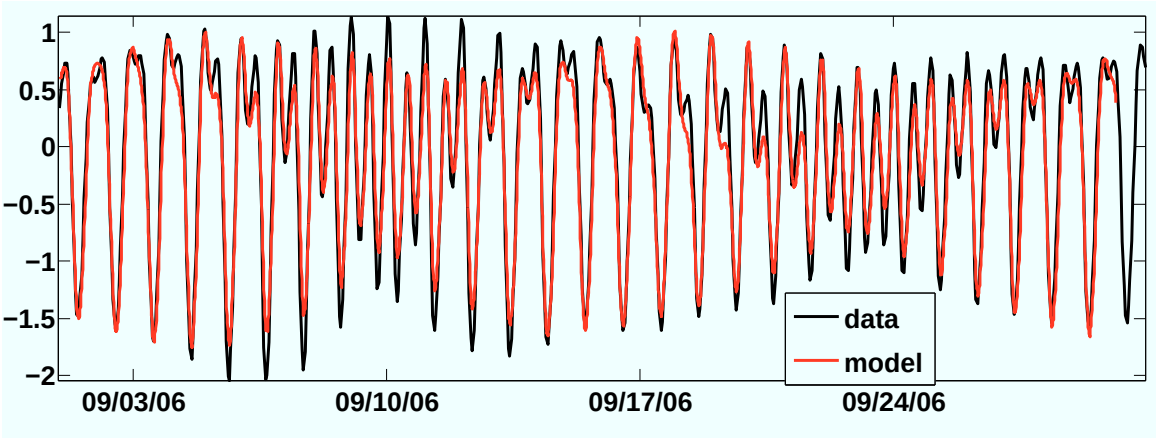


Figure 3.13: Comparison between NOAA tidal gage data at Port Townsend (black) and model output interpolated to the same point (red). Units are meters.

coincident data sets for comparison with simulation output in order to increase the number of model-data comparisons possible.

A straight-forward yet physically-based way to do this is to align time series based on their free surface signals at a specific location. Investigation of model output showed that the elevation range covered during a half-cycle along with the time taken correlate with many of the flow feature behaviors in the system. By lining up the free surface signals from the two time series by range and duration and finding consecutive similarly-sized half-cycles between the data and model free surface signals, we can find realistic comparisons between the data and model flow fields. See Figure 3.14 for an illustration. This method is used repeatedly in this research to make comparisons between data and model output that were not taken at the same time but display similar behavior.

*OTS ADCP Data*

Figure 3.15 shows model output and data from an over-the-side (OTS) ADCP track taken from a ship moving across the channel. As the ship travelled, velocity data was collected from the water column below the ship. By assuming that the track was instantaneous and taking model output at the same spatial locations, as well as employing the time series

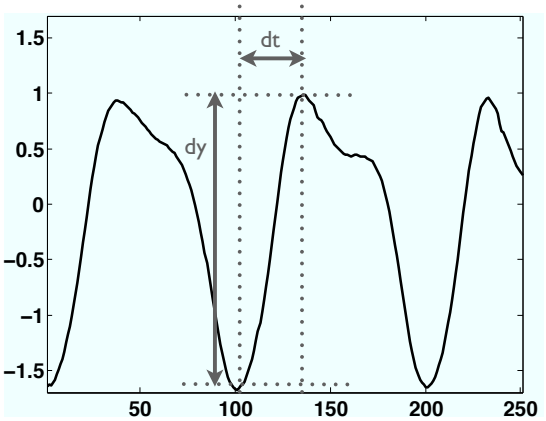


(a) Match with Figure 3.14(c)

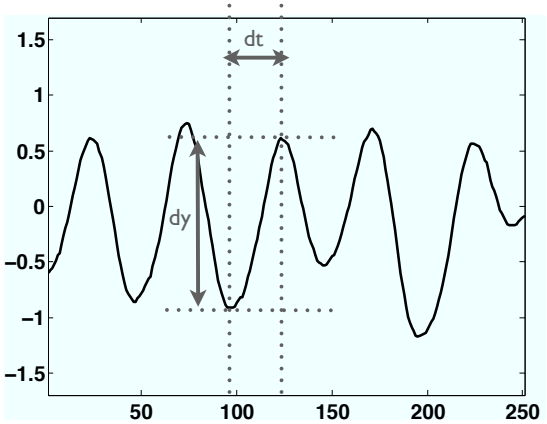


(b) Not a good match

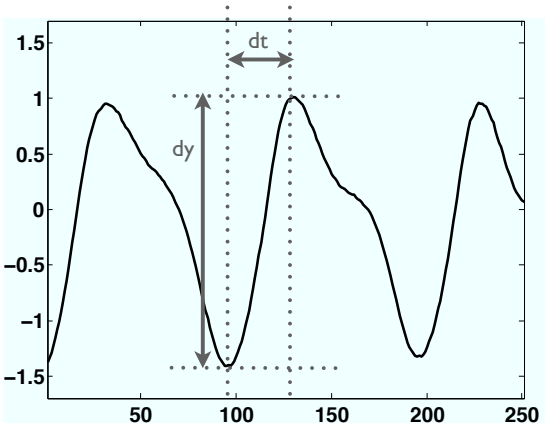


(c) Match with Figure 3.14(a)

Figure 3.14: Time series information from non-coincident times are aligned by finding consecutive half-cycles with similar range and duration between the free surface signals at the same location from each time series. Shown is an example of comparing the $y$-axis free surface elevation between three different signals for a single half-cycle. The signals in Figures 3.14(a) and 3.14(c) are similar to each other and may be aligned to find a reasonable comparison for fields from the sources and times represented by the two signals. In our case, one of the signals represents model output and the other represents field data. Figure 3.14(b) shows a signal that displays much different behavior from the other two signals. This process could be repeated to find multiple consecutive matches for a longer comparison.

comparison method described in the previous section, a meaningful comparison is made. The model output gives context to the data transect in the arrow plot showing that the bend in the ship path shown in black can be explained by the ship being in the vortex shown in the model flow field (in red). This transect cuts through fast, uniform currents on ebb tide until about 800 meters in when the horizontal speed suddenly drops and changes direction. This transition is also associated with a negative vertical velocity field, which in Chapter 4 is identified as due to convergence in the presence of bottom friction.

Note that the limits on the color bars for the model output are different than for the data. The pattern seen that connects the two is the relative change across the transect, not the absolute numbers. The relative change, or the gradient, are what is significant for some important flow features, such as vortices. For reference, the absolute comparison is shown in Figure 3.16, where a known speed deficiency is apparent. The data shows some smaller horizontal scales than are captured in the simulation, perhaps due to smoothed bathymetry and horizontal resolution. Additionally, we do not expect this hydrostatic code to necessarily reproduce vertical velocities well. The changes made to the bathymetry in order to have a stable simulation, accomplished by smoothing the bathymetry, may have contributed to a slightly altered trajectory on ebb tide, as shown in the velocity direction plot. The important things to note here are the processes and mechanisms that seem to be the same between data and simulation in an eddy, which are explored in-depth in Chapter 4.

*Currents and Density, Salinity, and Temperature*

Comparisons for salinity, temperature, and density were completed using data from the simulation period (Washington State Department of Ecology, 2011). A map showing the two station locations is shown in Figure 3.17, and timing of the casts in relation to simulation time is shown in Figure 3.18. Temperature, salinity, and density are shown at Port Townsend in Figure 3.19. The temperature gradient is not steep enough and the salinity and density profile shapes are a little too steep. The temperature, salinity, and density are all too stratified and too cold/salty/dense in the model when compared with the data at Bush

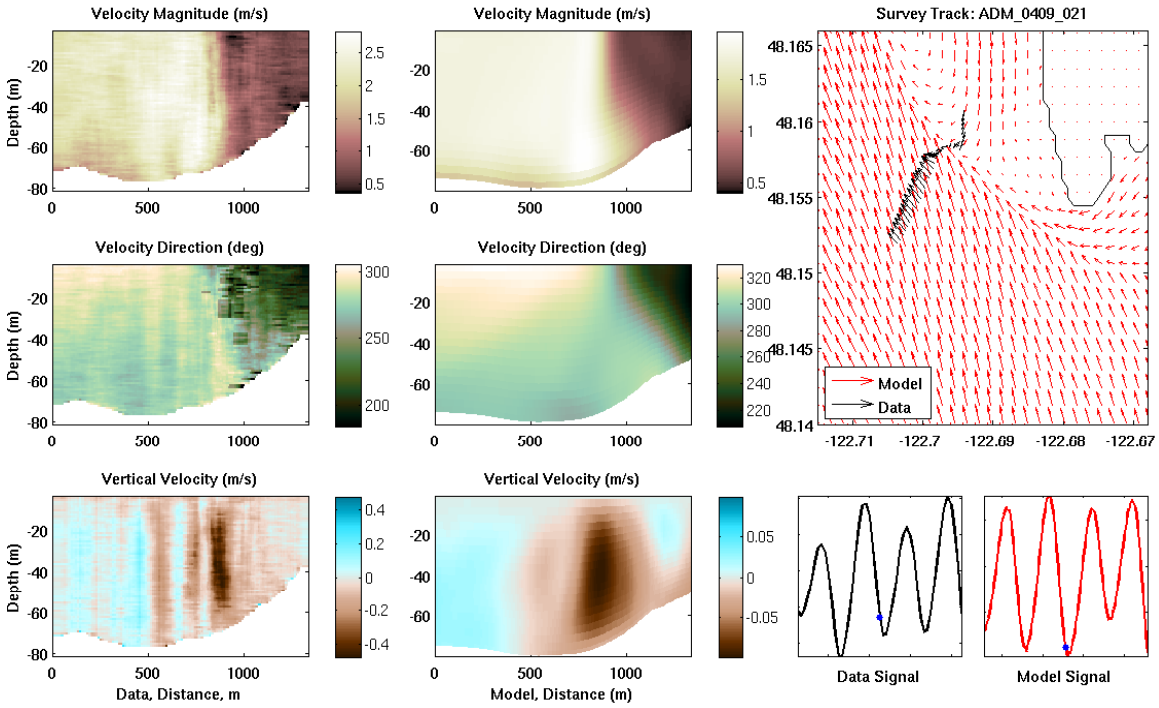


Figure 3.15: OTS ADCP data (left column) and model output (middle) showing, from top to bottom, speed and directionality of horizontal currents, and vertical velocity. The right column shows surface currents from the data (black) and model (red) near Admiralty Head, and the free surface signals of each that were used for alignment.

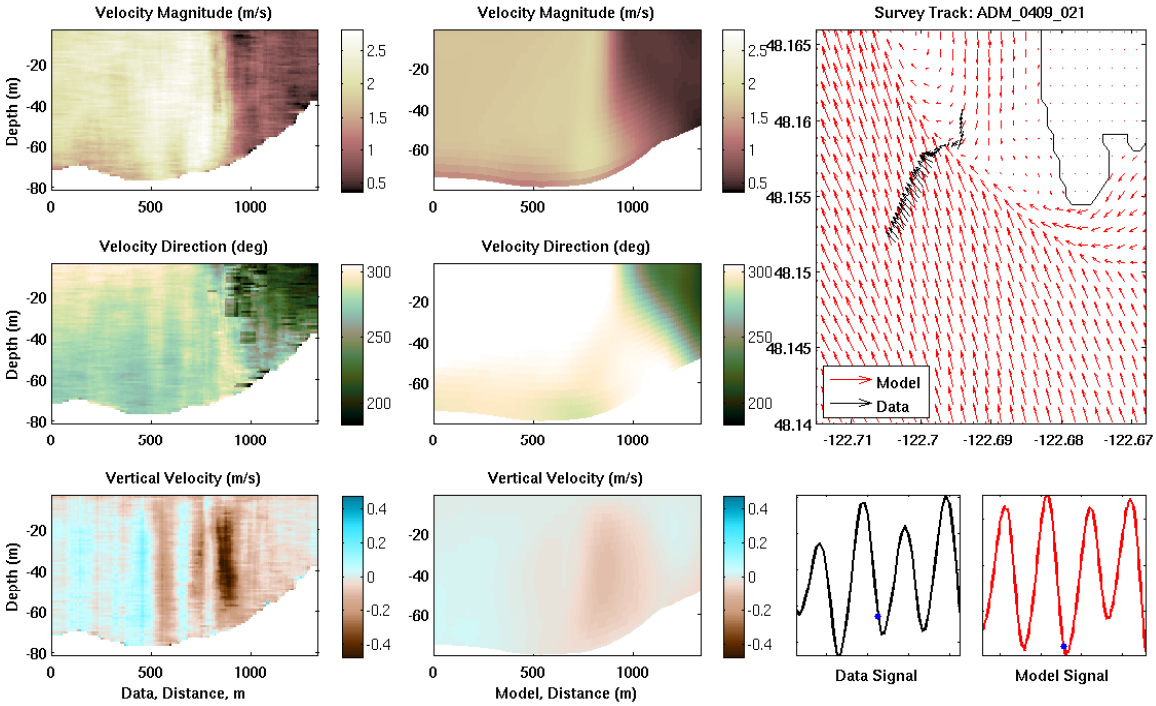


Figure 3.16: Figure 3.15 but with matched color bar limits for absolute comparison.

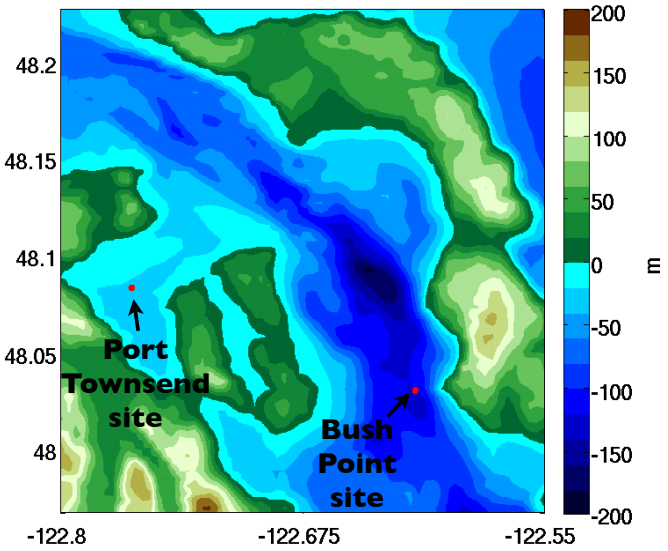


Figure 3.17: Map of CTD comparison points: near Port Townsend (Station PTH005, at 11:42AM on 9/11/06) and Bush Point (station ADM001 at 11:45AM on 9/19/06)

Point in Figure 3.20.

*Harmonic Analysis*

**Free Surface** One-to-one comparisons are shown here for free surface tidal constants following harmonic analysis (see Section 1.3.3). A map showing comparisons points is given in Figure 3.21. Inference was used in the harmonic analysis to separate the $K_1$ and $P_1$ tides, which have very similar frequencies and otherwise require a long data set to separate.

The $M_2$ constants for the free surface are shown in Figure 3.22. The amplitudes are consistently low, which is a known problem in the larger forcing regional model, and inherited by this model (Section 2.7.2). The phases also do not match up correctly. However, because the phases are consistently mismatched, the correct phase propagation is occurring in the model through the domain as in the data, as demonstrated by the comparison points having the same slope as the one-to-one line, just not along the actual one-to-one dashed line. The phase propagation through the domain is related to dissipation and is more important dynamically than the absolute values (Mofjeld and Larsen, 1984). The exception to this is a

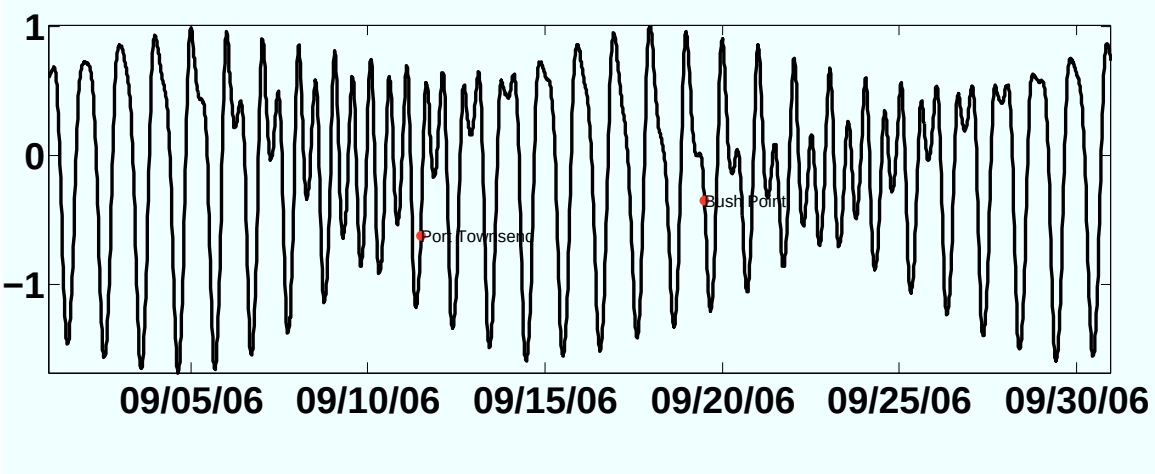


Figure 3.18: Timing of CTD casts in relation to model time

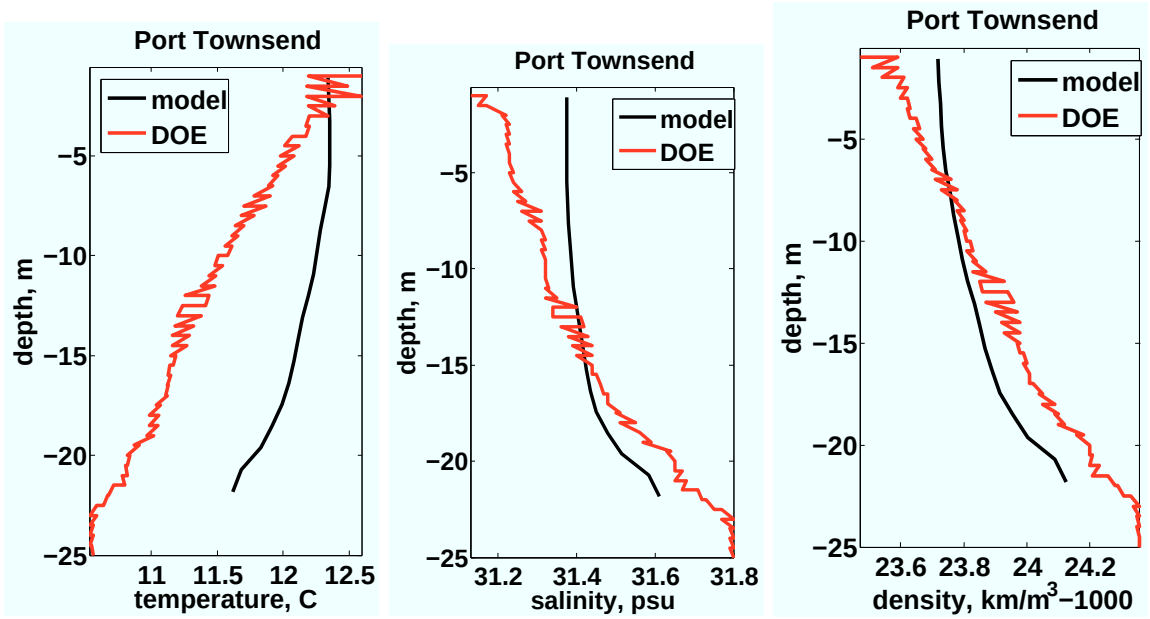


(a) Temperature (b) Salinity (c) Density

Figure 3.19: CTD comparisons at Port Townsend

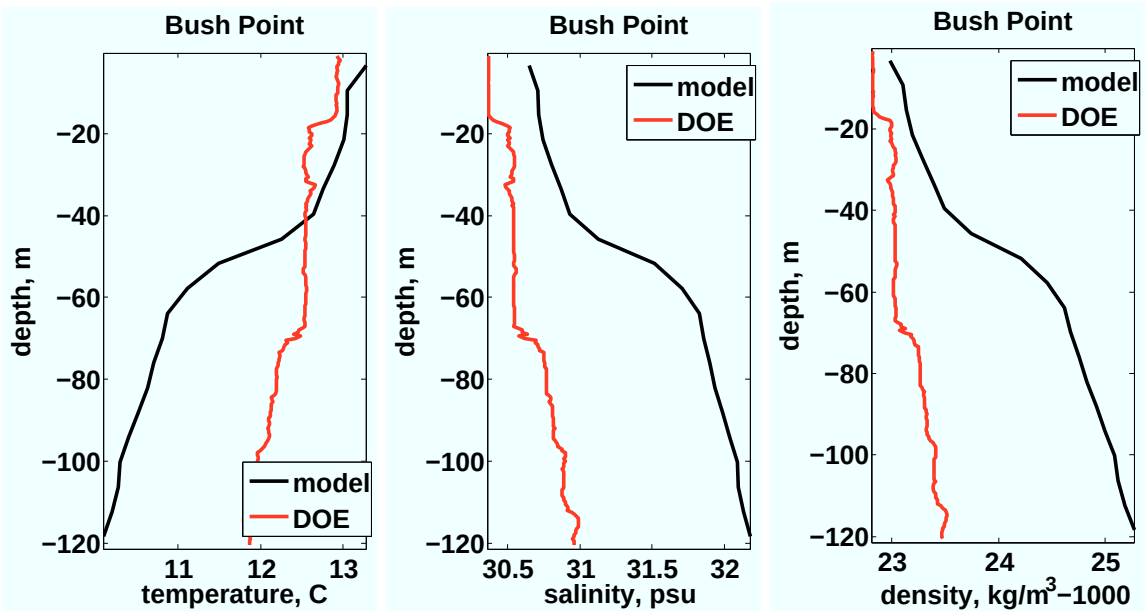


(a) Temperature (b) Salinity (c) Density

Figure 3.20: CTD comparisons at Bush Point

location which in the model has a phase of close to 370 degrees and is too large as compared with the data, more so than the other points. This point is located near Admiralty Head near several other data sources and it is not clear why it has an inconsistent relationship.

Figure 3.23 shows the model-data comparison of free surface harmonic constants for $K_1$. The amplitudes line up well, as do the phases.

**Hub Height Velocity** Velocity harmonic constants at a hub height of 10 meters above the seabed are shown in this section. A map indicating data comparison locations is shown in Figure 3.24. These sets of stationary ADCP data were analyzed in previous studies (Gooch et al., 2009; Polagye and Thomson, 2011). Inference was not used in this case due to a lack of available information about the $K_1$ tide compared with the $P_1$ tide, so we expect these $K_1$ values to be low in both model output and data, based on comparisons made in the analysis. Also note that the assumptions necessary for this analysis do not hold as well for velocities as they do for the free surface, so the results are not as reliable (see Section

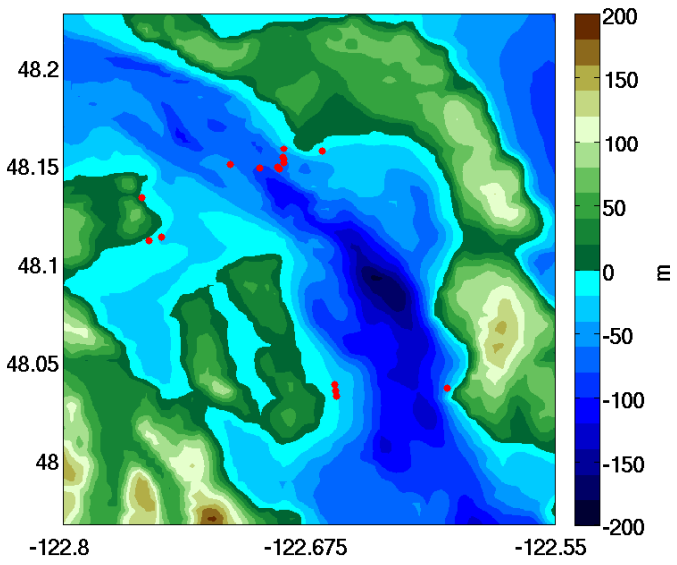


Figure 3.21: Map with free surface comparison points

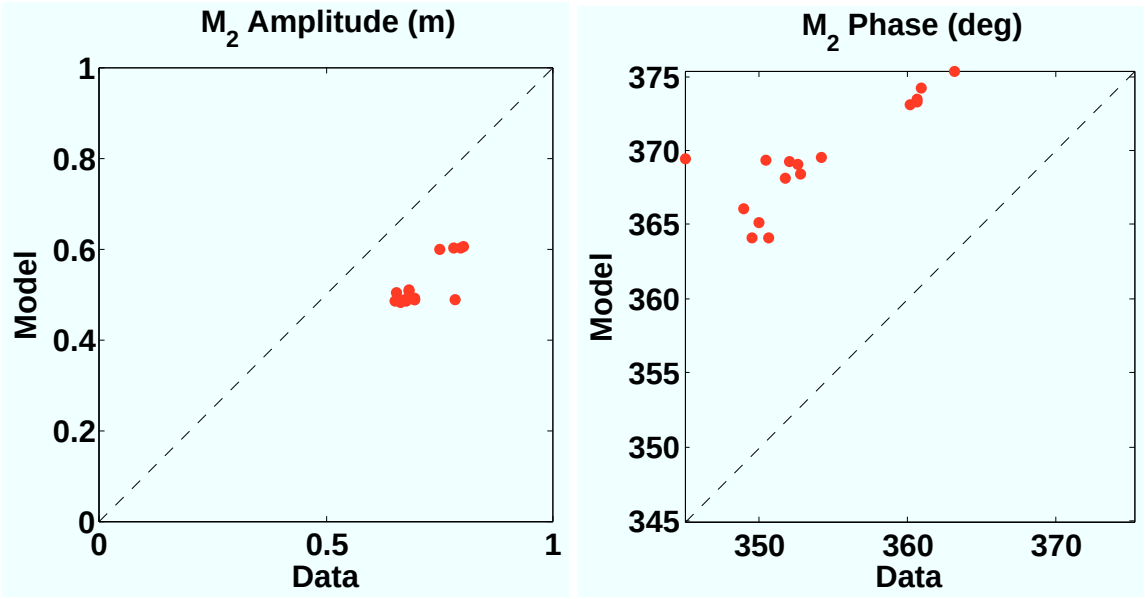


Figure 3.22: $M_2$ free surface 1-1 comparison

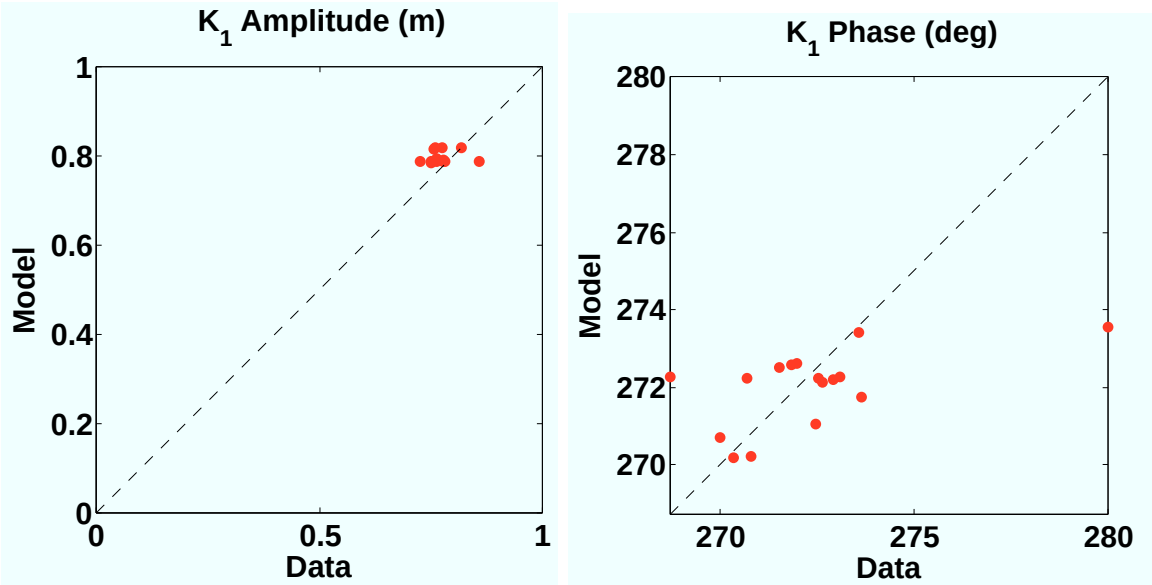


Figure 3.23: $K_1$ free surface 1-1 comparison

1.3.3).

$M_2$ velocity constants are shown in Figure 3.25. The amplitudes are low, as they are for the tidal amplitudes and in the forcing model (Section 3.3.2), though not quite as consistently. Both the free surface and velocity amplitudes from the model output are approximately 75% the size of the values from the field data. Some of the phases line up much better in this case, but there is more scatter as well. Since velocity is much more affected by nonlinearity, the scatter in the comparison may be unavoidable. The $K_1$ tides have similar behavior. In most of the plots, there are three points that separate from the others. These three are from the southeast corner of Marrowstone Island and are in a very different environment from the others.

### *3.4 Summary and Discussion*

Interesting flow features were found in the simplified headland case, particularly in the eddy field and its effects on other parameters. The eddies produced by the headland are advected downstream, causing dips in the free surface and speed. Density fronts travel with the speed

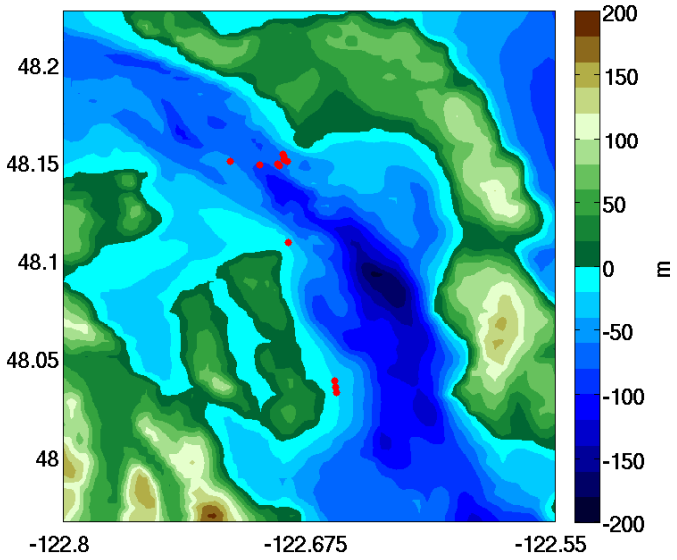


Figure 3.24: Map of velocity comparison points

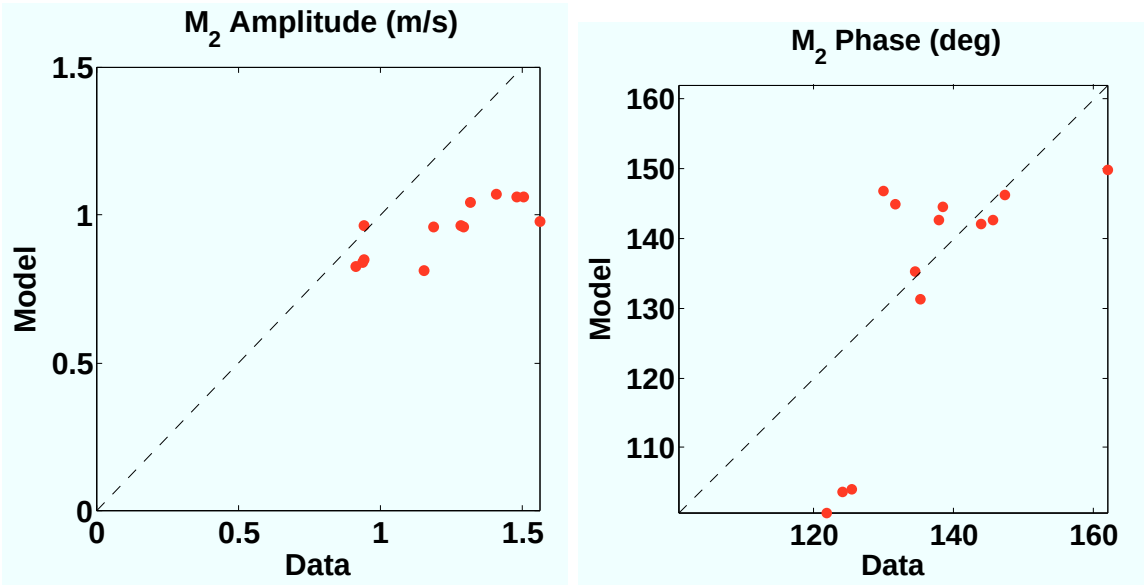


Figure 3.25: $M_2$ hub height velocity 1-1 comparison

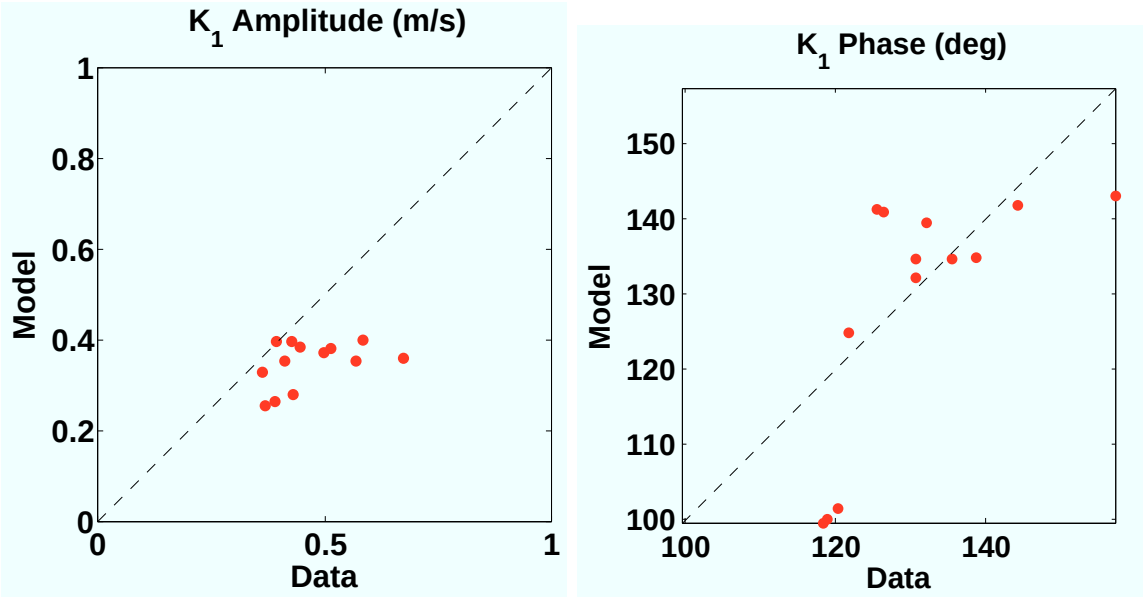


Figure 3.26: $K_1$ hub height velocity 1-1 comparison

front as the tide changes and pushes past the headland each half-tide.

These features are found in the Admiralty Inlet simulation as well, but with more complexity. Instead of just one headland, there are several headlands in Admiralty Inlet, and Admiralty Head is, in particular, very asymmetric. Multiple vortices can interact and strongly affect the flow in terms of speed and the density, among other things.

Some of the most interesting features will be explored in other chapters. Chapter 4 goes into a more detailed look at the vortices on ebb and flood tide as well as analysis of vorticity generation. Chapter 5 has comparisons of output from the model's turbulence closure scheme to compare with data.

Comparisons of the model with data show that the model has the ability to reproduce relevant features in the system, particularly vortices. Compelling comparisons are made with the surface behavior of a vortex and a vertical slice through the vorticity field, indicating that vortex behavior can be better understood using this simulation. While the speeds are low in the model, this deficiency is understood and can possibly be accounted for in metrics for assessing the actual resource in the system. Regardless, this model is a useful tool and

can be used to understand the relative changes and behavior within Admiralty Inlet, which is key to understanding and deciding upon turbine placement.

# Chapter 4

# VORTICITY DYNAMICS

## *4.1 Introduction*

Tidal headland-generated eddies in Admiralty Inlet have been identified as potentially important to turbine siting due to their significant effect on the flow fields, including generation of sharp changes in horizontal speed, directionality, and density gradients; significant vertical velocities; and increased turbulence (NNMREC, University of Washington, 2010; Thomson et al., 2011).

The high resolution simulation of Admiralty Inlet enables examination of many details in the system dynamics. A visualization of the vorticity time history can reveals many different behaviors, including vortices of various sizes and trajectories. Additionally, the interaction of competing terms in the governing equation for vorticity must be determined in order to understand the interplay of mechanisms for vorticity generation, advection, and destruction. The focus here is on the area around and affecting Admiralty Head, as it is the area of interest for tidal energy development. However, it is important to note that every piece of land protruding into the flow in this area can spin off vortices that contribute to the complex dynamics of the region.

In this chapter, the variety of vortices seen around Admiralty Head throughout different tidal cycles is described in detail (Section 4.2). This includes information about distinct features in the system associated with the vortices, including fronts, jets, and vertical velocity. When appropriate, reference is made to the idealized headland simulation, in which some of the same features are seen. However, much of the behavior seen in the Admiralty Inlet simulation is due to the complexity of the problem. Note that the color bars on plots are kept largely consistent; limits for vorticity are kept at $\pm 0.025$ 1/s for plots in Admiralty Inlet, unless otherwise noted. Section 4.3 steps through a derivation of the vertical vorticity governing equation, starting from the ROMS horizontal momentum equations described in

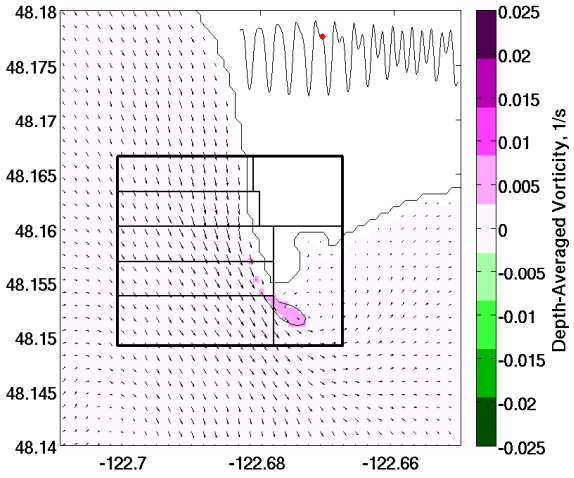


Figure 4.1: Example of a small flood vortex, shown in the depth-averaged vorticity field. Overlaid box lines are used in future analysis but also serve here for visual reference. Arrows indicate horizontal depth-averaged velocity and the upper right corner curve shows the free surface signal near Admiralty Head with location in time indicated in red.

Chapter 2. Section 4.4 uses a calculation of the volume-integrated form of the equation for vertical vorticity to understand the generation rate of vorticity around Admiralty Head, along with other mechanisms that are pertinent to the dynamics. After discussing the equations, a detailed analysis of the results will be presented. Summary and a discussion of the application to turbine siting are in Section 4.5.

## *4.2 Description of Vorticity in Admiralty Inlet*

### *4.2.1 Flood Tide*

*Vortex Behavior Through a Cycle*

On flood tide, the size of vortices can range from small, as in Figure 4.1, to large, as in Figure 4.2(c). It is necessary to begin with the previous ebb tide in order to understand a typical flood tide in detail. Often during ebb tide, there is a secondary induced vortex of sign opposite to that of the main vortex and formed between the main negative ebb eddy (with rotation direction defined by the right-hand rule such that negative is clockwise rotation)

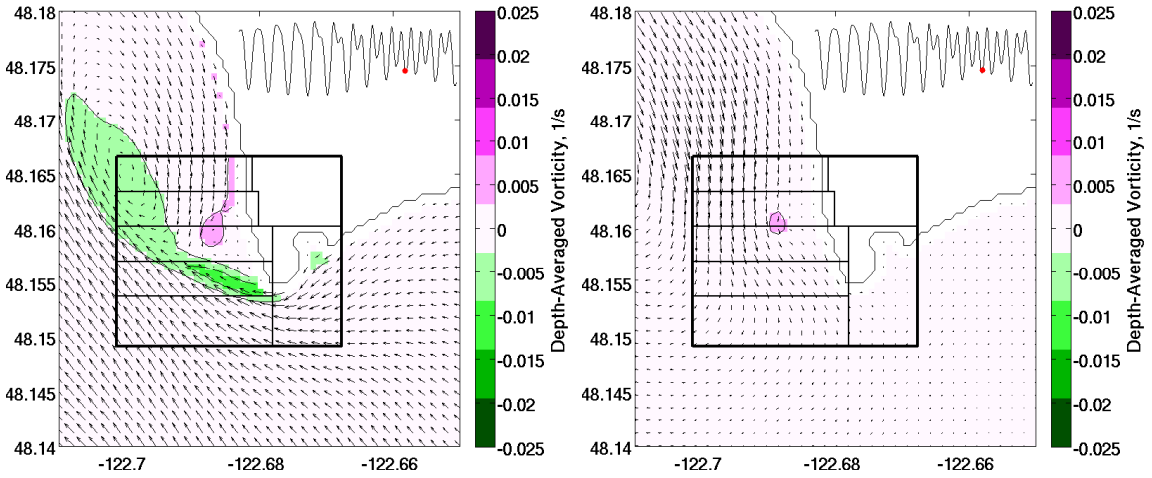


(a) 6:30PM: secondary induced vortex forms on ebb tide

(b) 8:30PM: old positive vortex advects with new flood tide

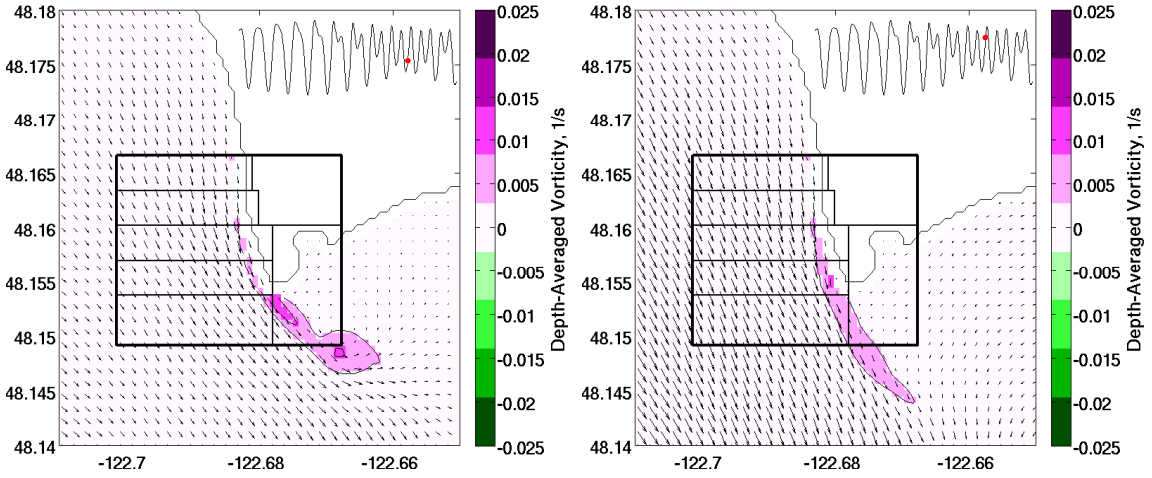


(c) 10:00PM: reach of vorticity region, first to the east

(d) 12:15AM: reach of vorticity region, second to the south

Figure 4.2: Flood tide process example from 9/9/06-9/10/06, showing depth-averaged vorticity at multiple times.

and the coastline, as shown in Figure 4.2(a). The recirculation region near the boundary due to the negative vortex generates a counter-rotating eddy. As ebb tide finishes and flood begins, this positive vortex persists and advects with the flood tide to jump-start the positive vorticity accumulation (Figure 4.2(b)). The vorticity builds up near the headland until it sheds from the headland tip with a first, strong reach to the east, as shown in Figure 4.2(c). This initial reach to the east is due to a surge of water toward the beginning of flood tide that comes from the vortex from the previous ebb tide, as will be explored further in Section 4.2.3. After this initial surge, the vorticity pulls back to recollect, then pushes forward again, but this time more to the south with less momentum behind it, as in Figure 4.2(d). If the flood tide has only a small initial surge from the previous ebb tide vortex moving through, the flood tide vorticity will still reach out to the east, but will have a smooth clockwise movement throughout the cycle as opposed to the somewhat distinctive reach to the east followed by a temporary retreat and a push more to the south.

The size of the vortex generated on flood tide is related to the behavior of the free surface of that half-cycle as well as the previous half-cycle. A large diurnal flood tide would have behavior similar to the tide shown in Figure 4.2(c), as would a moderate semi-diurnal flood tide following a moderate ebb. A small lower high water diurnal flood tide produces a small vortex, as in Figure 4.1, and the half-cycle following a small tide would have reduced behavior as well.

*Jets*

As flood tide pushes south into Admiralty Inlet, it is squeezed between various points of land: Port Wilson and the north-east corner of Marrowstone Island on the west and Admiralty Head on the east (Figure 4.3(a)). Vorticity is generated at and near these points, which builds up until the flow separates from each point and reaches downstream. The flow field is strongly affected by these various points and is redirected drastically lee of the headlands, often altering the rest of the flow in that area, and recirculating behind the point. As shown in Figure 4.3(b), the eddy from Marrowstone Island reaches east across the channel, pushing against and redirecting the main channel flow in the process. A large eddy develops

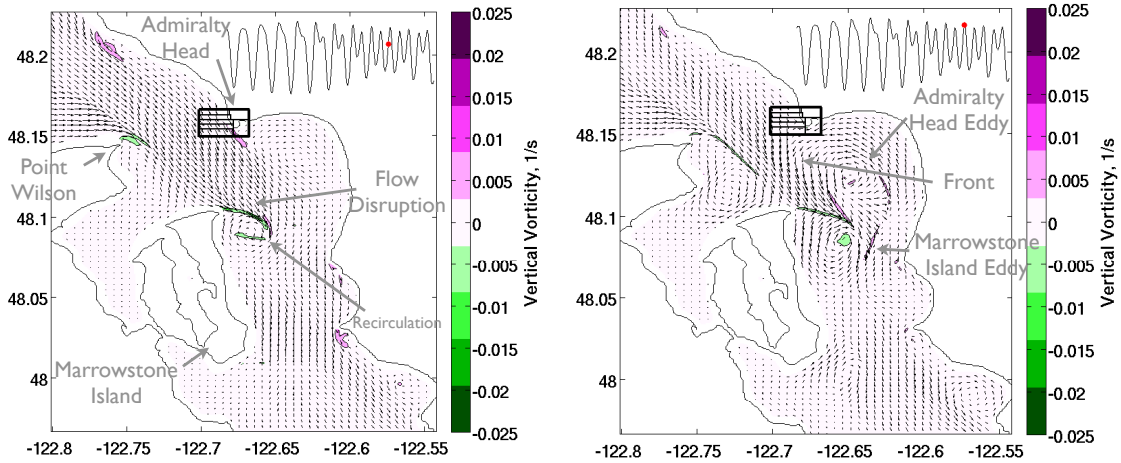


(a) 11:45PM: example of typical flood tide

(b) 1:45AM: large Marrowstone Island and Admiralty Bay eddies with front starting ebb tide

Figure 4.3: Flood tide jetting on 9/9/06-9/10/06, showing 10 meter depth vorticity at two snapshots.

in shallow Admiralty Bay just south of Admiralty Head. As flood tide slows and reverses, the Admiralty Bay vortex leads ebb tide, even while flood is still finishing.

This jetting behavior can be found in the idealized headland case as well. Figure 4.4 shows the vorticity and speed at hub height in the idealized headland case discussed in Chapter 3. As ebb tide begins, the flow pushes past the headland with newly generated negative vorticity on one side and old persistent vorticity on the other, with the jet in between.

### *4.2.2 Ebb Tide*

*Vortex Behavior Through a Cycle*

The range of sizes of ebb vortices is from small (Figure 4.5) to huge (Figure 4.7(d)). Generally, the vorticity on ebb starts to build up near Admiralty Head (Figure 4.6(a)), eventually separating and curling in a sheet to the northwest of the headland (Figure 4.6(b)), moving further west as the tide continues (Figure 4.6(c)). In some cases, a noticeable sec-

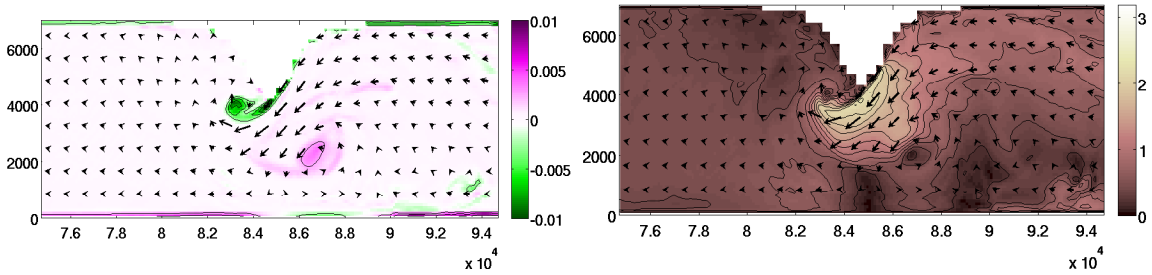


(a) Vorticity (b) Speed

Figure 4.4: Flow field properties at hub height in the idealized headland case, showing jetting behavior analogous to the realistic case.

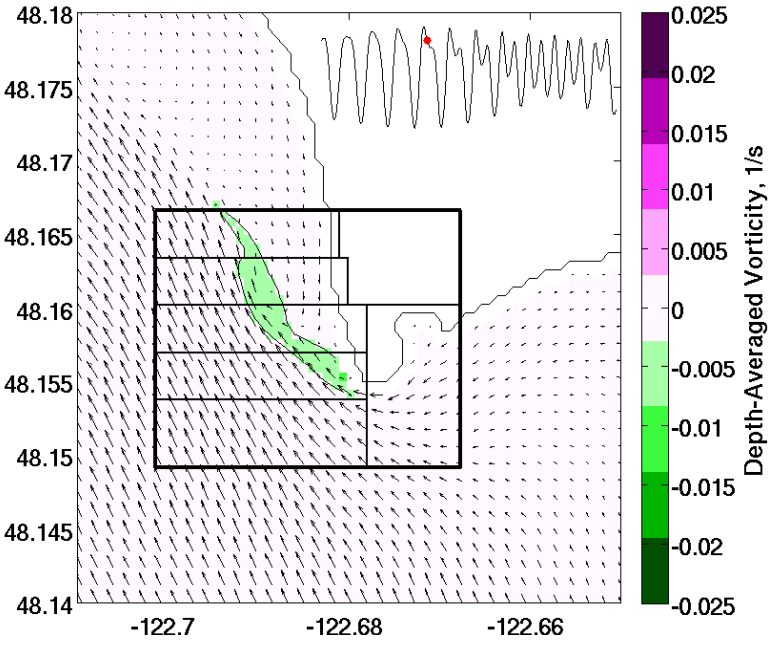


Figure 4.5: Example of a small ebb vortex, shown in depth-averaged vorticity field.

ondary vortex of opposite sign is induced between the main negative eddy and the coastline, as discussed in Section 4.2.1 (Figure 4.6(d)).

During some ebb tides, eddies from the previous flood tide persist and affect the flow. In an example semi-diurnal tide shown in Figure 4.7, the vorticity builds up as typical, but in this case is accompanied by positive vorticity and a velocity surge from the previous cycle (Figure 4.7(a)). An initial vortex reaches out to the north under the influence of the previous vorticity and initial speed surge (Figure 4.7(b)), weakens momentarily (Figure 4.7(c)), then pushes out strongly more to the west (Figure 4.7(d)). Initial velocity surges and persistent vortices will be addressed in detail in Section 4.2.3.

*Fronts*

At the start of flood tide, the layout of the density field can look very different for different tidal cycles. Generally there is denser water to the northwest, which is the opening to the Strait of Juan de Fuca and to the Pacific Ocean, and there is less dense water in the south, toward the main basin of Puget Sound where there are rivers inputting fresh water (Figure 4.8(a)). As flood tide begins, the denser water from the northwest corner pushes southward, pushing the water in the Inlet southward with it (Figure 4.8(b)). As the typical flood jet discussed earlier pushes further between the points on the coastlines and eddies develop on either side, the dense water pushes straight with the jet while the fresher water is carried to the sides and northward in the eddies lee of Marrowstone Island and in Admiralty Bay (Figure 4.8(c)). As flood continues, the eddies carry the fresh water further but, before the water has a chance to fully recirculate, it is pushed past Admiralty Head as a front as ebb tide starts, even while flood tide is still finishing (Figure 4.8(d)). In this manner, many of the ebb tides begin with a sharp gradient of speed and density around Admiralty Head, often with strong flood tides still flowing in other areas, until the whole area eventually ebbs.

A density front was also seen in the idealized headland case and shown in Figure 3.1(d). As in Admiralty Inlet, the front in the headland case is associated with a jet of strong currents down the middle of the flow past the headland, and eddies of opposite sign on

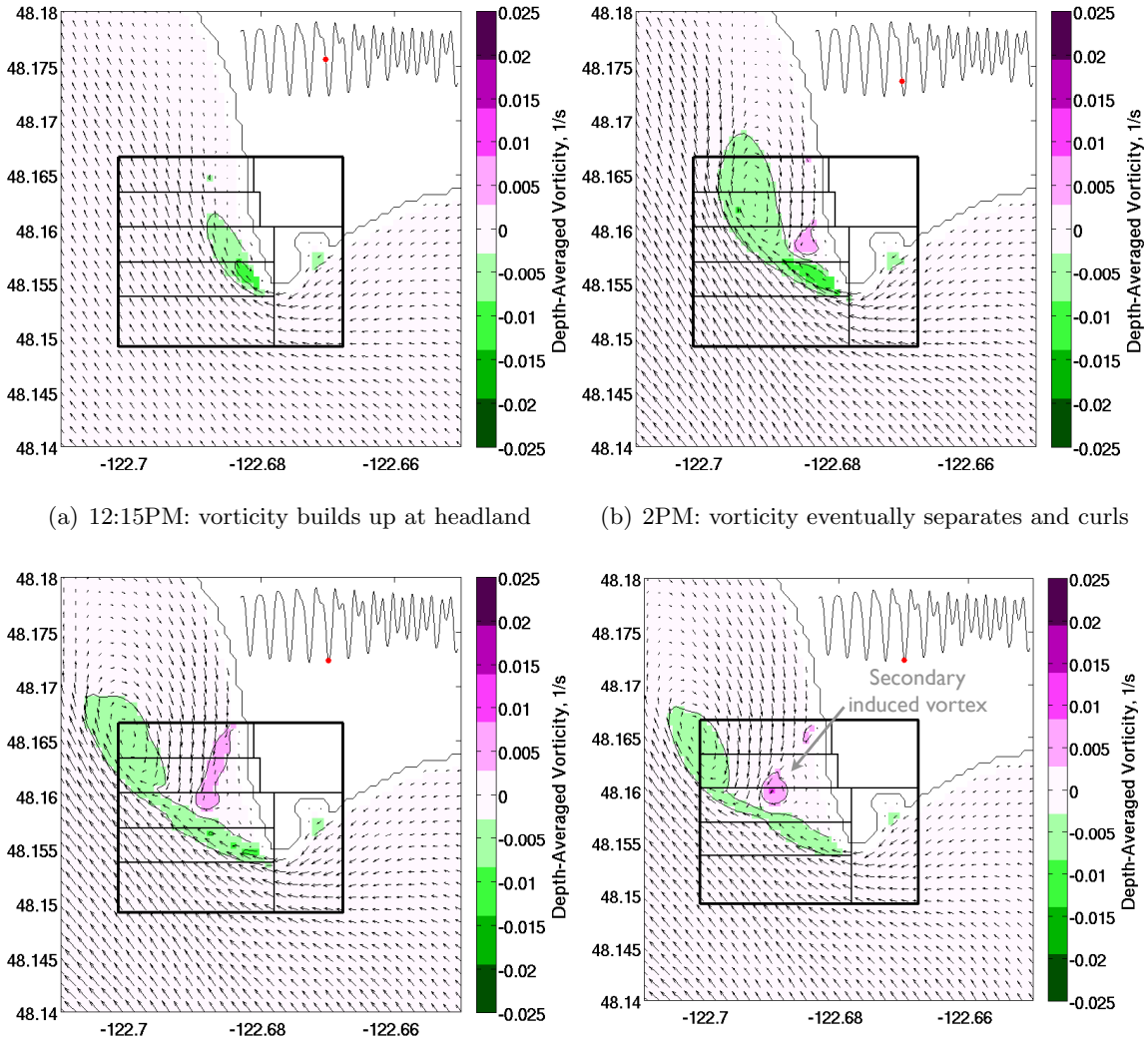


(a) 12:15PM: vorticity builds up at headland

(b) 2PM: vorticity eventually separates and curls

(c) 3:45PM: vortex moves counterclockwise with flow

(d) 4:15PM: can also have secondary induced eddy of opposite sign

Figure 4.6: Ebb vortex process on 9/5/06, showing depth-averaged vorticity at multiple snapshots in time.

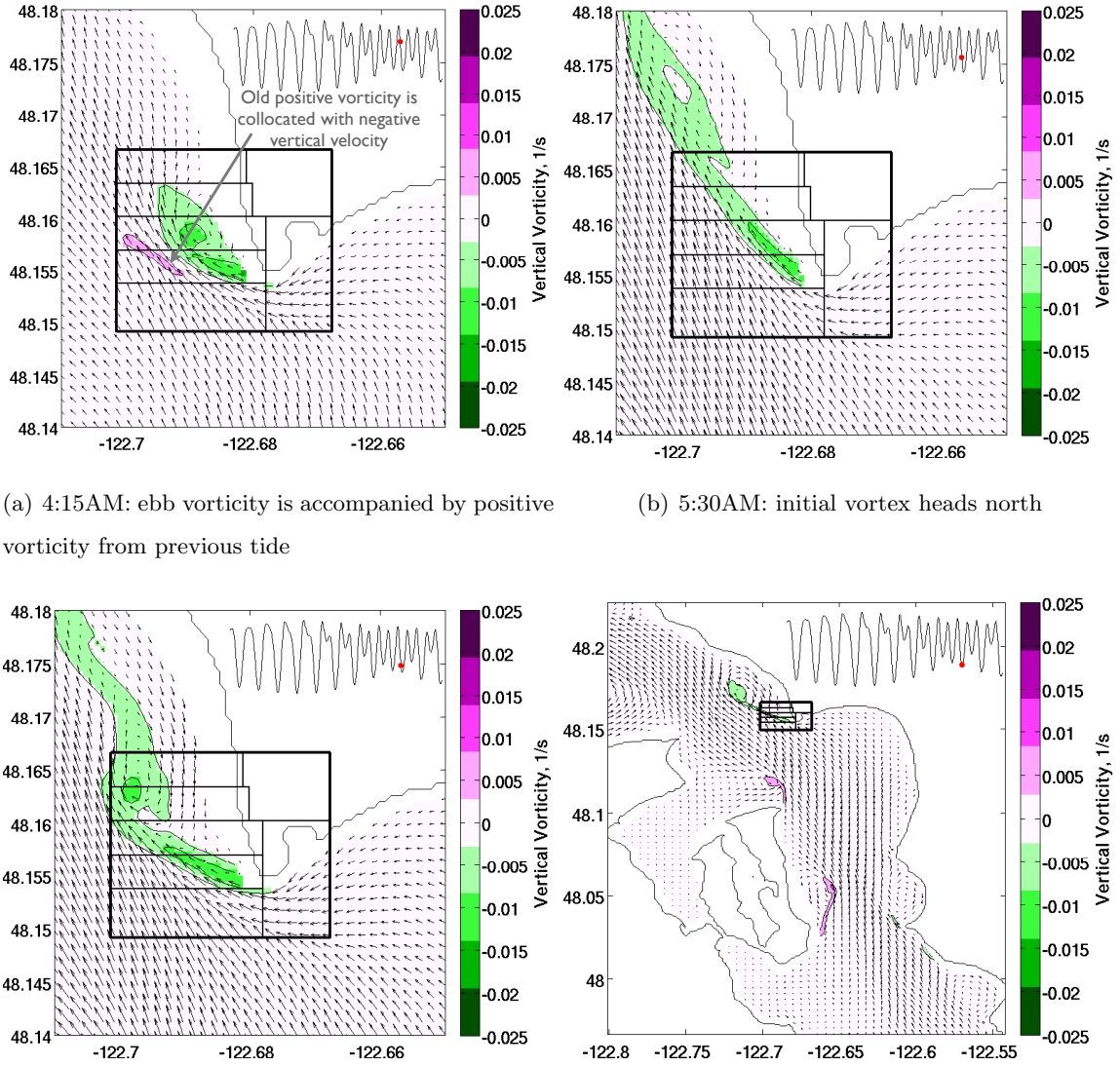


(a) 4:15AM: ebb vorticity is accompanied by positive vorticity from previous tide

(b) 5:30AM: initial vortex heads north

(c) 6:15AM: vortex weakens

(d) 8AM: in second phase, vortex reaches west; zoomed out to accommodate large vortex

Figure 4.7: Behavior modification on ebb tide on 9/10/06 with persistent old vortices and strong initial surge. Shown are snapshots of vorticity at a depth of 10 meters below mean sea level.

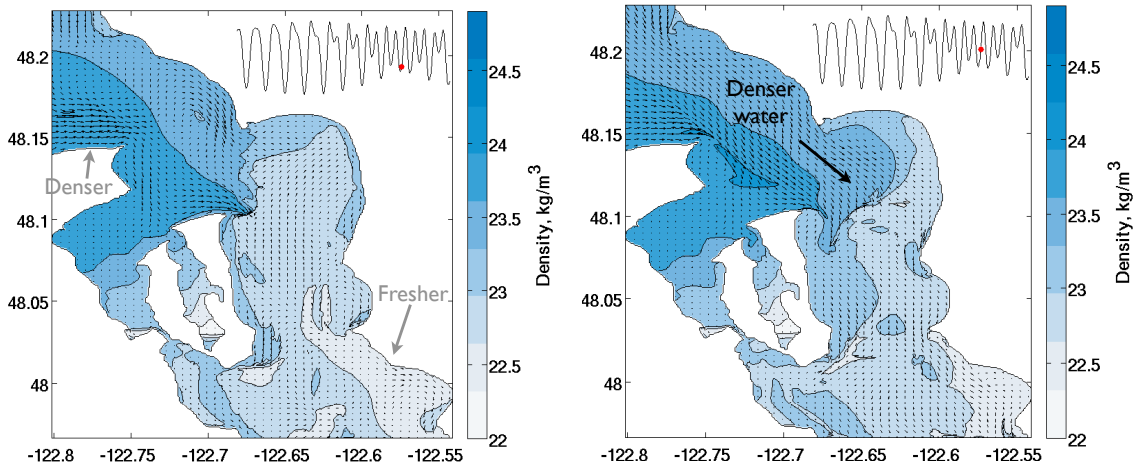


(a) 9PM: the density field at the start of flood typically has denser water toward the ocean and fresher water toward the main basin.

(b) 10:45PM: flood tide pushes denser water south

(c) 12:30AM: fresher water is carried with the eddies

(d) 2:15AM: fresher water with a speed surge begins ebb tide while flood finishes

Figure 4.8: Flood tide front example on 9/9/06-9/10/06. Shown are plots of surface density at multiple snapshots in time.

either side. The strong velocities that lead the tide also carry the less dense water, as in Admiralty Inlet.

### *4.2.3 Initial Surges and Persistent Vorticity from Previous Tides*

When tides are strong enough, they can create vortices with enough momentum to persist into the next tidal cycle. This vorticity advects around Admiralty Inlet with the tides and is accompanied by an area of increased speed. These surges and persistent vortices are most noticeable on flood tide; however, the effects are seen on some ebb tides as well. The coastline and bathymetry conspire to generate and shape smaller patches of stronger vorticity on ebb tide that then affect flood tide. On flood tide, eddies have larger area, taking up Admiralty Bay, and are weaker, and thus are less often noticeable on ebb tide. However, as will be seen in Section 4.4.2, persistent vortices on ebb tide, while less visible, still sometimes traverse the area, affecting all of the mechanisms in the vorticity equation.

Figure 4.9 has a series of plots showing two different ebb to flood situations. The left hand column of the set of figures are from an ebb to flood transition when there is a large ebb eddy, shown in Figure 4.9(a). This ebb vortex persists strongly into the subsequent flood tide, traveling adjacent to the newly generated positive flood vorticity (Figure 4.9(c)), and is accompanied by a strong, discrete packet of increased speed (Figure 4.9(e)). The right hand column of figures shows a small ebb eddy after a relatively slow-moving ebb tide and tiny previous flood tide (Figure 4.9(b)). This eddy advects into the following flood tide, but with weaker vorticity (Figure 4.9(d)) and a smaller, weaker packet of increased speed (Figure 4.9(f)).

On the transition from flood to ebb tide, the same effects as seen on the ebb to flood tide transition can be found, but because the area of vorticity in shallow Admiralty Bay is relatively large and the vorticity weak, the effects are more difficult to pick out. Figure 4.10 shows the transition from flood to ebb tide. In Figure 4.10(a) there are two large eddies on flood tide. Each of these eddies is accompanied by an area of increased speed (Figure 4.10(b)). As ebb tide begins, much of the old vorticity is dissipated, but in this case enough remains to be seen in Figure 4.10(c) advecting past Admiralty Head. Sometimes the

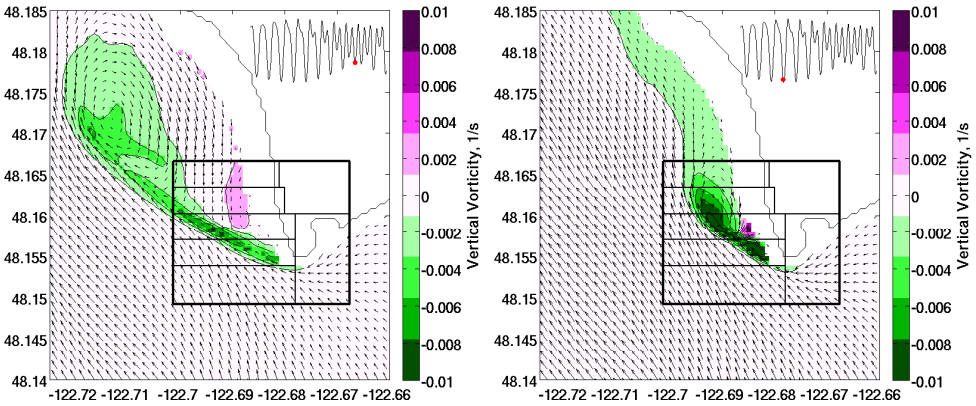


(a) Vorticity, 7:30PM: large ebb vortex




(b) Vorticity, 2:15PM: small ebb vortex

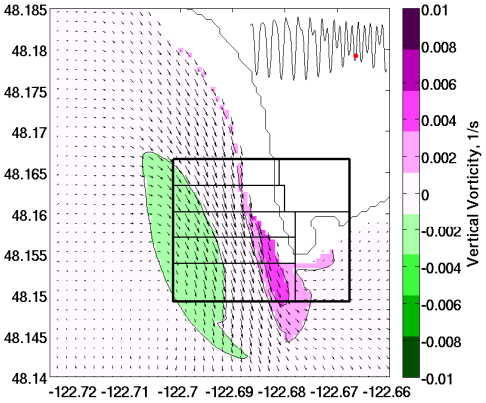


(c) Vorticity, 9:15PM: persists into flood

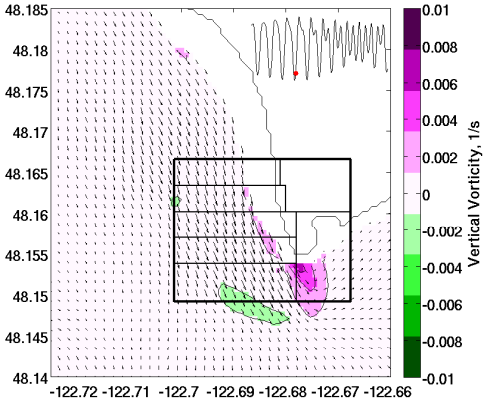


(d) Vorticity, 5:30PM: persists into flood

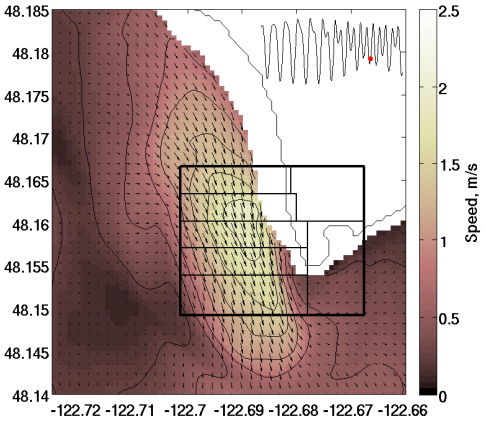


(e) Speed, 9:15PM: speed pocket with eddy

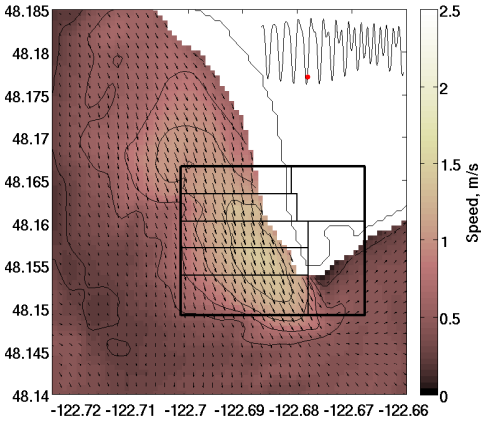


(f) Speed, 5:30PM: speed pocket with eddy

Figure 4.9: Two examples of speed surges and persistent vortices on flood tide, large on left (9/9/06) and small on right (9/4/06), shown at 10 meter depth. Note the lower color bar limits in these figures, for visual illumination.

flood Marrowstone Island eddy vorticity is advected back to Admiralty Head to affect the dynamics there as well. Accompanying this persistent vorticity from flood tide is a surge of increased speed from the faster-moving outer edge of the large Admiralty Bay vortex, pushing past the headland (Figure 4.10(d)). This packet is quickly followed by a speed surge from the Marrowstone Island negative vortex from flood tide, and then the rest of ebb tide pushing through, such that while there are multiple small peaks of speed in the area off Admiralty Head, none are as extreme as on flood tide (Figure 4.11).

This behavior is not limited to the numerical simulation; it is seen in the data as well. An example is shown in Figure 4.12. At this data location near Admiralty Head, peaks are seen in the speed profile on both flood and ebb tides.

Vortices persisting into the next half-cycle were also seen in the idealized headland case, as shown in Figure 3.1(b). In the figure, the old negative ebb vortex has persisted into the flood tide to travel alongside the newly shed positive vortex. The strongest currents can be found between the two counter-rotating eddies.

### *4.2.4 When is slack tide?*

Slack tide is difficult to determine in such a dynamic system as Admiralty Inlet. There are times when ebb and flood currents are simultaneously pushing, sometimes strongly, in neighboring areas (Figure 4.13). In the figures shown, there is never a time when the entire horizontal surface area is at slack tide. Often, the same is true vertically. For example, Figure 4.14 shows a typical ebb-flood transition. Slack tide is different horizontally and vertically, even in this small region near the headland.

### *4.2.5 Vertical Structure of Vorticity*

Vorticity changes with depth due to bottom friction, changing bathymetry, and density effects, among other possible causes. Looking at a case examined earlier in this section, it is possible to see how significant the differences with depth can be.

A typical ebb tide was shown previously in Figure 4.6 using depth-averaged plots of vertical vorticity. Figure 4.15 shows the vertical vorticity in depth near Admiralty Head at

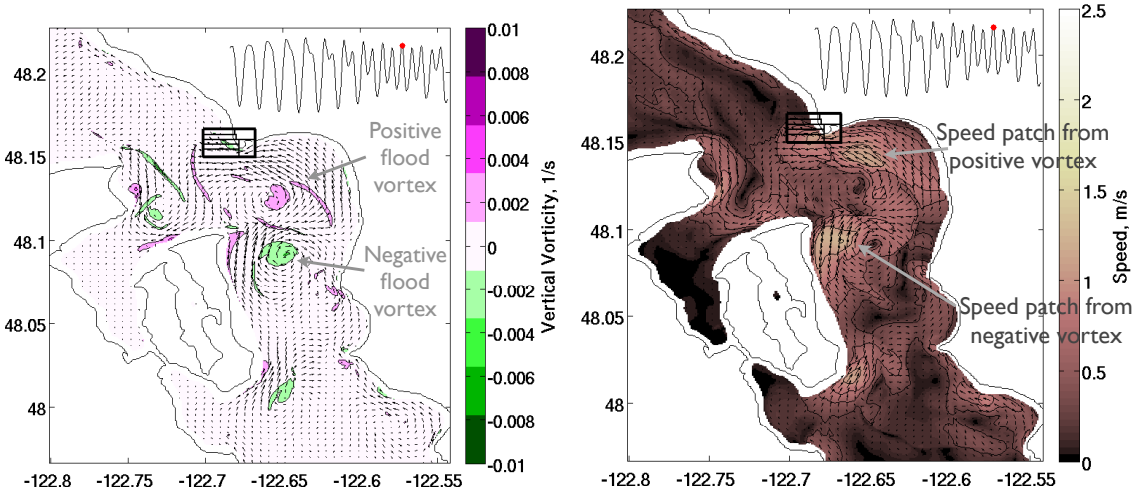


(a) Vorticity, 2:45AM: two oppositely signed vortices on flood tide

(b) Speed, 2:45AM: speed pockets corresponding to flood vortices

(c) Vorticity, 4:00AM: most northward old vortex persists and advects with ebb tide

(d) Speed, 4:00AM: speed pocket corresponding to old positive vortex

Figure 4.10: Example of speed surge and persistent vortices on ebb tide on 9/10/06, shown at 10 meter depth. Note the lower color bar limits in these figures, for visual illumination.

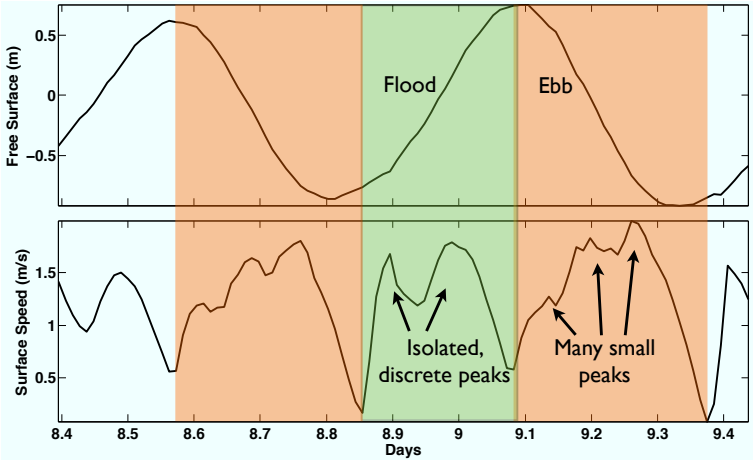


Figure 4.11: Speed peaks in model output due to old vortices advecting into the next tide near Admiralty Head tend to be large on flood tide and small on ebb tide.

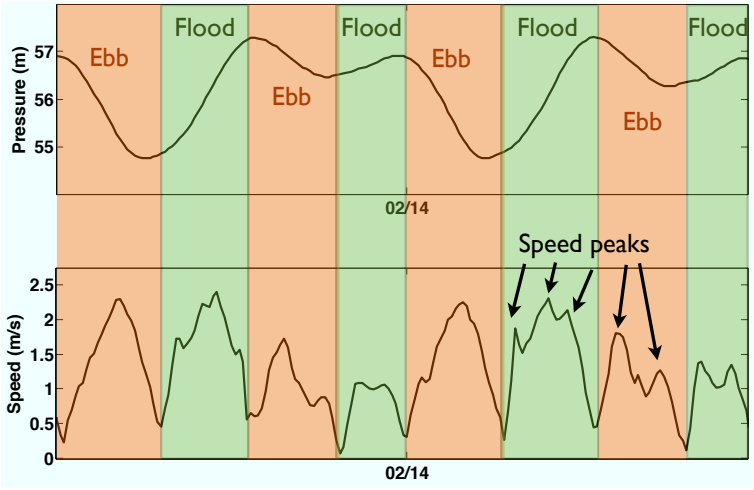


Figure 4.12: ADCP data near the surface of the water column near Admiralty Head shows evidence of complex vortex interactions in the system. Data from NNMREC, University of Washington (2010).

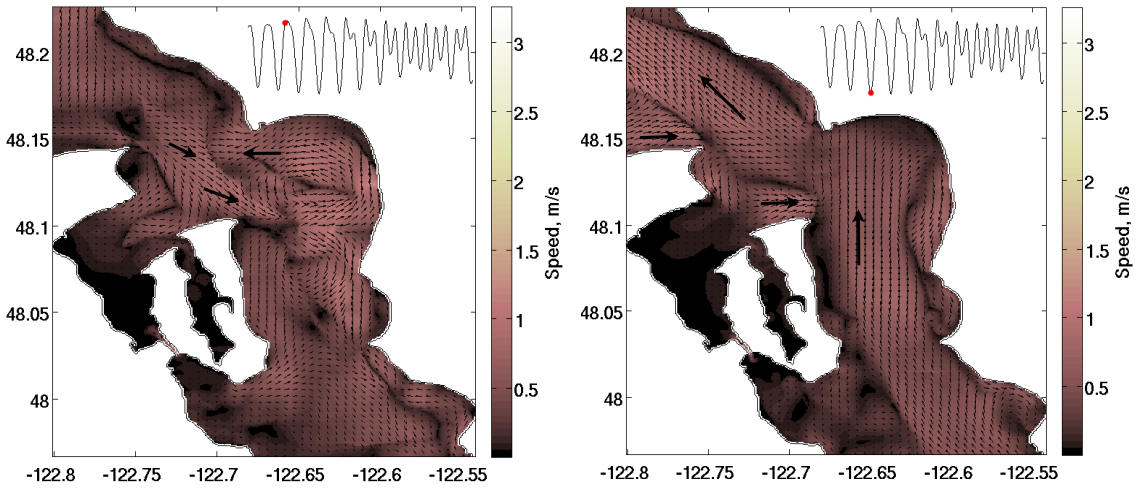


(a) 9/2/06, 10:00PM: flood and ebb competing

(b) 9/3/06, 3:00PM: multiple directions of tides simultaneously

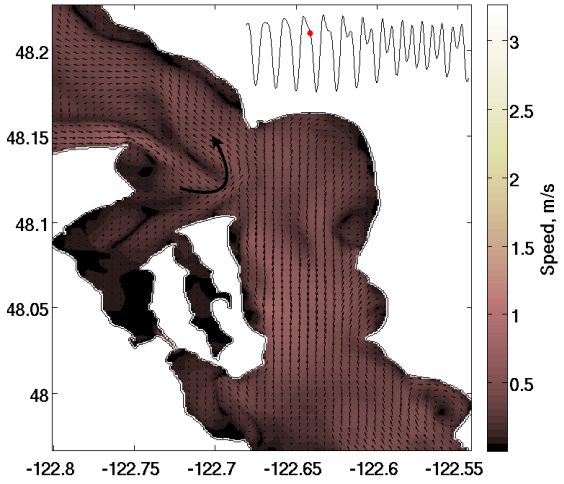


(c) 9/4/06, 8:15AM: flood tide does not come fully into the channel

Figure 4.13: It can be flood and ebb tide at the same time, in many different ways. Shown are snapshots at various times of the surface speed.

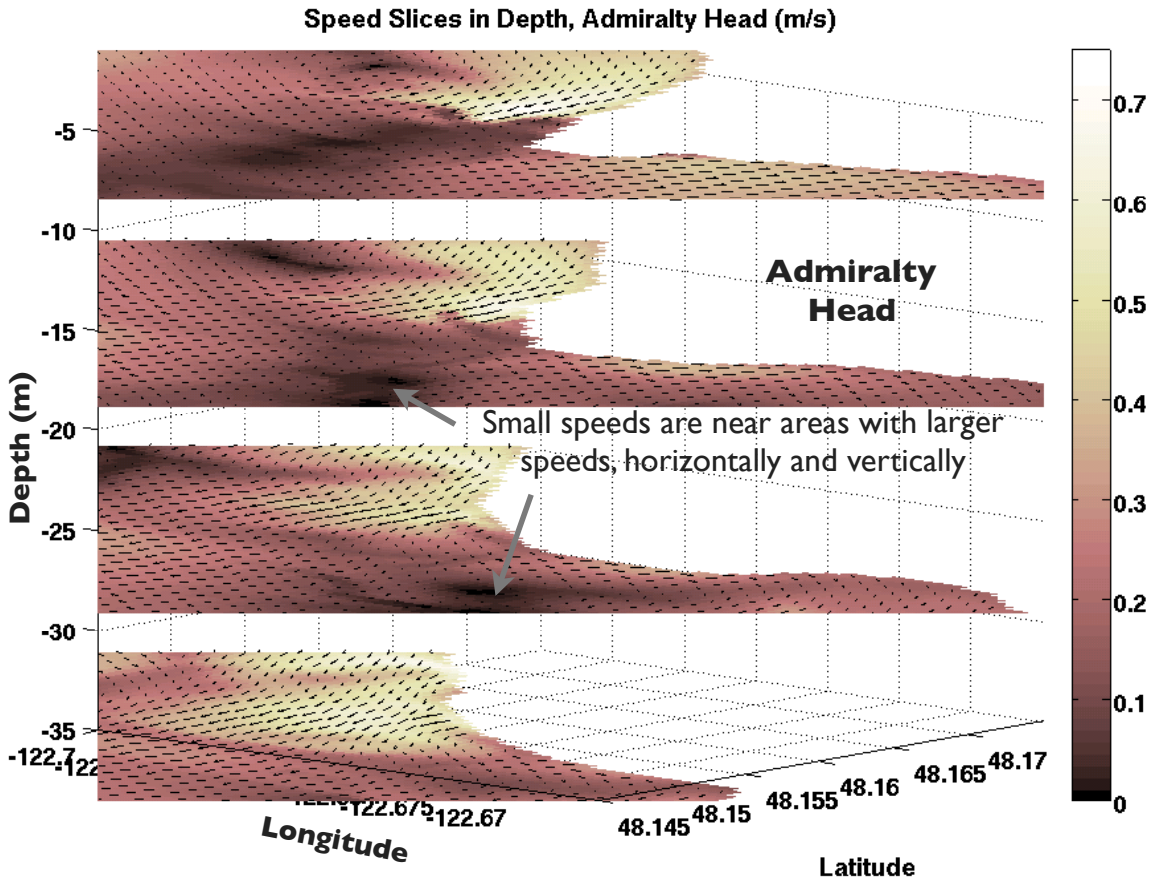


Figure 4.14: Four slices of speed at constant depth shown near Admiralty Head, looking northwest past the headland. Arrows show horizontal velocity vectors and color represents horizontal speed. Note that the limits on the color bar are lower than typical to better see this low-speed time in the flow field.

the same time as shown in Figure 4.6(c). Much of the difference seen in the vorticity at different depths is due to the increase in the size of Admiralty Head with depth, such that the vortices hit the seabed and do not show up in the plots. The biggest difference in depth seen for the vorticity is in its magnitude. The vorticity is stronger near the surface where the pressure gradient established along the seabed is the largest (due to sharper headland tip and stronger flows near the surface) and smallest nearer the seabed, where the speeds are reduced due to bottom friction. Overall, the vortices are fairly coherent with depth because the separation point of the flow past the headland does not have much vertical variation.

Vorticity on flood tide is less vertically coherent than the vorticity on ebb tide. Figure 4.16 shows vorticity on a typical flood tide. The flow moves quickly parallel to the headland past the headland tip near the surface, strongly generating vorticity due to the strong pressure gradient. Lower in the water column, the bathymetry is less sharp and the flow tends to wrap around the headland more, generating less vorticity and generating it further downstream around the headland. The vertical variation in vorticity on flood tide is due to the vertical variation of the separation point, due to the headland bathymetry. This leads to vorticity that is twisted in multiple dimensions.

### *4.2.6 Vertical Velocity*

#### *Upsloping and Upwelling Velocities*

Significant vertical velocities are frequently seen near the headland, associated with fronts and vortices. Vertical velocities can be roughly split into two categories: upsloping, $w_{us}$, and upwelling, $w_{uw}$ (Deleersnijder, 1989). Upsloping vertical velocity is bathymetrically-induced. Upwelling vertical velocity is due to other effects such as vertical variations of horizontal convergence or divergence. In ROMS, the upwelling velocity is solved for directly due to the code's use of terrain-following coordinates (`omega` is the variable name in ROMS for upwelling vertical velocity). Upsloping velocity is the difference between the full vertical velocity and the upsloping velocity: $w_{us} = w - w_{uw}$. The derivation of the upsloping velocity and more example plots are given in Appendix A. Note that in a flat-bottomed channel, all vertical velocity would be categorized as upwelling.

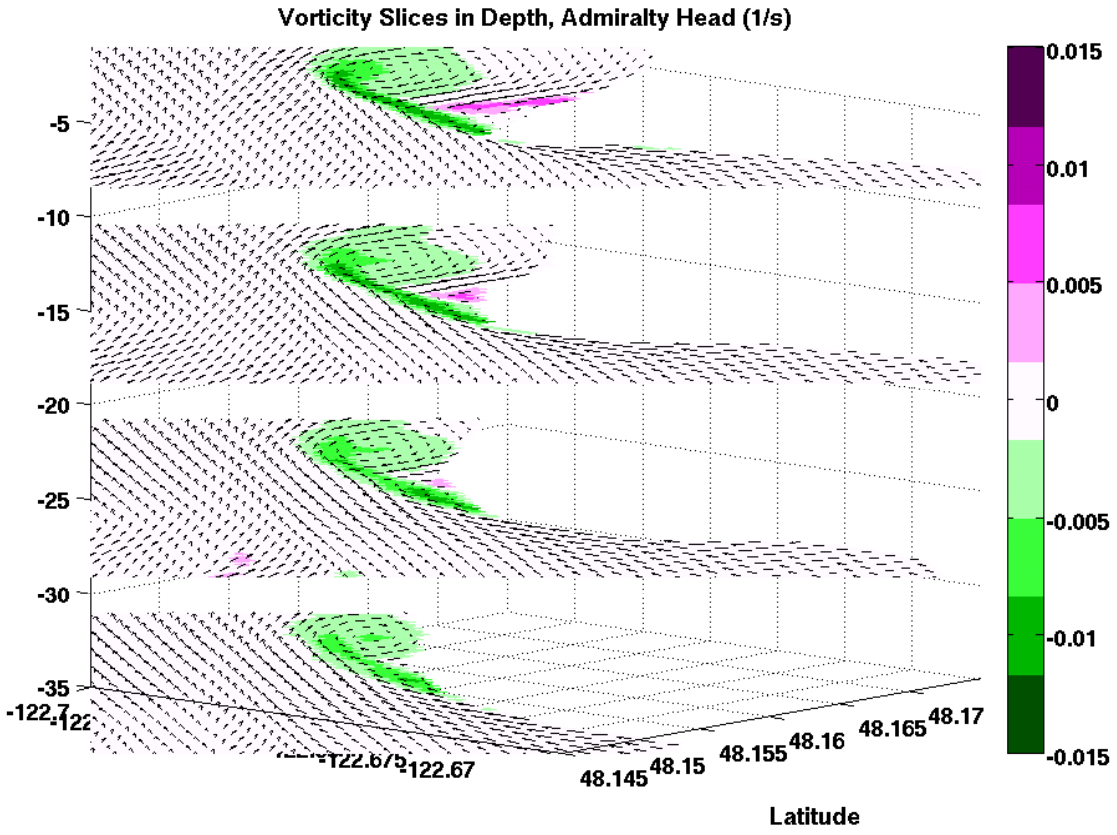


Figure 4.15: Ebb vorticity at 3:45PM on 9/5/06, shown in four slices at constant depth of vorticity near Admiralty Head, looking northwest past the headland. Ebb tide shown is the same as in Figure 4.6. Note the lower vorticity color bar limits in this figure, for visual illumination.

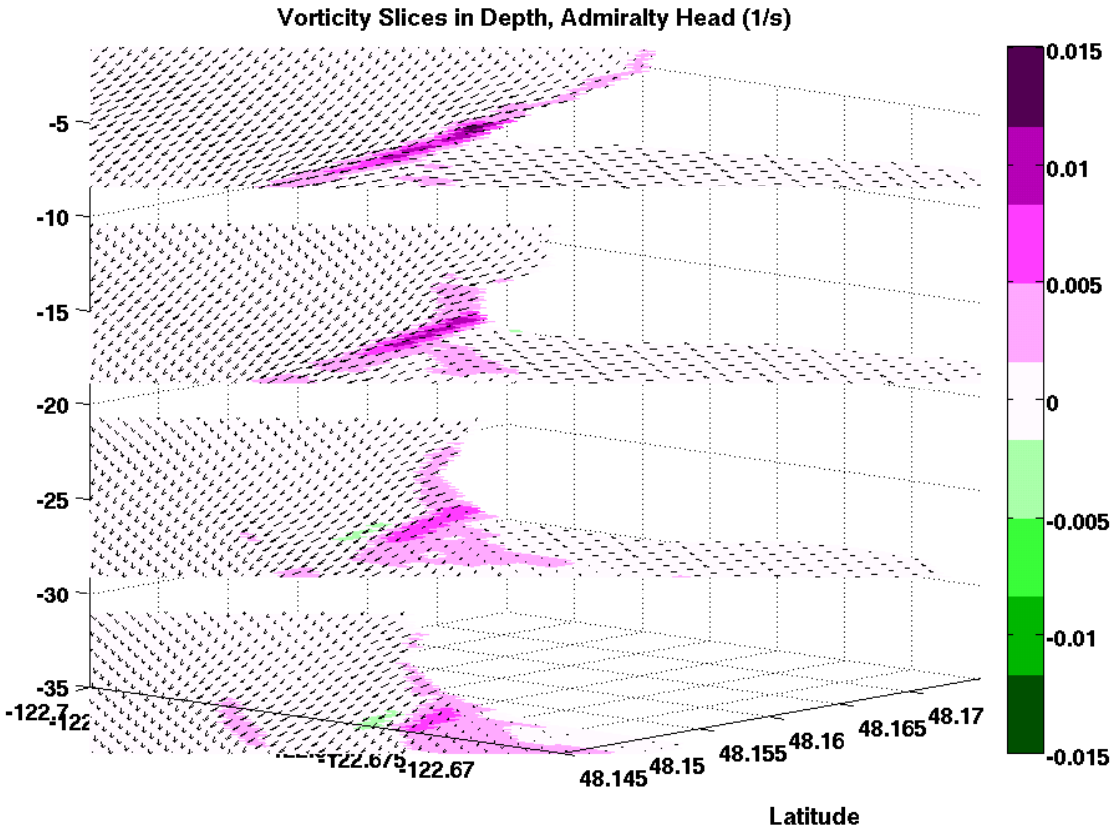


Figure 4.16: Flood vorticity at 9:30PM on 9/4/06, shown in four slices at constant depth of vorticity near Admiralty Head, looking northwest past the headland. Note the lower vorticity color bar limits in this figure, for visual illumination.

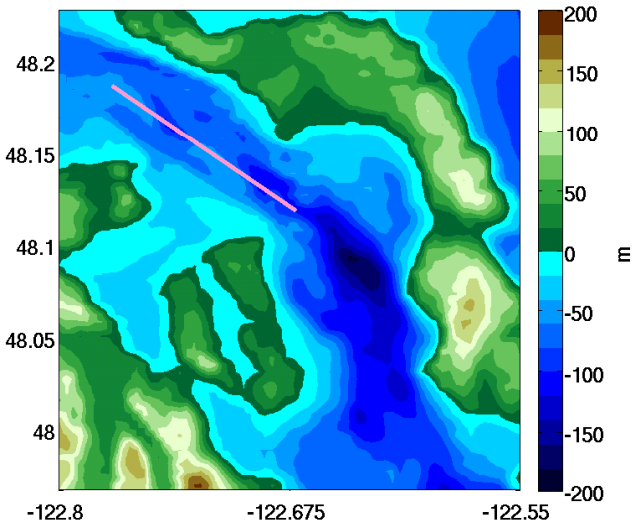


Figure 4.17: Domain bathymetry with slice location indicated

An along-channel slice of the mean magnitude of each designation of vertical velocity is shown in Figure 4.18 to illustrate the difference in character between the upsloping and upwelling velocities (the slice location is shown in Figure 4.17). The upsloping velocity is correlated with the steepness of the slope along the slice. The largest values are seen at the steepest bathymetric features, and every sloped area has increased values of upsloping. The upwelling velocity is found mid-water column, away from the seabed and sea surface, between the hills. More plots of upsloping and upwelling velocities can be found in Appendix A. A comparison of the mean plots shown in this section and maximum/minimum plots in Section A.2.1 indicates that upsloping velocity is generated more frequently that upwelling velocity, but that upwelling velocity is stronger when it is present.

*Causes of Upwelling Velocity*

White and Wolanski (2008) found that vertical velocity near an island was caused by converging or diverging flow in the presence of active bottom friction. The vertical velocity studied in that research was exclusively upwelling velocity in order to distinguish generation

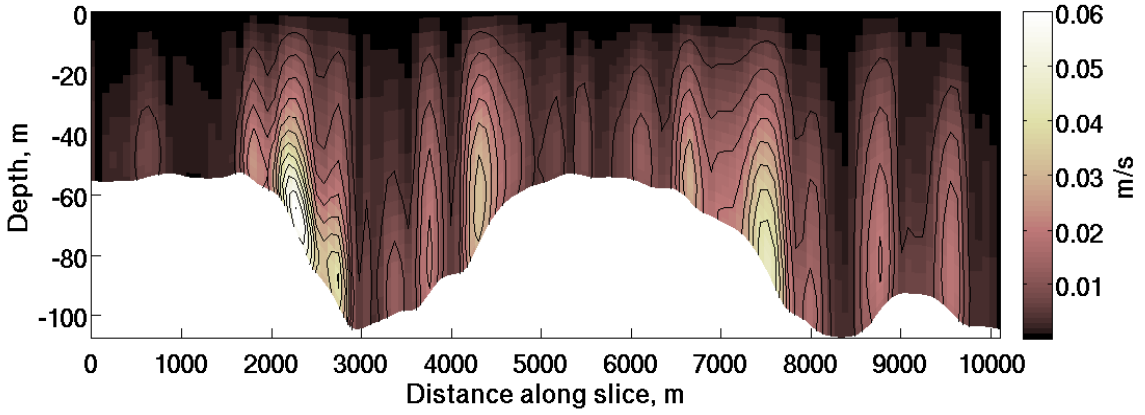


(a) Upsloping Velocity

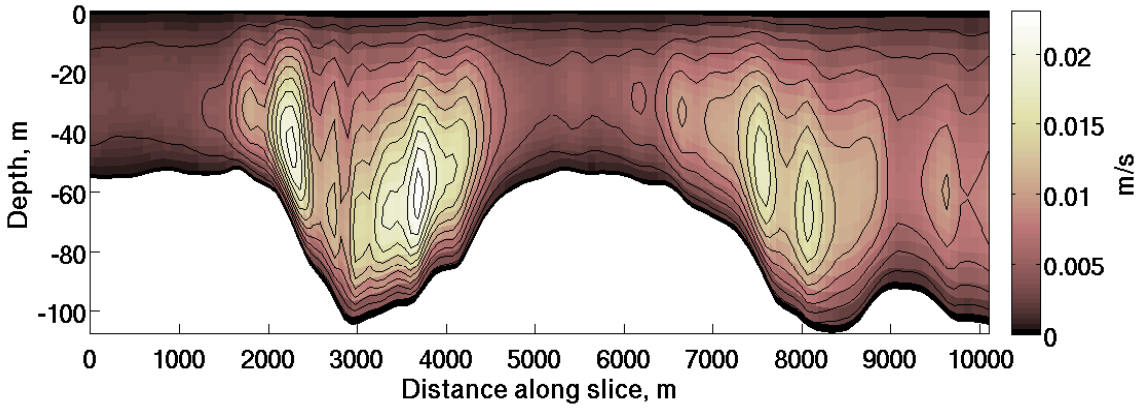


(b) Upwelling Velocity

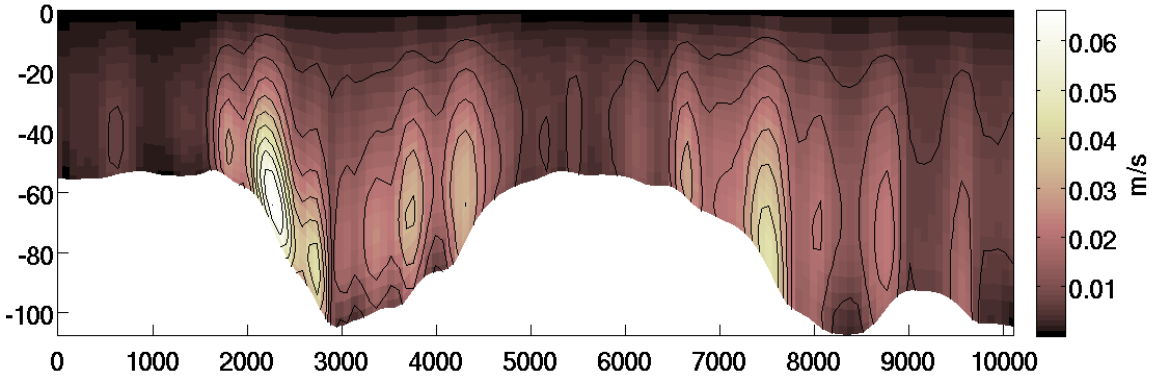


(c) Vertical Velocity

Figure 4.18: Time-averages over 30-day simulation of the magnitude of various vertical velocities. The north end of the slice is at the left end of the subplots.

mechanisms of vertical velocity from simply topographic.

Figure 4.19 shows a diagram of possible behaviors seen in the study. In diverging flow combined with bottom friction (to create a vertical shear profile), there is upwelling, whereas in converging flow there is downwelling. The onshore flow case is similar to the converging flow case but with a solid wall replacing one side of converging flow, and similarly results in downwelling. Positive vertical velocity may be seen near a headland tip due to competing mechanisms of the pressure gradient and the centrifugal acceleration.

These regions of upwelling and downwelling are strongest mid-water column, which would typically be caused by an area on the surface of horizontal divergence or convergence (divergence and convergence are strongest near the surface where the currents are typically the strongest and the headland tip is the sharpest). Therefore, typically associated with upwelling velocities are vertical gradients of vertical velocity of varying sign above and below the upwelling region, and horizontal gradients of vertical velocity of varying sign on either side of the region.

A snapshot for the example ebb tide shown for vorticity in Figures 4.6(c) and 4.15 is shown in Figure 4.20 for upwelling velocity. It is clear that velocity magnitudes tend to be larger mid-water column, which is below the areas of strongest horizontal convergence/divergance, and there are patches of velocity greater than 0.1 m/s. Some of the patches of velocity have been labelled using the categories of mechanisms possibly leading to upwelling and downwelling, as described in Figure 4.19. In particular, eddies generate areas of diverging flow (A) at the "outside" of the circulation, and areas of converging flow (B) where the flow turns back into itself, at the "inside" of the eddy. These areas lead to upwelling and downwelling, respectively, in the presence of bottom friction. There also appears to be convergence where the horizontal flow pushes against the headland (C), causing downwelling, and possibly curved flow near the headland tip (D), with a small positive velocity signal. An additional comparison of the categories of vertical velocity can be seen in Section A.2.2 of this plot.

Vertical velocity can also be seen associated with fronts in the simulation. This could be due to several mechanisms. A front moving through the system typically carries fresher water and is pushing through denser water. The density difference between the two could

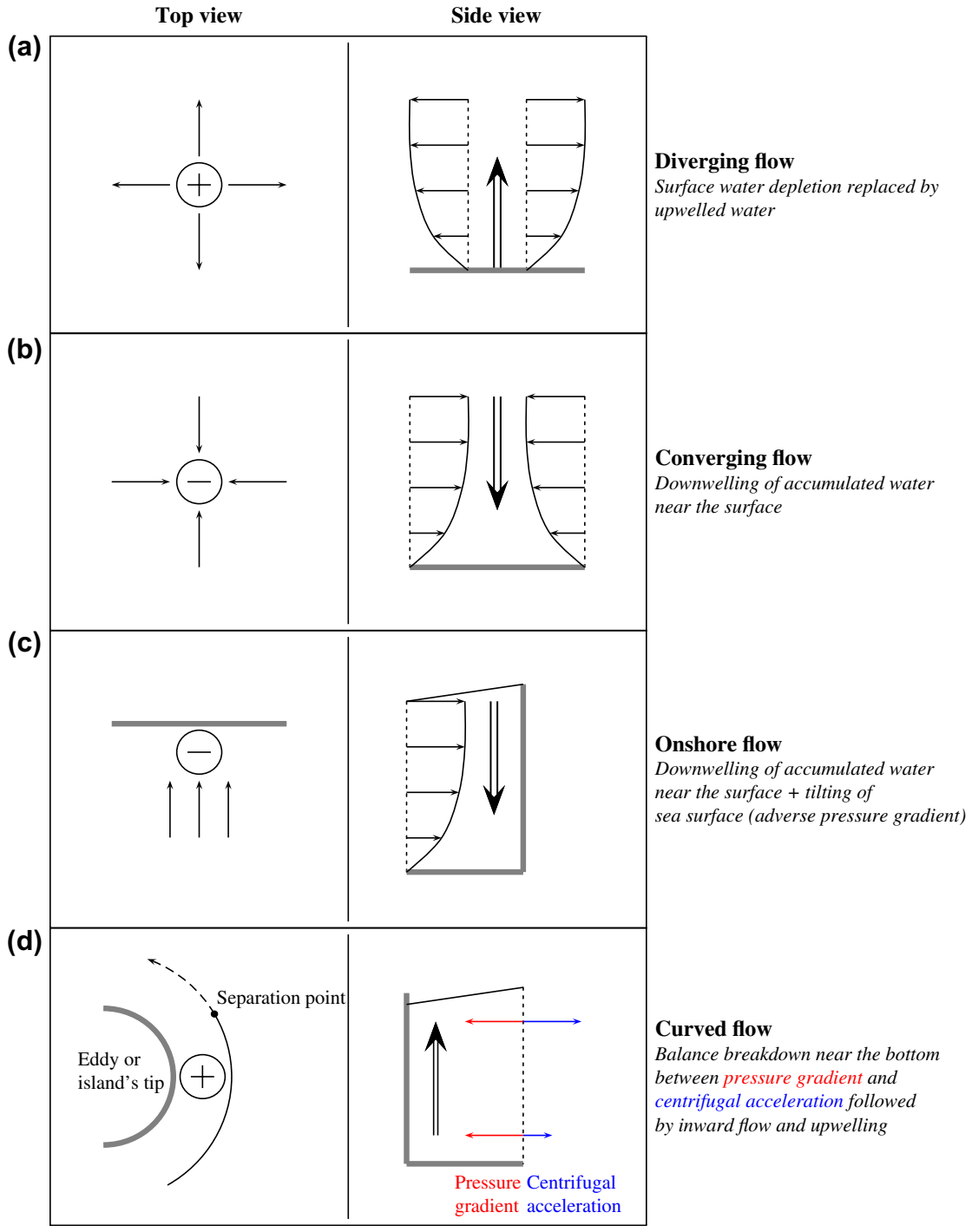


Figure 4.19: Summary of possible mechanisms for upwelling and downwelling flows when bottom friction is an important factor. Each of these situations is possible near Admiralty Head. From White and Wolanski (2008).

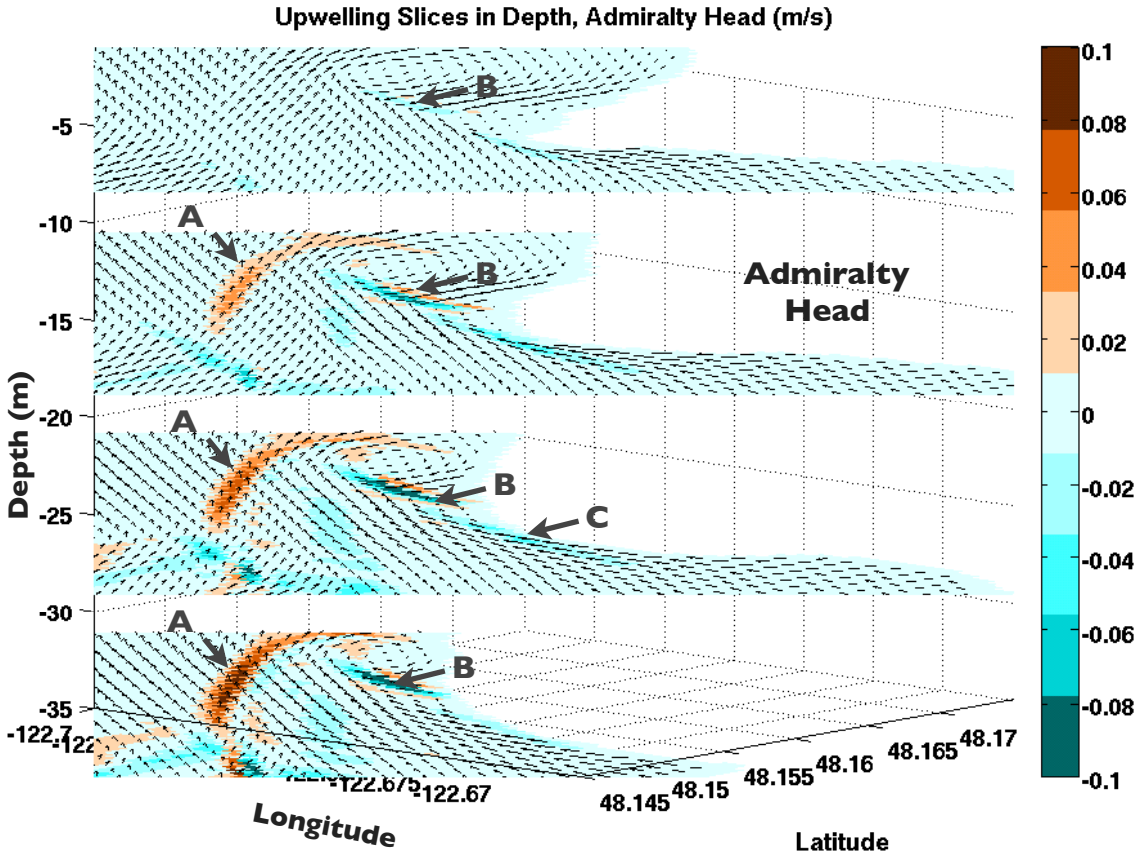


Figure 4.20: Snapshot from an ebb tide on 9/5/06, showing slices in depth of upwelling velocity, looking northwest past Admiralty Head. Areas of velocity are approximately labelled using categories shown in Figure 4.19. Snapshot is at the same time as shown in Figures 4.6(c) and 4.15.

push the fresher water up and/or the denser water down. Also, the front is made up of stronger speeds pushing into slower-moving water. This could be considered to be similar to category B or C in Figure 4.19 of converging flow.

These vertical velocities could have important ramifications for turbine siting near the headland, as is explored further in Section 6.3.2.

### *4.2.7 Vortex Changes in Time*

Vortices on consecutive similar tidal cycles (taking into account the diurnal inequality of tidal cycles, such that "similar" tidal cycles are typically every other cycle) tend to be similar to each other. Consecutive similar vortices change significantly on a weekly time scale. Figure 4.21 shows snapshots of ebb vortices at their approximate half-cycle maximum extent. The first two snapshots are from consecutive similar ebb tides, *i.e.*, a lower low water ebb tide, then skipping a higher low water ebb, and showing another lower low water ebb tide. The two vortices are markedly similar. Over the subsequent few lower low water ebb tides, the shape and size of the vortex maximum changes a little until about a week later when they are significantly different on lower low water, as shown in Figures 4.21(c) and 4.21(d). This time scale of change in behavior is similar for higher low water ebb tides, and flood tides as well.

## *4.3 Vertical Vorticity Governing Equation*

Understanding the details of vorticity generation and dynamics requires beginning with the governing equation itself. Vorticity equations have been derived many times in the past for various situations. In this case, the vorticity governing equation is derived starting with the horizontal momentum equations employed in this ROMS simulation, as stated in Chapter 2. In addition to the typical ROMS terms, this modified form includes expressions to account for truncation errors, in order to discover their level of effect in the analysis described in the following section. The focus in this research is on the vertical vorticity, and this derivation is for that component alone. First, scaling analysis will be discussed that stems from the assumptions built into ROMS (the hydrostatic approximation and incompressibility) before addressing the governing equation itself.

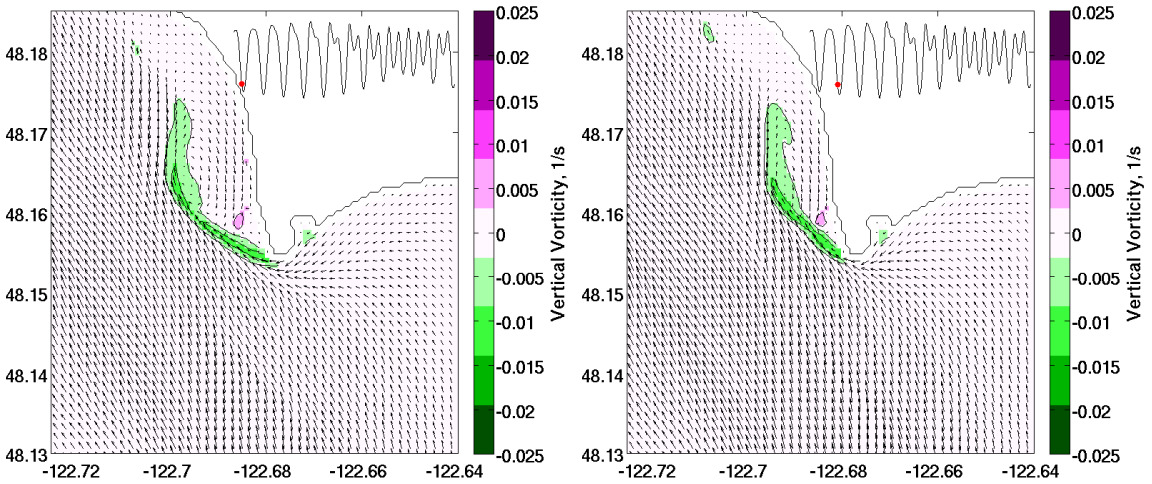


(a) 9/1/06, 10:30AM

(b) 9/2/06, 11:15AM

(c) 9/10/06, 8:00AM

(d) 9/11/06, 8:45AM

Figure 4.21: Representative snapshots of the ebb vortex on two consecutive similar ebb tides and two consecutive ebb tides a week later.

### *4.3.1 Scaling Analysis of Vorticity*

In order to perform scaling analysis on the definition of vorticity, we follow analysis in O'Donnell et al. (1998) and begin with the hydrostatic approximation, which states

$$\frac{Dw}{Dt} \ll \frac{1}{\rho}\frac{\partial p}{\partial z} \text{ or } \frac{Dw/Dt}{1/\rho\partial p/\partial z} \ll 1. \tag{4.1}$$

Using characteristic scales U, W, L, D, and T=L/U for horizontal and vertical velocity, horizontal and vertical length, and time scales, respectively, gives

$$\frac{Dw}{Dt} = \frac{\partial w}{\partial t} + u\frac{\partial w}{\partial x} + v\frac{\partial w}{\partial y} + w\frac{\partial w}{\partial z} \tag{4.2}$$

$$= \mathcal{O}\left(\frac{UW}{L}, \frac{W^2}{D}\right). \tag{4.3}$$

From the continuity equation,

$$u_x + v_y + w_z = 0,$$

so that

$$\frac{U}{L} = \mathcal{O}\left(\frac{W}{D}\right). \tag{4.4}$$

Equations 4.3 and 4.4 together imply

$$\frac{Dw}{Dt} = \mathcal{O}\left(\frac{W^2}{D}\right) = \mathcal{O}\left(\frac{UW}{L}\right). \tag{4.5}$$

A simple form of the $u$-momentum equation is

$$u_t + (\underline{v}\cdot\nabla)u - fv = -\frac{p_x}{\rho_0}.$$

Scaling analysis of these terms gives the balance

$$\frac{U^2}{L} = \mathcal{O}\left(\frac{p}{\rho L}\right),$$

$$\text{or} \qquad p = \mathcal{O}(\rho U^2), \tag{4.6}$$

which is advective scaling.

Using Equation 4.6,

$$\frac{1}{\rho}\frac{\partial p}{\partial z} = \mathcal{O}\left(\frac{\rho U^2}{\rho D}\right) = \mathcal{O}\left(\frac{U^2}{D}\right). \tag{4.7}$$

Overall, starting from the scaling balance from the hydrostatic approximation and combining it with the scaling of the continuity equation, the material derivative of vertical velocity, and the horizontal momentum equation, another scaling expression can be found:

$$\begin{aligned} \frac{Dw/Dt}{1/\rho\partial p/\partial z} &\ll 1, \text{ from Equation 4.1} \\ \frac{UW/L}{U^2/D} &\ll 1, \text{ using Equations 4.5 and 4.7} \\ \frac{W/L}{U/D} &\ll 1. \end{aligned} \tag{4.8}$$

The definition of vorticity is

$$\underline{\omega} = (w_y - v_z, u_z - w_x, v_x - u_y)\,.$$

Scaling analysis of the vorticity using Equation 4.8 gives

$$\frac{w_y}{v_z} = \mathcal{O}\left(\frac{W/L}{U/D}\right) \ll 1$$

implying that

$$\frac{W}{L} \ll \mathcal{O}\left(\frac{U}{D}\right)$$

so that

$$w_y \ll v_z,$$

and similarly, $w_x \ll u_z$. The vorticity can therefore be written approximately as

$$\underline{\omega} = (-v_z, u_z, v_x - u_y) \text{ or } \underline{\omega} = \nabla \times \underline{u}, \tag{4.9}$$

where $\underline{u} = (u, v, 0)$. Equation 4.9 will be used as the definition of relative vorticity in the following vorticity analysis. While the expression for vertical vorticity is not changed, the expressions for the other two components of vorticity in the governing equation for vertical vorticity are altered by the hydrostatic approximation and the incompressibility condition.

### *4.3.2 Derivation of Governing Equation for Vertical Vorticity*

The horizontal momentum equations derived in Section 2.6.3 are

$$u_t + (\underline{v} \cdot \nabla)u - fv = -\frac{1}{\rho_0}p_x + (K_M u_z)_z + \frac{h}{4}(uv)_{yy} + \frac{h}{2}u_y v_y \tag{4.10}$$

$$v_t + (\underline{v} \cdot \nabla)v + fu = -\frac{1}{\rho_0}p_y + (K_M v_z)_z + \frac{h}{4}(uv)_{xx} + \frac{h}{2}u_x v_x, \tag{4.11}$$

and the incompressible continuity equation is

$$u_x + v_y = -w_z. \tag{4.12}$$

Vertical vorticity is given as

$$\omega^z = v_x - u_y.$$

The vertical vorticity governing equation can be derived by taking the derivative with respect to $x$ of Equation 4.11, and subtracting the derivative with respect to $y$ of Equation 4.10. Rearranging, this gives

$$\begin{aligned} v_{tx} - u_{ty} + (\underline{v}_x \cdot \nabla)v - (\underline{v}_y \cdot \nabla)u + (\underline{v} \cdot \nabla)v_x - (\underline{v} \cdot \nabla)u_y + fu_x + f_x u + fv_y + f_y v \\ = \left[(K_M v_z)_x - (K_M u_z)_y\right]_z + \frac{h}{4}\left[(uv)_{xxx} - (uv)_{yyy}\right] + \frac{h}{2}\left[(u_x v_x)_x - (u_y v_y)_y\right]. \end{aligned}$$

Various groups of terms can be rewritten as follows:

- $v_{tx} - u_{ty} = \frac{\partial}{\partial t}(\omega^z + f)$, assuming that the space and time derivatives commute, and adding in the constant (in time) Coriolis force for future convenience
- $(\underline{v}_x \cdot \nabla)v - (\underline{v}_y \cdot \nabla)u = -(\underline{\omega} \cdot \nabla)w$, using Equations 4.9 and 4.12 and rearranging
- $(\underline{v} \cdot \nabla)v_x - (\underline{v} \cdot \nabla)u_y = (\underline{v} \cdot \nabla)\omega^z$
- $fu_x + fv_y = f(u_x + v_y) = -fw_z$, using Equation 4.12
- $f_x u + f_y v = (\underline{v} \cdot \nabla)f$
- $\left[(K_M v_z)_x - (K_M u_z)_y\right]_z = \left[\nabla \times (\nabla \cdot \underline{\underline{\tau}}_R)\right] \cdot \hat{n}_z$, where $\hat{n}_z$ is the unit vector in the vertical direction

- $\frac{h}{4}\left[(uv)_{xxx} - (uv)_{yyy}\right] = \left[\nabla \times (\nabla \cdot \underline{\underline{\tau}}_N)\right] \cdot \hat{n}_z$
- $\frac{h}{2}\left[(u_x v_x)_x - (u_y v_y)_y\right] = (\nabla \times \mathcal{T}) \cdot \hat{n}_z$

Two of these can change further:

$$\begin{aligned}(\underline{v} \cdot \nabla)\omega^z + (\underline{v} \cdot \nabla) f &= (\underline{v} \cdot \nabla)(\omega^z + f) \\ &= (\underline{v} \cdot \nabla)\omega_a^z \\ &= \nabla \cdot [\underline{v}\omega_a^z] - \omega_a^z \cancelto{0}{(\nabla \cdot \underline{v})},\end{aligned}$$

using Equation 4.12 and defining the absolute vorticity as

$$\underline{\omega}_a = (\omega^x, \omega^y, \omega^z + f).$$

Combining the above forms, the governing equation for the absolute vertical vorticity is given by:

$$\begin{aligned}\overbrace{\frac{\partial \omega_a^z}{\partial t}}^{\text{Rate-of-change}} &= \overbrace{\left(\underline{\omega}_a \cdot \nabla\right) w}^{\text{Tilting/stretching}} - \overbrace{\nabla \cdot (\underline{v}\omega_a^z)}^{\text{Advection}} \\ &+ \underbrace{\left[\nabla \times (\nabla \cdot \underline{\underline{\tau}}_R)\right] \cdot \hat{n}_z}_{\text{Reynolds stress generation}} + \underbrace{\left[\nabla \times (\nabla \cdot \underline{\underline{\tau}}_N)\right] \cdot \hat{n}_z + (\nabla \times \mathcal{T}) \cdot \hat{n}_z}_{\text{Numerical generation}}\end{aligned} \tag{4.13}$$

### *4.3.3 Interpretation of Terms*

The terms in the governing equation for vorticity can be interpreted following the interpretations in Kundu and Cohen (2004). The left-hand-side in Equation 4.13 is the time rate of change of the absolute vorticity. The first term on the right-hand-side (RHS) is the tilting, rotating, and stretching of absolute vorticity. Tilting of vertical vorticity into horizontal or vice versa neither creates nor destroys vorticity in the system but can significantly change the amount in any one direction. Stretching of vorticity generates vorticity from angular momentum conservation while contracting of vorticity reduces it. The second term on the RHS is the advection of absolute vorticity. The rest of the terms on the RHS create and destroy vorticity. The Reynolds stress term can result in vorticity generation or turbulent diffusion of vorticity. The numerical terms similarly may generate vorticity or cause viscous

eddy diffusion of vorticity. The Reynolds stress term and the numerical terms generate most of the new vorticity in the system at closed boundaries, where horizontal gradients are the largest.

## *4.4 Integrated Vorticity Dynamics in a Region*

In Dong et al. (2007), a study on boundary vorticity generation in flow past a cylindrical island in the deep ocean, the authors derive and use a diagnostic method for calculating the vorticity generation at the sidewalls of the island. The same methodology will be employed here using an integrated form of the governing equation for vorticity derived in the previous section in order to understand the various mechanisms influencing vorticity, including boundary generation. The integration is performed over a domain that is bounded horizontally by vertical sidewalls and is bounded vertically by two of the following: the seabed, the free surface, and a constant depth level. The vertical sidewalls are aligned with the coordinate axes and may cross active water grid cells or inactive land cells (in which case the bounding wall to the active domain is the closed wall at the land-sea interface). Significant vorticity generation is expected at the boundaries because, as shown in Panton (2005), vorticity is generated at boundaries in the presence of pressure gradients and unsteady flow, both of which occur strongly in Admiralty Inlet, especially near the headland.

### *4.4.1 Analysis*

The 3D divergence theorem states that

$$\iiint (\nabla \cdot \underline{F}) \mathrm{d}V = \oiint \underline{F} \cdot \hat{n} \mathrm{d}S,$$

where $\hat{n}$ is the unit normal outward from the surface, $\underline{F}$ is a vector function of $\underline{x}$, and $\mathrm{d}S$ is a differential surface along the boundary of the volume. Stokes' theorem states that

$$\oint \underline{F} \cdot \mathrm{d}\underline{\ell} = \iint (\nabla \times \underline{F}) \cdot \hat{n}_z \mathrm{d}S,$$

where $\mathrm{d}\underline{\ell}$ is a differential length along the circumference of a horizontal surface and $\hat{n}_z$ is a unit normal in the vertical direction.

In this analysis, the volume integral of the governing equation for $\omega_a^z$, Equation 4.13, is first taken, and then the result is examined term-by-term. This integration is done over three-dimensional sub-domains of the entire numerical domain. Multiple domains will be analyzed.

Using the Leibniz rule to address the first term of the volume integral of Equation 4.13 gives:

$$\iiint \frac{\partial \omega_a^z}{\partial t} \mathrm{d}t = \frac{d}{dt} \iiint \omega_a^z \mathrm{d}V - \iint_\zeta \omega_a^z (\underline{v}_b \cdot \hat{n}) \mathrm{d}A \tag{4.14}$$

where the second integral on the RHS is over the free surface, $\underline{v}_b$ is the velocity of the free surface, and $\hat{n}$ is the unit normal outward from the surface. The second integral on the RHS is zero for the surfaces of the analysis domain other than the free surface because none of the other boundaries are time-dependent.

The integral of the first term on the RHS of Equation 4.13 could be presented in an alternative form using the divergence theorem, but the original form is preferred in this case, for ease of interpretation. Splitting between horizontal and vertical vorticity terms gives

$$\iiint (\underline{\omega}_a \cdot \nabla) \, w \mathrm{d}V = \iiint \left( \omega^x \frac{\partial w}{\partial x} + \omega^y \frac{\partial w}{\partial y} \right) \mathrm{d}V + \iiint \omega_a^z \frac{\partial w}{\partial z} \mathrm{d}V.$$

The first volume integral is the tilting between horizontal vorticity and vertical vorticity, which does not create nor destroy vorticity but does change its directionality, and the second volume integral is the the stretching and shrinking of vertical vorticity, which does create and destroy vorticity.

Using the divergence theorem, the integral of the second term on the RHS in Equation 4.13 can be written, for a general analysis domain, as

$$\begin{aligned} -\iiint \nabla \cdot (\omega_a^z \underline{v}) \, \mathrm{d}V &= -\oiint \omega_a^z (\underline{v} \cdot \hat{n}) \mathrm{d}S \\ &= -\iint_o \omega_a^z (\underline{v} \cdot \hat{n}_h) \mathrm{d}S - \iint_z \omega_a^z (\underline{v} \cdot \hat{n}_z) \mathrm{d}S - \iint_\zeta \omega_a^z (\underline{v} \cdot \hat{n}_\zeta) \mathrm{d}S, \end{aligned} \tag{4.15}$$

where the surface integral has been broken into integrals over different surfaces with $\hat{n}$ as the unit normal outward from a general surface, $\hat{n}_h$ as the horizontal unit normal outward, $\hat{n}_z$ as the vertical unit normal outward, and $\hat{n}_\zeta$ as the unit normal outward from the free

surface. The subscripts $z$, $o$, and $\zeta$ indicate taking the integral at the vertical and horizontal open analysis boundaries and the free surface, respectively. The surface terms along the closed sidewall and seabed are zero due to the impermeability condition. The terms along the vertical open analysis boundaries represent the advection of vertical vorticity into and out of the analysis domain. Due to the kinematic boundary condition at the sea surface, the normal component of the fluid must be equal to the velocity of the boundary normal to itself. That is, at the free surface,

$$\underline{v} \cdot \hat{n}_\zeta = -\underline{v}_b \cdot \hat{n}_\zeta,$$

and the expression in Equation 4.15 can be rewritten as

$$-\iiint \nabla \cdot (\omega_a^z \underline{v})\,\mathrm{d}V = -\iint_o \omega_a^z (\underline{v} \cdot \hat{n}_h)\mathrm{d}S - \iint_z \omega_a^z (\underline{v} \cdot \hat{n}_z)\mathrm{d}S + \iint_\zeta \omega_a^z (\underline{v}_b \cdot \hat{n}_\zeta)\mathrm{d}S \qquad (4.16)$$

Comparing Equations 4.14 and 4.16, it can be seen that the final term from Equation 4.14 is equal and opposite to the sea surface term here and they cancel, leaving only the terms at the vertical open boundaries in this expression.

The integral of the third term on the RHS in Equation 4.13, using Stokes' theorem, can be rewritten as

$$\begin{aligned}
\iiint \nabla \times (\nabla \cdot \underline{\underline{\tau}}_R) \cdot \hat{n}_z \mathrm{d}V &= \int \oint \left(\nabla \cdot \underline{\underline{\tau}}_R\right) \cdot \mathrm{d}\underline{\ell}\mathrm{d}z \\
&= \int \oint \left( K_M \frac{\partial^2 \underline{u}}{\partial z^2} + \left(0, 0, \frac{\partial u}{\partial z}\frac{\partial K_M}{\partial x} + \frac{\partial v}{\partial z}\frac{\partial K_M}{\partial y}\right)\right) \cdot \mathrm{d}\underline{\ell}\mathrm{d}z \\
&= \int \oint K_M \frac{\partial^2 \underline{u}}{\partial z^2} \cdot \mathrm{d}\underline{\ell}\mathrm{d}z \\
&= \int \oint K_M \left(\frac{\partial^2 u}{\partial z^2}\mathrm{d}\ell_x + \frac{\partial^2 v}{\partial z^2}\mathrm{d}\ell_y\right)\mathrm{d}z \\
&= \int \oint K_M \frac{\partial^2 \underline{u}}{\partial z^2} \cdot \hat{\ell}\mathrm{d}\ell\mathrm{d}z,
\end{aligned}$$

where $\mathrm{d}\underline{\ell} = (\mathrm{d}\ell_x, \mathrm{d}\ell_y, 0)$ is the differential unit vector in the counterclockwise direction along the horizontal boundary and $\hat{\ell} = (\ell_x, \ell_y, 0)$ is the unit tangent vector clockwise around the boundary. In analogy with the eddy-viscous flux terms in Dong et al. (2007), the term on the RHS represents vertical vorticity generation due to Reynolds stresses at the closed boundaries, and represents the eddy-viscous flux of vertical vorticity at the open boundaries.

This indicates that the vertical vorticity generation due to the Reynolds stresses can be determined by integration along the boundary walls instead of by integration throughout the volume. That is, Stokes' theorem allows us to deal with the full analysis domain indirectly by dealing with the sidewalls. This integral will be split into two parts for analysis: one part along the closed sidewalls/sloping seabed, which are the boundary generation terms, and the other part representing the diffusive flux through the open analysis boundaries, and will be written as

$$\int \oint K_M \frac{\partial^2 \underline{u}}{\partial z^2} \cdot \hat{\ell} \mathrm{d}\ell \mathrm{d}z = \int \oint_o K_M \frac{\partial^2 \underline{u}}{\partial z^2} \cdot \hat{\ell} \mathrm{d}\ell \mathrm{d}z + \omega_{bg}^R,$$

where the subscript $o$ indicates integration over the open boundaries and the second term on the RHS represents the boundary generation of vorticity due to the Reynolds stress. The second term will be solved for indirectly.

Applying Stokes' theorem to the integral of the fourth term on the RHS in Equation 4.13 gives

$$\begin{aligned}
\iiint \nabla \times (\nabla \cdot \underline{\underline{\tau}}_N) \cdot \hat{n}_z \mathrm{d}V &= \int \oint \left( \nabla \cdot \underline{\underline{\tau}}_N \right) \cdot \mathrm{d}\underline{\ell} \mathrm{d}z \\
&= \frac{h}{4} \int \oint \left( \frac{\partial^2 (uv)}{\partial y^2}, \frac{\partial^2 (uv)}{\partial x^2}, 0 \right) \cdot \mathrm{d}\underline{\ell} \mathrm{d}z \\
&= \frac{h}{4} \int \oint \left( \frac{\partial^2 (uv)}{\partial y^2} \mathrm{d}\underline{\ell}_x + \frac{\partial^2 (uv)}{\partial x^2} \mathrm{d}\underline{\ell}_y \right) \mathrm{d}z \\
&= \frac{h}{4} \int \oint \left( \frac{\partial^2 (uv)}{\partial y^2}, \frac{\partial^2 (uv)}{\partial x^2}, 0 \right) \cdot \hat{\ell} \mathrm{d}\ell \mathrm{d}z.
\end{aligned}$$

The terms can be interpreted as horizontal numerical eddy viscous generation of vertical vorticity at the walls and eddy viscous-flux across the open boundaries. Accordingly, the terms will be split between the wall and open boundary terms in a similar manner to the Reynolds stress terms, and written as:

$$\frac{h}{4} \int \oint \left( \frac{\partial^2 (uv)}{\partial y^2}, \frac{\partial^2 (uv)}{\partial x^2}, 0 \right) \cdot \hat{\ell} \mathrm{d}\ell \mathrm{d}z = \frac{h}{4} \int \oint_o \left( \frac{\partial^2 (uv)}{\partial y^2}, \frac{\partial^2 (uv)}{\partial x^2}, 0 \right) \cdot \hat{\ell} \mathrm{d}\ell \mathrm{d}z + \omega_{bg}^{N_1},$$

where the second term on the RHS represents the boundary generation of vorticity due to the first numerical mixing term.

Stokes' theorem is applied once again, this time to the integral of the fifth term, to find

$$\begin{aligned}\iiint (\nabla \times \underline{\mathcal{I}}) \cdot \hat{n}_z \mathrm{d}V &= \int \oint \underline{\mathcal{I}} \cdot \mathrm{d}\underline{\ell} \mathrm{d}z \\ &= \frac{h}{2} \int \oint \left( \frac{\partial u}{\partial y}\frac{\partial v}{\partial y}, \frac{\partial u}{\partial x}\frac{\partial v}{\partial x}, 0 \right) \cdot \mathrm{d}\underline{\ell} \mathrm{d}z \\ &= \frac{h}{2} \int \oint \left( \frac{\partial u}{\partial y}\frac{\partial v}{\partial y}\mathrm{d}\underline{\ell}_x + \frac{\partial u}{\partial x}\frac{\partial v}{\partial x}\mathrm{d}\underline{\ell}_y \right) \mathrm{d}z \\ &= \frac{h}{2} \int \oint \left( \frac{\partial u}{\partial y}\frac{\partial v}{\partial y}, \frac{\partial u}{\partial x}\frac{\partial v}{\partial x}, 0 \right) \cdot \hat{l} \mathrm{d}\ell \mathrm{d}z.\end{aligned}$$

This term will be split into parts along the walls and parts along the open analysis boundaries, and this term, like the previous, contributes to vorticity generation at the seabed and sidewalls and viscous flux across the open analysis boundaries. This term will be written as

$$\frac{h}{2} \int \oint \left( \frac{\partial u}{\partial y}\frac{\partial v}{\partial y}, \frac{\partial u}{\partial x}\frac{\partial v}{\partial x}, 0 \right) \cdot \hat{l} \mathrm{d}\ell \mathrm{d}z = \frac{h}{2} \int \oint \left( \frac{\partial u}{\partial y}\frac{\partial v}{\partial y}, \frac{\partial u}{\partial x}\frac{\partial v}{\partial x}, 0 \right) \cdot \hat{l} \mathrm{d}\ell \mathrm{d}z + \omega_{bg}^{N_2},$$

where the second term on the RHS represents the boundary generation of vorticity due to the second numerical mixing term.

The overall form for the volume-integrated equation for $\omega_a^z$ is now

$$\begin{aligned}\overbrace{\frac{d}{dt}\iiint \omega_a^z \mathrm{d}V}^{\text{Rate-of-change of total volume vorticity}} &= \overbrace{\iiint \left( \omega^x \frac{\partial w}{\partial x} + \omega^y \frac{\partial w}{\partial y} \right) \mathrm{d}V}^{\text{Tilting throughout volume}} + \overbrace{\iiint \omega_a^z \frac{\partial w}{\partial z} \mathrm{d}V}^{\text{Stretching throughout volume}} \\ &- \overbrace{\int \oint_o \omega_a^z (\underline{v} \cdot \hat{n}) \mathrm{d}\ell \mathrm{d}z}^{\text{Advection through walls}} + \overbrace{\int \oint_o K_M \underline{u}_{zz} \cdot \underline{\ell} \mathrm{d}\ell \mathrm{d}z + \omega_{bg}^R}^{\text{Reynolds viscous flux along walls}} \\ &+ \overbrace{\frac{h}{4} \int \oint_o ((uv)_{yy}, (uv)_{xx}, 0) \cdot \hat{\ell} \mathrm{d}\ell \mathrm{d}z + \omega_{bg}^{N1}}^{\text{Numerical viscous flux along walls}} \\ &+ \overbrace{\frac{h}{2} \int \oint_o (u_y v_y, u_x v_x, 0) \cdot \hat{l} \mathrm{d}\ell \mathrm{d}z + \omega_{bg}^{N2}}^{\text{Numerical viscous flux along walls}},\end{aligned} \tag{4.17}$$

where the $o$ subscripts represent surface integrals across or along the open analysis boundaries (horizontal or vertical), and the $\omega_{bg}$ terms represent sources of boundary generation of vorticity at the closed boundaries and are unknown. Vertical vorticity generation at the closed boundaries can be found diagnostically by solving for the boundary generation terms $\omega_{bg} = \omega_{bg}^R + \omega_{bg}^{N1} + \omega_{bg}^{N2}$ in Equation 4.17.

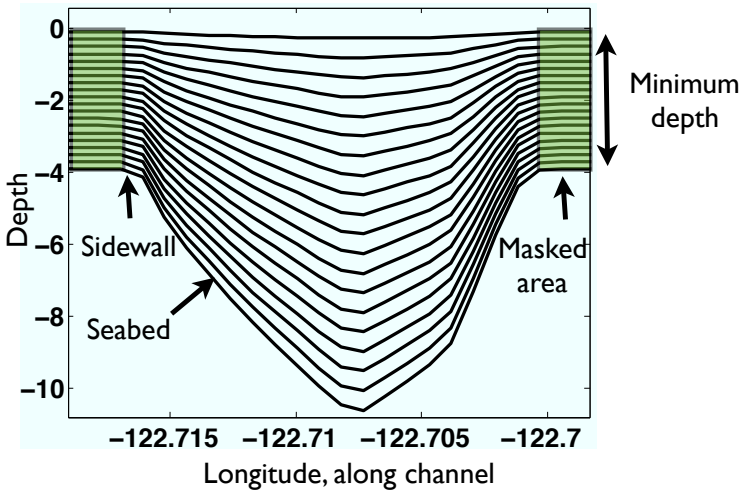


Figure 4.22: The vertical sidewalls have a no-slip condition imposed whereas the seabed has a quadratic drag law and so are considered separately.

### *4.4.2 Results*

To perform the calculations of the various terms in Equation 4.17, model output was read in, then interpolated onto a fixed three-dimensional grid with 65 meter horizontal resolution, as in the actual horizontal grid, and a very highly resolved vertical grid. The fixed grid was necessary to be consistent in time since ROMS has terrain-following coordinates vertically which change each time step due to the changing free surface. The vertical grid spacing of the fixed grid is $\Delta z = 0.2$ meters, which is the smallest vertical layer thickness found in the domain, and occurs where the twenty simulation layers are divided evenly (in this simulation) into the minimum vertical thickness of four meters (see Figure 4.22). This was done to preserve the information found at the sidewalls.

A few example tide half-cycles will be examined in detail in this section in order to understand the interacting dynamics in time and various possible behaviors of the terms in Equation 4.17. Analysis was done for the larger encompassing box shown in Figure 4.23 as well as for the sub-domains, numbered 1 through 6. The sub-domains were chosen to learn the source of boundary generation at a better spatial resolution than the larger analysis

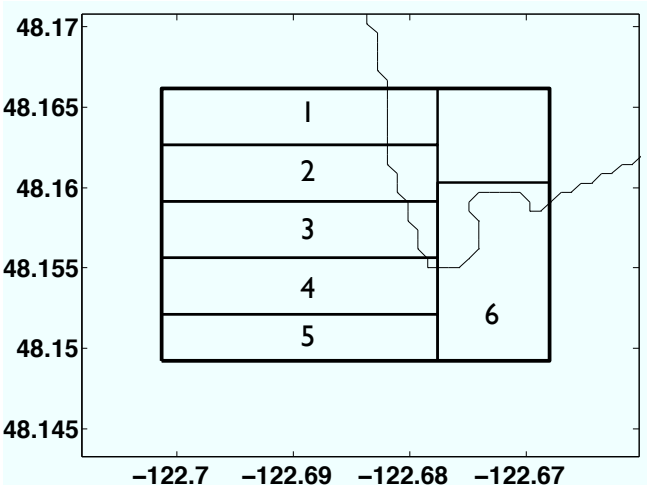


Figure 4.23: Zoom-in of Admiralty Head with lines indicating location of main analysis box (thicker line) around Admiralty Head, which is subdivided into smaller boxes 1 through 6 starting at the north and counting down and to the right. Analysis can be for the full domain, the subdomains, or for bounding walls in a domain, as referred to by geographic direction (North, West, South, and East).

domain, but still contain enough points to have a meaningful calculation.The encompassing box will be referred to as the large box and is the default analysis domain. The subdomains will be referred to by their box number. Each domain that is used for analysis has four bounding walls; these will be referred to by their relative position in the box: north, east, south, or west. Plots of the terms in Equation 4.17 are shown below with subplots of the local free surface, the volume-integrated vorticity, and the surface speed at a point near Admiralty Head. The vertical vorticity discussed throughout the section is the absolute vertical vorticity, though the Coriolis force is not significant in the simulations. The horizontal axis is labelled with the time and date of the model output. Terms in the following analysis are referenced using a descriptor of their role in the governing equation for vorticity as noted in Equation 4.17 (*e.g.*, advection, tilting, and Reynolds stresses). Terms also include the sign given in Equation 4.17.

*Comparison of Seabed and Sidewall Generation Rates*

The vorticity generation rate at the vertical no-slip sidewalls and the vorticity generated at the seabed are compared, as illustrated in Figure 4.24, since the boundary conditions applied in the code are different for these two cases (see Section 2.3.2). From a numerical simulation perspective, it is important to know the sensitivity of a simulation in ROMS to the minimum depth prescribed in a simulation as well as how a flat-bottomed channel may alter the amount of vorticity present in a system. Figure 4.24(a) appears to show that the vorticity generation rate is largely due to the seabed rather than the sidewalls. However, much more of the domain is bounded by the seabed instead of the sidewall, since in this case the sidewall is four meters deep. Looking instead at the generation rate at the sidewall and seabed as normalized per unit volume, as shown in Figure 4.24(b), the sidewalls and seabed are actually generating vorticity at about the same rate. Therefore, changing the minimum depth in the system by small amounts should not significantly affect the vorticity generation rate, and having a flat-bottomed channel, such that all frictional walls are sidewalls instead of seabed, should produce a comparable rate of vorticity as a similar simulation with any vertical seabed area. Note that despite this, the characteristics of the vorticity produced in a flat-bottomed tidal channel as compared with a simulation with realistic bathymetry would certainly be different, since, for example, the slope of the bathymetry can have a large effect on the tilt of a vortex tube.

*Case I: Basic Flood Tide*

Plots at a few snapshots in time during a typical diurnal flood tide on September 3, 2006, at higher high water are shown in Figure 4.25. Figure 4.26 shows the terms, in time, from the governing equation, volume-integrated throughout the large analysis domain shown overlaid in the flow figures. The resulting headland-generated vortex is medium in size, relative to those in other ebb tides. Note that the Reynolds stress and numerical viscous flux terms play a only a small role here. Also note that the total integrated vertical vorticity in the analysis domain peaks just before the speed peaks, and just before the advection of vorticity out of the system peaks (as shown in the top subplot in Figure 4.26). The vorticity generation

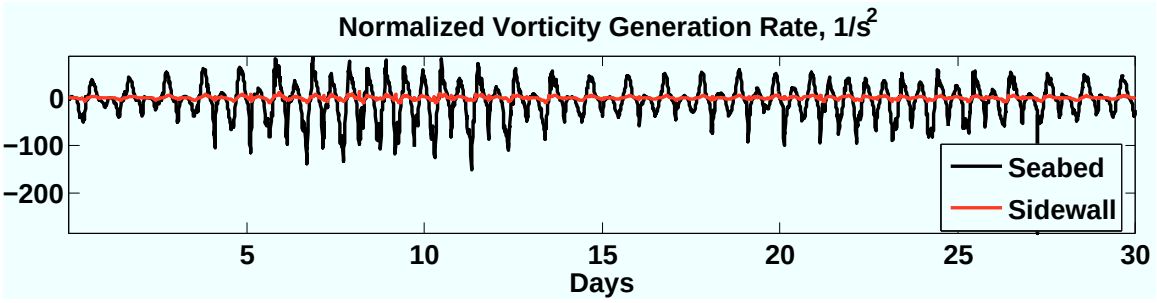


(a) Volumetric vertical vorticity generation rate

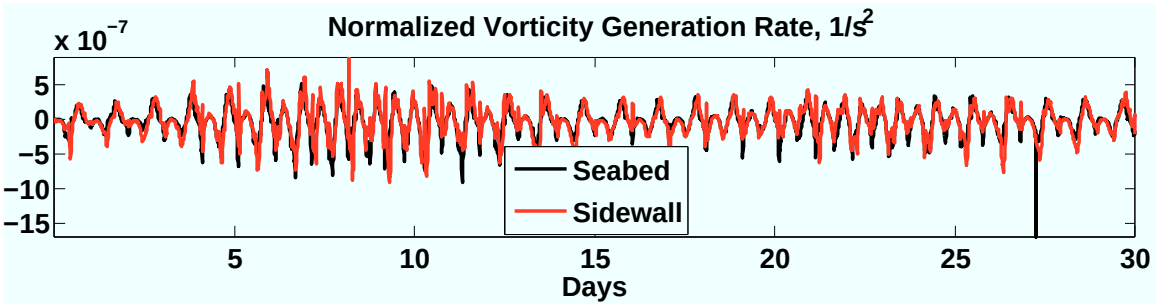


(b) Vertical vorticity generation rate normalized by the volume

Figure 4.24: Vertical vorticity generation rate in main analysis domain due to the sidewall and the seabed, shown with and without normalization by the volume.

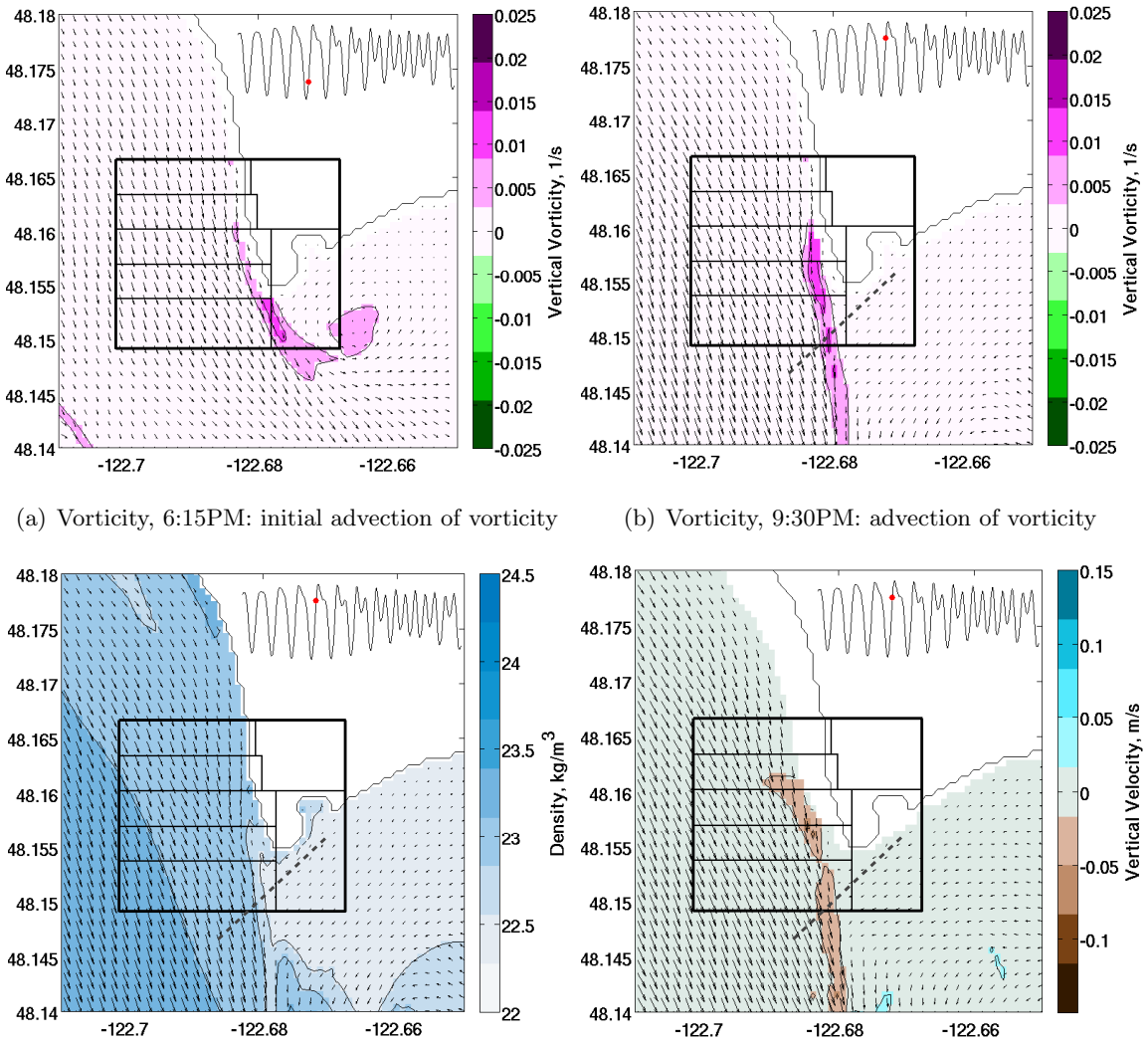


(a) Vorticity, 6:15PM: initial advection of vorticity

(b) Vorticity, 9:30PM: advection of vorticity

(c) Density, 9:30PM: density front develops

(d) Vertical velocity, 9:30PM: downwelling with convergence

Figure 4.25: Surface vorticity and density and 10 meter depth vertical velocity snapshots from 9/4/06. The first two vorticity images show how the vorticity develops during this flood tide. The density and vertical velocity are shown at the same time as the second vorticity snapshot to correlate related fields. Dashed lines indicate transect locations discussed in Section 4.4.2.

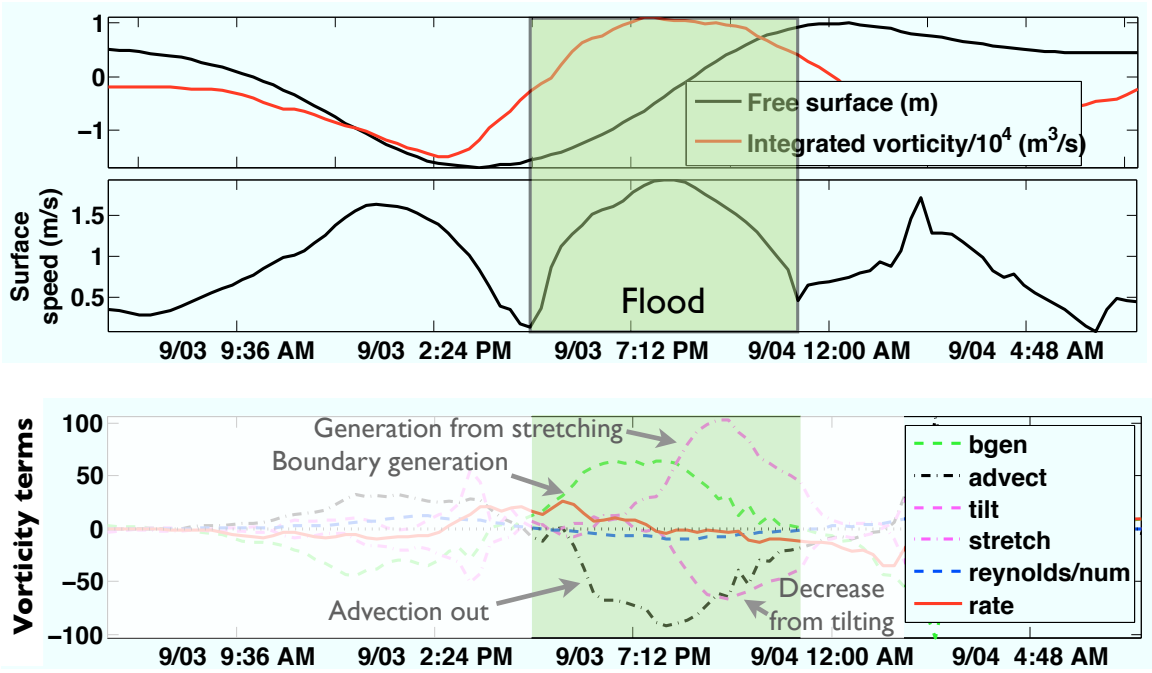


Figure 4.26: Case I free surface, integrated vorticity, surface speed, and terms in the vorticity governing equation for the main analysis domain.

rate peaks earlier in the cycle and decreases for the rest of the tide.

The free surface and speed curves in Figure 4.26 give timing and context to the various terms in Equation 4.17 given in the bottom subplot. As the flood tide in Case I begins, boundary generation of positive vorticity increases, followed shortly by the advection out of the analysis domain of positive vorticity. During the second half of the tide, tilting and stretching are significant effects: the positive vorticity is stretched, generating more vorticity, but is also tilted into horizontal vorticity. Generation due to stretching of vorticity is larger than the boundary generation at times. The Reynolds stresses and numerical terms have been combined together and are not important to the dynamics, but are associated with a small amount of positive vorticity reduction.

This analysis gives an overall perspective of the interplay of terms in the vorticity governing equation around Admiralty Head, but misses details since the analysis is over a domain with many complexities. To understand the terms in better spatial detail, the larger anal-

ysis domain was split into six subdomains (Figure 4.23), as shown in the following sections describing the relevant terms. Note that the advection of vertical vorticity is examined as movement through the open bounding walls of the analysis domains, whereas the stretching and tilting terms, for example, are integrated over the domain or sub-domain.

**Generation and Advection** Figure 4.27 shows the volumetric vorticity generation rate for each sub-domain box, and also shows the advection of vorticity through each bounding wall, along with the free surface signal and surface speed for context. The generation rate subplot shows that boundary generation starts in box 4 at the tip of Admiralty Head. While most of the boundary generation occurs in box 4 through the first half of this half-cycle, vorticity is also generated in boxes 6, 5, 3, 2, and 1, in that order in terms of magnitude and time, as the tide progresses. As described in Section 4.2.1, the vorticity follows a pattern in which it first reaches to the east (Figure 4.25(a)), and in this case, in the absence of noticeable persistent old vortices, has a smooth transition to reaching toward the south as it is advected by the horizontal currents (Figure 4.25(b)). It is the first reach out to the east that is associated with an increase in generation in box 6, due to the flow over the bathymetry in the area generating tilted vorticity with a vertical component. The reach to the south is associated with increased boundary generation in boxes 3 and 5 due to the tidal flow's changing direction.

There are rapid changes in generation in box 5. These appear to be due to the horizontal velocity field oscillating at the south bounding wall, causing the advection term at the south bounding wall to rapidly oscillate. In turn, the generation rate term in box 5 has the same oscillating behavior since it is determined diagnostically from the other terms in Equation 4.17. The oscillations appear much more dramatic in the generation rate plot than the advection plot due to the different span of the axis limits. These oscillations are probably not meaningful but are rather a function of the calculation. Also note that they are much less noticeable in Figure 4.26, which is calculated for the larger analysis domain.

Advection of vorticity into and out of the analysis domain boundaries is shown in the bottom subplot of Figure 4.27. This term first shows a small amount of persistent negative vorticity from the previous ebb tide exiting the analysis domain out the south bounding

wall. The first reach of vorticity to the east is evident in this plot when there is a small peak showing positive vorticity exiting the system via the east bounding wall (Figure 4.25(a)). Most of the advection in the system is of positive, newly generated vorticity exiting the analysis domain out the south boundary (Figure 4.25(b)), though there is some positive vorticity generated outside the analysis domain that enters via the north and west bounding walls.

**Tilting and Stretching** The main increase in tilting of vorticity and stretching of vertical vorticity corresponds to the presence of a downwelling convergence zone in the system where flood pushes past Admiralty Head while a large eddy in Admiralty Bay begins to push into the main flood flow. In the convergence area, vertical vorticity and negative vertical velocities, which increase with depth to mid-water column, are collocated. The two fields mostly stay in the same location while the flood tide pushes on and prevents the ebb tide from coming out from Admiralty Bay, but the ebb tide slows pushes west. Meanwhile, the tilting term is converting vertical vorticity into horizontal due to horizontal gradients of vertical velocity while the stretching term is strengthening the vertical vorticity. This can be seen directly in the governing equation for vertical vorticity, Equation 4.13. Figure 4.28(a) shows vorticity and Figure 4.28(b) shows vertical velocity in depth to demonstrate the collocation of vertical vorticity and vertical velocity.

Transects in depth at the time and location indicated in Figure 4.25 are shown in Figure 4.29 to more specifically show the mechanisms. The magnitude of the horizontal velocity, shown in the first plot, has spatially varying vertical and horizontal gradients on flood tide. This can be more readily seen in Figure 4.30. The surface flow pushes past a sharp headland tip and has a strong gradient associated with the separation point. Lower in the water column, the headland is less steep and the gradient near the separation point is less strong.

The shear feature in the speed dominates the behavior in each other field shown in Figure 4.29. The downwelling vertical velocity is located mid-water column, below the area of strongest convergence near the surface. The (positive) vertical and negative horizontal vorticity are perpendicular components of a relatively cohesive region of three-dimensional

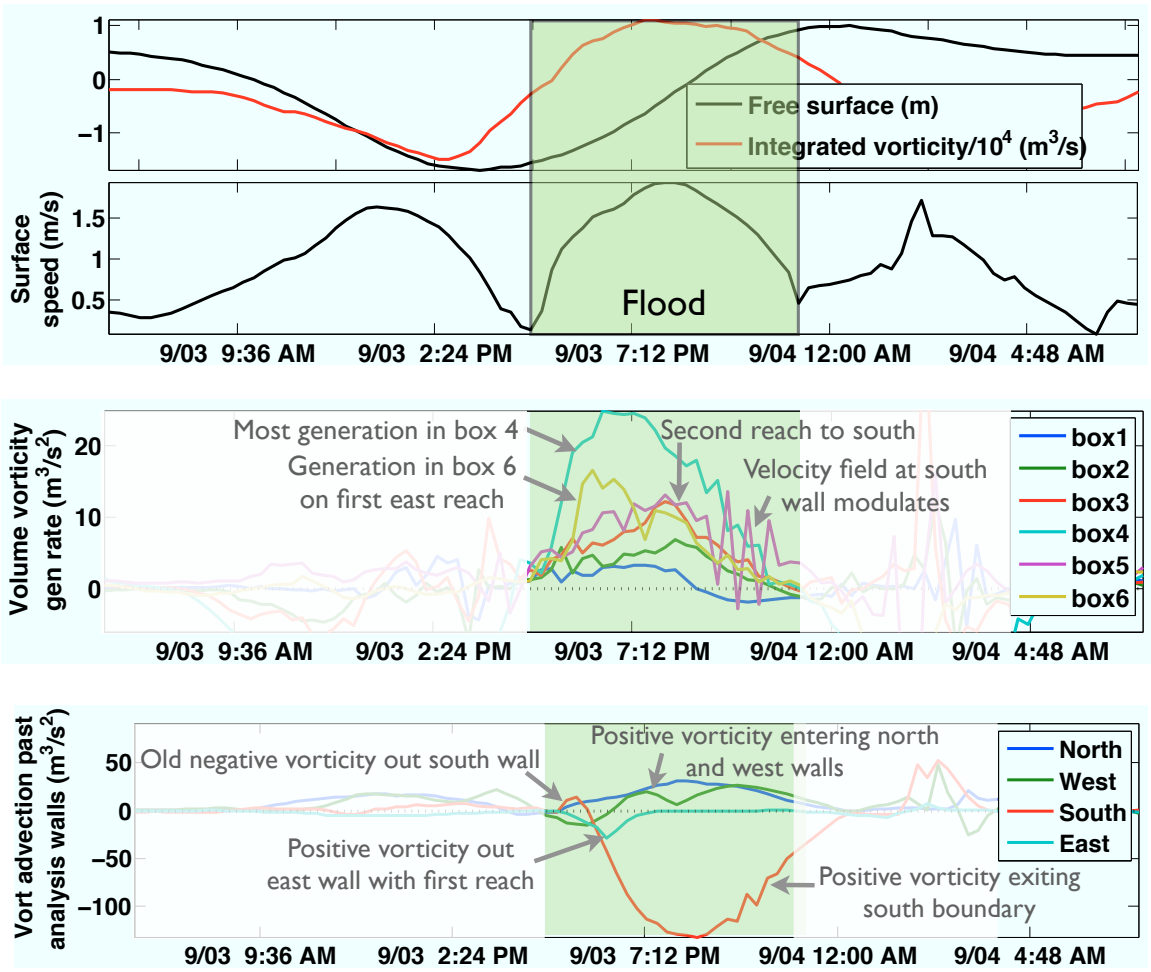


Figure 4.27: Case I free surface, integrated vorticity, surface speed, volumetric boundary generation rate by box, and advection by bounding wall.

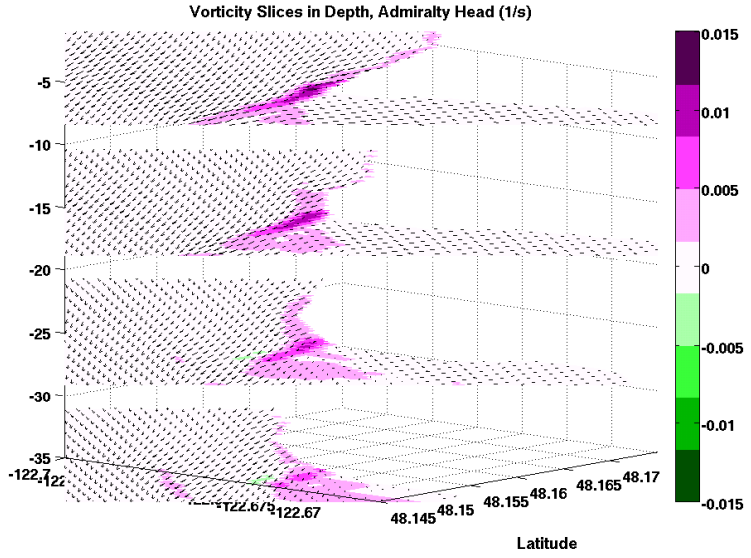


(a) Vorticity

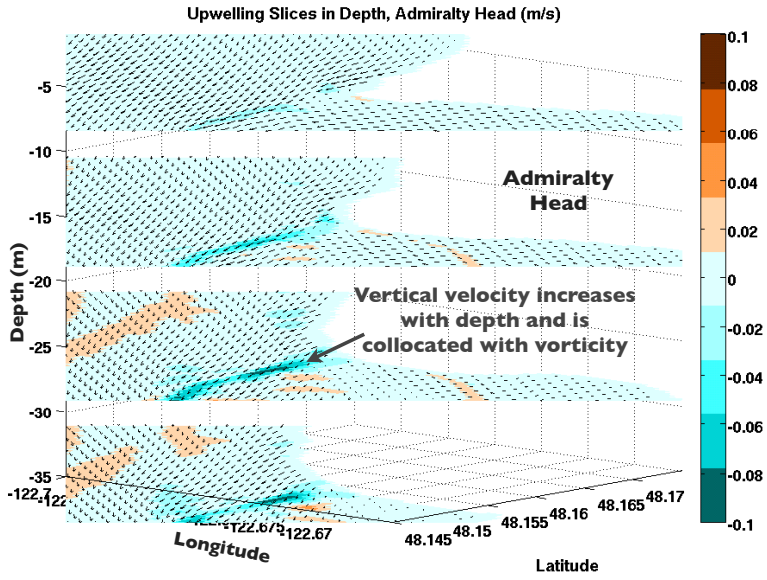


(b) Upwelling velocity

Figure 4.28: Vorticity and upwelling velocity snapshots in depth at 9:15PM on 9/4/06, illustrating the increase of vorticity with increasing negative upwelling velocity. Note the lower vorticity color bar limits in these figures, for visual illumination.

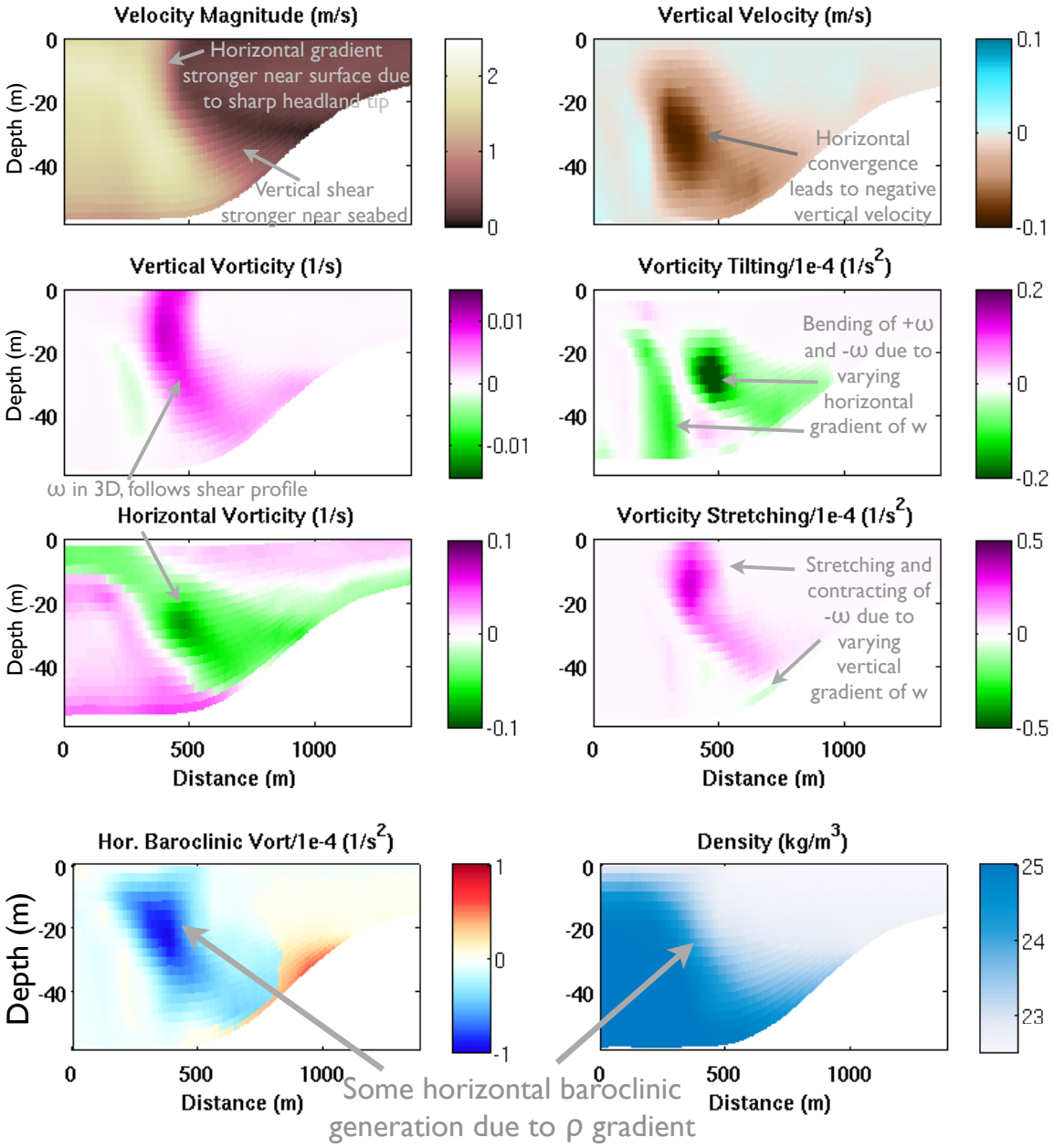


Figure 4.29: Case I transects at the location shown in Figure 4.25 at 9:30PM on 9/3/06. Shown in order from left to right, top to bottom, are the horizontal speed; vertical velocity; vertical vorticity; vertical vorticity tilting; the horizontal vorticity, where $\omega_+^h = \sqrt{\left(\omega_+^x\right)^2 + \left(\omega_+^y\right)^2}$ and $\omega_-^h = \sqrt{\left(\omega_-^x\right)^2 + \left(\omega_-^y\right)^2}$; vertical vorticity stretching; horizontal baroclinic generation rate (with positive and negative calculated analogously to the horizontal vorticity); and the density.

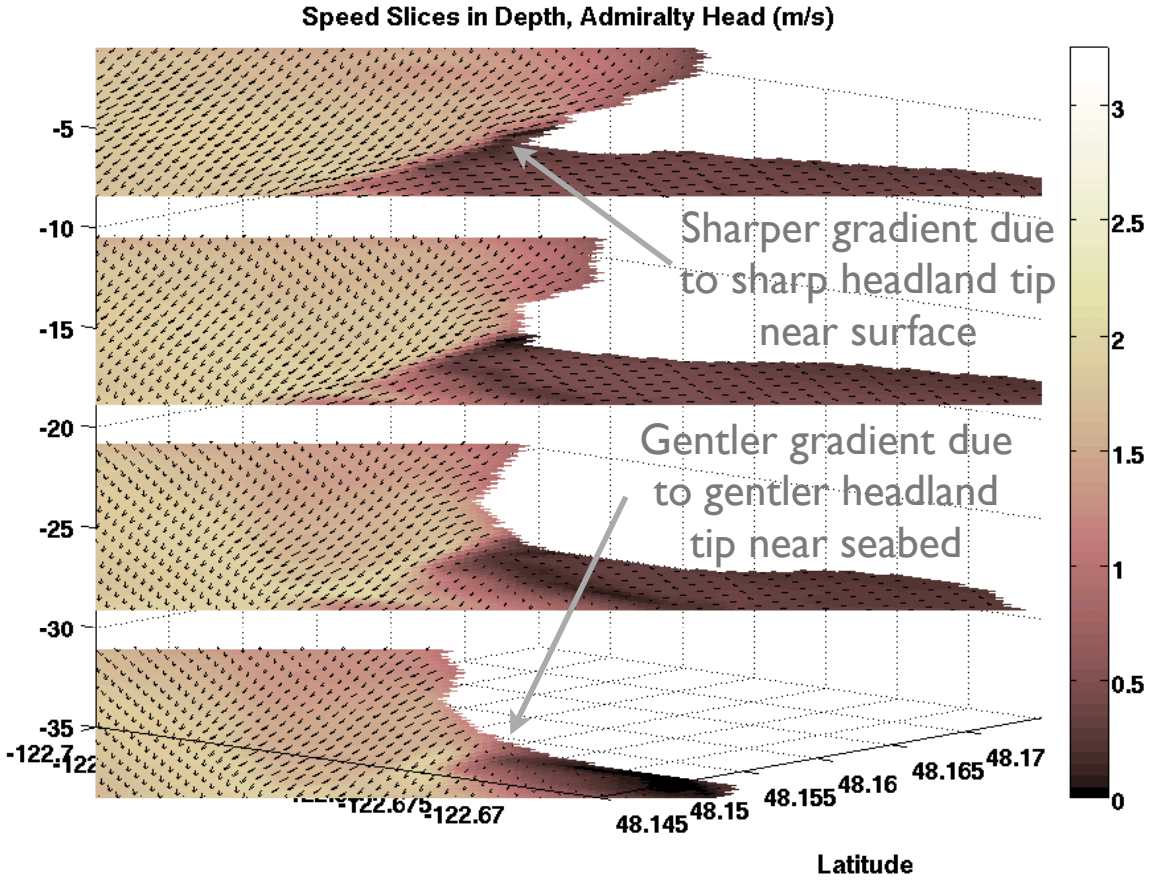


Figure 4.30: Constant depth slices of speed at 9:30PM on 9/3/06 in Case I, looking northwest past Admiralty Head. The horizontal and vertical gradients in the speed vary lee of the headland due to changing sharpness of the headland with depth.

vorticity. The positive horizontal vorticity in the main flow channel (left side) is probably due mainly to the typical shear in the tidal flow over the seabed. The negative horizontal vorticity in the recirculation area (right side) is probably generated by the recirculation flow over topography.

The stretching of the vertical vorticity near the surface, increasing the vertical vorticity, is due to the collocation of the vertical vorticity and a positive vertical gradient of vertical velocity near the surface. There is a hint of contracting of the vertical vorticity decreasing the vertical vorticity near the seabed at the low end of the vorticity trail, due to a negative vertical gradient of vertical vorticity. The negative tilting of vorticity in the main channel flow (left side of plot) is due to the positive horizontal vorticity being tilted into negative vertical vorticity by the negative horizontal gradient of vertical velocity. The negative tilting of vorticity in the recirculation area (right side of plot) is due to the negative horizontal vorticity being tilted into negative vertical vorticity by the positive horizontal gradient of vertical velocity on the right side of the vertical velocity region.

There is a strong horizontal density front that is approximately coincident with the other features. This generates negative horizontal vorticity, as shown in the seventh plot, which shows the horizontal baroclinic generation rate. This vorticity generation appears to be a secondary effect relative to the other mechanisms due to the main tidal flow and convergent downwelling.

Volume-integrated tilting and stretching of vorticity in the subdomain boxes for Case I are shown in Figure 4.31. The tilting and stretching are usually observed to follow the typical behavior described in the previously paragraph; that is, stretching of the vertical vorticity near the surface that is collocated with a positive vertical gradient of convergent downwelling, and tilting decreasing the magnitude of the vertical vorticity due to the horizontal gradient of convergent downwelling that is aligned with oppositely-signed horizontal vorticity. There is some different behavior initially in the flood tide, in which newly-generated positive vorticity contracts in box 6 in the shallower Admiralty Bay with the first reach of vorticity east, because it is collocated with positive vertical velocity that increases with depth such that $\partial w/\partial z < 0$ (not shown), decreasing positive vorticity. Simultaneously, the vorticity moving into box 6 tilts upward given the horizontal vertical velocity gradient, con-

verting horizontal vorticity into vertical vorticity. As the vorticity moves south, it follows typical behavior. It stretches and increases in the presence of the positive vertical velocity gradient near the surface in boxes 5, 4, 3, 2, and 1, in that order, while it decreases due to tilting at the same time as it is pushed west down the slope south of the headland.

*Case II: Double Peak due to Previous Tide and Persistent Eddies*

The semi-diurnal flood tide examined in this case produces a large vortex from the headland. Overall analysis details are shown in Figure 4.32. The relative sizes of the terms are different and generally smaller than in Case I. In the previous case, stretching was the largest term and advection was just smaller (though oppositely-signed), and boundary generation and tilting were about the same magnitude and oppositely-signed. In this case, boundary generation and advection are the most comparable and oppositely-signed, stretching is a smaller affect overall than in the previous case, and tilting is insignificant. As before, the numerical and Reynolds stress flux terms are insignificant but do slightly reduce the positive vorticity.

A few of the terms show a double peak pattern. The stretching and tilting terms both have two peaks, and the advection shows a complex pattern. This will be explored further in the following paragraphs.

A notable feature in this case is the double peak in speed accompanied by a dip in total vorticity present in the domain. This double speed peak was explained by examining plots of vorticity in Section 4.2.3 to be the result of persistent vortices associated with speed pockets. The size of these double peaks is related to the size of the previous negative ebb vortex. In Case I, the amount of negative vorticity generated during the previous ebb tide was small, leading to a small, barely noticeable surge of water pushed around the headland at the start of the next flood tide (see the right-hand column of Figure 4.9). In this case, Case II, the amount of negative vorticity from the previous ebb is larger, leading to a large initial peak in speed followed by a secondary peak in speed, each of which is associated with advection of vorticity in the system (see the left-hand column of Figure 4.9). The effect of the persistent vortices can be understood by examining the terms from Equation 4.17.

The advection terms for each bounding wall for this case are shown in Figure 4.33, along

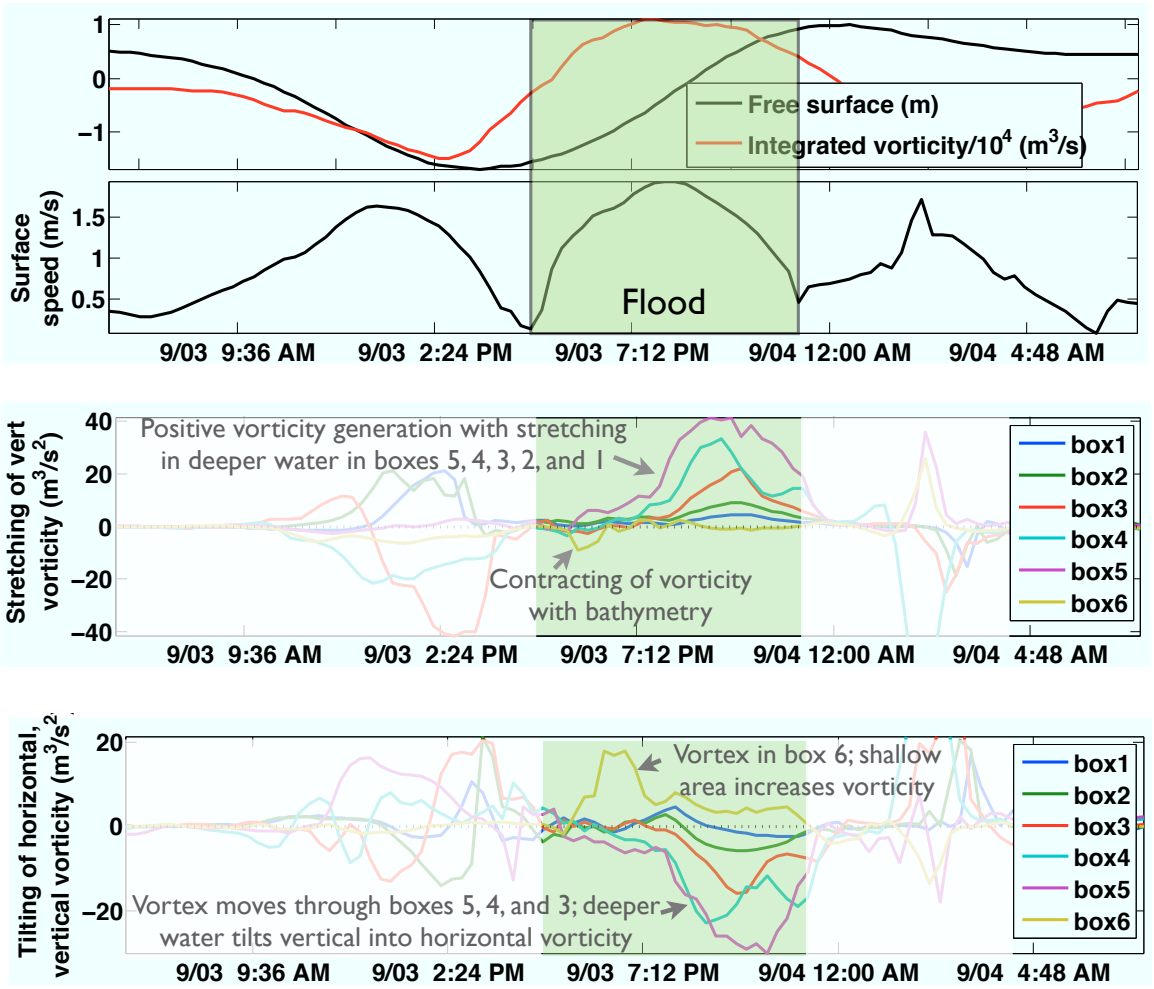


Figure 4.31: Case I free surface, integrated vorticity, surface speed, and tilting and stretching by box.

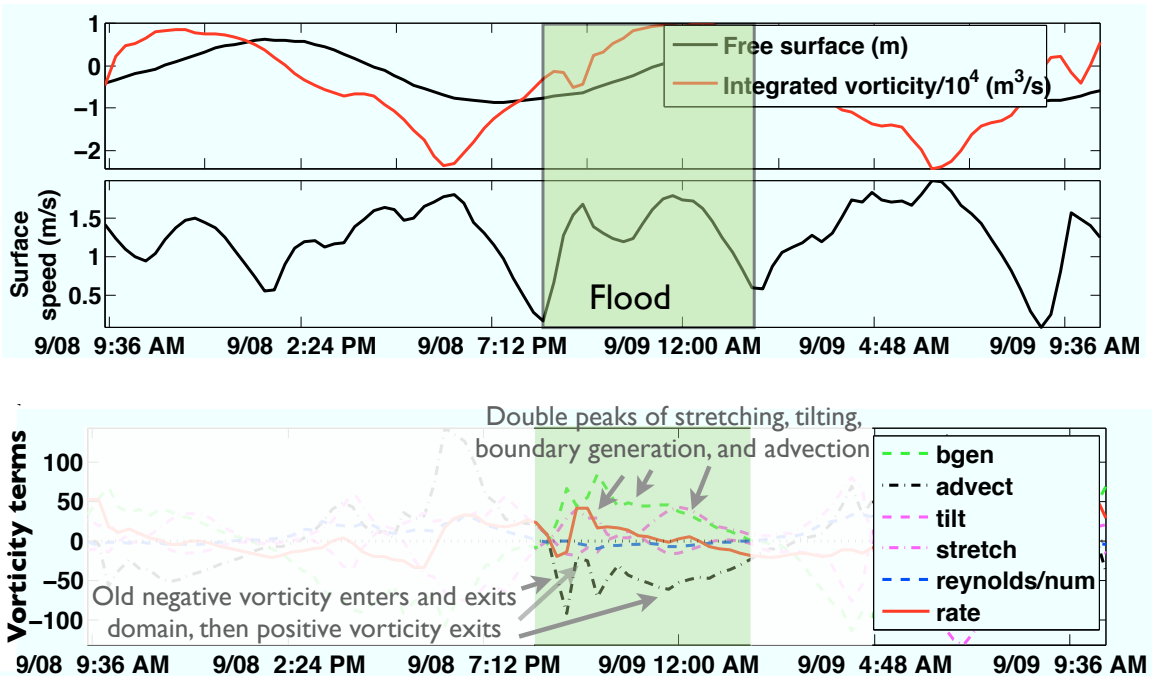


Figure 4.32: Case II free surface, integrated vorticity, surface speed, and vorticity governing equation terms

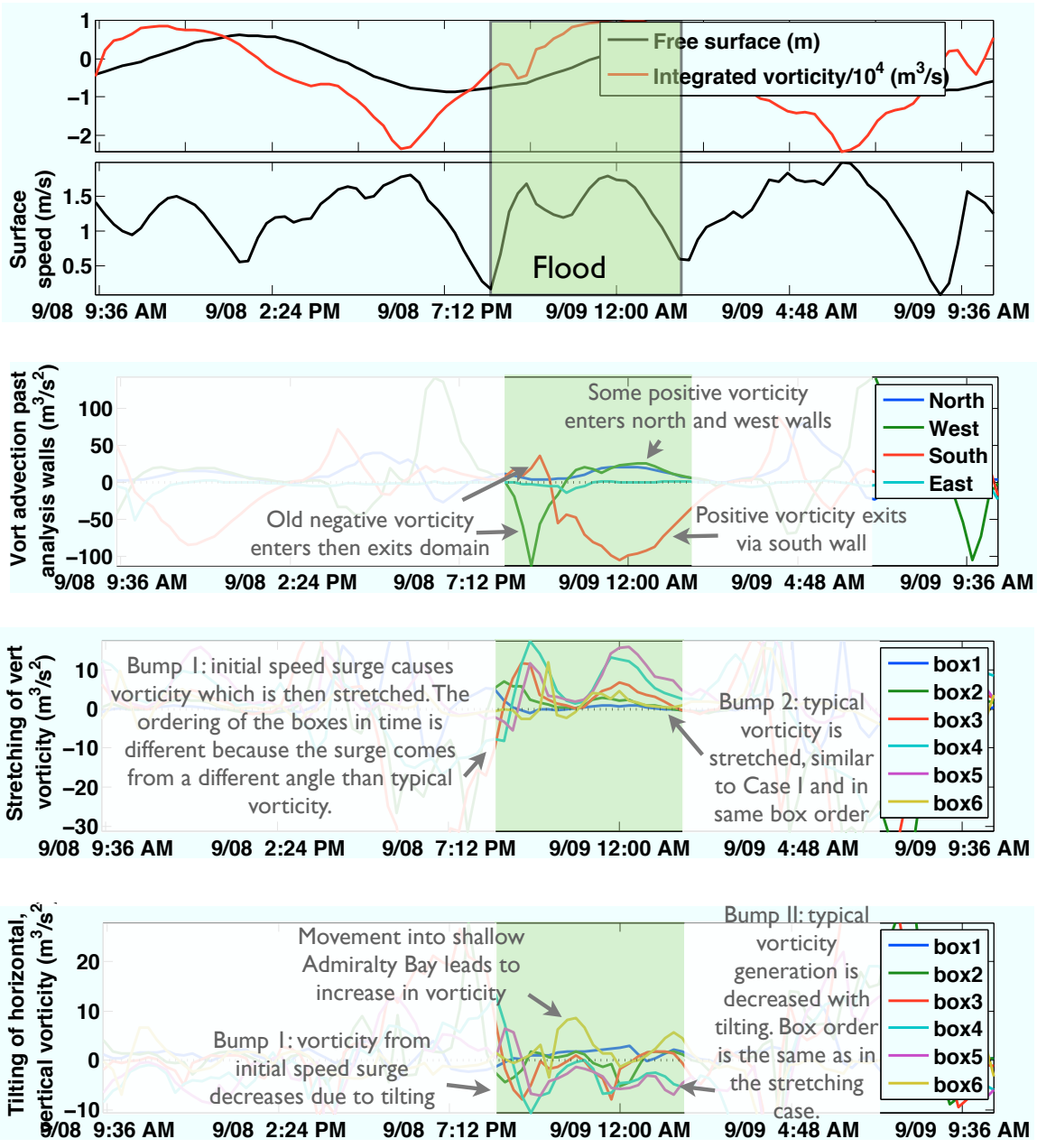


Figure 4.33: Case II free surface, integrated vorticity, surface speed, advection by bounding wall, and stretching and tilting by box.

with stretching and tilting by box, since each of these terms shows the effect of the persistent vortices. In the subplot of advection terms, the first two peaks in time are due to residual vorticity from the previous tide. The negative vortex from the previous ebb tide, shown in Figure 4.9(a), persists into this tide. It continues advecting with the beginning flood tide through the analysis domain via the west and south bounding walls, bringing with it a surge of speed and negative vorticity (Figure 4.9(c)). The large advection peak shows that as the typical flood tide begins, the positive vortex streaming from the headland exits the analysis domain via the south bounding wall, as expected. There is also some positive vorticity that is generated outside the analysis domain that is advected into the system through the north and west bounding walls, but it is small relative to the amount of positive vorticity advected out the south bounding wall.

The peaks in vorticity and speed are noticeable in the subplots of the stretching and tilting terms, as well, as shown in Figure 4.33. These terms are much smaller in this case as compared with Case I. In these plots, two "bumps" are referenced: the first is due to the initial burst of new positive vorticity that is associated with the speed surge from the previous strong ebb vortex, and the second is due to the main flow of the flood tide. While the advection terms show the presence of the persistent old negative vorticity, the stretching and tilting are most affected by the surge of new positive vorticity that is generated due to the initial surge of speed past the headland tip. This new positive vorticity is collocated with spatial gradients of negative vertical velocity near the headland such that stretching and tilting is possible, unlike the old negative vorticity which passes through the corner of the analysis domain, opposite the headland tip. This is shown in Figure 4.34. Therefore, the effect of the previous tide on this half-cycle in terms of tilting and stretching is to generate an initial, additional surge of positive vorticity in the presence of vertical velocity gradients before the typical tilting and stretching of the positive vorticity generated with the main tidal flow. Because both of vortices that are stretched and tilted are the same sign, the sign of the bumps in the stretching and tilting terms have the same sign.

The dynamics of the tilting and stretching in this second flood case are similar to those described in Section 4.4.2. The stretching term in the various boxes for the second bump shows the same ordering of boxes around the headland contributing to the stretching term

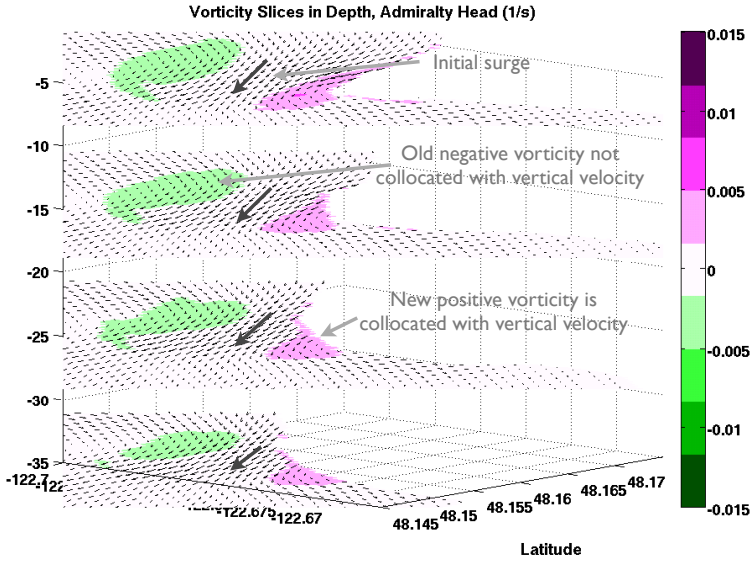


(a) Vorticity

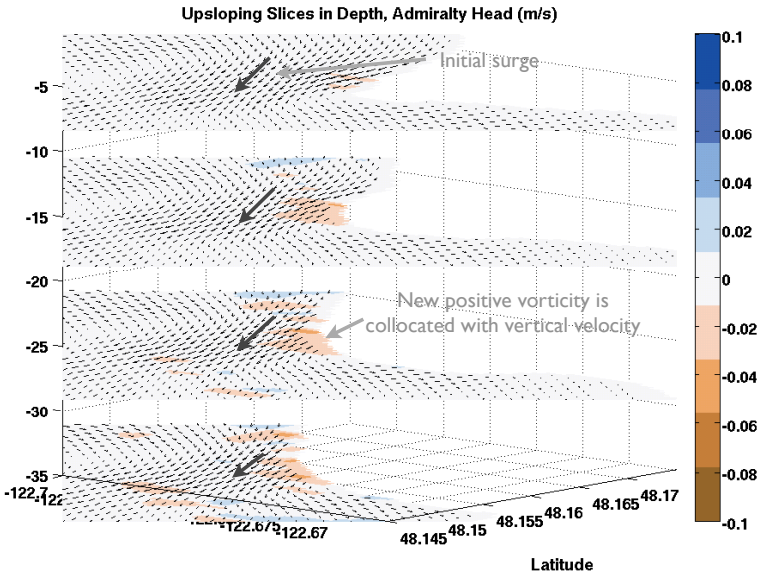


(b) Vertical velocity

Figure 4.34: Vorticity and upwelling velocity snapshots in depth at 9:15PM on 9/9/06, illustrating that initial new positive vertical vorticity due to an initial speed surge is collocated with a vertical velocity gradient in depth, but the old negative vorticity is not. Note the lower vorticity color bar limits in these figures, for visual illumination.

as was seen in the stretching term in Case I. The stretching for the second bump starts first in boxes 4 and 5 before moving more southward, showing the same vortex movement as in Case I. The first bump has the opposite timing of boxes contributing to the stretching term. The reason for this difference in timing of the location of stretching in the boxes is that the vorticity is initially generated at a different location around the headland in each case, then moves at a different angle near the headland. As shown in Figure 4.2(b), the initial positive vorticity in generated north of the headland tip, whereas vorticity generated by the main tidal flow is located near the headland tip.

The effect of the two phases of vorticity mechanisms is less distinguishable in the tilting subplot than in the stretching subplot, but it is still there. There are two negative peaks in roughly the same order as described for the stretching term. There is also an isolated positive peak in the tilting term for box 6 that is possiblys due to movement of the vorticity into shallow Admiralty Bay, as was seen in Case I.

As a final note, the noticeable dip in volume-integrated vorticity in the analysis domain is due to the advection through the system of the previous oppositely-signed vortex temporarily canceling out some of the positive vorticity in the volume integration.

*Case III: Basic Ebb Tide*

This diurnal ebb tide produces a negative vortex of moderate size. Terms from the volume-integrated governing equation for vorticity are shown in Figure 4.35. At the beginning of the tide, boundary generation begins, along with advection out of negative vorticity. Around peak ebb, stretching and tilting become major contributors, with negative vorticity generation through stretching and a decrease in negative vertical vorticity due to tilting. There is some decrease in negative vorticity due to the Reynolds stresses and numerical terms, but they are, again, not significant to the dynamics. Note that the signs of the terms in the ebb tides are expected to be opposite those in flood tides since the sign of the newly generated vorticity is opposite in each case.

**Generation and Advection** The rate of boundary generation in each sub-domain, along with details of advection of vorticity in and out of the analysis domain, are shown in Figure

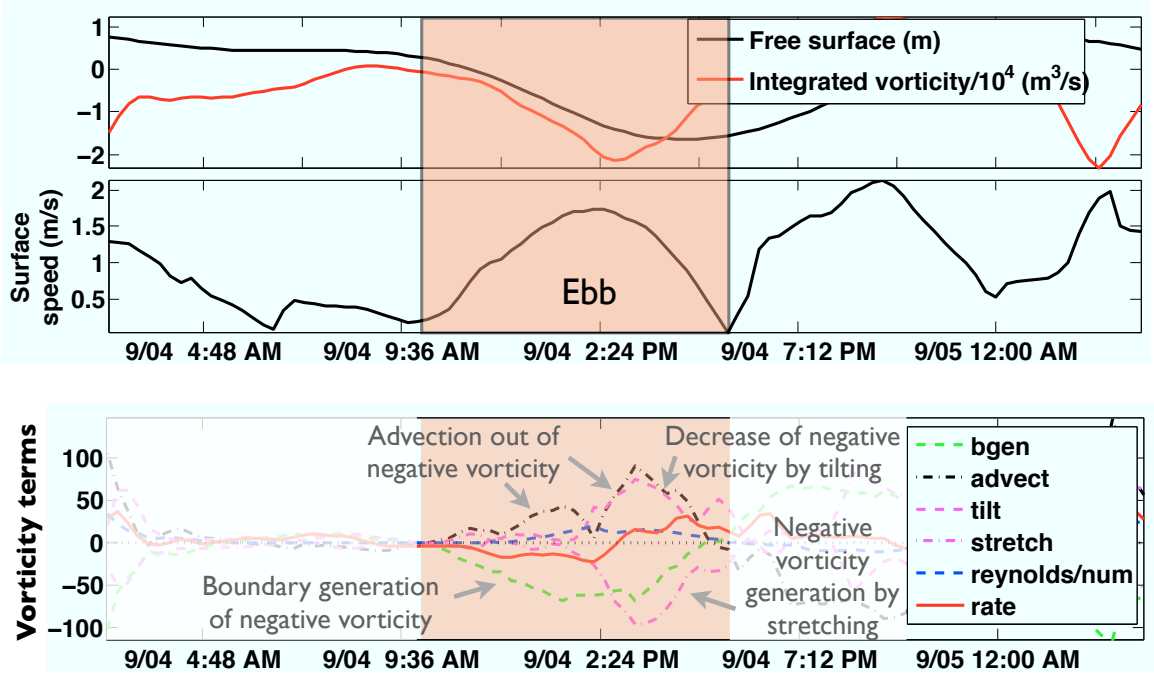


Figure 4.35: Case III free surface, integrated vorticity, surface speed, and vorticity governing equation terms

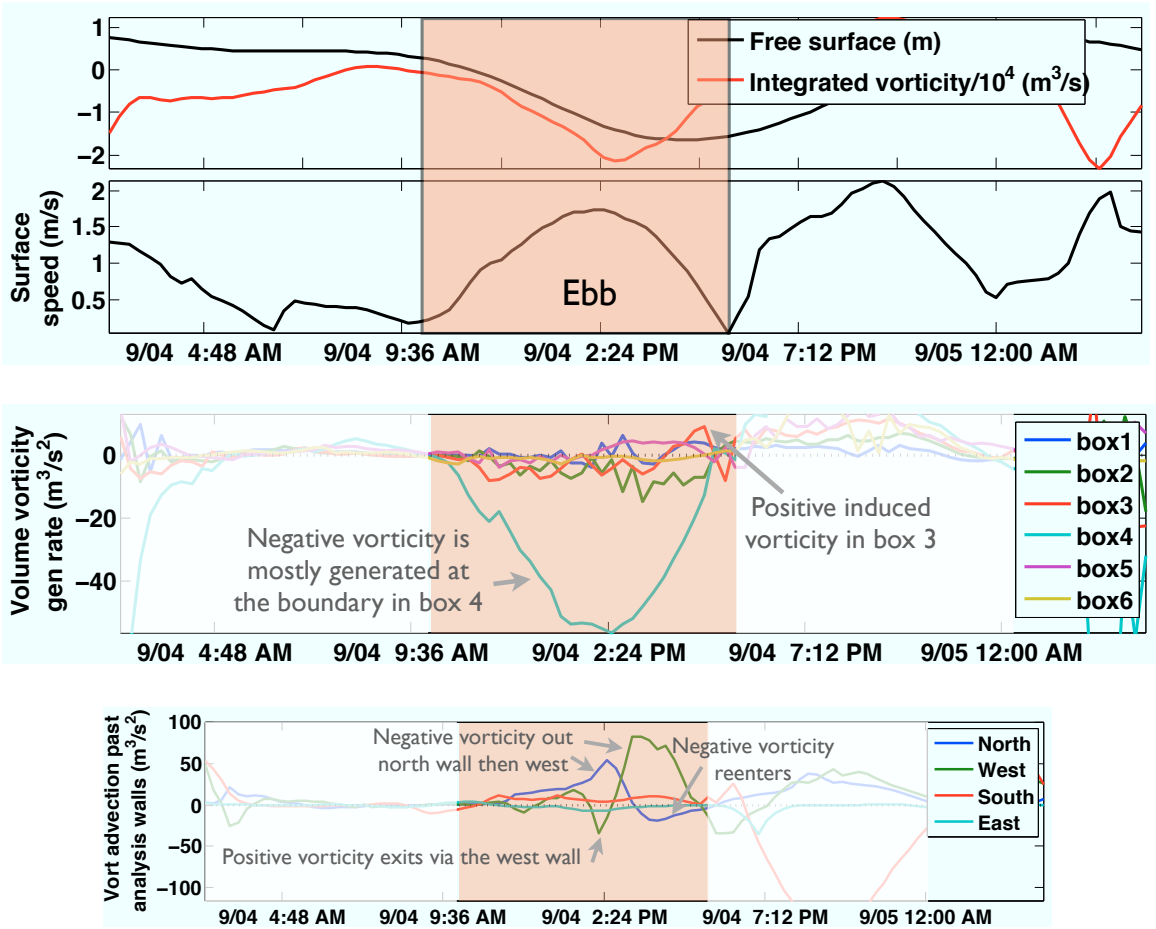


Figure 4.36: Case III free surface, integrated vorticity, surface speed, volumetric generation rate by box, advection by bounding wall of large analysis domain (bottom subplot)

4.36. Boundary generation is clearly accomplished primarily in box 4 during this half-cycle, unlike in the flood cases. This difference in where boundary generation takes place on ebb and flood is probably due to the asymmetry of the headland and surrounding channel geometry. The flow past Admiralty Head on a typical ebb tide mostly pushes past just the tip of the headland, whereas on flood tide the flow often pushes alongside the headland before the tip. See Figures 4.37(a) and 4.37(b) for examples. There is also some positive vorticity generated at the seabed near the coastline that is apparent in box 3, as seen in Figure 4.38(b).

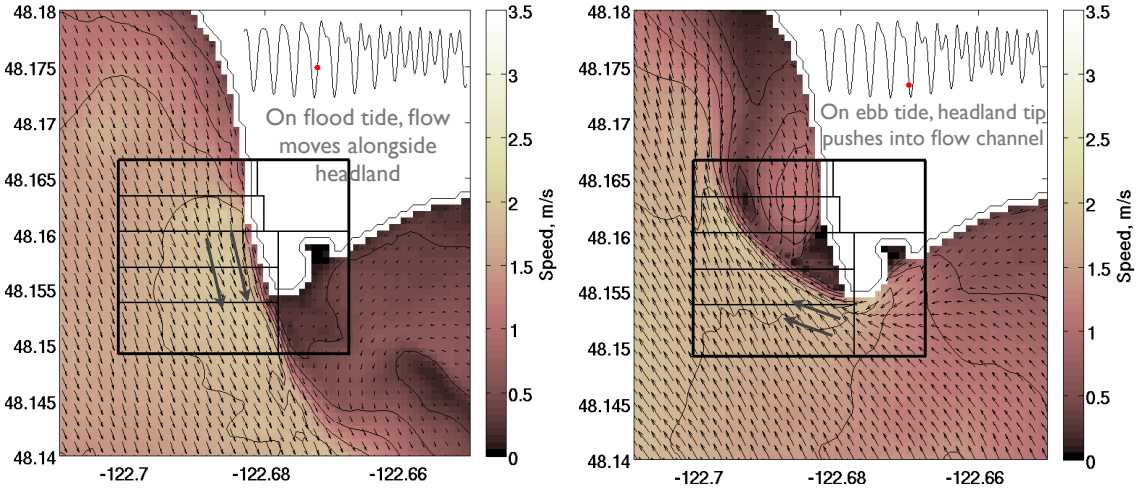


(a) Flood tide, 9/3/06 7:30PM

(b) Ebb tide, 9/5/06 2:15PM

Figure 4.37: Typical surface speed flow past the headland on flood and ebb tide show the asymmetry of the headland and channel geometry, which lead to vorticity being generated at the boundary in different locations on each tide.

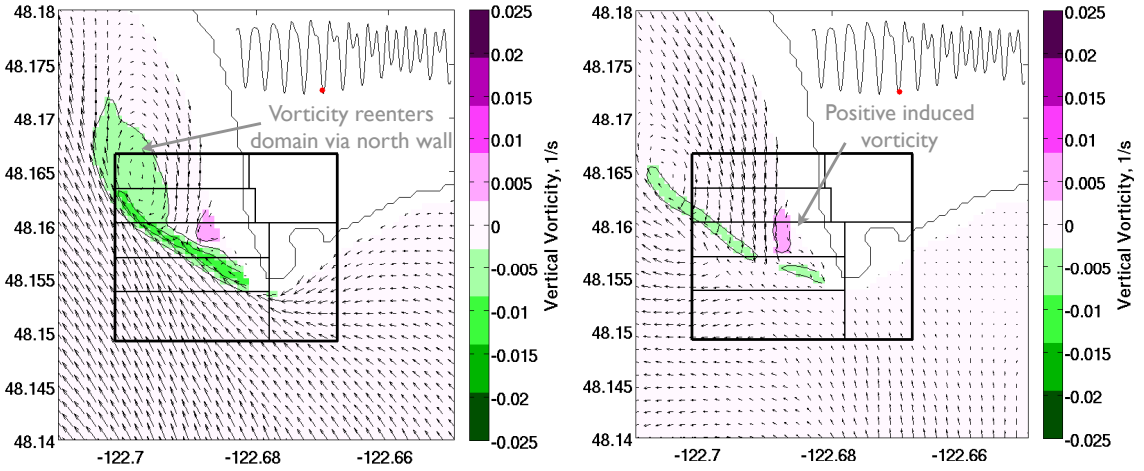


(a) 3:15PM

(b) 5:15PM

Figure 4.38: Sample 10 meter depth vorticity snapshots on 9/5/06 for Case III.

The advection into and out of the domain in Figure 4.36(c) shows the primary movement of newly generated negative vorticity moving out of the analysis domain, first through the north bounding wall with the first reach, then through the west bounding wall. As the vortex shifts counter-clockwise, directing the negative vorticity mainly westward, some of the vortex overlaps with the north analysis open boundary, such that the negative vorticity temporarily reenters the domain before exiting again out the west bounding wall, as shown in Figure 4.38(a).

Before these movements of vorticity through the open bounding walls, there is some positive vorticity that exits the west bounding wall. This positive vorticity is not obviously apparent in any of the other plots. The source of this positive vorticity exiting the domain is not clear.

**Tilting and Stretching** Similar tilting and stretching behavior is seen on ebb tide as was seen on flood tide in Section 4.4.2. Snapshots of surface vertical vorticity and ten meter depth vertical velocity are shown in Figure 4.39 for context, and to indicate the time and position of transects shown in Figure 4.40. The mean speed in the transect is shown in the first subplot of Figure 4.40. It is clear from this plot and the rest that there is different behavior between the west (left) and east (right) sides of the horizontal speed gradient. As in Case I, downwelling is found at the convergence of the main tidal flow and the recirculation area of the ebb eddy (more easily seen in Figures 4.39(a) and 4.39(b)). The horizontal and vertical vorticity can be aligned between the two subplots: negative positive vertical vorticity with negative horizontal vorticity, and positive vertical vorticity with positive horizontal vorticity. Negative horizontal vorticity is generated on the west side of the transect due to the main tidal flow over the seabed whereas the positive horizontal vorticity on the east side of the transect is generated by the recirculation flow that moves opposite the main flow, in the eddy.

The main negative vorticity is stretched, strengthening it, near the sea surface, and contracted near the seabed, weakening it. Each are due to the collocation of the vertical vorticity with gradients in the vertical velocity. The positive vertical gradient of vertical velocity near the surface leads to stretching while the negative vertical gradient of vertical

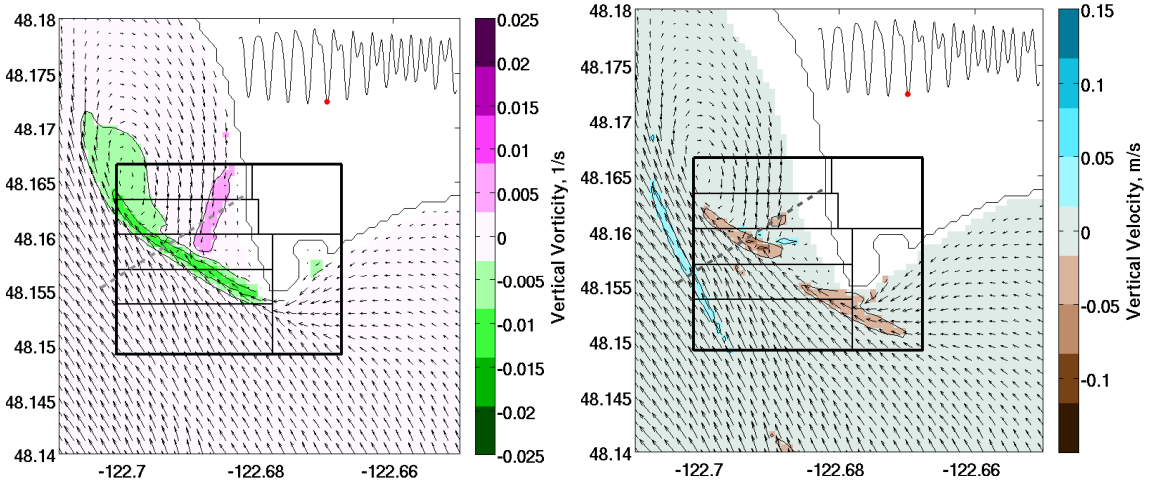


(a) Vorticity (b) Vertical velocity

Figure 4.39: Surface vorticity and vertical velocity at 10 meters below the mean sea level near peak ebb at 3:45PM on 9/4/06. Transect location discussed in Figure 4.40 is indicated.

velocity near the seabed causes contracting.

As was seen in Case I, the vertical vorticity tilting term is the same sign on both sides of the main vorticity region. The negative horizontal vorticity on the west side is tilted by a negative horizontal gradient of vertical velocity such that it is converted into positive vertical vorticity, reducing the magnitude of the negative vertical vorticity. On the east side, the positive horizontal vorticity is tilted by the positive horizontal gradient of vertical velocity, leading to the conversion of the positive horizontal vorticity into positive vertical vorticity, again reducing the magnitude of the main region of negative vertical vorticity.

There is some horizontal baroclinic generation present due to a horizontal gradient of density, as shown in the bottom subplots of Figure 4.40. However, it is not clear how large effect this is relative to the other dynamics. Additionally, any generation that is occurring baroclinically is to the side of the main vorticity dynamics.

The volume-integrated tilting and stretching terms are shown in Figure 4.41. As described in the previous paragraphs, the stretching near the headland is dominantly negative, increasing the negative vertical vorticity, and the tilting is dominantly positive, decreasing

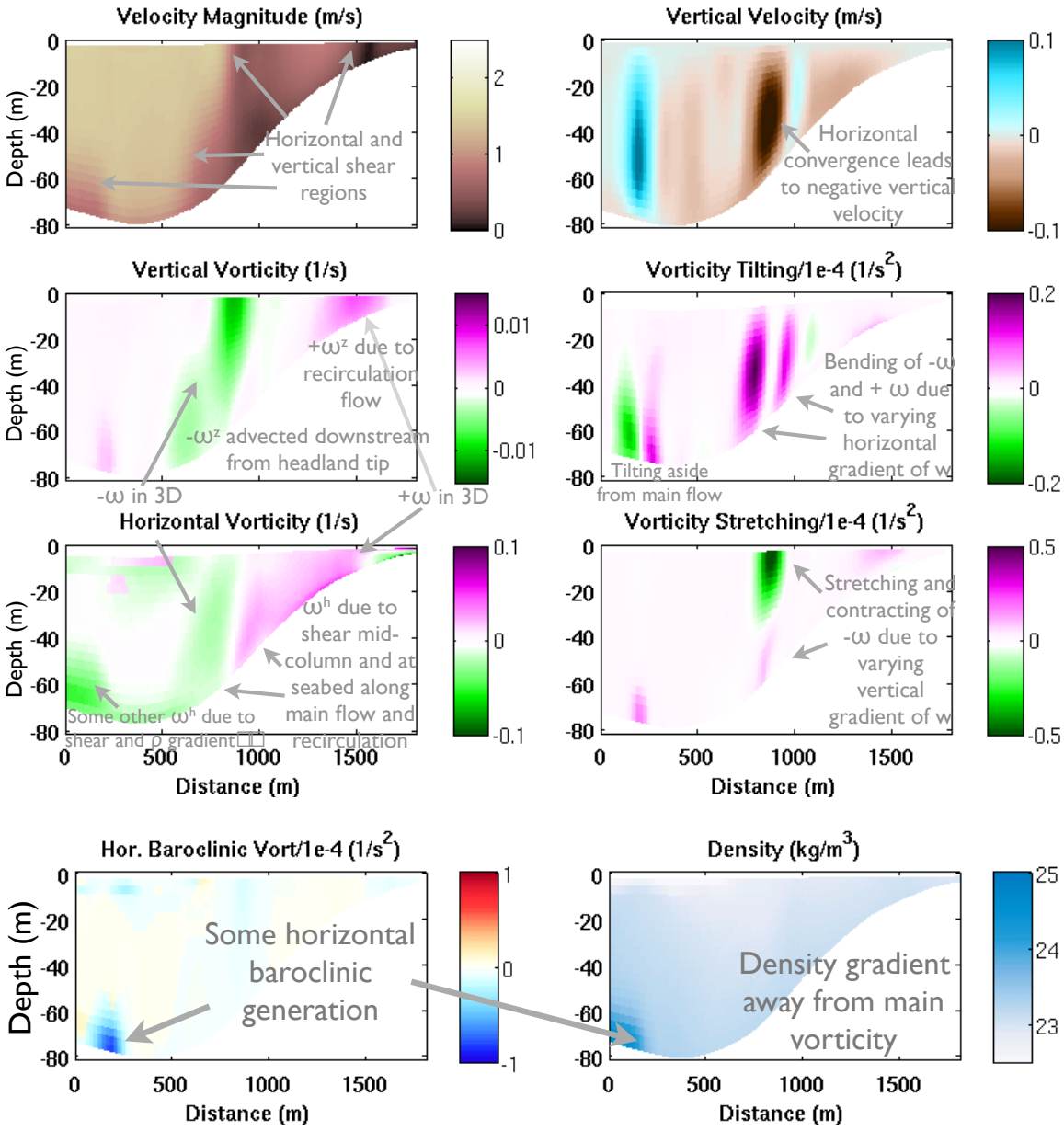


Figure 4.40: Case III transects at the location shown in Figure 4.39 at 3:45PM on 9/4/06. More details on plot can be found in Figure 4.29.

the main negative vertical vorticity. One of the exceptions in the plot is the contracting of the negative vorticity in box 1. This is due to a negative vertical gradient of the vertical velocity, as shown in Figure 4.42.

*Case IV: Double Peak due to Previous Tide and Persistent Eddies*

This semi-diurnal ebb tide, whose terms in the vorticity governing equation are shown in Figure 4.43, produces a huge headland-generated eddy, shown previously in Figure 4.7(d). The terms each clearly have two peaks, which, as will be shown in the following sections, are due to persistent vortices from the previous flood tide. Boundary generation is large in two distinct peaks throughout the cycle, as is the advection term. The tilting and stretching terms are both characterized by two peaks, but change sign partway through the half-cycle. Each of these four terms is of considerable size. An initial speed surge associated with a persistent vortex was noted in Case II and was particularly noticeable in the speed curve. It also had small but noteworthy same-signed double peaks in the terms in the equation for $\omega_a^z$. In this case, the speed curve shows only small bumps, hinting at the complex interactions occurring, but the analysis terms show that they are dramatically affected. Details of these effects are given in the following section.

Advection of vorticity in and out of the analysis domain bounding walls, along with tilting and stretching of vorticity, integrated throughout the analysis sub-domains, are shown in Figure 4.44 for Case IV. This more detailed examination of the advection of vorticity, made by distinguishing between advection through each bounding wall, allows for greater understanding of the processes. Looking at the previous tide helps to understand what is happening on the south bounding wall. The previous flood tide pushed a jet of water down Admiralty Inlet that was squeezed between Admiralty Head on the east, and Port Townsend and northeastern Marrowstone Island on the west. This jet induced a vortex on either side, each with opposite sign, as shown in Figure 4.45(a). As the tide switches direction, these eddies are advected northward and propagate back through the Inlet. In doing so, they pass through the south bounding wall of the analysis domain: first the more northward positive vortex and then the more southward negative vortex. The first appears in Figure

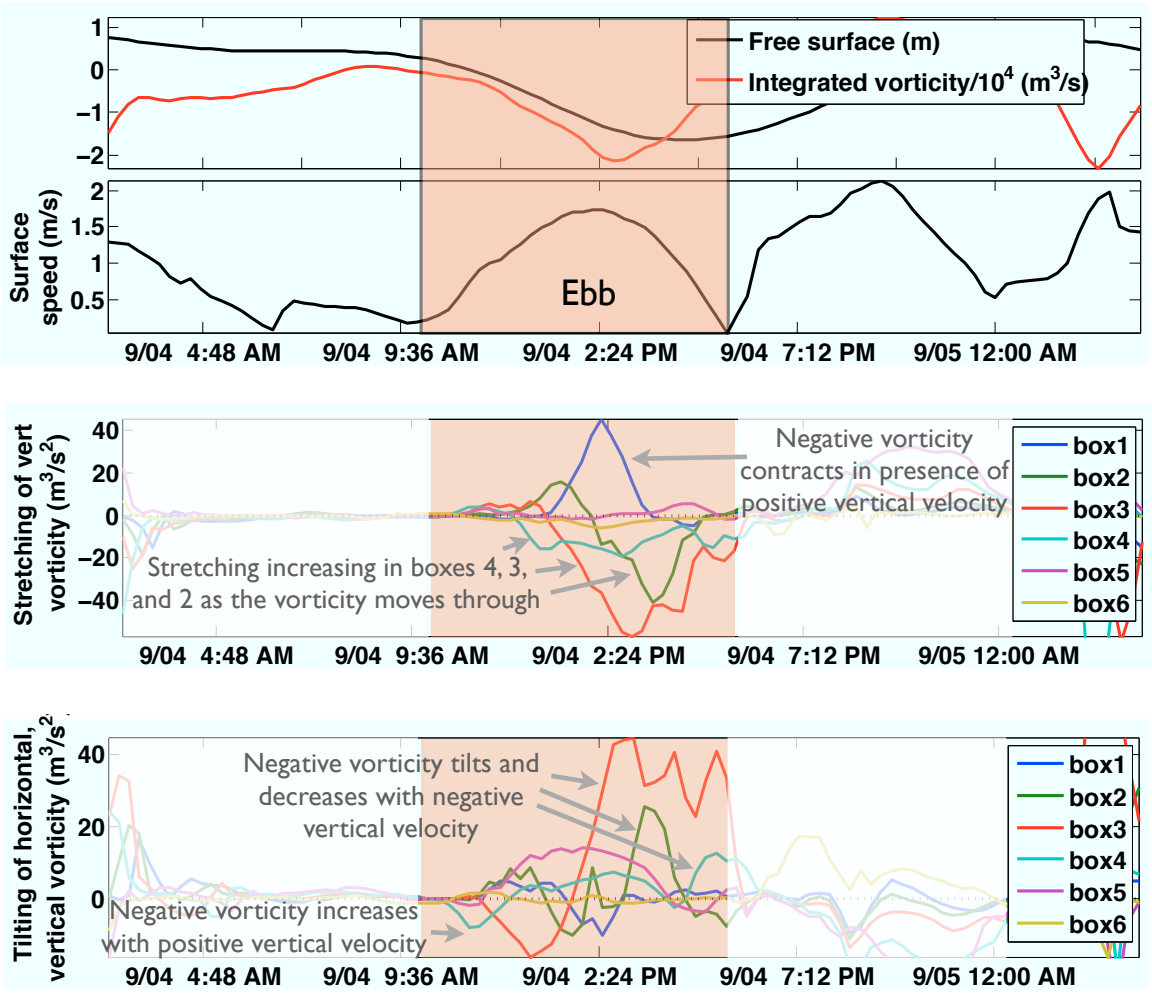


Figure 4.41: Case III free surface, integrated vorticity, surface speed, and tilting and stretching by box.

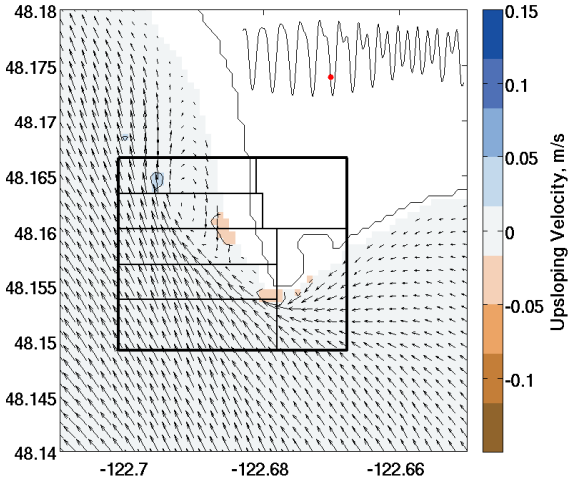


(a) 10 meter depth upsloping velocity

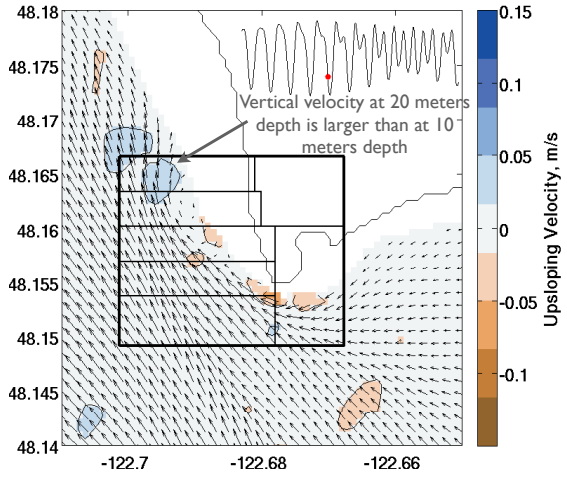


(b) 20 meter depth upsloping velocity

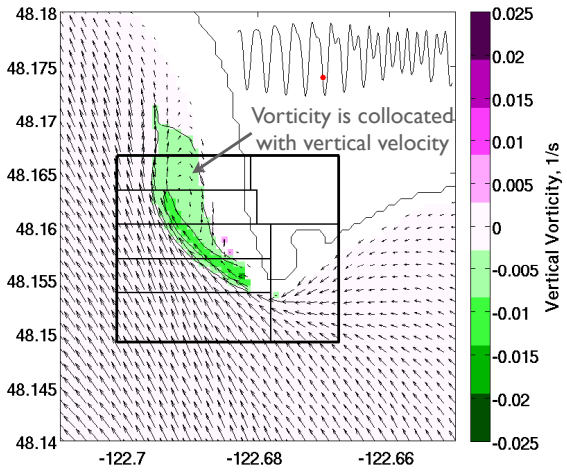


(c) 10 meter depth vorticity

Figure 4.42: Contracting of negative upsloping vorticity from Case III is seen in box 1, the most northward box, due to increasing positive vertical velocity with depth. Upsloping velocity and vorticity snapshots are shown from September 5 at 1:45PM

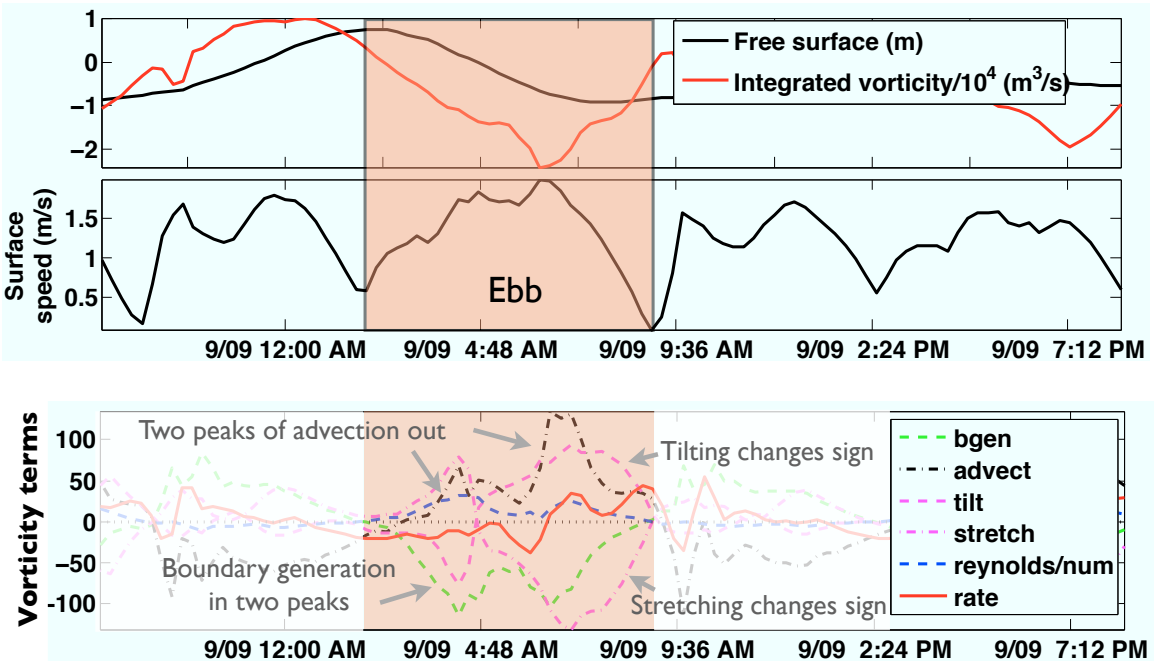


Figure 4.43: Case IV free surface, integrated vorticity, surface speed, and vorticity governing equation terms

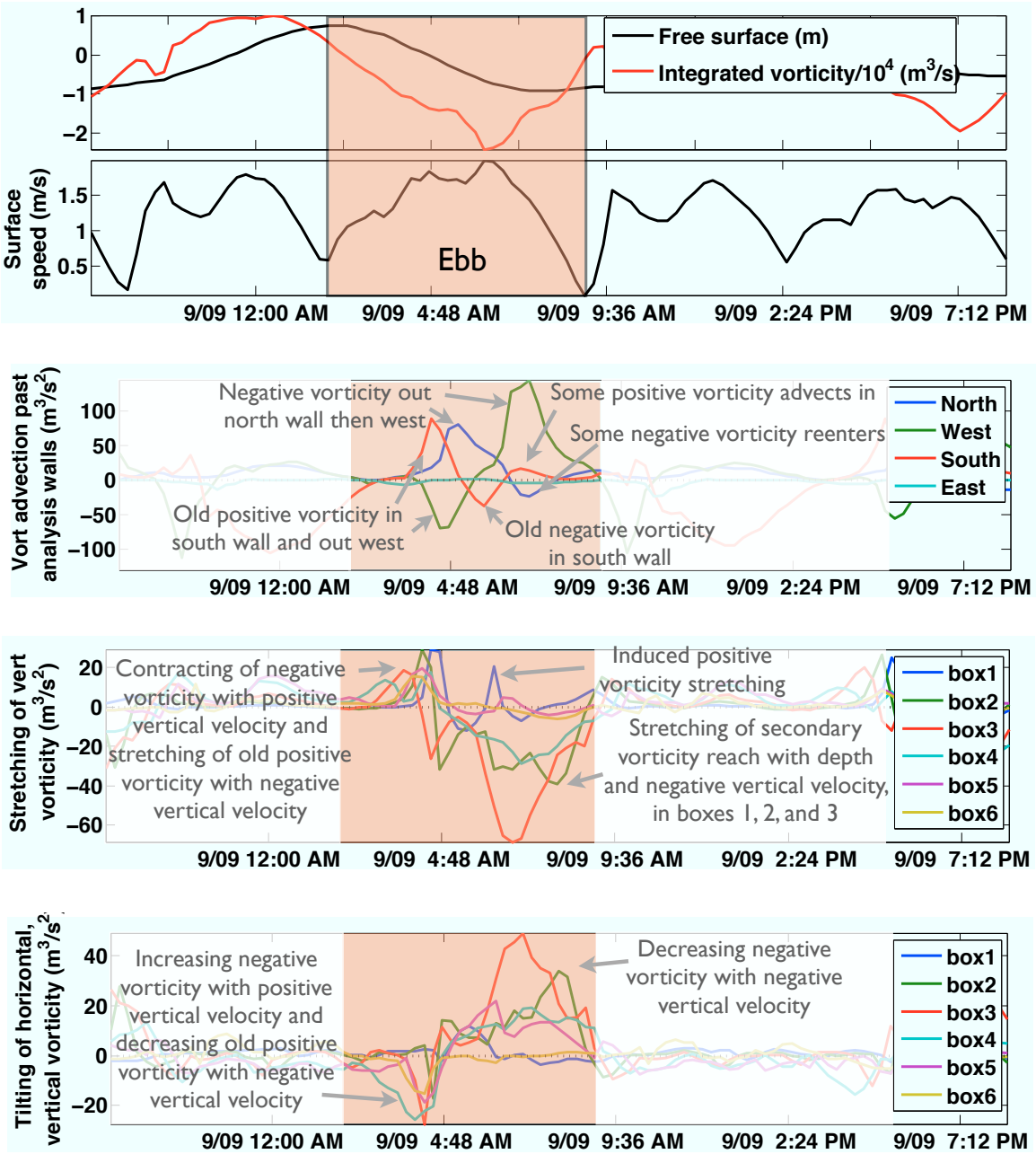


Figure 4.44: Case IV free surface, integrated vorticity, surface speed, advection by bounding wall, and stretching and tilting by box.

4.44 as positive advection at the south bounding wall when the old positive vorticity enters (Figure 4.45(b)), and negative at the west bounding wall when it exits. Shortly afterward, the second, old negative vorticity from the previous flood tide advects through the south bounding wall, causing the advection term at the south wall to be negative in sign. In the mean time, newly generated negative vorticity streams from the headland tip out the north bounding wall (Figure 4.45(c)), then out the west bounding wall (Figure 4.45(d)). Some of the negative vorticity that exits out the west bounding wall reenters the analysis domain via the north bounding wall.

In Case II, there were two peaks in all of the terms due to an initial surge of speed moving past the headland followed by the normal tidal flow. In the stretching term, both peaks were positive and in the tilting term, both peaks were negative (with a small positive peak in-between). In this case, Case IV, there is complex behavior with two peaks in the stretching and tilting terms due to persistent vortices; however, the peaks switch sign midway through the half-cycle. As seen in the stretching term in Case IV, first there is contraction of newly-generated negative vorticity with a negative vertical gradient of upsloping velocity near the headland tip (box 4), shown in Figure 4.46, causing the stretching term to be positive. This contraction due to the vorticity moving into a shallower area, with the associated velocity gradient, also tilts horizontal vorticity into vertical vorticity (causing a negative tilting term). The stretching term continues to be positive due to stretching of old positive vorticity that enters the analysis domain that coincides with a positive vertical gradient of convergent downwelling velocity (Figure 4.47).

The second peak of the stretching term is negative, as typical, and the behavior is similar to as described in Case III. Newly-generated negative vorticity coincides with a positive vertical gradient of downwelling velocity due to convergence with bottom friction, which stretches the negative vorticity, as shown in Figure 4.48. The horizontal vorticity is also tilted as in Case III, turning vertical vorticity into horizontal vorticity.

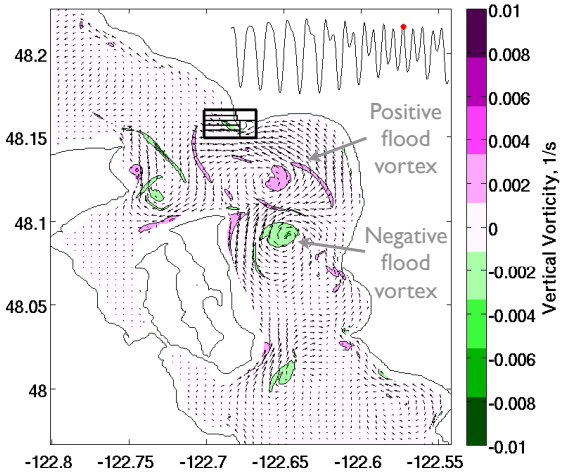


(a) 2:45AM: Eddies linger after flood tide

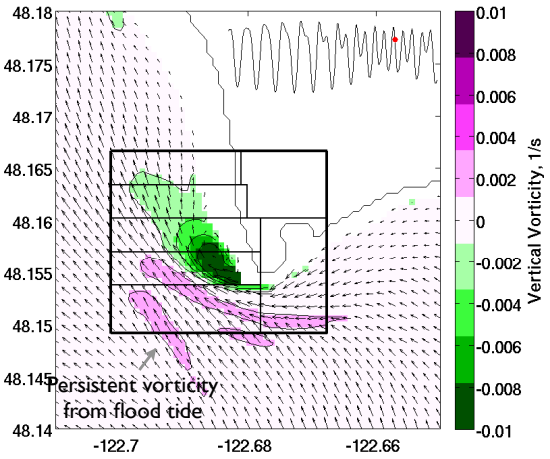


(b) 4:00AM: Old positive vorticity advects through analysis domain

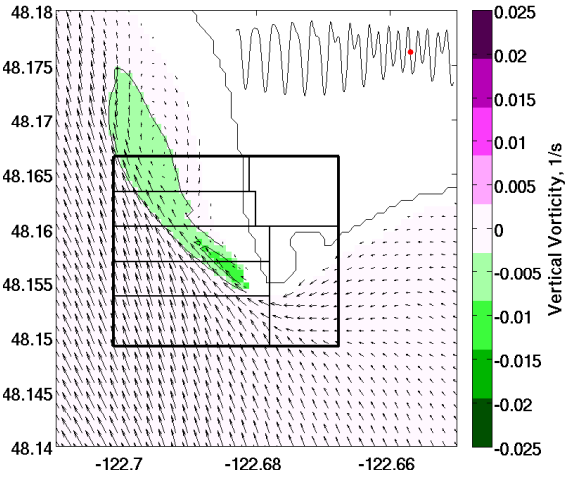


(c) 5:00AM: Negative vorticity reaches north first

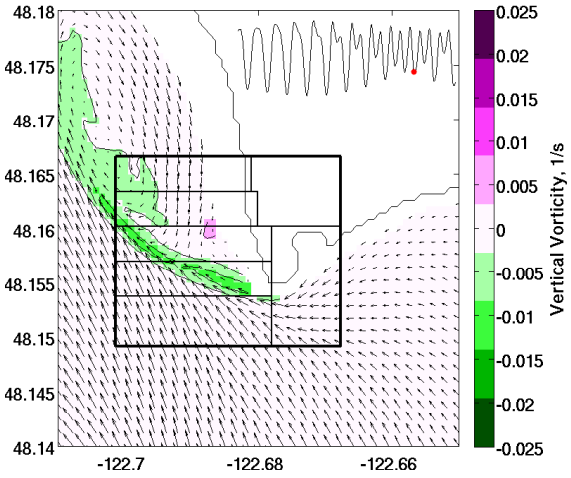


(d) 7:00AM: Negative vorticity reaches west second

Figure 4.45: Behavior modification on ebb tide in Case IV on 9/10/06 with persistent old vortices and strong initial surge. Shown are snapshots of vorticity at a depth of 10 meters below mean sea level. Note the lower vorticity color bar limits in Figures 4.45(a) and 4.45(b), for visual illumination.

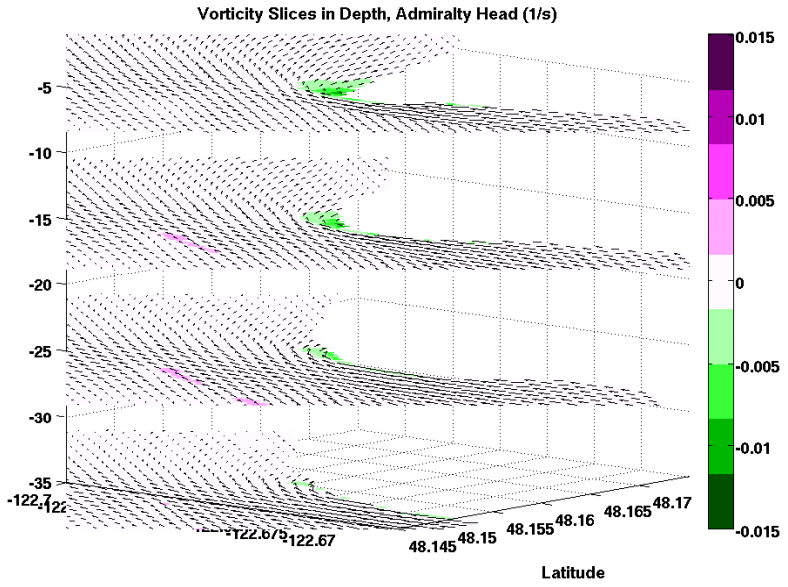


(a) Vorticity

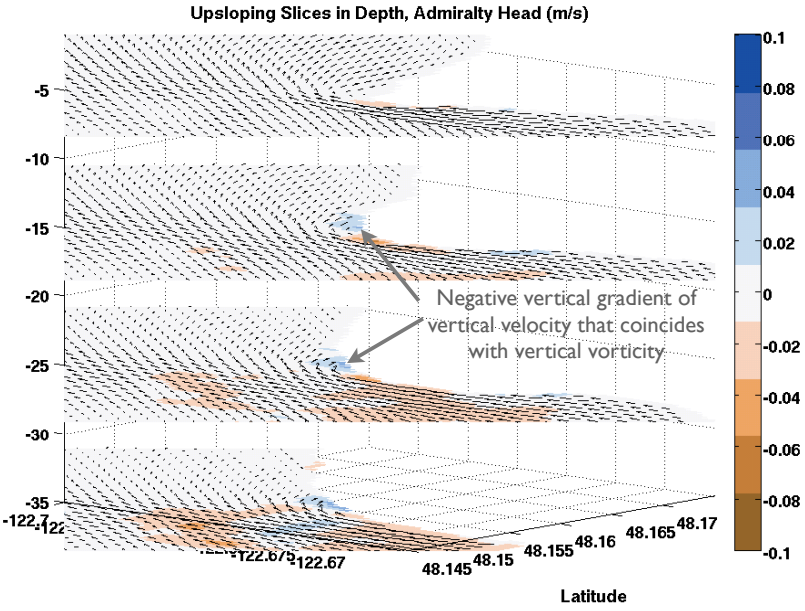


(b) Upsloping velocity

Figure 4.46: Depth slices of vertical vorticity and upsloping velocity near Admiralty Head at 3:30AM on 9/10/06. A negative vertical gradient of upsloping velocity right at the headland tip (in box 4) as the flow moves around the headland causes contracting of the negative vertical vorticity. Note the lower vorticity color bar limits in these figures, for visual illumination

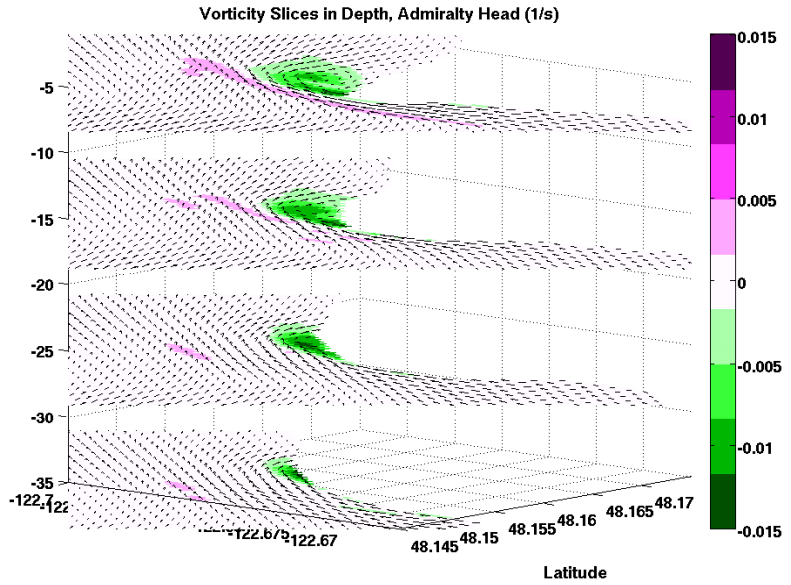


(a) Vorticity

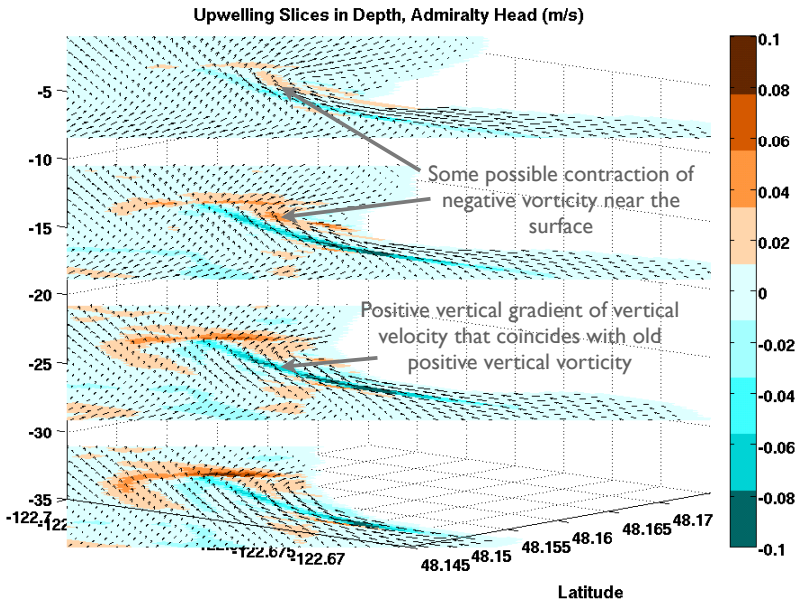


(b) Upwelling velocity

Figure 4.47: Depth slices of vertical vorticity and upwelling velocity near Admiralty Head at 4:15AM on 9/10/06. A positive vertical gradient of downwelling velocity west of the headland tip causes stretching of the old positive vorticity. Note the lower vorticity color bar limits in these figures, for visual illumination

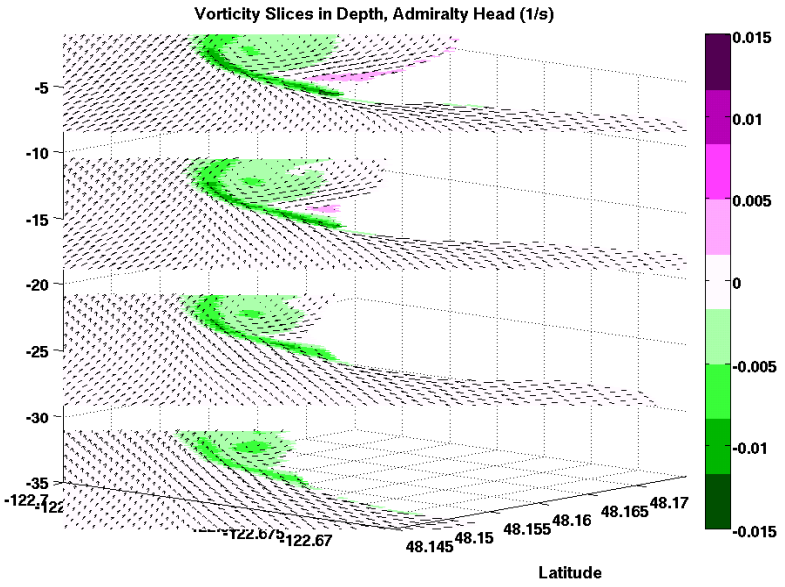


(a) Vorticity

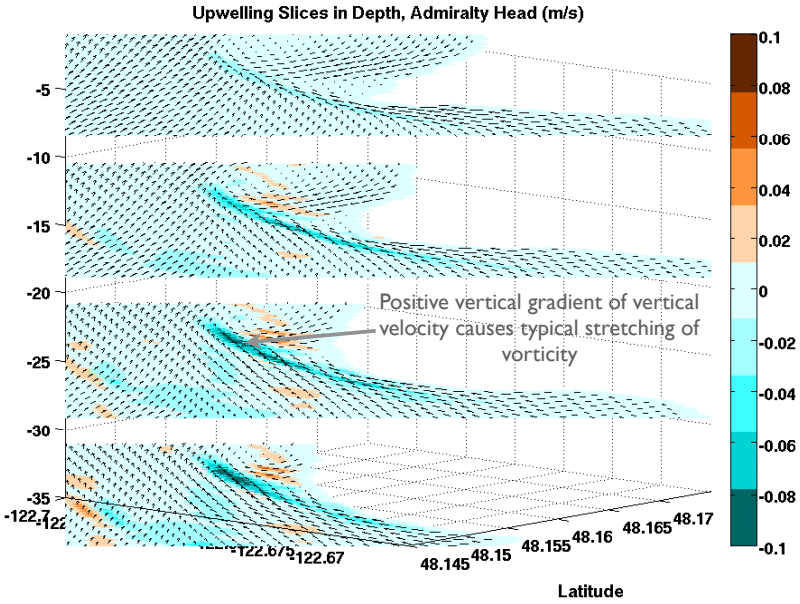


(b) Upwelling velocity

Figure 4.48: Depth slices of vertical vorticity and upwelling velocity near Admiralty Head at 7:00AM on 9/10/06. A positive vertical gradient of downwelling velocity west of the headland tip (boxes 3 and 4) causes stretching of the new negative vorticity. Note the lower vorticity color bar limits in these figures, for visual illumination. Snapshots are from the same time as shown in Figure 4.45(d).

## 4.5 Summary and Discussion

### *4.5.1 Summary*

There are many effects of the complex interactions of vortices in Admiralty Inlet. In this chapter, the presence of jetting through Admiralty Inlet on flood tide was discussed (Figure 4.3), along with fronts pushing past Admiralty Head on ebb tide (Figure 4.8). It was learned that vortices can persist long enough to advect through the subsequent tidal cycle, and can be accompanied by speed packets that significantly affect the flow fields (Figure 4.9 and seen in the speed signal of Case II). Vorticity is also associated with increased turbulence, which is shown in Figure 6.26.

The behavior of the horizontal currents is made complex by the presence of vorticity. Currents are increased or decreased, directions change, and sharp gradients are often found in different regions of an eddy field. Additionally, secondary eddies of the opposite sign from the main eddy can be induced near the coastline, which affect another region of horizontal currents (Figure 4.2(a)). These sharp gradients in eddy fields are areas of convergence which, combined with bottom friction, lead to patches of negative vertical velocity around the system, in space and time, and occasional patches of positive vertical velocity (Figure 4.20). The vertical velocity increases in strength with depth up to around mid-water column, below the area of strongest convergence near the surface. Vertical velocity can also be caused by flow over bathymetry, though vertical velocity generated this way near Admiralty Head tends to be smaller than vertical velocity due to convergence. Vertical velocity can be split by generation mechanism: upsloping velocity, which is topographically-induced, and upwelling velocity, which is caused by other effects, like horizontal convergence or divergence (Section 4.2.6).

Using a derivation of the equation for the absolute vertical vorticity describing the fluid movement simulated in ROMS, along with analysis employing an integral form of the equation, the behavior of vorticity in the vicinity of Admiralty Head was examined in detail. The most important terms in the vorticity equation were found to be boundary generation, advection, stretching, and tilting, though they had different relative magnitudes in different half-cycles.

Tilting and stretching/contracting of vertical vorticity were significant mechanisms of increasing and decreasing vertical vorticity. Typically, there were positive vertical gradients of vertical velocity near the surface, due to convergence, which stretched the vorticity, while near the seabed there were negative vertical gradients of vertical velocity collocated with vertical vorticity, causing contracting. Simultaneously, the collocation of horizontal vorticity with horizontal gradients of vertical velocity led to tilting of the horizontal vorticity, typically reducing the magnitude of the dominant sign of vertical vorticity. Upsloping and upwelling velocity were found to cause tilting and stretching in various cases, though downwelling was typically present and was strongly negative near the headland (due to convergence). Contracting of vertical vorticity was occasionally seen when an eddy moved into a shallower area and encountered a negative gradient of upsloping velocity.

It was most often newly-generated vorticity at the headland tip that was tilted and stretched/contracted during a half cycle. However, two cases were examined in which there was a noticeable presence of old, oppositely-signed vorticity. In one of these cases (Case II), old negative vorticity was present near Admiralty Head but it was still the newly-generated positive vorticity that coincided with a positive vertical gradient of vertical velocity, which stretched and tilted the vorticity. In another case (Case IV), it was the old vorticity which primarily coincided with a gradient of vertical velocity. The same typical pattern of vorticity stretching and tilting occurred in this case, but it was noteworthy because the vorticity primarily involved was of the opposite sign as would typically be seen in its half-cycle.

The ability to calculate the advection of vertical vorticity through a bounding wall enabled the determination of the persistence of the vortices beyond their half-cycle. Advection of vorticity into and out of the analysis domain and boundary generation were both significant features in the behavior of vortices in Admiralty Inlet. Reynolds stress and numerical truncation error terms did not play a significant role in the vorticity dynamics near Admiralty Head.

Boundary generation occurred primarily at the tip of Admiralty Head, where the bathymetry is steepest. This was particularly true on ebb tide, when the channel flow pushes most strongly past only the tip of Admiralty Head. On flood tide, generation also occurred along the headland north of the headland tip, but was largest at the tip itself. After being gen-

erated, the vorticity was then affected by other mechanisms previously described: it would be stretched or contracted, tilted, and advected out of the region.

### *4.5.2 Tidal Turbine Placement*

Each of the effects of vortices could be pertinent for turbine siting. The flood jets have an increase in speed in the areas through which they push. The fronts move through the system, particularly near Admiralty Head, and are associated with relatively sharp gradients in speed and density, which could matter for turbine survivability as well as power production. This will be discussed further in Chapter 6. Vorticity reaching from the headland tip can be associated with vertical velocity, mostly negative, which may affect turbine operation (Section 6.3.2). Vortices advecting around the area cause a change in directionality of the horizontal currents. The vortices are associated with an increase in turbulence, which is known to decrease turbine efficiency as well as increase stress on the turbines (Section 1.4.3). Vortices also can lead to multiple peaks in the speed profiles in the affected areas, which would then affect power production. It is possible that the effects of the vortices could be mitigated, avoided, or even utilized, but in any case, they need to be understood. These effects will be summarized and averaged into the metric maps presented in Chapter 6.

### *4.5.3 Pilot Site*

According to the simulation, among the many complexities passing through the pilot project site are vortices that can be persistent, traveling back with the subsequent tide, speed surges associated with vortices, and density and speed fronts pushing through the area. These features can be associated with increased turbulence levels as well. In particular, the simulation shows eddies moving through the pilot site on both flood and ebb for certain half-cycles, as shown in Figures 4.49(a) and 4.49(b). Figure 4.49(c) shows that strong patches of vertical velocity may move through the pilot site as well. In the discussion of simulation performance in Chapter 3, the true vertical velocity was found to be an order of magnitude larger than what was seen in the simulation. In this case, the vertical velocities in the pilot region could be significant.

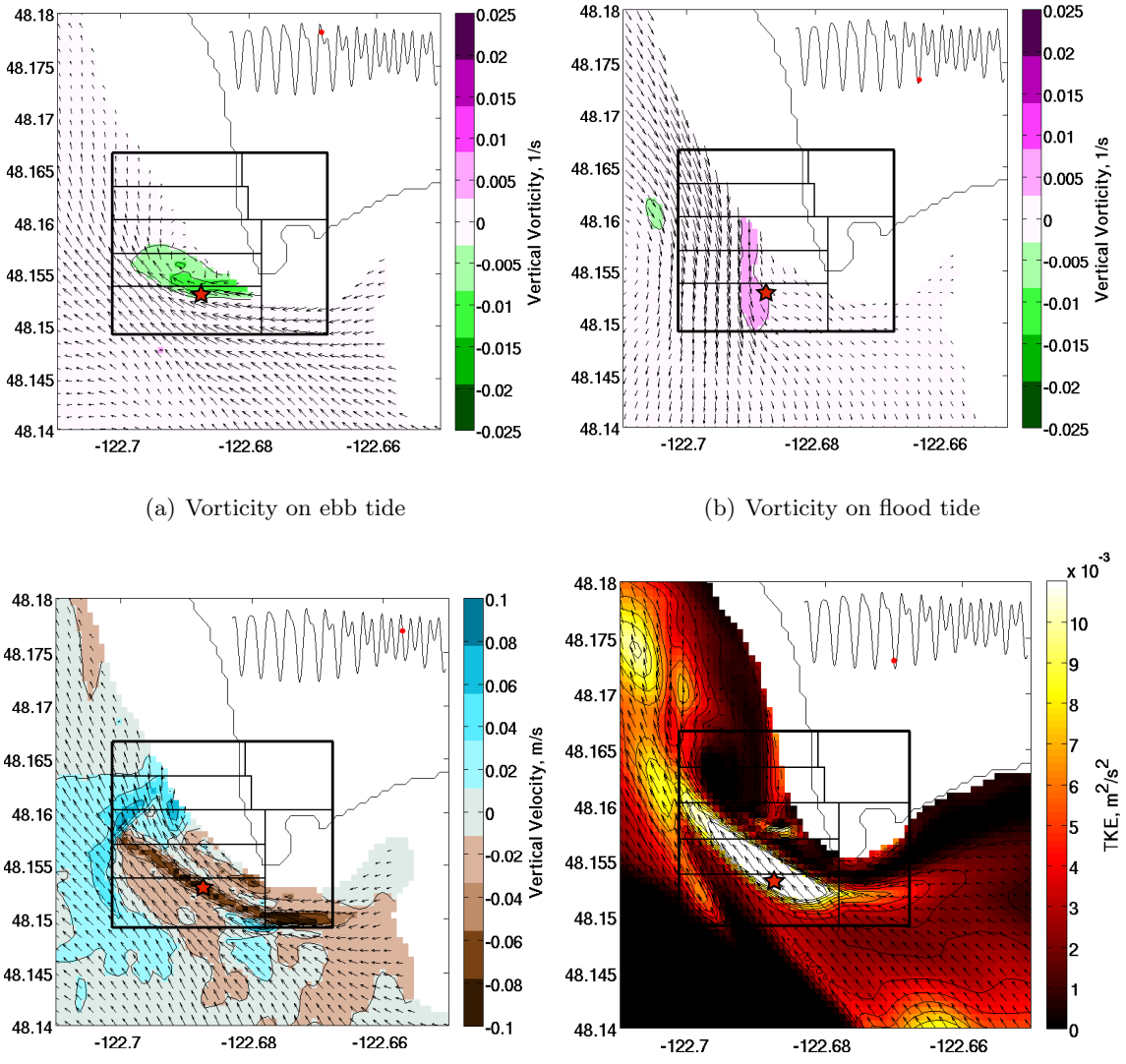


(a) Vorticity on ebb tide

(b) Vorticity on flood tide

(c) Vertical velocity

(d) Turbulent kinetic energy (10 meter depth)

Figure 4.49: Snapshots at 30 meter depth showing the pilot project location. Clearly the pilot project may be affected by some of the significant flow features near Admiralty Head.

### *4.5.4 Comparison with Dong et al Paper*

In Dong et al. (2007), a previous vorticity generation study, the authors found that the vorticity generation rate remained relatively constant in time as the other two terms, advection out of the analysis domain and rate-of-change of vorticity in the system, balanced each other out. Results were very different in the present case, because the situation is very different. In the previous study's simulation, the flow was steady in time and was forced from a single direction. The authors employed a flat-bottomed channel and a cylindrical island with vertical sidewalls. Because of this setup, they did not need to consider many of the terms that were retained in this study (Reynolds stress, implicit numerical viscosity in explicit form, tilting/stretching of vertical vorticity). On the other hand, the Coriolis term played an important role in their study but is much smaller than the size of the relative vorticity in this case.

The tilting of vorticity between horizontal and vertical and the stretching/shrinking of vertical vorticity are found here to play a significant role in the dynamics. This significance may have been related to the complex bathymetry in this simulation domain, and may not have been important in the Dong, McWilliams, and Shchepetkin's example. The main source of vertical velocity causing tilting and stretching was convergent downwelling, which was not caused by the bathymetry in this simulation. It is not clear whether or not a similar feature was seen in Dong et al. (2007).

The Reynolds stresses and implicit numerical viscosity did not play an important role in this simulation, in terms of the fluxes of vorticity across the open boundaries of the analysis domains. This is good in terms of the truncation error not playing a significant role at the open boundaries here.

In Section 4.4.2, it was shown that much less vertical vorticity was generated at the four meters of sidewall at the top of the water column than the rest of the water column in contact with the seabed. This means that the size of the minimum depth chosen for a simulation should not significantly alter the amount of vorticity generated in the system. It was additionally shown that when the boundary generation rate is normalized by the volume it has been integrated over, a comparable amount of boundary generation occurs at

the sidewall as at the seabed. This may mean that a flat-bottomed simulation which relies solely on sidewall generation will see the same order of vorticity generation as a comparable simulation with realistic bathymetry.

As mentioned earlier from Panton (2005), vorticity generation at boundaries is due to the unsteadiness of the flow and pressure gradients set up due to friction along the boundary. In Dong et al. (2007), the vorticity generation was due to pressure gradients since the flow was steady. In the present research, the vorticity generation is due to both mechanisms. The unsteadiness in the velocity field in this simulation was an integral part of the dynamics. This led to a changing vorticity location in space and time as well as allowed for vortex interaction from one tide to the next. None of this would be seen in a steady simulation. Additionally, as noted in Signell and Geyer (1991), unsteadiness leads to stronger vorticity and recirculation than seen in steady flows.

Chapter 5

# PERFORMANCE OF TURBULENCE CLOSURE SCHEME

## *5.1 Introduction*

The topics covered in this document are interconnected. Vortices correspond to areas of increased turbulence, and both pertain to turbine placement. Multiple high quality field data sets were gathered in the region of interest for turbine siting to determine baseline turbulence levels. With a numerical model covering the same region, it is possible to compare various quantities, such as turbulent kinetic energy and turbulent dissipation rate, to see how well the model performs at the data locations. Understanding how well the turbulence model performs allows informed application of turbulence properties obtained using the model to aid in turbine siting throughout the domain. It also presents an excellent opportunity to further understand how well the ocean modeling code ROMS performs on the difficult task of turbulence modeling. Very few studies exist where field turbulence data is compared to the turbulence output from ROMS simulations. The existence of the field data sets allow such a comparison. These model-data comparisons will be presented in Section 5.2.

In addition to direct model-data comparisons of turbulence properties, two approaches will be outlined and followed in order to account for a difference between the turbulent kinetic energy in the model output and the data. A proposed method of inferring turbulent kinetic energy from other quantities computed in the simulations, and based on properties of the field data and on an extension of Kolmogorov's theory is provided in Section 5.3. Additionally, described there is a method for accounting for the inherent numerical mixing in the system that is not included in the turbulent closure scheme. Summary of the results and discussion of relevant questions and applications to tidal energy can be found in Section 5.4.

### *5.1.1 Data Sets*

Multiple data sets of the currents in Admiralty Inlet were taken in 2010 and thoroughly analyzed and discussed in Thomson et al. (2011). Two sets of acoustic Doppler current profiler (ADCP) data were gathered near Admiralty Head in February 2010 and May to June 2010. One acoustic Doppler velocimeter (ADV) set and one ADCP set were gathered near Nodule Point on Marrowstone Island in February 2010. Data locations are shown in Figure 5.1. The ADV data, taken at a projected turbine hub height of 4.7 meters above the seabed, have less noise (error) in the measurements than the ADCP data, and are thus the most trusted source for comparison. The ADCP gives data with depth. In order to use the ADCP data as well at the ADV data at Nodule Point, the ADCP data is "pinned" to the ADV data such that data taken at approximately the same height above the seabed by the two systems have approximately the same values for the turbulent kinetic energy and for the turbulent dissipation rate. In other words, the ADCP data at Nodule Point is multiplied by a single factor (the ratio of the average value from the ADV over the average value from the ADCP at hub height) for each turbulence parameter in order to match the hub height ADCP data to the hub height ADV data. In addition, the method presented in Section 3.3.2 of aligning non-coincident time series is used to find meaningful comparisons between the simulation run in 2006 and the data from 2010. Both data sets from Nodule Point are used, but only the Admiralty Head set from May to June is used. The data sets include measures of speed, turbulent dissipation rate, and horizontal and vertical turbulent kinetic energy for both sites at hub height, as well as for a 20 meter profile above the seabed (from the ADCPs). In addition, the ADV set has a measurement of Reynolds stress.

The data are taken at the sampling rate of 1 to 32 Hz, then split into five minute turbulent averaging windows. The horizontal currents are rotated onto the principal axes for each window, with the mean flow pointing in the major principal axis direction and the turbulent velocity fluctuations as deviations around the mean flow and major principal axis direction. There is Doppler noise error associated with each device in the measurement of horizontal currents, and the error is much smaller for vertical velocities. When examining the frequency spectrum of the ADV data, the velocities are analyzed in three overlapping

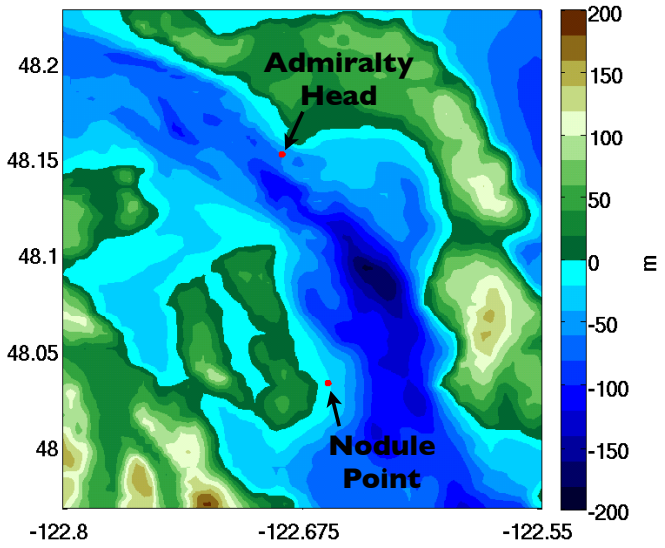


Figure 5.1: Map of Admiralty Inlet with turbulence data locations indicated.

sub-windows of 128 seconds, which are then averaged together to reduce confidence intervals in the five minute period analysis.

The turbulent kinetic energy is largely contained along the $u'$ axis, which is in the major principal direction for each 5-minute window. However, the energy contained in the perpendicular direction, $v'$, will also be considered, given the high resolution data at Nodule Point from the ADV.

### *5.1.2 Turbulence Overview and Terminology*

Kolmogorov theorized about the behavior of spectral energy transfer in turbulent flows. He understood energy to be input into a flow system at large scales (*e.g.*, in this case via the tides or large headland eddies). With increasing wave number, at and above some critical wave number, the spectral energy density in the system is approximately a function of only the wave number, the turbulent dissipation rate, and the viscosity. This region is called the equilibrium range and can be subdivided into two regions: the inertial subrange and the viscous subrange. In the inertial subrange, the energy can be interpreted as eddies which degenerate into eddies of smaller scale (or larger wave number), cascading the energy to

smaller and smaller scales at the turbulent dissipation rate, $\varepsilon$, without the influences of viscosity. In this region, Kolmogorov's theory says that the spectral energy density is a function of only the wave number and the turbulent dissipation rate (and is independent of the viscosity). Dimensional analysis dictates that the relationship be

$$E(\kappa) = \alpha \varepsilon^{2/3} \kappa^{-5/3},$$

where $E$ is the turbulent kinetic energy spectral density, $\kappa$ is the horizontal wave number, $\alpha$ is a universal constant whose approximate value has been found experimentally, and $\varepsilon$ is the turbulent kinetic energy dissipation rate. The turbulence is three-dimensional in nature and the three components of the root-mean-square velocities are assumed to be isotropic in the inertial range. The viscous subrange is at higher wave numbers where viscosity becomes important, and in which energy is removed from the system at the turbulent dissipation rate.

For analysis of the turbulence data and model output, it is desirable to use Kolmogorov's theory. However, his work is in terms of the wave number, whereas the data being used are found as a function of frequency $f$. In order to relate the two, Taylor's frozen field approximation is utilized, which assumes that the turbulence is advected without distortion over the length $L$ at the mean speed of the horizontal motion, $u$, in the major principal axis direction. The relationship between $f$, $L$, and $u$ is

$$L = u/f.$$

Using this expression, it is possible to find the form for Kolmogorov's theory in terms of frequency as follows, where the wave number $\kappa$ is given in terms of $L$ as $\kappa = 2\pi/L$:

$$\begin{aligned} E &= \alpha \varepsilon^{2/3} \kappa^{-5/3} \\ &= \alpha \varepsilon^{2/3} \left( \frac{2\pi}{L} \right)^{-5/3} \\ &= \alpha \varepsilon^{2/3} \left( \frac{2\pi f}{u} \right)^{-5/3} \\ &= \frac{\alpha}{(2\pi)^{5/3}} \varepsilon^{2/3} u^{5/3} f^{-5/3}. \end{aligned} \tag{5.1}$$

Figure 5.2 shows the time-averages of major principal axis, minor principal axis, and

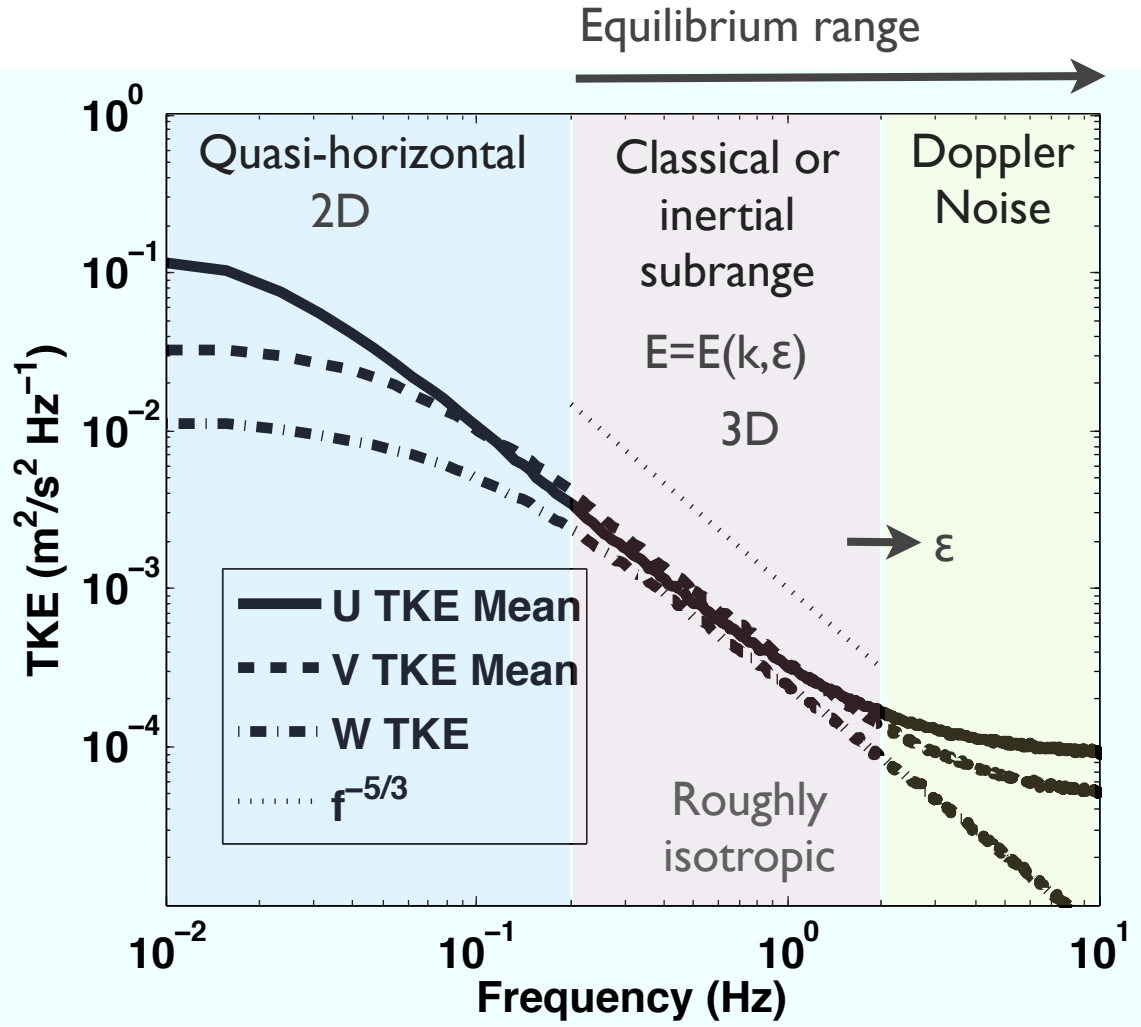


Figure 5.2: Mean horizontal turbulent kinetic energy density (solid) and vertical turbulent kinetic energy density (dashed) vs. frequency for data at Nodule Point at hub height of 4.7 meters. Individual occurrences of data in time spread around the mean half to a full order of magnitude but follow the same trend. Data from Thomson et al. (2011).

vertical components of the turbulent kinetic energy density data at Nodule Point from Thomson et al. (2011), compared with the function $f^{-5/3}$. There are three distinct areas of behavior in this plot. The lower frequencies, below 0.1 Hz, show a distinct deviation between the horizontal and vertical components of turbulent kinetic energy spectral density in frequency space, with the $u$ component an order of magnitude larger than the vertical, and the $v$ component in between. This illustrates highly anisotropic turbulence, where there is different behavior for horizontal versus vertical motions, indicating large, energetic, horizontal eddies dominating the energy. Energy may be input directly into the system at these or larger scales. The middle frequencies, from about 0.2 to 2 Hz, make up the classical, shear flow turbulence range where all three root-mean-squared components of the turbulent velocities are similar and approximately follow Kolmogorov's law in frequency form. The turbulent kinetic energy calculated from this frequency range will be referred to as from the classical turbulence range. The far right of the plot shows the level of Doppler noise where the horizontal component average flatlines (Thomson et al., 2011). The vertical component of the turbulent kinetic energy has less error and continues downward at about the same rate as in the middle frequency range.

An analogous spectrum plot is not available at Admiralty Head. The spectra at Admiralty Head and throughout the region are expected to behave similarly to those of Nodule Point, though with the frequency/length scale at which the vertical motions plateau with lower frequency to depend on location. This is discussed further in Section 5.2.3.

The spectrum shown in Figure 5.2 for the field data is at a much higher temporal resolution than has been output from the simulation. Similarly, the spatial resolution of the grid used in the simulation limits the ability of the model to capture the scales seen in this spectrum. The turbulence closure scheme attempts to address the resulting deficiency in the spectral energy density of the model output, but there remains a gap between the scales captured in the model and those modeled with the closure scheme. An attempt to address this is pursued in Section 5.3 by inferring a form to extend the spectral density function.

### *5.1.3 Data Considerations*

High quality data from the ADV are available for all components of the velocity field at hub height for the Nodule Point location. The horizontal components have been projected onto a major and a minor principal axis for each five minute averaging window. The relative ratio of the horizontal components from the ADV data set at Nodule Point is used to infer the size of the off-axis component for the ADCP data sets. The ratio of the minor to the major principal axis turbulent kinetic energy is approximately 1.64, over the full frequency range included in the data sets. This will be used in the comparisons for turbulent kinetic energy between data and model output for the Admiralty Head location and for the Nodule Point comparisons that are at multiple depths (as the Nodule Point data from the ADV at hub height already includes both components).

This may be a low estimate for the relationship between $v'$ and $u'$ at Admiralty Head since the flow behavior there is different from the behavior at Nodule Point, with evidence that the major and minor principal axes are similar in size over a larger frequency range than at Nodule Point (see discussion in Section 5.2.3).

The turbulent kinetic energy in the classical, approximately isotropic range is found by integrating the turbulent kinetic energy spectral density data using values from only the frequencies in the range $0.2 < f < 2$ Hz (ranges described in Section 5.1.2). The full turbulent kinetic energy calculations use the full range of frequency data included in the 128-second averaging window. Only the ADV data set at Nodule Point has detailed spectral information, so all references to limiting frequency bands for analysis are accomplished only at Nodule Point.

For more details of the data gathering and analysis see Thomson et al. (2011).

### *5.1.4 Calculations*

Expressions used to calculate turbulent properties from the field velocity data can be found in Thomson et al. (2011). This section details the expressions used for the model output, given parameterizations used in the simulation. Note that the turbulence closure scheme itself is detailed in Section 2.4.

The Reynolds stress component for the principal axis horizontal direction and the vertical direction, $\overline{u'w'}$, is given in the Nodule Point ADV data set. For the turbulence data, $u'$ and $v'$ are the turbulent velocity fluctuations along the major and minor principal axes and $w'$ is in the vertical direction. For the model output, the magnitude of the two components of the Reynolds stress tensor, $\overline{u'w'}$ and $\overline{v'w'}$, are calculated using the parameterization in ROMS and combined for comparison with the principal axis data:

$$\begin{aligned}
\overline{u'w'} &= -K_M \frac{\partial u}{\partial z} \\
\overline{v'w'} &= -K_M \frac{\partial v}{\partial z} \\
\text{Reynolds stress}_{\text{model}} &= \sqrt{\overline{u'w'}^2 + \overline{v'w'}^2} \\
&= K_M \sqrt{\left(\frac{\partial u}{\partial z}\right)^2 + \left(\frac{\partial v}{\partial z}\right)^2}
\end{aligned}$$

where $K_M$ is the vertical eddy viscosity defined in Equation 2.9.

Shear production is given by

$$P_s = -\overline{u'w'}\frac{\partial u}{\partial z} - \overline{v'w'}\frac{\partial v}{\partial z},$$

and is a measure of turbulence produced due to vertical shear in the water column. Combined with the parameterization of Reynolds stress in ROMS, it is calculated for model output as

$$P_s = K_M \left[ \left(\frac{\partial u}{\partial z}\right)^2 + \left(\frac{\partial v}{\partial z}^2\right) \right].$$

Buoyancy production is given by

$$P_B = -\frac{g}{\rho_0}\overline{\rho' w'},$$

which in ROMS is calculated using the parameterization for the turbulent scalar flux as

$$\begin{aligned}
P_B &= K_H \frac{g}{\rho_0}\frac{\partial \rho}{\partial z} \\
&= -K_H N^2,
\end{aligned}$$

where $K_H$ is the vertical eddy diffusivity defined in Equation 2.10 and $N$ is the buoyancy frequency. The buoyancy production measures turbulent kinetic energy exchange with turbulent potential energy.

Turbulent kinetic energy from the model is compared with data alternately with just horizontal and with both horizontal and vertical components (as noted in figures). The turbulent kinetic energy that is output directly from the model is assumed to include all three components and to be approximately isotropic, in the absence of distinguishing information about the individual velocity fluctuation components. Therefore, to compare with horizontal data using only horizontal scales from the model output, the full turbulent kinetic energy from the model is multiplied by 2/3, to account for two of the three components.

The effect of turbulence on a turbine is typically calculated using the turbulence intensity metric used in wind energy analysis. This metric is given by the level of turbulent velocity fluctuations divided by the mean velocity. In the field data analysis, this is calculated for the principal horizontal velocity fluctuation component, and is assumed to approximately account for both horizontal components. A similar calculation should be used for the model output. To do so, the velocity fluctuation $u'$ is found in terms of turbulent kinetic energy, the quantity output from the turbulence closure scheme: $k = \frac{1}{2}(u'^2+v'^2+w'^2) \approx \frac{1}{2}(3u'^2) = \frac{3}{2}u'^2$, so $u' = \sqrt{\frac{2k}{3}}$. A turbine rotor face would encounter a single directional component of turbulence intensity, and the model output turbulent kinetic energy has no directional preference. Therefore, for the model output, the turbulence intensity is calculated as $I = u'/s = \frac{\sqrt{2k/3}}{s}$. In presentation of turbulence intensity, values corresponding to currents below the cut-in speed are removed because the mean speeds approach zero. A cut-in speed of 0.8 m/s is used for this purpose for both the data and model analysis (Thomson et al., 2011).

## *5.2 Model Output-Data Comparisons*

### *5.2.1 Nodule Point*

A comparison in time of turbulence data with model output at hub height at Nodule Point is shown in Figure 5.3, with data in black and model output in red. The top panel shows the free surface agreement using the previously-discussed comparison method for two non-coincident time series (Section 3.3.2). Given the known errors in turbulence modeling, the mean speed, turbulent dissipation rate, and Reynolds stress in the field data and model

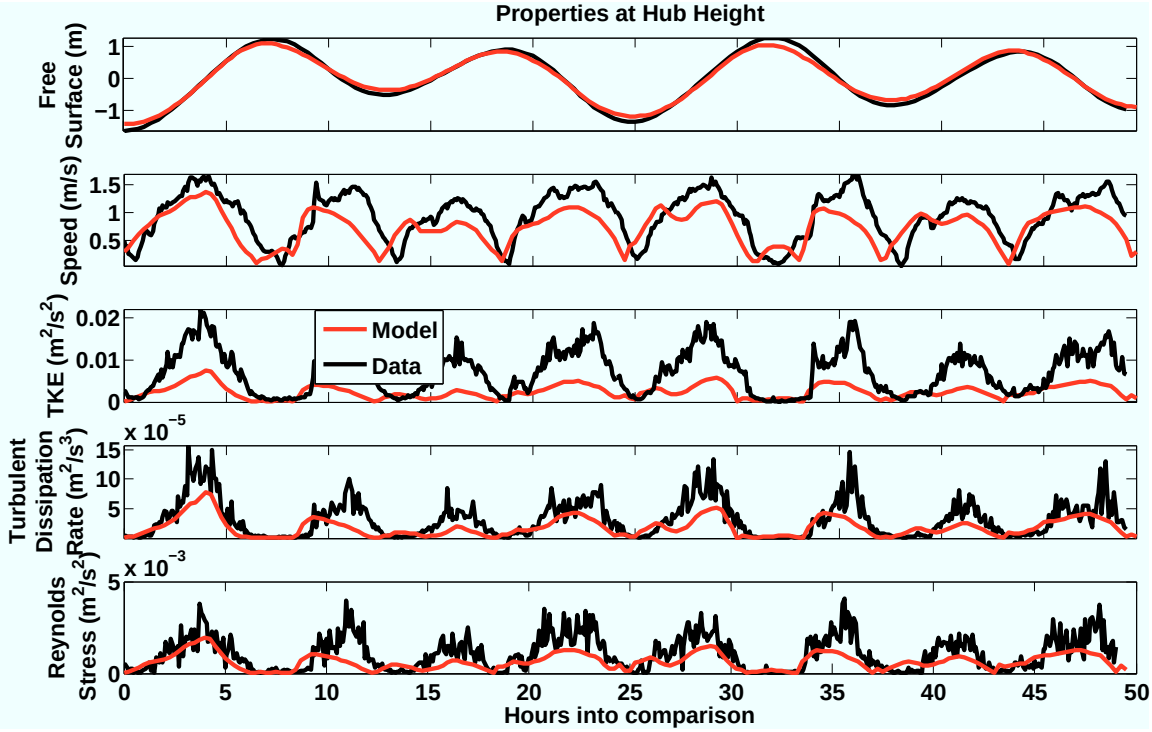


Figure 5.3: Turbulence comparison between data (black) and model (red) at hub height of 4.7 meters at Nodule Point. Both model and data turbulent kinetic energy include vertical and horizontal components.

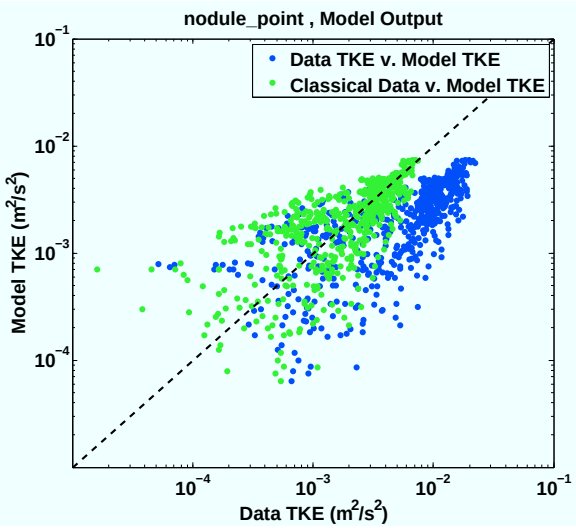


Figure 5.4: Hub height 1-1 comparisons of types of turbulent kinetic energy at Nodule Point. Blue shows model turbulent kinetic energy compared with the full turbulent kinetic energy data. Green shows the model turbulent kinetic energy compared with the turbulent kinetic energy data taken only over the classical turbulence frequency range. Both model and data turbulent kinetic energy include vertical and horizontal components.

output are in reasonable agreement (Pope, 2000). The latter two turbulence parameter model predictions are each within a factor of two of the field data, on average.

*Turbulent kinetic energy*

The turbulent kinetic energy predicted by the model does not compare particularly well with the data; in the data, turbulent kinetic energy is three times larger than the model predictions. However, following the frequency classifications of the data suggested in Figure 5.2, the turbulent kinetic energy data can be split into two main classes: the anisotropic lower frequency, higher energy values, and the classical higher frequency, roughly isotropic, lower energy values, as described in Section 5.1.2. Two comparisons between the classical and model turbulent kinetic energy data are shown in Figure 5.4. In blue, the turbulent kinetic energy comparison shown originally in Figure 5.3 is presented on a one-to-one log-log

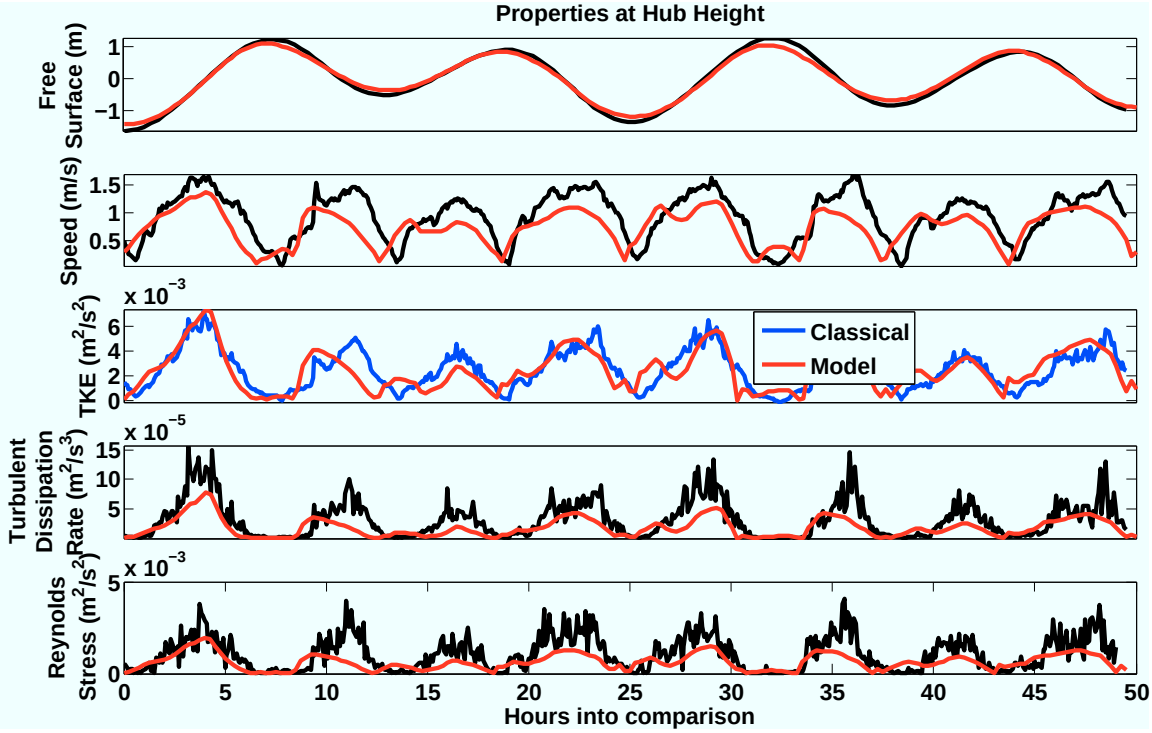


Figure 5.5: Turbulence comparison between data (black) and model (red) at hub height of 4.7 meters at Nodule Point. The turbulent kinetic energy comparison has been made here between the model (red) and data restricted to the classical frequency range (blue), giving a much better agreement. Both model and data turbulent kinetic energy include vertical and horizontal components.

plot. It is clear that the data values are larger than the model output values. However, when the turbulent kinetic energy data is calculated using only data from frequencies in the classical turbulence range, from about $0.2 < f < 2$ Hz, the model output-data comparison is greatly improved, as shown in green in Figure 5.4.

This is consistent with the output from ROMS being the classical turbulent kinetic energy. This is reinforced in Figure 5.5, which shows a comparison of turbulence properties at hub height for Nodule Point, updated with the comparison for turbulent kinetic energy between model output and classical-range data. The large discrepancy in the comparison

of turbulent kinetic energy shown in Figure 5.3 is due to the fact that the data set includes length scales (or frequencies) larger than what is included in the classical turbulence subrange. For example, frequencies between $10^{-2}$ and $10^{-1}$ $s^{-1}$, which are included in the data turbulent averaging window, correspond roughly to length scales of 100 and 10 meters, respectively. These are too large to be considered classical turbulence, especially given the very strong anisotropy in the kinetic energies shown in Figure 5.2. Because of this, a better comparison between the data and the turbulence model, which is intended to model classical turbulence, is to restrict the turbulent kinetic energy data to frequencies in the classical range. An attempt will be made in Section 5.3 to address in the model the gap in classical and "full" turbulent kinetic energies seen in the data.

*Variation of turbulent dissipation rate with depth*

Data from the ADV set at hub height for Nodule Point is the most reliable available. However, the ADCP data at the site can be used to examine the variation in turbulent dissipation rate with height above the seabed. Because there is so much more noise in the ADCP data compared to the ADV data (causing the ADCP data to be always larger than the ADV data) to correct the ADCP output, the bottommost ADCP data level is pinned to the ADV data at almost exactly the same height. To roughly connect the two data sets and perform a basic shift, the ADCP turbulent dissipation rate at hub height is multiplied by the time-average of the ADV dissipation rate and divided by the time-average of the ADCP dissipation rate at hub height. Time-averages are performed over the comparison period shown in the figures. The results for the turbulent dissipation rate with depth at Nodule Point are shown in Figure 5.6. The bottommost comparison is at about hub height and shows reasonable agreement, as was also obtained with the ADV data. Moving up the water column, the same patterns continue, though, as seen in the time-mean profile on the right; the data switches from being larger than the model prediction on average to smaller on average, but the two quantities are fairly close.

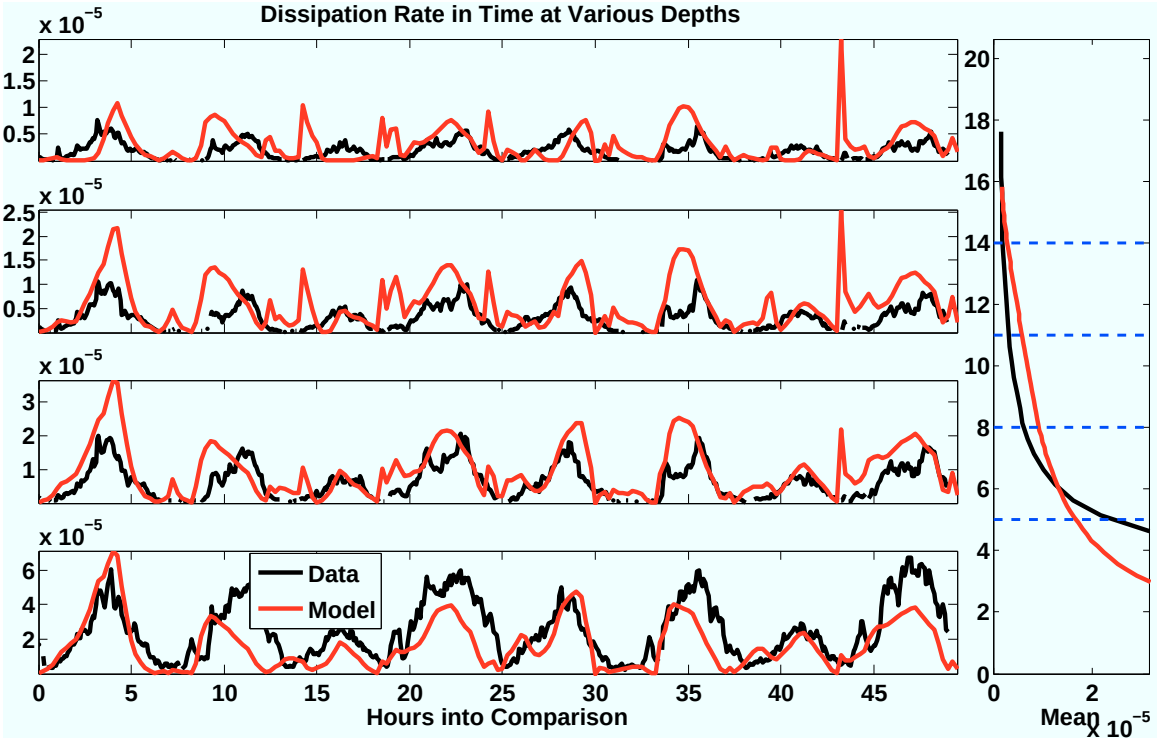


Figure 5.6: Turbulent dissipation rate comparisons between data (black) and model (red) at Nodule Point for the same time as Figure 5.3 but at multiple depths. The comparison depths are indicated, in order, as blue dashed lines on the time-mean profile of the turbulent dissipation rate profiles on the right side of the figure.

*Performance of turbulence model*

There is a known horizontal speed deficiency in the model (Section 3.3.2) such that the mean speed predicted by the model is on average about 75% the mean speed measured in the data. This can be seen in this speed comparison in Figure 5.3. This deficiency is also expected in the turbulence values, which may help to partially explain why the turbulence fields predicted by the model are somewhat low in comparison to the data. In this particular time series comparison, the speed predicted by the model, averaged over the time series, is 78% the value of the speed found in the field data. Classical turbulence theory indicates that the turbulent dissipation rate is expected to scale approximately with the cube of the speed (Pope, 2000). This is close to what is seen in the comparison: the model prediction of the dissipation rate at about 56% the size of the field data dissipation rate (as measured by a time-average at hub height of each quantity), which is slightly larger than the direct cube of the model speed size relative to the data, $0.78^3 = 0.47$. Therefore, the turbulent dissipation rate predicted by the model is low as compared with the field data by a factor of about two, and this is roughly consistent with the known speed deficiency in the model.

Classical turbulence theory indicates that the turbulent kinetic energy is expected to approximately scale with the square of the speed. The horizontal components of the turbulent kinetic energy predicted by the model for this time period, at hub height, are, on average, about 25% the size of the horizontal components of the turbulent kinetic energy from the field data. This is lower than the deficiency in turbulent kinetic energy that is expected, based on a scaling with velocity squared, which would give $0.78^2 = 0.61$. However, as is discussed in Section 5.2.1, the turbulent kinetic energy predicted by the turbulence closure scheme is limited to the classical turbulence range, whereas the turbulent kinetic energy from the field data includes energy from a larger frequency range. Thus, there are two distinct sources of the deficiency for the turbulent kinetic energy from the model output: less energy in the system due to a speed deficiency, and the limited intended frequency range of the turbulence model. Both are expected to be contributing to the deficiency in the model-predicted turbulent kinetic energy. In Section 5.3, an approximation is made to infer the energy in the model over a larger frequency range of the turbulent spectrum than

in the turbulence model itself. This adjusted calculation does improve the match between the model output and data for the horizontal turbulent kinetic energy, such that the model output is, on average, about 84% the size of the data. The inferred calculation (that will be discussed in detail in Section 5.3) addresses, and even over-predicts, the source of deficiency in the model prediction of the turbulent kinetic energy due to differing frequency ranges of spectral energy in the model and the data. However, the inferred turbulent kinetic energy is still low relative to the data due to the remaining deficiency in speed in the system.

The dissipation rate versus depth (from the ADCP data) is shown in Figure 5.6. The ADCP data was pinned to the ADV data at hub height using a simple ratio of their relative magnitudes because the data from the ADCP is noisier than the data from the ADV (see Section 5.2.1). Accordingly, the relative behaviors of the model and ADCP data dissipation rate time series at hub height in the bottom panel of Figure 5.6 are similar to the model and ADV data behaviors seen in Figure 5.3. However, this is a simple shift of the data by an order of magnitude at all depths based on a comparison of data sets at hub height (the only depth comparison between the data sets that is possible) and it may have over-corrected the ADCP data higher in the water column where the dissipation rate is lower. This is difficult to verify because the ADV data is only available at hub height and comparative mean vertical profiles between the ADV and ADCP data cannot be examined to find if the ratio between the two datasets is consistent with depth.

*Flow features*

The speed curves from both the model output and the data in Figure 5.3 or 5.5 show two peaks for some half-cycles, but do not always show the same behavior. This is likely due to the smoothed, imperfect bathymetry in the simulation, altering the trajectory of vortices, along with the fact that the two surface signals are only approximately matched, but are not actually coincident. Regardless, more can be learned about what is occurring in the region by examining times when there is similar behavior in the speed curves from the model and data. For example, near hour 40 into the Nodule Point model-data comparison, there is a double peak in the simulation and the data speed signals. This is due to behavior described

in Section 4.2.3. An eddy from the previous ebb tide (Figure 5.7(a)) is associated with a patch of increased speed, which passes by Nodule Point at the beginning of flood tide (Figure 5.7(b)), followed by the main flood tide a few hours later (Figure 5.7(c)). Turbulent kinetic energy is also increased following a similar pattern as the increased speed (not shown).

### *5.2.2 Admiralty Head*

Comparisons of turbulence quantities versus time at Admiralty Head are shown in Figure 5.8. The alignment in the data and model time series is not as good as in the Nodule Point case, as shown in the more pronounced mismatch in the free surface signal. The comparisons are reasonable between the model output and data. The turbulent kinetic energy from the model output is lower than from the data set, but not as low as at Nodule Point. This will be discussed further in Section 5.2.3. The comparisons of speed and dissipation rate between the data and model output are similar to those from Nodule Point. As in the Nodule Point case, it is important to keep in mind that the speeds are low throughout the domain, which will lower the magnitude of the turbulence properties accordingly.

#### *Variation of turbulent dissipation rate with depth*

Comparisons for the turbulent dissipation rate at Admiralty Head with depth are given in Figure 5.9. Shown on the left side of Figure 5.9 are data-model comparisons for the same time period shown in Figure 5.8, but at various depths. These depths are indicated on the plot of the right side of the figure of the time-average of the dissipation rates over the comparison period. There is a feature clearly visible in the model output around hour 35, which appears to correspond to a similar feature in the data (though shifted in time due to misalignment of the free surface signals). This feature is explored in the following section. In general, the time series comparisons are similar at each depth and the mean profiles agree very well.

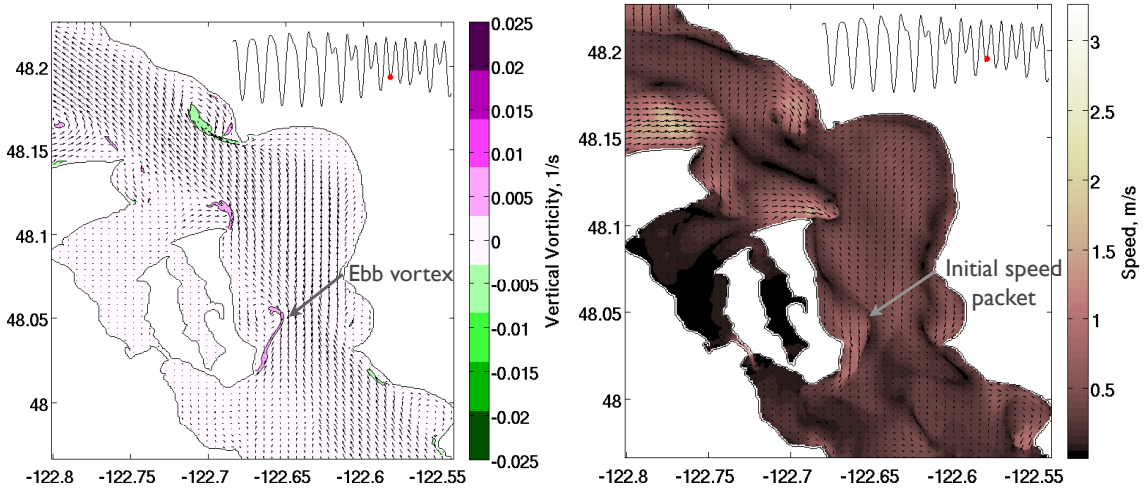


(a) Vorticity, 37.25 hours into comparison

(b) Speed, 39 hours into comparison

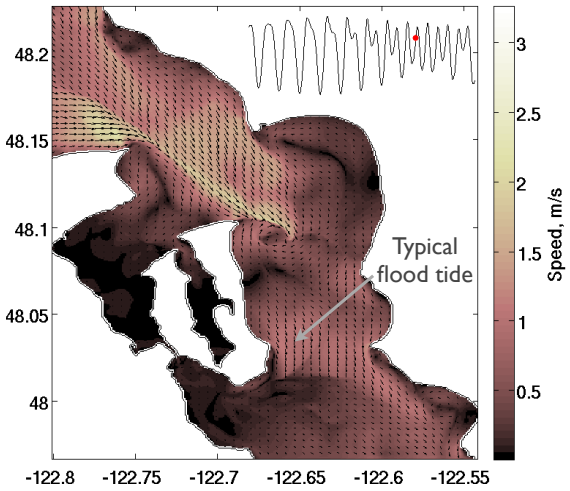


(c) Speed, 42 hours into comparison

Figure 5.7: Surface fields from around 40 hours into the comparison showing the progression of an ebb vortex near Nodule Point that causes a double speed peak on the subsequent flood tide.

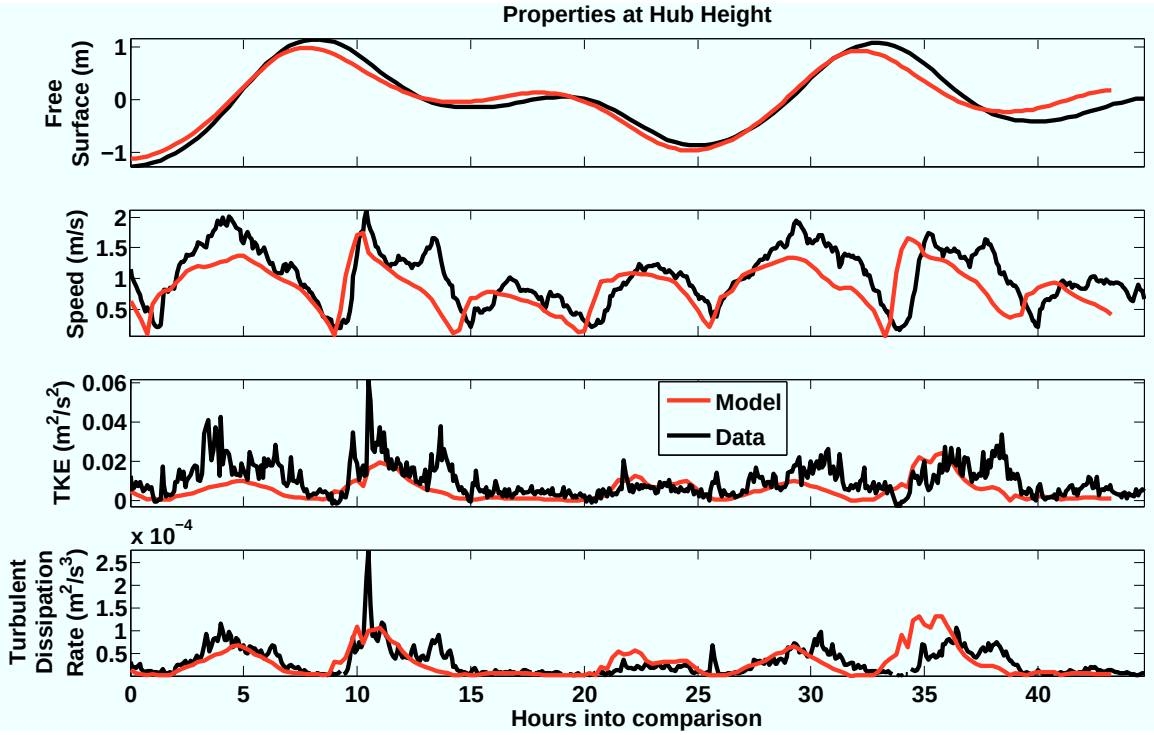


Figure 5.8: Turbulence comparison between data (black) and model (red) at hub height of 8.1 meters at Admiralty Head. Both model and data turbulent kinetic energy include vertical and horizontal components.

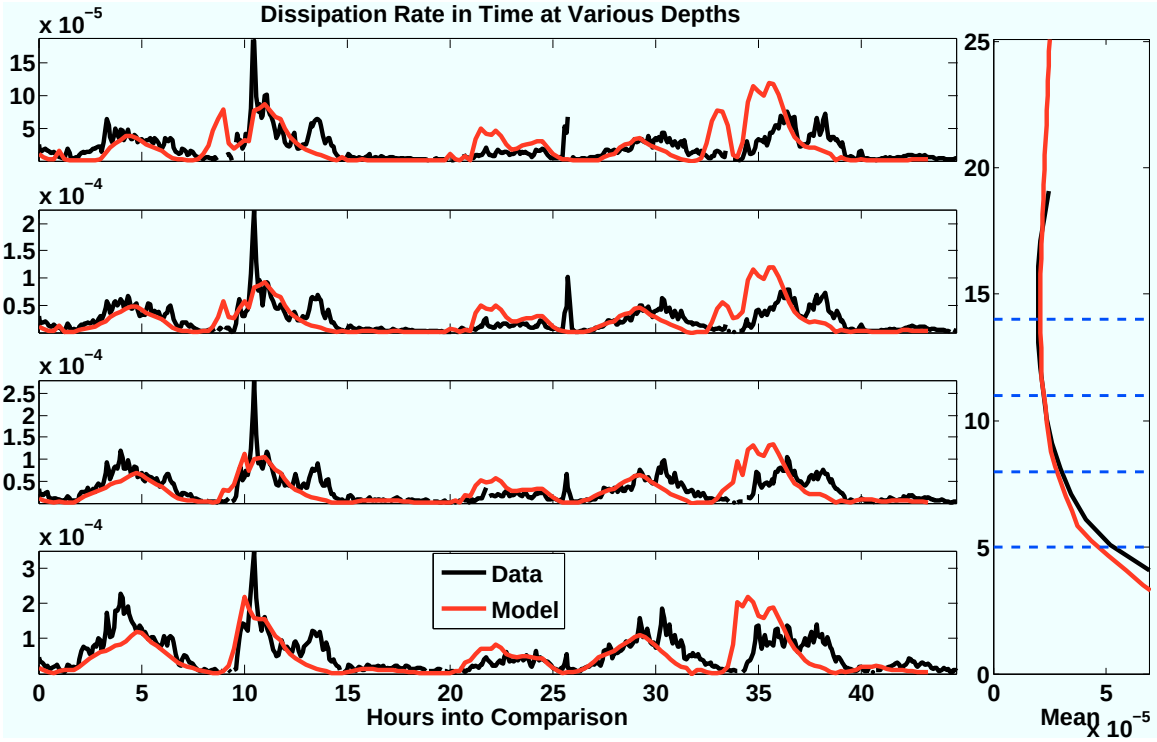


Figure 5.9: Turbulent dissipation rate comparisons between data (black) and model output (red) at Admiralty Head for the same time as Figure 5.8 but at multiple depths. The comparison depths are indicated, in order, as blue dashed lines on the time-mean profile of the turbulent dissipation rate profiles on the right side of the figure.

*Performance of Turbulence Model*

The relative behavior of the model predictions to the field data was examined in detail for Nodule Point in Section 5.2.1. The deficiencies seen in the model predictions for turbulence parameters were largely explained by the known speed deficiency as well as a difference in the frequency range of the modeled turbulence spectrum, which models classical turbulence, compared with the larger frequency range of the field data (see Section 5.2.1). Similar arguments are difficult to make in the model-data comparisons at Admiralty Head. The energy spectrum at Admiralty Head may behave differently than at Nodule Point (see Section 5.2.3), in such a way that the turbulence model is better able to represent the turbulent kinetic energy in the system. Additionally, the only data available at Admiralty Head are from Acoustic Wave and Current Profilers (AWACs), which are similar to ADCPs and have more noise than ADVs. Because of this, the data available at Admiralty Head is less reliable than the ADV data at Nodule Point. While it is still useful to compare the Admiralty Head data with model output, it is more difficult to explain nuanced behavior in the system based on the noisier AWAC data.

*Flow features*

The ebb tides shown in the data in Figure 5.8 at approximately hours 10 and 35 into the comparison both have double peaks in speed. While the first speed peak in each ebb tide data is seen in the model output, the second peak is not. In Section 4.2.3, persistent eddies and associated speed surges were discussed in detail. It was shown that eddies that persisted from flood tide into ebb tide were not as strong, and therefore not as noticeable, as those persisting from ebb tide into flood tide. However, the data shown here indicates that there can be a notable effect on the speed due to persistent vortices from flood tide lasting into ebb tide. While multiple speed peaks are not evident in the model speed at hub height, they are present higher in the water column, as shown in Figure 5.10. These peaks are also seen in the turbulent dissipation rate and turbulent kinetic energy in Figure 5.8. Section 4.2.5 showed that vorticity decreases with depth. The vorticity in the simulation is expected to be weaker than in reality due to a combination of smoothed bathymetry, lack of resolution,

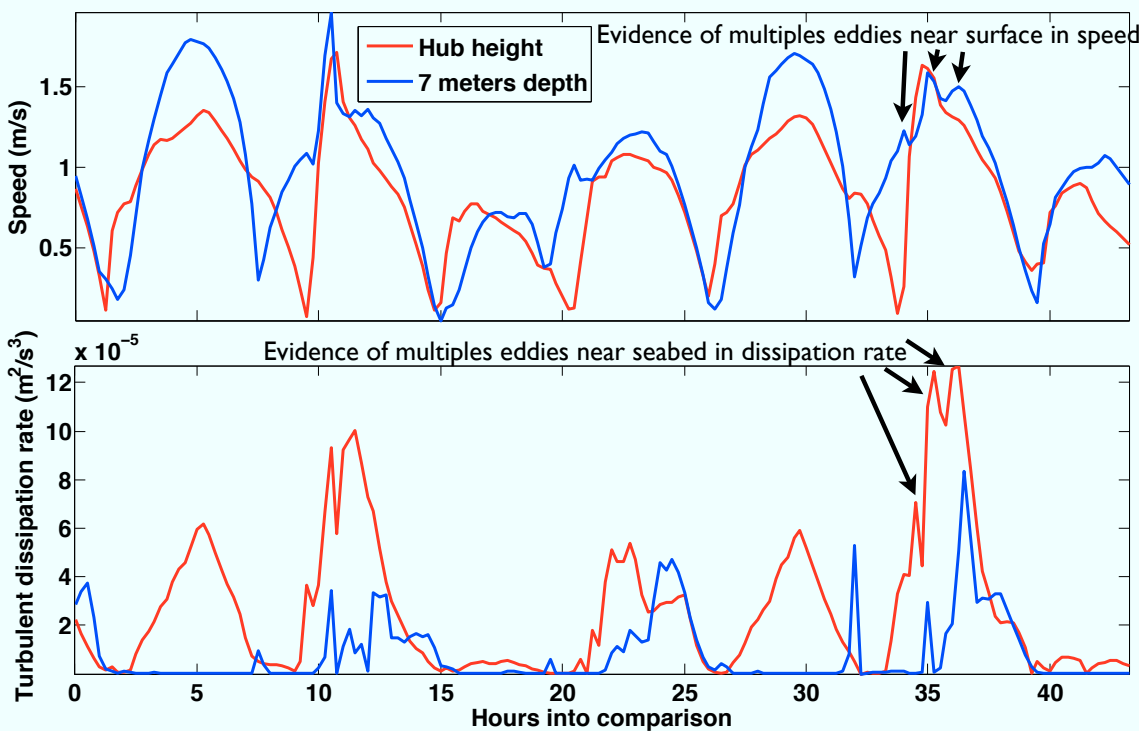


Figure 5.10: Model speed and turbulent dissipation rate at hub height and near the surface. The effect from multiple eddies are not seen in the model speed at hub height but are seen higher in the water column. The eddies are seen the turbulent dissipation rate signal throughout the water column.

and weaker overall horizontal speeds, leading to weaker vortex persistence. Thus, it may be that the vorticity is weaker overall in the simulation, or that it dissipates more quickly, as compared with reality, but evidence of the persistent vortices in the form of speed increases can still be seen near the surface. It is compelling that similar behavior is seen both in the model output and data.

### *5.2.3 Comparison of Turbulent Kinetic Energy at Nodule Point and Admiralty Head*

The turbulent kinetic energy comparisons are different between the data and model output at Nodule Point and Admiralty Head. At Admiralty Head, turbulent kinetic energy from

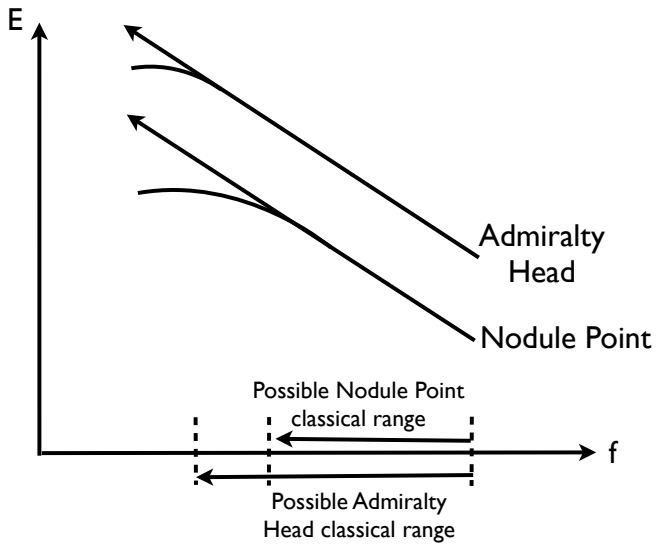


Figure 5.11: Cartoon with a possible explanation for the difference in comparisons at Nodule Point and Admiralty Head between data and model. It is possible that the turbulence at Admiralty Head behaves more as classical turbulence to a lower frequency than at Nodule Point, so that the turbulence closure scheme is able to capture more of the energy.

the model aligns with the data closer than at Nodule Point (at Admiralty Head the model to data horizontal turbulent kinetic energy ratio is, on average, 0.41, while at Nodule Point it is 0.25). This may be due to a difference in the energy spectrum behavior at each site. Referencing the only spectrum available, which is at Nodule Point and shown in Figure 5.2, the data has a classical range from about $0.2 < f < 2$ Hz. It was also found that the model output compared well with turbulent kinetic energy in the classical range. If this is true at Admiralty Head as well, then the fact that the data-model comparison is better may imply that the classical range at this site spans a broader frequency range (see Figure 5.11 for an illustration of this). The larger classical turbulence frequency range at Admiralty Head may be because it is a deeper site, allowing larger vertical scales (this is mentioned in Thomson et al. (2011)). The larger depth at Admiralty Head could extend the band of frequencies included in the classical range out further into larger scales, improving the comparison between the model and data accordingly.

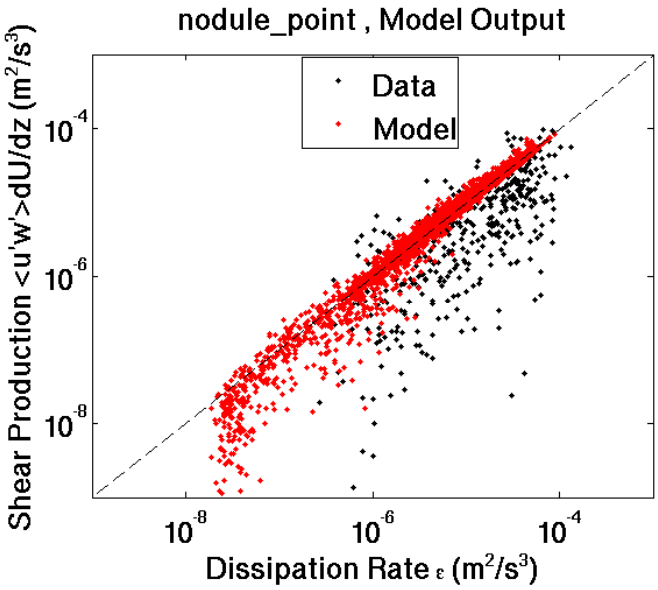


Figure 5.12: Hub height shear production compared with dissipation rate at Nodule Point

### *5.2.4 Comparison of Terms in the Governing Equation for Turbulent Kinetic Energy*

Figure 5.12 shows a one-to-one log-log plot of shear production versus the turbulent dissipation rate for the data and model output. The spread in the data is much larger than in the model output. This spread was interpreted in the data analysis as indicating important turbulent kinetic energy transport at the location due to eddies shedding from the headland (Thomson et al., 2011). While both data and model predictions line up somewhat along the one-to-one dotted line, the model output does not show the same scatter at larger values.

Buoyancy production is positive in unstable stratification and negative in stable stratified flows. In this simulation, the buoyancy production is almost always negative, which means that the mean density profile is almost always stable. When $P_B < 0$, the constant $c_{\varepsilon 3} = -1$, which is multiplied with $P_B$ in the governing equation for the turbulent dissipation rate (Equation 2.20), making the term positive overall. In the governing equation for the turbulent kinetic energy (Equation 2.19), $P_B$ has no multipliers and remains negative. In the case of stable stratified flows, then, $P_B$ is a sink for the turbulent kinetic energy and a source for the available potential energy. In other words, the effect of buoyancy in the

turbulence closure scheme is of the loss of kinetic energy to background mixing. In a stable flow, the buoyancy term is actually typically a destruction term, but it commonly referred to as a production term. Because the buoyancy production is negative, the absolute value has been taken in order to plot on a logarithmic axis.

Figure 5.13 shows the relative size of the shear production term and the buoyancy production term, two terms in the governing equation for the turbulent kinetic energy (Equation 2.19). Results from both Admiralty Head and Nodule Point are included. At both locations, the shear production dominates the buoyancy production, except at low values, where buoyancy production dominates. Buoyancy production may dominate when there is less energy in the system because when the speed is lower, the ratio of the buoyancy force to the inertial force is larger.

There is more spread in the comparison at Admiralty Head than at Nodule Point, perhaps indicative of the more active eddy field at Admiralty Head. Both sites show a further preference toward shear production nearer the seabed, moving closer to the one-to-one line away from the seabed. This indicates the bottom friction near the seabed generating more shear as well as increased likelihood of buoyancy effects higher in the water column.

The "tail" seen in Figures 5.12 and 5.13 indicates a minimum value in the turbulent dissipation rate and the buoyancy production, but not in the shear production. The limitation is imposed to limit mixing in stable stratification (Warner et al., 2005b).

## *5.3 Addressing the Turbulent Kinetic Energy Gap with An Extension of Kolmogorov Theory*

The turbulent kinetic energy from the data depends heavily on the averaging time period being used. The previous section showed that the model output and data for turbulent kinetic energy agree well when the frequency range used for calculating the turbulent kinetic energy in the data is limited to the classical turbulence range. From this it may be concluded that the model may be performing well in terms of classical turbulence, and this may well be the most important measure for tidal turbines (see a discussion on this at the end of the chapter). However, there are cases when it is important to find the total effective turbulent kinetic energy in the model as well, out to the smaller frequencies included in the data. One

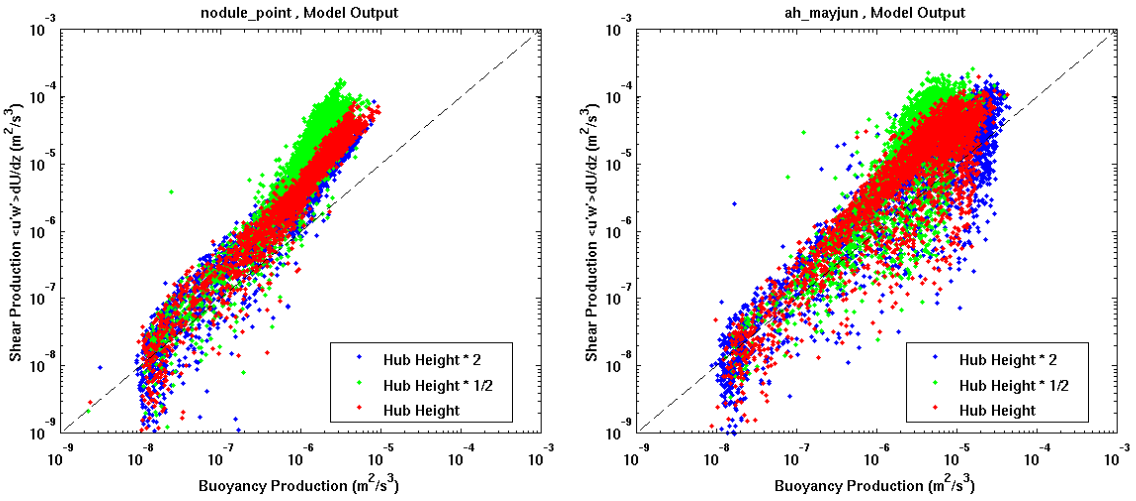


(a) Nodule Point

(b) Admiralty Head

Figure 5.13: Model shear production compared with buoyancy production at multiple depths. The absolute value of buoyancy production is shown because it is less than zero in this simulation.

such reason to find the total effective turbulent kinetic energy from model output could be for understanding and predicting pollutant dispersal. One approach is followed to address the gap in turbulent kinetic energy predicted by the model compared with that found in the data.

In this approach, two facts are used: that (i) the model dissipation rates and velocity fields compare reasonably well with the data, and (ii) the behavior of the data suggests an extension of the Kolmogorov spectrum to lower wave numbers than for classical turbulence. In this way, the turbulent kinetic energy is calculated from other, more reliable sources in order to find a better representative turbulent kinetic energy for the system.

### *5.3.1 Behavior of Data*

An overview of Kolmogorov's approach to turbulence was given in Section 5.1.2. He theorized that the spectral energy density is a function of only wave number and turbulent dissipation rate in the inertial subrange. As described previously, Taylor's frozen field ap-

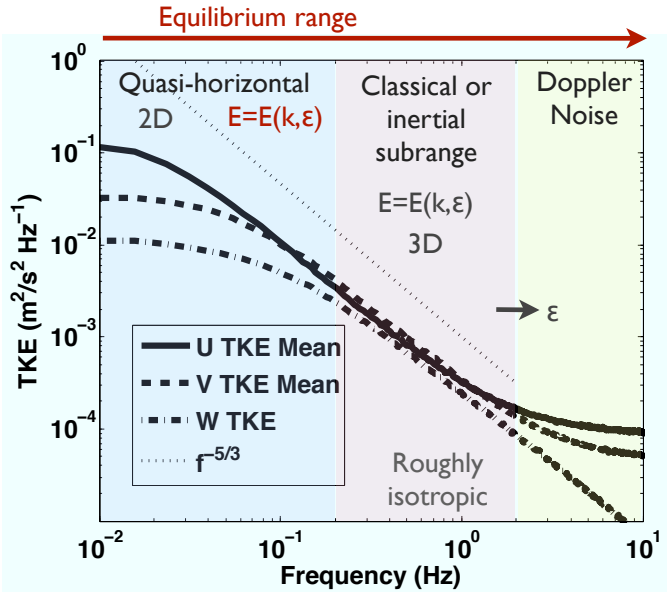


Figure 5.14: Mean horizontal turbulent kinetic energy density (solid) and vertical turbulent kinetic energy density (dashed) vs. frequency for data at Nodule Point at hub height of 4.7 meters. This plot shows an extension of the behavior shown in Figure 5.2. Data from Thomson et al. (2011).

proximation can be used to express Kolmogorov's result in terms of frequency. The data indicate that, for the principal horizontal component of the energy spectral density, this relationship extends beyond the classical subrange into the range of quasi-horizontal motion, extending the equilibrium subrange to lower frequencies. Therefore, we propose to extend Kolmogorov's law over a larger range of frequencies than used in his original theory. This approach is indicated in Figure 5.14, which has been updated from Figure 5.2 for this extension. The empirical behavior of the data is used to infer a relationship for the kinetic energy spectrum that captures a greater range of frequencies than intended in Kolmogorov's original theory. This approach will help to improve the comparison between the data and model output seen in the turbulent kinetic energy in Figure 5.3. Some support for this extension can be found for flows where the vertical velocity is suppressed by density stratification or the free surface (Chickadel et al., 2011), and is discussed further in Section

5.4.1. In our case, the vertical velocity is suppressed at horizontal scales of the order of, or greater than, the water depth.

### *5.3.2 Analysis*

The Kolmogorov theory predicts that

$$E = \alpha \varepsilon^{2/3} \kappa^{-5/3}, \tag{5.2}$$

where $E$ is the turbulent kinetic energy spectral density, $\alpha$ is a constant taken from literature and, from the data analysis, taken to be 0.5, $\varepsilon$ is the turbulent dissipation rate, and $\kappa$ is the horizontal wavenumber. Note that the value of $\alpha$ used is for the spectrum of the velocity which is transverse to the measurement direction. The viscosity is absent since the energy is postulated to be independent of the viscosity in the inertial subrange. Taylor's frozen field approximation, $L = u/f$, can be used to connect the length scale in $\kappa$ to the local mean horizontal speed and the frequency$f$ as

$$\kappa = \frac{2\pi}{L} = \frac{2\pi}{u/f} = \frac{2\pi f}{u}. \tag{5.3}$$

From Equation 5.3, a change of variables can be performed in the integral over frequency $f$. Integrating over the same range of frequencies as are included in the Nodule Point spectral data in order to find an expression for the turbulent kinetic energy gives

$$\begin{aligned}
\int_{\kappa_1}^{\infty} \alpha \varepsilon^{2/3} \kappa^{-5/3} \mathrm{d}\kappa &= \int_{f_1}^{\infty} \alpha \epsilon^{2/3} \left(\frac{2\pi f}{u}\right)^{-5/3} \frac{2\pi}{u} \mathrm{d}f \\
&= \int_{f_1}^{\infty} \alpha \varepsilon^{2/3} \left(\frac{2\pi}{u}\right)^{-2/3} f^{-5/3} \mathrm{d}f \\
&= \frac{\alpha}{(2\pi)^{2/3}} (\varepsilon u)^{2/3} \int_{f_1}^{\infty} f^{-5/3} \mathrm{d}f \\
&= \frac{\alpha}{(2\pi)^{2/3}} (\varepsilon u)^{2/3} \left[-\frac{3}{2} f^{-2/3}\right]_{f_1}^{\infty} \\
&= \frac{3}{2} \frac{\alpha}{(2\pi)^{2/3}} (\varepsilon u)^{2/3} f_1^{-2/3},
\end{aligned} \tag{5.4}$$

where $f_1 = 1/T_1$ is the lowest frequency included in the data analysis averaging time period, $T_1$. These spectra were calculated from the data using three 128-second sub-windows of the

five-minute turbulent averaging window, so $f_1 = 1/128$ s. Equation 5.4 gives an alternative expression for the turbulent kinetic energy, calculated as a function of turbulent dissipation rate and mean local horizontal speed. This will be referred to as the "inferred" turbulent kinetic energy.

Equation 5.4 gives an expression that approximates the energy contained in only the principal horizontal component of velocity. The principal component, $u'$, is the component which best follows an extension of Kolmogorov's theory to smaller frequencies (Figure 5.14). This expression could be compared with the turbulent kinetic energy data from the principal component only. However, in this analysis, the inferred turbulent kinetic energy is multiplied by the factor to account for the off-axis horizontal turbulent kinetic energy, a multiplier of 1.64 (see Section 5.1.3). In this way, the inferred signal accounts for both horizontal components and will be compared with both horizontal components in the data. The same could be done to account for the vertical turbulent kinetic energy, but is not shown here.

### *5.3.3 Adjusted Comparisons*

#### *Hub Height Turbulence Kinetic Energy*

Figure 5.15 shows turbulent kinetic energy comparisons at hub height at Nodule Point and Admiralty Head, including the turbulent kinetic energy from the ROMS model output, the data, the inferred turbulent kinetic energy, and the data computed over only the classical turbulence range. The inferred turbulent kinetic energy calculation improves the comparison significantly at Nodule Point and moderately at Admiralty Head, although in the latter case less improvement is needed. As discussed in Section 5.2.3, the comparisons between the model output and full data turbulent kinetic energy are better at Admiralty Head without modification, possibly because of a broader classical range at Admiralty Head relative to that at Nodule Point.

#### *Turbulent Kinetic Energy in Depth*

Comparisons for turbulent kinetic energy are given at multiple depths at Nodule Point in Figure 5.16. As before when showing dissipation rate with depth from the ADCP data, the

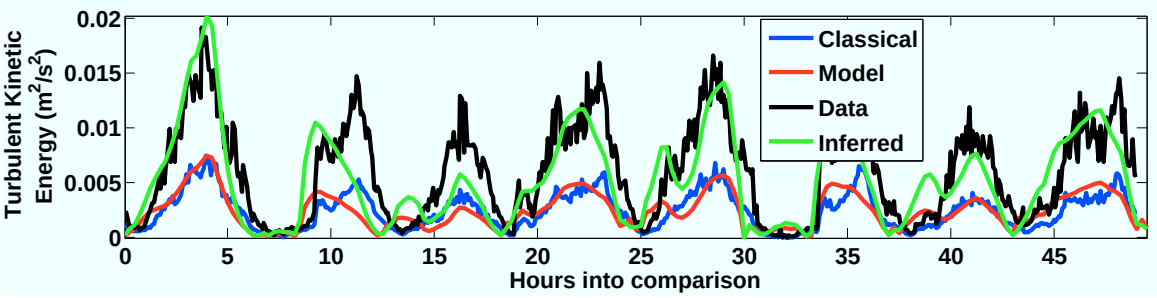


(a) Nodule Point

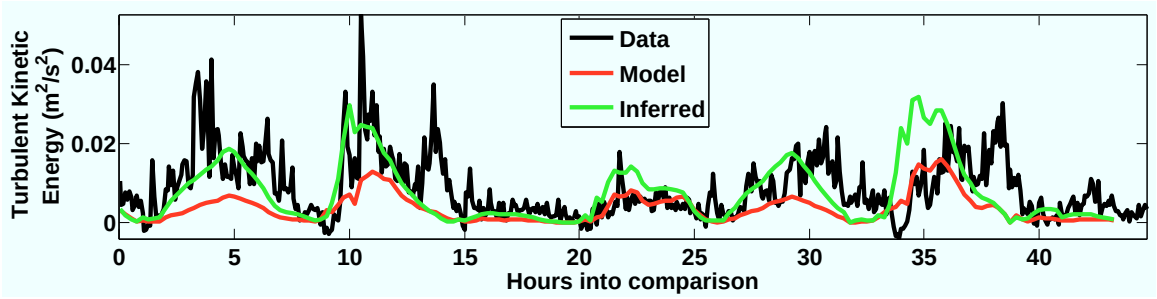


(b) Admiralty Head

Figure 5.15: Hub height time series comparison with inferred turbulent kinetic energy at Nodule Point and Admiralty Head. At Nodule Point, "classical" and "model" turbulent kinetic energy include vertical and horizontal components, and "inferred" and "data" turbulent kinetic energy include only $u$ and $v$ energy. At Admiralty Head, all turbulent kinetic energy signals include only horizontal components.

turbulent kinetic energy data from the ADCP are shifted by multiplying by a factor of the ratio of the average ADV hub height value to the nearest ADCP depth mean value. The inferred signal for turbulence kinetic energy matches very well with the data nearest the seabed and continues to improve the model output-data comparisons higher in the water column, but less so than nearer the seabed. This larger increase in the inferred signal closer to the seabed and lesser higher in the water column can be readily seen in the time-mean profiles of the ROMS model output, the inferred turbulent kinetic energy, and data on the right side of the plot. Given that the turbulent dissipation rate is largest nearest the seabed, it is expected that a calculation based on it would have this behavior.

Figure 5.17 shows a similar comparison at Admiralty Head. The second time series plot from the bottom is approximately at hub height. Though the Admiralty Head turbulent kinetic energy comparisons were already fairly good, the inferred turbulent kinetic energy matches the data better for most of the time series. The time-mean vertical profiles on the right side of the figure show great improvement over the turbulent kinetic energy from the ROMS model. The improvement is throughout the depths shown in the time series on the left. However, near the seabed, the inferred model prediction is much too large. This may be expected since the inferred model is a function of the turbulent dissipation rate, which is very large near the seabed. For the purpose of tidal turbine siting using this model, a mismatch in values very near the seabed is acceptable since potential hub heights are higher in the water column.

*Turbulence Intensity*

Turbulence intensity using the unadjusted model output turbulent kinetic energy is calculated as shown in Section 5.1.4. A slightly different expression should be used for the case when using the inferred turbulent kinetic energy, because it represents only the horizontal components of the turbulent kinetic energy. The turbulent kinetic energy field directly output from the model represents all three components. Therefore, the expression for turbulence intensity as calculated from the inferred expression for turbulent kinetic energy is

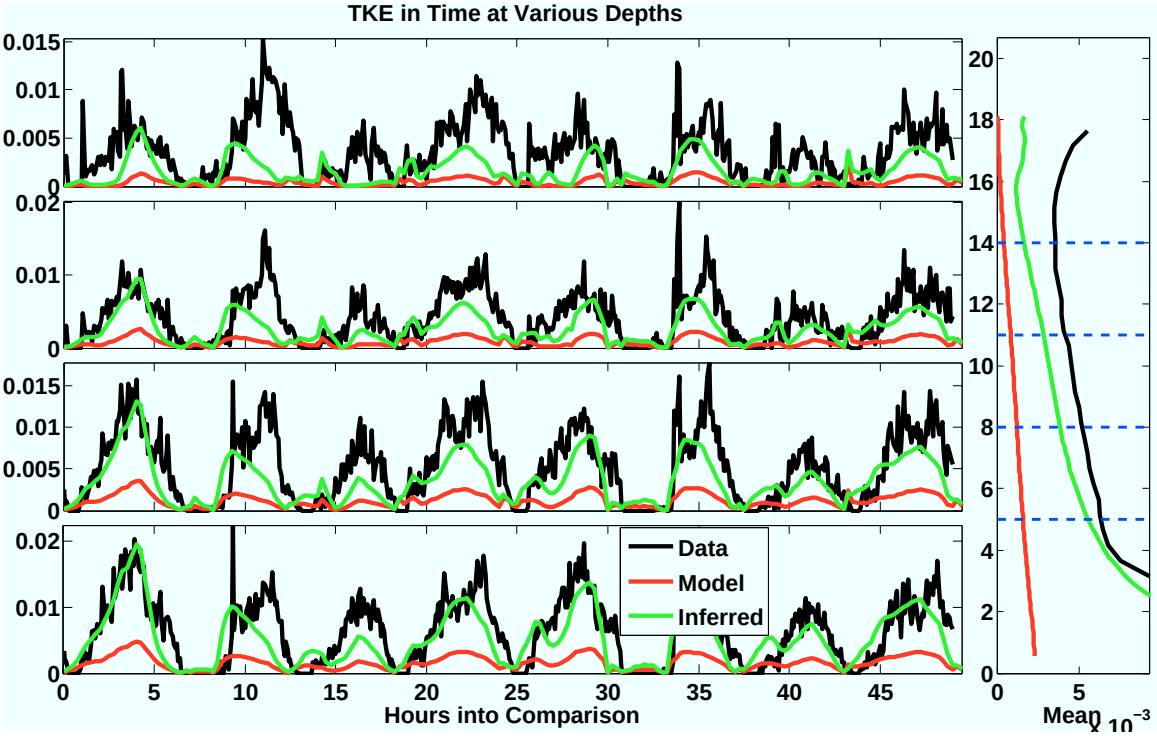


Figure 5.16: Turbulent kinetic energy comparisons between data (black), model output (red), and inferred model calculation (green) at Nodule Point for the same time as Figure 5.3, but at multiple depths. The comparison depths are indicated, in order, on the time-mean profile of the turbulent kinetic energy profiles on the right side of the figure as blue dashed lines. All turbulent kinetic energy curves include only horizontal components.

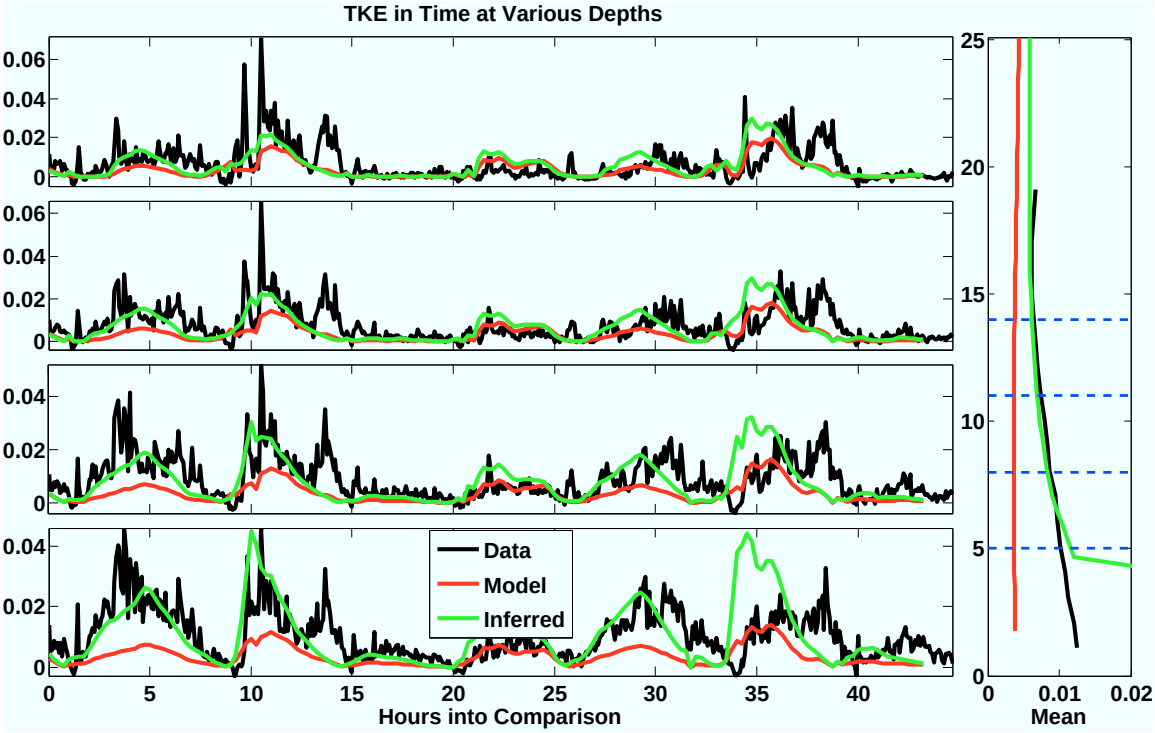


Figure 5.17: Turbulent kinetic energy comparisons between data (black), model output (red), and inferred model calculation (green) at Admiralty Head for the same time as Figure 5.3 but at multiple depths. The comparison depths are indicated, in order, on the time-mean profile of the turbulent kinetic energy profiles on the right side of the figure as blue dashed lines. All turbulent kinetic energy curves include only horizontal components.

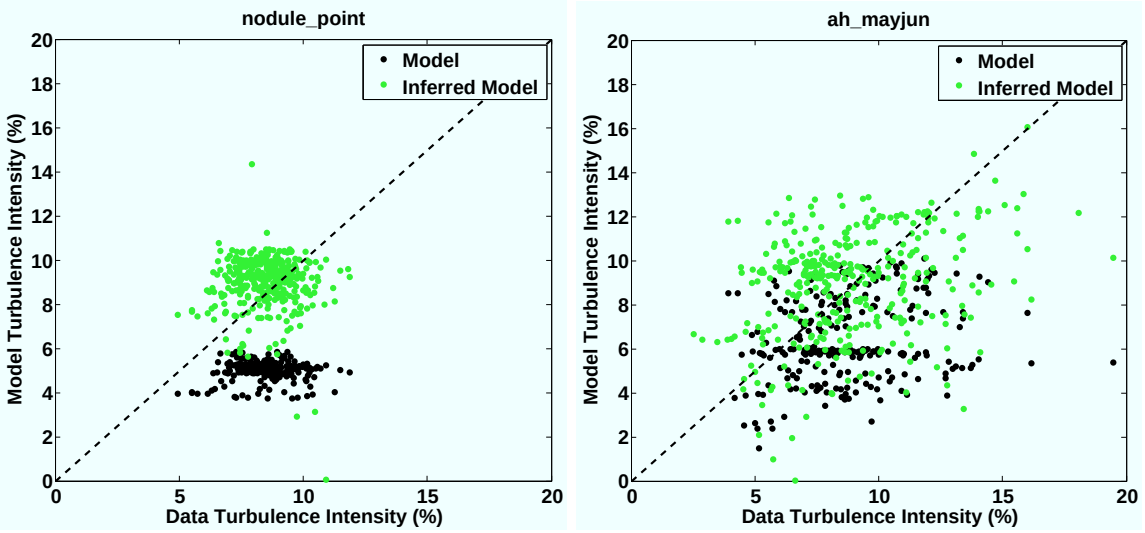


(a) Nodule Point

(b) Admiralty Head

Figure 5.18: Turbulence intensity comparison between ADV data, model output, and inferred model output at hub height of 4.7 meters at Nodule Point and Admiralty Head. The time period is the same as in all of the Nodule Point comparisons.

given by

$$I = u'/s = \sqrt{k_{inf}}/s,$$

where $k_{inf}$ is the inferred turbulent kinetic energy.

The turbulence intensity is shown for hub height at Nodule Point in Figure 5.18(a). Inferred model values compare well with the data, but the ROMS model output itself underestimates the turbulence intensity. Thus, the inferred model calculation gives an improved estimate of turbulence intensity.

Figure 5.18(b) shows the turbulence intensity for Admiralty Head. The spread in both data and model output is larger at this location than at Nodule Point, but the comparison is reasonable. The ROMS model output compares well with the field data, but the inferred model calculation compares better.

### *5.4 Summary and Discussion*

Model-data comparisons are shown here between output from a high resolution model of Admiralty Inlet employing a two-equation turbulence closure scheme and high-quality turbulence measurements at several locations within Admiralty Inlet. The comparisons emphasize the behavior at hub height in order to understand how well the model performs at the depth that pertains most to turbine siting. Comparisons for turbulent dissipation rate, Reynolds stress, and classical turbulent kinetic energy between the data and model output suggest that the model performs reasonably well. The turbulent dissipation rate and Reynolds stress from the model prediction are lower than the data values but within a factor of two. The deficiency in the model prediction can largely be explained by the known speed deficiency in the model. Given relatively accurate values for the classical-range turbulent kinetic energy and dissipation rate from the turbulence closure scheme, a significant amount of information can be gained. Other parameters can be solved for using these variables, including the turbulence time scale, $\tau = k/\varepsilon$, and the Kolmogorov time scale, $\tau_\eta = \sqrt{\nu/\varepsilon}$. Assuming a specific form for the kinetic energy spectrum consistent with the field data, *e.g.*, $\kappa^{-5/3}$, can enable even more information about the turbulence of the area being modeled to be inferred.

The model output compares well with the data for turbulent kinetic energy when the data are restricted to the classical turbulence range. However, the averaging period used in the data analysis includes a larger spectral range than is assumed in the turbulence model. The turbulent kinetic energy predicted by the model is lower than the full turbulent kinetic energy found in the data set. One approach to address the gap between the predicted turbulent kinetic energy and the data was to examine the effect of numerical truncation error on the energy equation. This magnitude of this effect was compared with the magnitude of the shear production and turbulent dissipation rate in the model. At both Nodule Point and Admiralty Head, the numerical dissipation tended to be much lower than the shear production and dissipation rate.

Another attempt to reduce this difference in model predictions and data for turbulent kinetic energy was to extend Kolmogorov's result to lower frequencies than the inertial

subrange, using an argument based on the spectral behavior of the field data. This extension was then used to estimate the turbulent kinetic energy in terms of the turbulent dissipation rate and mean velocity field, whose model predictions compared fairly well with the data. The model output-data comparisons were improved by this inferred calculation of turbulent kinetic energy, particularly at Nodule Point.

This latter method could be used to improve estimates of the turbulent kinetic energy in other similar situations as well as some other somewhat different situations, as several turbulence data sets from other types of problems show similar quasi-horizontal behavior at low wave numbers (see discussion in Section 5.4.1).

In the extension presented in this work, the energy spectrum and the frequency are assumed to be related by $f^{-5/3}$. However, there are other functions that could be used to approximate the extension of the inertial subrange. The data in the spectrum starts to roll off at the lowest frequencies (Figure 5.2 or 5.14), such that the $f^{-5/3}$ relationship is an overestimate at those frequencies. In another study, more sophisticated estimates of energy density data was found using Kaimal curves (Walter et al., 2011). These reproduced the roll-off at lower frequencies seen in the data, and were found to be more appropriate in locations that are limited by depth, as in Admiralty Inlet. It would be worthwhile to try a range of methods for capturing the spectral behavior of the energy as a function of frequency.

### *5.4.1 Behavior of Turbulence Spectrum*

The data examined in this chapter contained a regime of classical turbulence behavior, in the middle frequency range. The lower frequency region had quasi-horizontal behavior. In this lower frequency region, there are a few possible contributing factors to the behavior of the energy spectrum. It is clear that the vertical energy component is smaller than the horizontal components. This may be because of the small aspect ratio of the system at lower frequencies; the depth is shallow relative to the horizontal length scales. This in turn limits the vertical components to a smaller scale than the horizontal components, leading to the distinct differences in the size of the component energies seen in the data between

the components.

Quasi-horizontal behavior in the frequency spectrum has been seen in other cases. For example, in a shallow tidal river system at another location in the Puget Sound, the energy density spectrum has similar behavior as at Nodule Point (Chickadel et al., 2011). There is a region of roughly isotropic behavior, representing classical-type turbulence. At lower frequencies there is quasi-horizontal behavior, similar to Nodule Point, with the horizontal component energies two orders of magnitude larger than the vertical component energies, and the horizontal spectral energy density approximately following an $f^{-5/3}$ trend. In this situation, the vertical motions probably are suppressed by close proximity to the flat surface of the river.

From these situations and others, there is a growing body of literature indicating that when there is a factor limiting the vertical component of motion, there can be a region of quasi-horizontal behavior in the energy spectrum at frequencies lower than and including the classical range. The energy in this region may follow the $f^{-5/3}$ trend predicted by Kolmogorov's theory, when combined with Taylor's frozen field approximation, which indicates that the energy for the horizontal components is a function of only the turbulent dissipation rate, mean velocity, and frequency. Essentially, the horizontal components behave according to an extension of the inertial subrange to lower frequencies.

### *5.4.2 Application to Tidal Hydrokinetic Energy*

The turbulence property comparisons in this chapter give confidence that turbulence parameters being output from the numerical model are representative of real situations. For wind and tidal turbine siting, a commonly-used turbulence metric for assessing a site is turbulence intensity, described in Section 5.1.4. Turbulence intensity at hub height for Nodule Point (Figure 5.18(a)) and from Admiralty Head (Figure 5.18(b)) both compared well between the inferred model output and the data.

Table 5.1 summarizes the mean values in time of the turbulence intensity at each location, and gives further evidence that the inferred calculation for the turbulence intensity gives a good estimate of the measured values. Turbulence intensity maps throughout Admiralty

| | I, Data (%) | I, Model (%) | I, Inferred Model (%) |
|---|---|---|---|
| Nodule Point | 8.5 | 4.9 | 9.3 |
| Admiralty Head | 8.9 | 6.1 | 9.2 |

Table 5.1: Average turbulence intensity values for the comparison time periods from the data and the model output.

Inlet will be shown in Chapter 6.

Many measures of turbulence do not differentiate between the scales of the turbulence at a site, but rather average over a wide spectrum of scales. However, there is evidence that not all turbulent length scales have the same effect on a turbine. In one study, researchers found that increasing the turbulence intensity increased the load on a wind turbine, but they also found that decreasing the length scale increased the load (Thomsen and Sørensen, 1999). It is possible that it is actually the smaller, higher frequency motions that are most detrimental to a turbine, though presumably this would also depend on the specific turbine design characteristics. These are the scales in the classical range, and that appear to be most accurately captured by the turbulence closure model examined here. In this regard, it may be helpful to consider a turbine siting metric that includes energy from only smaller length scales/higher frequencies/larger wave numbers, as the most relevant measure for a turbine. One such metric, the fractional turbulence intensity, which gives the turbulence intensity as a function of length scale, has been suggested (Thomson et al., 2011)

# Chapter 6

# SITE CHARACTERIZATION METRICS

## *6.1 Introduction*

Site characterization metrics are used to evaluate how viable a potential tidal energy development site is for turbine placement. The metrics can be split into two general categories: those that quantify the resource available, *i.e.*, how strong the resource is, and those that qualify it, *i.e.*, how extractible the resource is. Mean kinetic power density and electrical power metrics are examples of quantification metrics (Polagye and Thomson, 2011). This type of metric provides an important primary examination of the site since a resource of which to take advantage is the primary requirement for generating electricity. Qualification metrics include measures such as the bi-directionality of the flow, which potentially can affect both the power that can be captured by a turbine in the location, and the lifetime of the turbine if affected by the increased stress of speed gradients across its face. Both power production rate and life of the turbine will affect the overall cost. The Admiralty Inlet simulation provides an opportunity to quantify the metrics throughout Admiralty Inlet.

In Section 6.2, some design characteristics of turbines will be explained. Next, Section 6.3 will define the metrics used and give motivation for their purpose. Section 6.4 compares metrics calculated from field data and from model output for assessment of model performance. Domain metric maps at hub height of the model output will be shown in Section 6.5. The last section will summarize the results, then demonstrate an approach for turbine siting based on design characteristics.

## *6.2 Turbine Design Considerations*

A few considerations that may go into tidal turbine designs can also help to motivate site characterization metrics. The larger the cross-sectional area of a turbine, the more power produced, but also the more capital cost. Some turbine designers consider a cross-sectional

area of at least 300 $m^2$ to be necessary for a tidal turbine to be economic (Fraenkel, 2009). For a single rotor turbine, this is about 20 meters in diameter, or for a dual rotor, as in the Marine Current Turbines design (Marine Current Turbines, 2010), this is two 14 meter diameter rotors. Considering that areas with good characteristics for turbine siting may be limited in spatial extent, the sizing of turbines is important to consider.

A horizontal-axis turbine utilizes currents that are incoming normal to its face. However, currents may approach at an angle at different times through the tidal cycle. Some turbine designs are static and are best placed in areas with largely bi-directional flow. Others are able to yaw with the currents and therefore can align themselves with the direction of the flow, though this design would be more complex than a fixed-axis turbine, possibly making it more susceptible to failure and causing it to cost more to build.

The choice of hub height depends on many factors. A pilot project run by the Public Utility District No. 1 of Snohomish County that is going into Admiralty Inlet will have fixed, horizontal axis turbines from Open Hydro placed at a hub height of 10 meters (Public Utility District No. 1 of Snohomish County, 2012). The optimum hub height depends on many factors, including resource location in the water column and capital costs of the turbine foundation. Higher speeds tend to be higher in the water column, but the higher the turbine is in the water column, the more it costs in materials (Kawase and Beba, 2010). For this chapter, a nominal hub height of ten meters above the seabed is used for all hub height plots.

A turbine has a few basic properties. The cut-in speed of a turbine is the speed below which there is too much friction for the turbine to rotate and above which power is produced. The rated speed of a turbine is the speed at which the power produced by a turbine reaches a plateau, so that any increase in speed above the rated speed does not produce additional power. The turbine also has an efficiency for producing power. For current magnitudes between the cut-in and the rated speed, the power density in the flow field that could be utilized by a generic turbine is given by

$$P = \frac{1}{2}\rho s^3 \eta,$$

where $\eta$ is the turbine efficiency. The cross-sectional area of the turbine has been neglected in

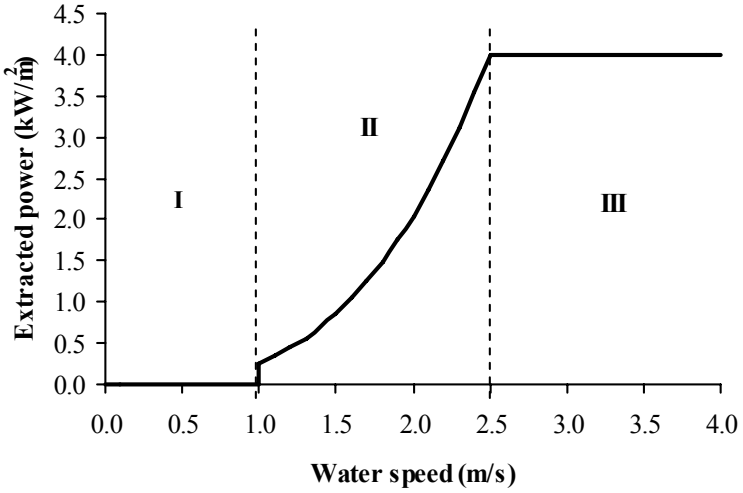


Figure 6.1: Illustration of turbine design properties. In this example, no power is produced below the cut-in speed of 1 m/s, and power production plateaus above the rated speed of 2.5 m/s. From Polagye (2009).

order to keep results general, but the power density can be multiplied by the cross-sectional area of a turbine face in order to calculate the producible power at a location. The turbine parameters chosen here are taken from a study on field data analysis for turbine siting in the same region (Polagye and Thomson, 2011). The efficiency is taken to be constant, as $\eta = 0.45$. This can be considered to be a combination of the performance coefficient of the rotor and the efficiency of the power train used in Polagye and Thomson (2011). In this analysis, the density is set equal to $\rho = 1.024\text{kg/m}^3$. Data sets do not typically include the density throughout the water column in time, and the variation in values seen is insignificant compared to this nominal value. The cut-in speed is taken as 0.7 m/s and the rated speed is taken as 2.25 m/s (giving a rated power of $2.6\text{kW/m}^2$) in order to attain an economically-viable capacity factor (Polagye and Thomson, 2011). An illustration of some of these properties is shown in Figure 6.1.

## 6.3 Metric Definitions

### 6.3.1 Resource Quantification

*Mean Speed and Kinetic Power Density*

The mean speed is the measure of the magnitude of the horizontal tidal currents over a time period. It is calculated as

$$s_M(x, y, z) = \frac{1}{T} \int_0^T s(x, y, z, t) \mathrm{d}t, \tag{6.1}$$

where $s = \sqrt{u^2 + v^2}$ is the magnitude of the horizontal velocity and $T$ is the time period. The averaging time period would ideally be chosen as an integer number of cycles, but given that a real tidal signal continuously modulates in time, such a cycle is not easily defined. A previous study of tidal current data found that averaging over 30 days of observations results in reasonable mean statistics (Polagye and Thomson, 2011). For the Admiralty Inlet simulation, a time period of 30 days is used. For the idealized headland simulation, an integer number of cycles (six are used) can be chosen because the simulation is forced by only the $M_2$ tide and so the flow field is approximately periodic.

While mean speed gives information about the tides themselves, the local kinetic power density, $D$, gives a measure of power resource at a location and reflects the difference that a small amount of speed change can make in available resource due to the cubic relationship between speed and power. It is calculated as

$$D(x, y, z, t) = \frac{1}{2} \rho s^3(x, y, z, t), \tag{6.2}$$

where $\rho$ is the fluid density and $s$ is the speed.

The primary requirement of a tidal hydrokinetic energy site is to have strong enough currents to produce a viable amount of power. This can be quantified by calculation of the mean kinetic power density. A mean kinetic power density of 1 kW/m$^2$ and higher is considered economically viable (Bedard et al., 2006).

*Mean Power*

The electrical power is the water-to-wire electricity production by a turbine when accounting for several turbine characteristics. The power density $P$ is calculated as the kinetic power density (Equation 6.2) times an efficiency. Below the cut-in speed, no power is produced and above the rated speed, power production remains constant. The power density can be found as

$$P(x,y,z,t) = \begin{cases} 0 & \text{if } s < s_{cut-in}, \\ \frac{1}{2}\rho s(x,y,z,t)^3\eta & \text{if } s_{cut-in} \leq s \leq s_{rated}, \\ \frac{1}{2}\rho s_{rated}^3\eta, & \text{if } s > s_{rated}, \end{cases} \tag{6.3}$$

where $s$ is the speed, $s_{cut-in}$ is the cut-in speed, $s_{rated}$ is the rated speed, and $\eta$ is the efficiency. To obtain the instantaneous power for a specific turbine of diameter $d$, multiply $P$ by the area of the turbine, $\pi d^2/4$. The mean electrical power density is the average of the instantaneous electrical power density over time. This calculation is more realistic than the mean kinetic power density because of the incorporation of a few of the realities of turbine energy production.

*Operation Timing*

The fraction of turbine operating time, $t_{op}$, is calculated using the cut-in speed as an indicator for the percent of time a turbine would operate. Time in which the speed at a location is greater than or equal to the cut-in speed contributes to the turbine operation time. This metric indicates how much of the time power would be produced by the turbine as well as how much of the time the area would be affected by the turbine's movement. One relevant example of the importance of this metric is that harassment of marine mammals and increase of environmental stressors by tidal turbines may be increased when the turbine is operating (Polagye and Thomson, 2011).

*Capacity Factor*

The capacity factor is defined as the averaged power produced divided by the rated power (the power generated assuming the incoming speed to the turbine is constant and equal to

the rated speed of the turbine). A capacity factor of 30% is considered to be economically viable for tidal turbines (Bedard et al., 2006).

### *6.3.2 Resource Qualification and Turbine Survivability*

Resource qualification includes metrics that may affect the extractability of the resource available, and turbine survivability metrics measure flow field qualities that may add undue stress on turbines, potentially causing early failure. These two areas of turbine siting metrics are closely related because many of the metrics in one category are also in the other. For example, directionality of the horizontal flows and shear can affect the cross-sectional resource seen by a turbine face. These metrics can each also add additional stresses on the turbines. Increased turbulence can both decrease the efficiency of a turbine and increase the stresses on it.

#### *Asymmetry of Flow*

The asymmetry of the tidal currents between ebb and flood tide can significantly affect the resource that a turbine rotor face will encounter and be able to utilize.

At a single $(x, y, z)$ location, the horizontal currents change in time in both magnitude and direction. For example, Figure 6.2 shows plots of the $u$ and $v$ velocities at an $(x, y, z)$ location plotted against one another. Each marker represents a separate measure of the horizontal velocity vector in time. Throughout multiple tidal cycles, a pattern is developed. In these examples, it is relatively clear that markers in the one general direction are flood tide and the other, ebb. However, depending mainly on layout of the coastline and bathymetry, both of which can severely alter the flow from a simple back-and-forth motion with the tide, the pattern can be anything from very spread out and circular, to falling along a line.

The asymmetry of flow can be characterized using several measures: bi-directionality; directional deviation, or the "spread" of directions on each flood and ebb; and the strength of speed and power generation on ebb versus flood tides. Each of these calculations relies on a method to separate one tidal direction from the other. The principal axis decomposition is used to accomplish this.

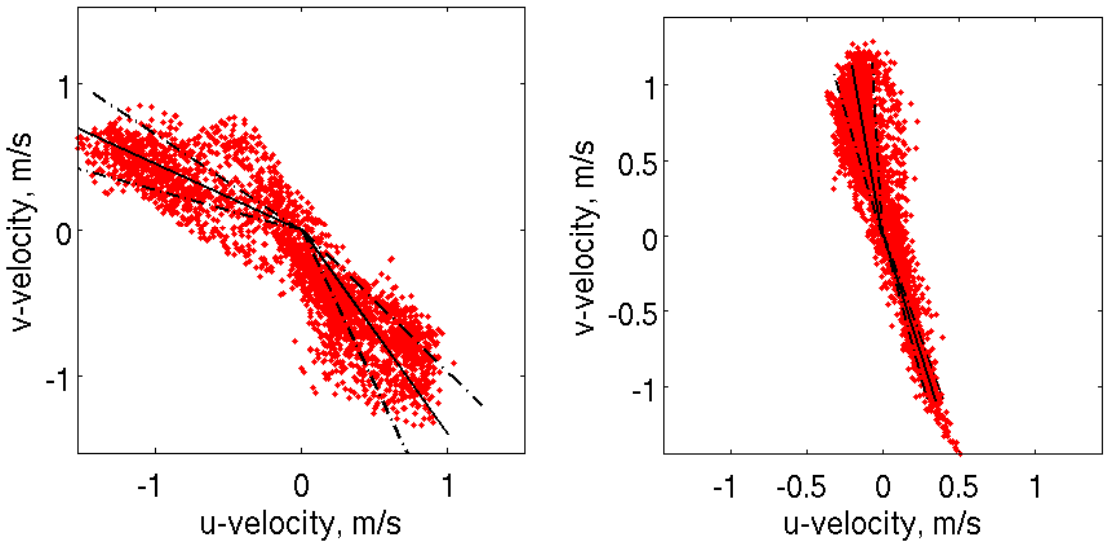


(a) Low bi-directionality, large directional deviation (b) High bidirectionally, small directional deviation

Figure 6.2: Tidal asymmetry example points from Admiralty Inlet simulation. Weighted mean angles are indicated in each tidal direction with a solid black line. Dashed black lines indicate the directional deviation of the angles, shown in each direction from the mean angle.

**Principal Axis Decomposition** The principal axis decomposition is an algorithm that identifies the direction of the main axis of flow that is described by the $u$- and $v$-velocities. Generally, this is in the along-channel direction of the flow, though in some cases large bathymetric and coastline features can significantly alter the flow direction. The rotation of the horizontal velocities onto the principal axis is used to differentiate between ebb and flood tide. The specifics of the algorithm are available in Boon (2004).

In this work, tidal currents are available everywhere in the domain, including areas that are difficult to decompose because of channel features. Therefore, for this analysis, currents are broken into separate half-cycles, but no attempt is made to distinguish flood from ebb tide and vice versa. In other words, the analysis splits the velocity vectors into two sets, and these sets can then be analyzed for the following asymmetry metrics; but rather than identifying one set as ebb and one as flood, velocity sets are just kept as separate half-cycles. This helps to avoid difficulties in eddy fields in which nearby locations can sometimes have flow directions that are 180° out of phase.

**Bi-directionality and Directional Deviation** A quantitative measure of the bi-directionality of tidal flow at an $(x, y, z)$ point can be calculated by finding the mean direction of flow on ebb and on flood tide, then finding the difference. In order to accomplish this, a principal axis decomposition is first used to categorize the flow at each point into separate tide directions. Next, the angle of each $(u, v)$ vector is found and weighted based on the magnitude cubed of the velocity vector (the functional relationship of power to speed). Then the mean of the ebb and flood angles, $\theta_{M,ebb}$ and $\theta_{M,flood}$, are calculated separately. Normalized weights for each $(u, v)$ pair are found as follows:

$$w_i = \frac{|s_i^3|}{\sum_{i=1}^{N} |s_i^3|}, \tag{6.4}$$

where $s_i$ is the horizontal speed for time $i$ and $N$ is the number of times over which the sum is made. The weighted average is then

$$\theta_M = \sum_{i=1}^{N} w_i \theta_i, \tag{6.5}$$

for ebb and flood tide separately, where $\theta_i$ is an angle representing the horizontal velocity vector for each time $i$. The bi-directionality parameter can then be calculated as:

$$a = |\theta_{M,ebb} - \theta_{M,flood} - 180^\circ|. \tag{6.6}$$

From this definition, if a flow is perfectly bidirectional, $a = 0$.

Closely linked to the bi-directionality parameter is the spread in direction of the horizontal currents, $\Theta$, called the directional deviation. After calculating the weighted mean angle for each $(x, y, z)$ point on ebb and flood, the standard deviation of that mean angle, $\theta_{std,ebb}$ and $\theta_{std,flood}$ is calculated, giving another measure of bi-directionality throughout a tidal cycle. This is also weighted:

$$\Theta = \sqrt{\sum_{i=1}^{N} w_i(\theta_i - \theta_M)^2}, \tag{6.7}$$

where the $w_i$ are given above, and there is a separate value for $\Theta$ for ebb and for flood tide. The maximum value of $\Theta$ between ebb and flood is used for the values of $\Theta$ at a given location.

This is not how these asymmetry parameters have been calculated in other research (Gooch et al., 2009; NNMREC, University of Washington, 2010; Polagye and Thomson, 2011). In other works, there have been no weighting factors, and currents below cut-in speed have been removed before analysis. This did not seem to be the best option in this research given that the simulation predicts the horizontal speeds throughout the domain, whether or not they are large. Preemptively discarding all values below a cut-in speed leaves the domain with much less information available. While these locations may not be best suited for tidal siting, combining these metrics with quantitative resource metrics will give a full picture of the flow fields. Regardless, by including a weighting on the angles based on the speed cubed, the relative importance of each velocity vector is maintained in the analysis such that more energetic measures are given more weight than less energetic points at a given location. More details of the effect of different weighting and cut-in speed choices for these calculations are available in Appendix B.1.

These two parameters, bi-directionality and directional deviation, are illustrated together in Figure 6.2. The mean angle on each tide is indicated by a solid line and the

standard (directional) deviation is shown relative to the mean angle in each direction. The first plot shows a location with a moderate spread in directionality as well as a "kink" in the pattern, the latter of which is probably due to a nearby coastline feature redirecting the flow. The second case is a more typical back and forth tidal flow that is largely unobstructed by other effects. The first case has a larger directional deviation and is less bidirectional than the other.

A fixed axis turbine would perform better in a bidirectional flow since it cannot align itself with the currents and is aligned just when placed on the seabed. However, ebb and flood tide are often not 180° out of phase with each other, mainly because of coastline features, in which case a turbine that can align itself with the flow may be more appropriate. Additionally, the flow may approach the turbine face perpendicularly, with low directional deviation, or may have components that are parallel to the face, which would be indicative of a higher directional deviation. This sort of flow may not be as effectively utilized even by a turbine that can yaw if the changes in direction are too rapid.

A horizontal tilting of the flow away from the direction perpendicular to the turbine face, as calculated in these asymmetry metrics, leads to a reduction in power due to reduced incoming normal velocity to the turbine. The velocity is reduced by $\cos\theta$, where $\theta$ is the angle off-axis of the flow, since that will give the projection of the velocity perpendicular to the rotor disc. That is, $s_{tilt} = s\cos\theta$. The relationship for power is $P = \frac{1}{2}\rho A s^3$, where $\rho$ is the density of the water, $A$ is the cross-sectional area of the turbine rotor, and $s$ is the horizontal speed that is perpendicular to the rotor face. Then power from horizontally tilted flow is given by

$$\begin{aligned} P_{tilt} &= \frac{1}{2}\rho A s_{tilt}^3 \\ &= \frac{1}{2}\rho A (s\cos\theta)^3 \\ &= \frac{1}{2}\rho A s^3 \cos^3\theta \\ &= P\cos^3\theta. \end{aligned}$$

Therefore, there is a geometric power reduction factor of $\cos^3\theta$ for incoming flows at an angle of $\theta$ from normal-flow to the turbine face.

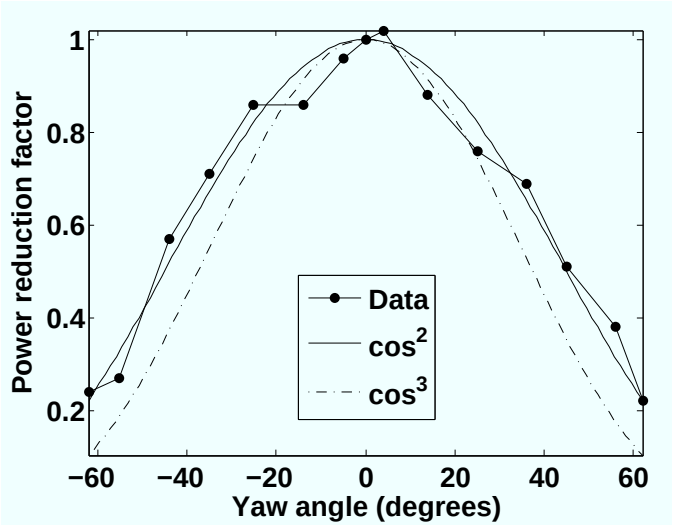


Figure 6.3: Power reduction factor due to yaw angle; adapted from Madsen (2000). The author has added in a $\cos^3\theta$ line for comparison and left out numerical results.

Experimental results for wind turbines show similar but not identical results (Madsen, 2000). Figure 6.3 shows reproduced experimental results with a line for $\cos^3\theta$ added for comparison. The authors of that study found the function $\cos^2\theta$ to describe the set of experimental data and simulation output. However, at smaller angles (up to nearly 20 degrees) the $\cos^3\theta$ line matches better, and has the advantage of being geometrically derived. It is possible that a smaller tilt angles, the effect on the power production is controlled primarily by the reduced normal component of horizontal speed, while some mitigating effect occurs at larger tilt angles. Regardless, the affect on power reduction of tilted horizontal flows is well-approximated by a factor between $\cos^2\theta$ and $\cos^3\theta$. Figure 6.3 and these relationships show that even a moderate tilting of 15° reduces power production to about 87% of full power, and a more extreme angle of 40° reduces power production to 59% of full power. Clearly this sort of power reduction cannot be ignored, particularly since it would be present through at least half the tidal cycles and not an atypical occurrence.

**Mean Speed and Power Generation Bias** Another measure of asymmetry of tidal direction is power generation on flood versus ebb tide. This is calculated by splitting the

horizontal velocities into separate tidal directions. Mean kinetic power density, $D_M$, is calculated, for each tidal direction, then a ratio is formed between the two as follows:

$$P_b(x,y,z) = 1 - \frac{\min(D_{M,ebb}, D_{M,flood})}{\max(D_{M,ebb}, D_{M,flood})}. \tag{6.8}$$

$P_b$ is a measure of the deviation from equal power production on flood and ebb tide. As $P_b$ approaches 0, power is produced evenly throughout the tidal cycle at that location. As $P_b$ approaches 1, the power production at that location becomes more biased toward either flood or ebb tide.

The same calculation can be made for speed bias through the tidal cycle, given as

$$s_b(x,y,z) = 1 - \frac{\min(s_{M,ebb}, s_{M,flood})}{\max(s_{M,ebb}, s_{M,flood})}. \tag{6.9}$$

These two metric calculations have been altered from their form in previous studies in order to give a linear parameter between 0 and 1. Additionally, distinction is not made between whether the location is biased toward ebb or flood, but instead gives the deviation from a resource that is balanced throughout tidal cycles. Because these two metric calculations have been altered from previous usage, more details in reasoning are given in Appendix B.2.

*Mean Vertical Velocity*

The mean vertical velocity is calculated using the magnitude of the vertical velocities, as

$$w_M(x,y,z) = \frac{1}{T}\int_0^T |w(x,y,z,t)|\mathrm{d}t. \tag{6.10}$$

Vertical velocities in a potential development area are significant due to their possibly impact on a turbine. One study about wind turbines described a site with a vertical velocity that was at times on the same order of magnitude as the horizontal velocity, which could induce dynamic stall effects on the blade (Hansen and Butterfield, 1993). If a potential development area for turbines frequently has vertical velocities, a turbine placed there should be designed accordingly to anticipate stresses from a different angle than the typical horizontal.

*Shear and Turbulence*

Vertical shear and turbulence both fatigue a turbine, but each has distinct behavior. Shear is a measure of the change in strength of the horizontal speed over the water column. An individual turbine blade that is rotating with the flow encounters changing forces in time due to the vertically varying strength of the flow, resulting in a periodic force in time (Figure 6.4).The forces on a turbine due to turbulence are stochastic in nature (Figure 6.5). A previous study about the failure of wind turbines modeled the loads on a turbine as a result of periodic and stochastic sources (Madsen and Frandsen, 1984). The authors found that the relative magnitude of the effects of the periodic and stochastic loads on turbine in an example case depended on the type of response. Flapwise blade bending moments were found to be equally due to periodic and stochastic sources whereas chordwise bending moments were due primarily to periodic forces, except at the highest wind speeds encountered, in which case the effect of turbulence accounted for nearly half the size of the moment. The turbulence was the major source of fluctuations caused in the response of the rotor thrust. Note that the example calculations were performed for a specific turbine design in which gravity was a major source of stresses to the blade, which enter into the periodic term, and the model environment was that of the actual examined data site. While the major source of periodic forcing in this example may be due to gravity, the differentiation made between periodic and stochastic loads holds as a distinction between the effect of shear and turbulence on a turbine.

The shear is calculated as the magnitude of the vertical shear in each horizontal component, or

$$s_z = \sqrt{\left(\frac{\partial u}{\partial z}\right)^2 + \left(\frac{\partial v}{\partial z}\right)^2}.$$

The shear in the incoming flow to a turbine should be accounted for when calculating the potential power available if an effective speed is used to approximate the flow over the turbine face, which is commonly done in wind energy (Martin, 2011).

Turbulence intensity is found from the model output as

$$I = \frac{\sqrt{k_{inf}}}{s} \cdot 100,$$

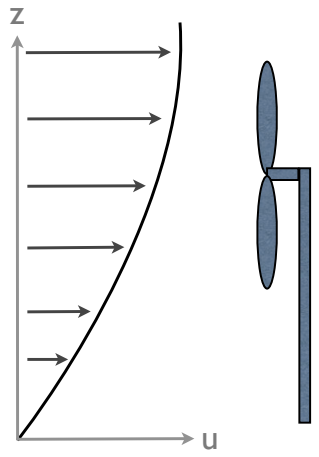


Figure 6.4: The blades of a horizontal-axis turbine in a flow field with vertical shear will encounter varying forces in time as the blades rotate.

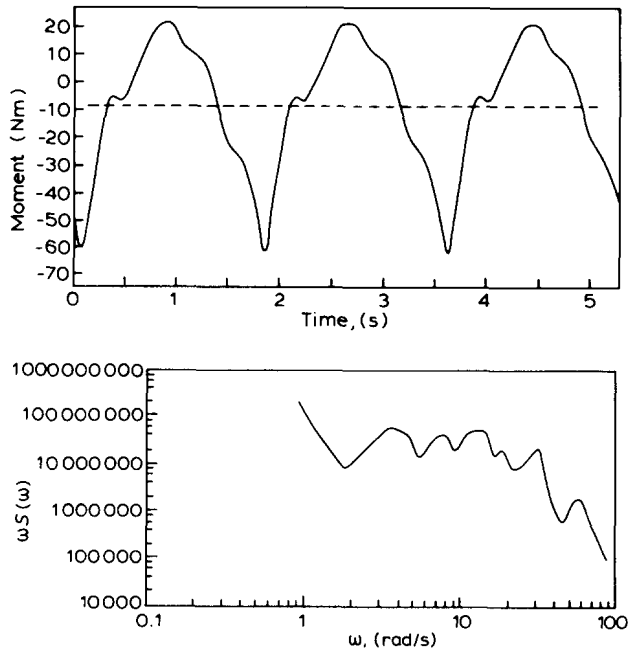


Figure 6.5: Periodic and stochastic loads on a wind turbine. From Madsen and Frandsen (1984)

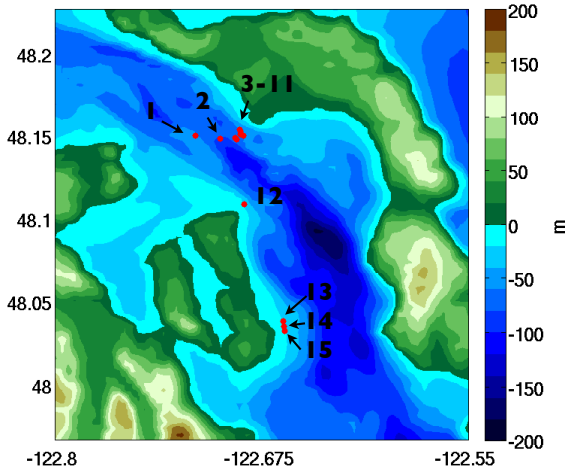


Figure 6.6: ADCP comparison points on topography/bathymetry map of domain, labelled in order from north to south in the domain.

where $k_{inf}$ is the inferred turbulent kinetic energy expression as found in Chapter 5 and $s$ is the horizontal speed.

The turbulence intensity measures the velocity fluctuations in the flow as normalized by the mean speed. Turbulence intensity has been found to correlate with both the fatiguing of turbine materials and decreased efficiency in wind (Frandsen, 2007; Madsen and Frandsen, 1984; Sheinman and Rosen, 1992; Thomsen and Sørensen, 1999; Wagner et al., 2010) and tidal (Maganga et al., 2010) turbines. Neglecting turbulence was found to result in an over-estimation of power production of up to 10% in Sheinman and Rosen (1992), but the decrease in efficiency changes with the level of turbulence intensity (Maganga et al., 2010).

## *6.4 Admiralty Inlet Simulation Metric Performance*

### *6.4.1 Quantitative Metrics*

A map of comparison points used to assess model performance in computing metric values is shown in Figure 6.6. These data were also used to assess model performance in Section 3.3.2. The comparisons for these metrics are shown in order in each set of plots below, moving south through the domain.

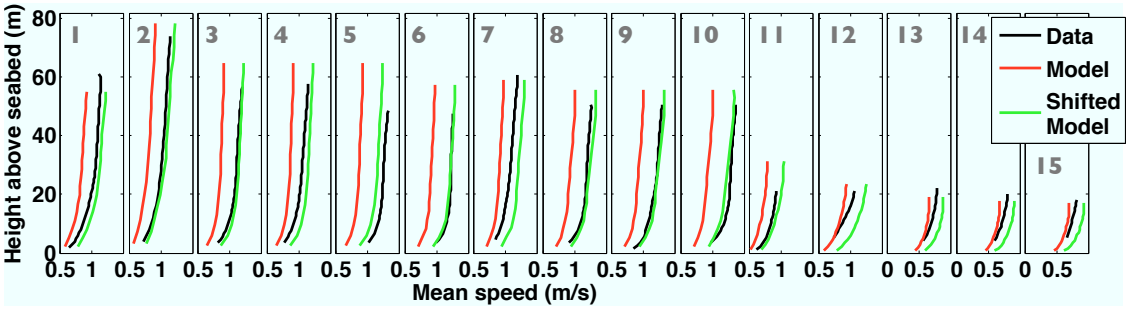


Figure 6.7: Mean speed profiles in order of comparison locations shown in Figure 6.6. Model output (red), data (black), and adjusted model output (green) are compared. The adjusted model output speeds are multiplied by a factor of 1.33, the ratio of the averaged model output mean speed to that of the data.

The mean speed profiles from the model output are, on average, 75% of the value of the data profiles, due to the known speed deficiency in the model, as discussed in Section 3.3.2. In order to roughly account for this, a multiplication factor, $F$, of the reciprocal, or 1.33, is used to shift the model output. Model output calculations involving speeds that have been multiplied by this factor are referred to as "adjusted" model output. The model-data comparisons of speed along with the adjusted model output are shown in Figure 6.7. The mean speed profiles are much improved by this adjustment at most of the locations shown. The comparisons around Marrowstone Island, though, are different than near Admiralty Head, and the mean speeds are too large after multiplying in the extra factor, as seen in subplots 12 through 15 in Figure 6.7. This over-compensation would be concerning in terms of understanding the dynamics themselves using this simple multiplication factor, but in this case the point is to have a reasonable representation of the resource in the system as it pertains to turbine siting. Given that the area of interest is primarily Admiralty Head and because the speeds are lower near Marrowstone Island, their relative importance is less.

The mean kinetic power density profiles, shown in Figure 6.8, display the model output as even lower relative to the data than in the speed. This is expected due to the cubic relationship of speed to power, which emphasizes the deficiency. To adjust the model, the

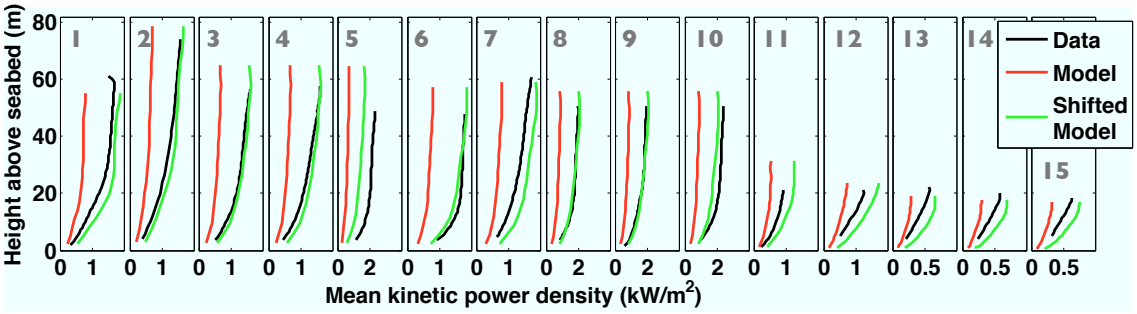


Figure 6.8: Mean kinetic power density profile comparisons. Details as in Figure 6.7.

same factor from the speed comparison is used to calculate the kinetic power density, as $D_{M,adj} = F^3 D_M$, where $D_{M,adj}$ is the adjusted mean kinetic power density and $F$ is the factor derived from the relative data and model speeds. These adjusted quantities are shown in the plots and match well with data near Admiralty Head.

Comparisons between the prediction of the model, adjusted model output, and field data are not shown for any following quantitative metrics. Speed and power density calculations from model output were shown to respond well to the adjustment factor. Given that the rest of the quantitative metrics are also based on the speed (and are similarly deficient for model output due to the known speed deficiency), similar results are found.

### *6.4.2 Qualitative Metrics*

Comparisons between model and data bi-directionality and directional deviation are shown in Figures 6.9 and 6.10, respectively. Both metrics agree well. The hub height comparisons, at nominally 10 meters above the seabed, are very good in directional deviation, though the comparisons deviate somewhat higher in the water column. The bi-directionality metric comparisons are reasonable, with most of the comparisons are within five degrees at hub height.

Speed and power bias comparisons are shown in Figures 6.11 and 6.12. They agree moderately well, and no alterations are made to the model output maps.

Mean shear profile comparisons are shown in Figure 6.13. The model shear matches the

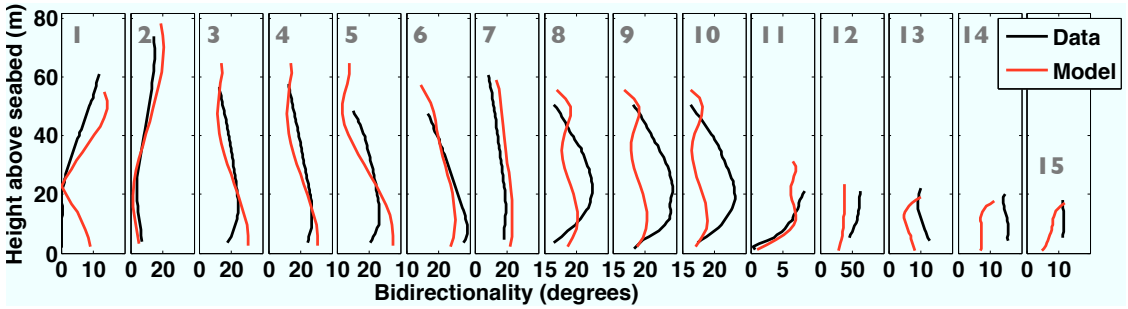


Figure 6.9: Bi-directionality profile comparisons. Comparison locations are shown in Figure 6.6.

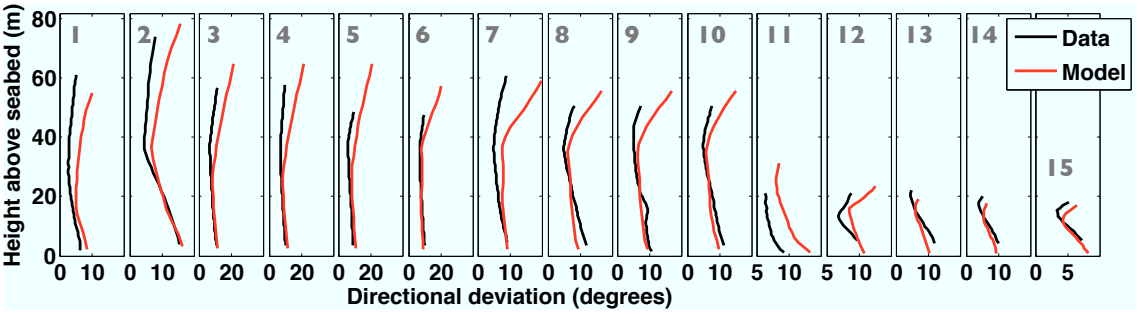


Figure 6.10: Directional deviation profile comparisons. Comparison locations are shown in Figure 6.6.

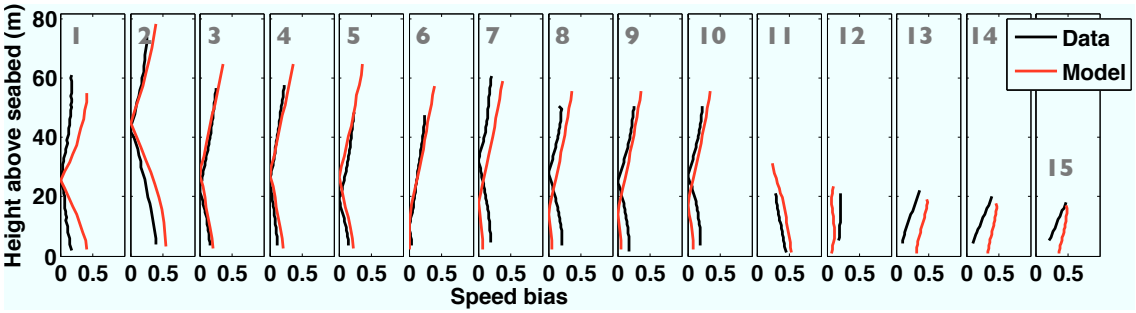


Figure 6.11: Speed bias profile comparisons. Comparison locations are shown in Figure 6.6.

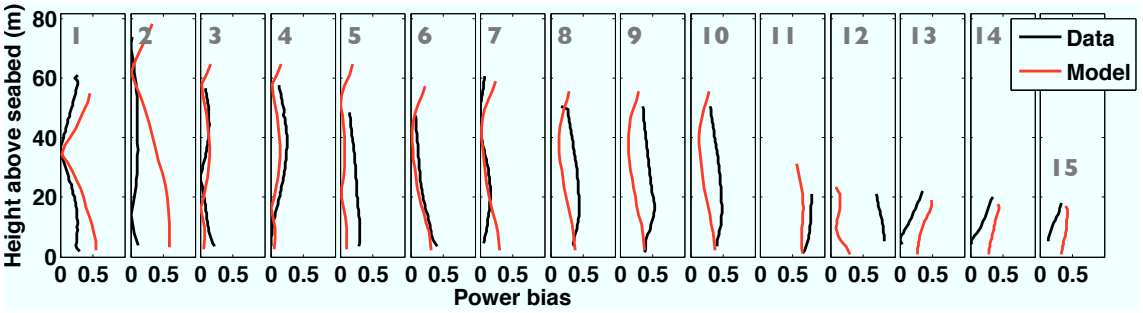


Figure 6.12: Power bias profile comparisons. Comparison locations are shown in Figure 6.6.

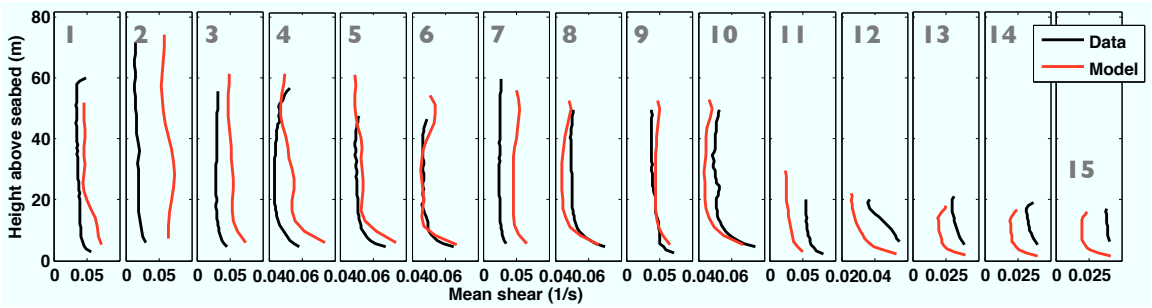


Figure 6.13: Mean shear profile comparisons. Comparison locations are shown in the order numbered in Figure 6.6.

data well except near Marrowstone Island.

## *6.5 Results and Discussion*

### *6.5.1 Resource Quantification*

The simulation of Admiralty Inlet provides an opportunity to evaluate a region for tidal turbine siting. In order to leverage the model output as much as possible, the quantitative metric results are adjusted to reflect the magnitude of the data. In doing this, we provide as realistic of values of the metrics as possible across the model domain.

All of the quantitative metrics are based on the magnitude of the speed. In an effort to make the most basic adjustment to the model output as possible, as well as address the

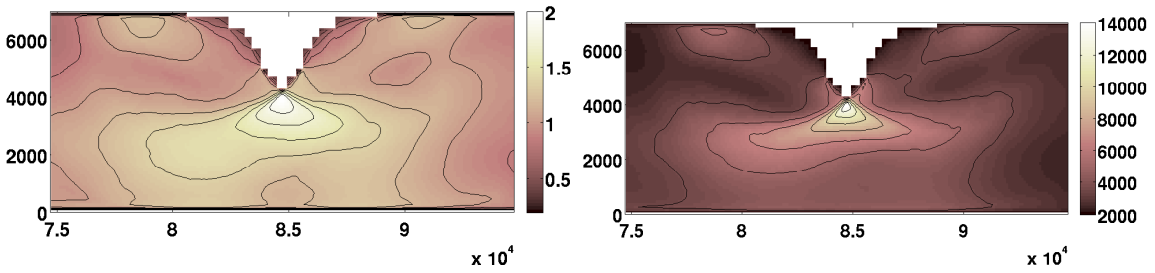


(a) Mean Speed (m/s)

(b) Mean Kinetic Power Density (W/m$^2$)

Figure 6.14: Mean speed and kinetic power density at hub height from the idealized headland model shown in both color and contours. $x$- and $y$-axis units are meters.

known deficiency in the model, a multiplication factor is used on the model's horizontal speeds (this is also discussed in Section 6.4). A single factor, as opposed to an adjustment factor for each metric, is used also in order to reduce any ambiguity in this adjustment. Additionally, the factor is generated as simply as possible. The ADCP data available are time- and depth-averaged together to find a single mean speed. Model output for the same locations as the data is also averaged in depth and over the length of the simulation to find a single mean speed. The factor used to shift the model predictions of speed is the ratio of the data mean speed to the model mean speed. This factor, $F$, is used to adjust each of the quantitative metrics. Note that $F$ is not used to alter model output as a function of time, but, rather, the already time-averaged model output. For example, the mean kinetic power density calculation from the model is multiplied by $F^3$ for the speed adjustment.

*Mean Speed and Kinetic Power Density*

Mean speed and mean kinetic power density plots are shown for the idealized headland case in Figure 6.14. The mean speed and, therefore, power are largest near the tip of the headland, a constricted area. The resource is also increased along the walls on each side of the headland, where large eddies that reach across the width of the channel lee of the headland cause increased speeds.

Maps of these metrics at the hub height of 10 meters for the domain are shown in Figure

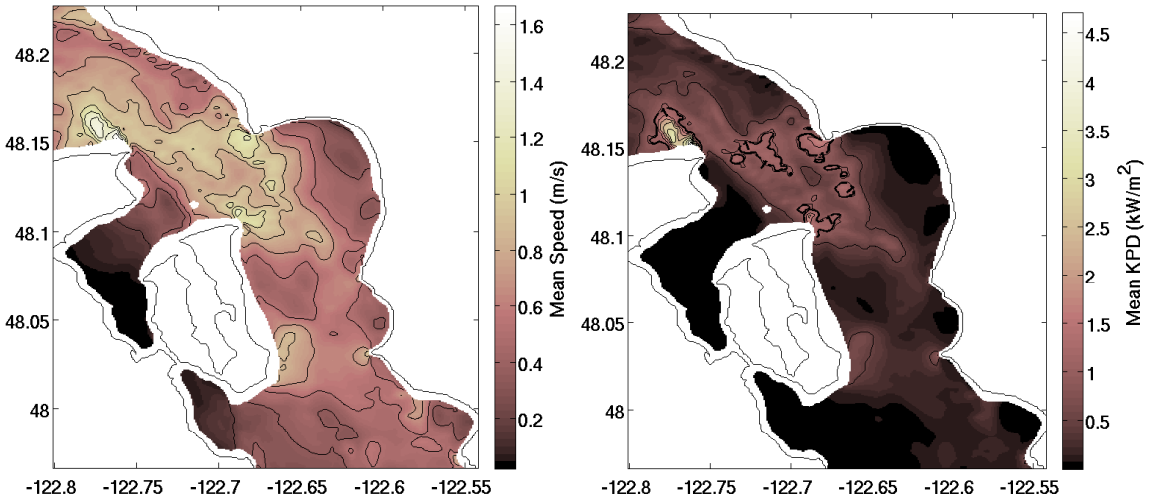


(a) Mean Speed

(b) Mean Kinetic Power Density

Figure 6.15: Mean speed and kinetic power density (KPD) at hub height from the model shown in both color and contours, with speeds multiplied by 1.33 to account for the known velocity deficiency. In the mean kinetic power density plot, a thick contour at 1 kW/m$^2$ indicates areas with the largest resource.

6.15. This model output has been adjusted as described with the factor to account for the known speed deficiency in the model. With this adjustment, the maps can be seen as an approximate tool for the assessing the resource at a nominal hub height throughout the domain. Some of the domain in the plots at hub height is empty since the free surface at these locations is shallower than hub height. For reference, a thicker contour marks the areas with mean kinetic power density greater than 1 kW/m$^2$.

As was seen in the idealized headland simulation, each promontory in the domain is associated with an area of increase in the mean speed, which is transformed into a tighter, sharper peak of mean kinetic power density. The headland case also shows some increased resource to the side of the headland. This is not found in the Admiralty Inlet case, possibly because of the changes in bathymetry in space, in which the shallower sides of the channel funnel the faster-moving flow away from the coastline. The peaks of resource near headland tips may be in the midst of eddy fields, which will be explored in Section 6.3.2. There are a

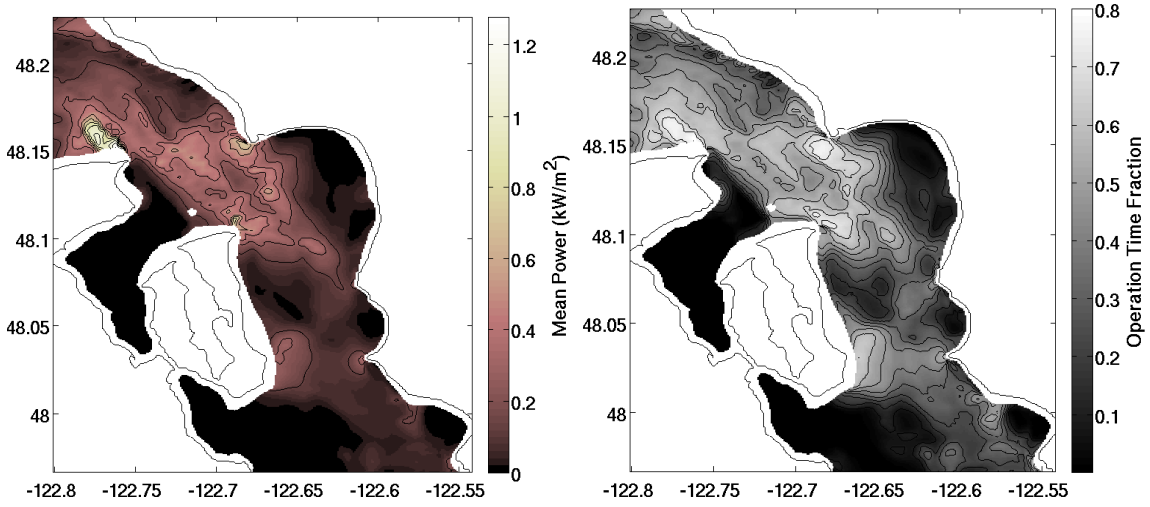


(a) Mean Power

(b) Turbine Operation Time Fraction

Figure 6.16: Mean power and turbine operation time fraction at hub height from the model with cut-in speed $s_c = 0.7$ m/s and rated speed $s_r = 2.25$ m/s, shown in both color and contours, adjusted by speed factor.

few other areas of large resource available, particularly in the middle of the channel between Point Wilson and Admiralty Head. This area is located over a sill, the most likely cause for the increase in speed.

*Mean Power and Operation Timing*

Mean power results from the model at hub height with the speed adjustment are shown in Figure 6.16(a). The plot shows the same pattern as the mean kinetic power density, but is a more realistic representation of the actual power accessible to a turbine.

Turbine operation time fractions are shown in Figure 6.16(b). Generally, a turbine would operate for more time at higher-speed locations, where power can be more readily produced. The locations in which a turbine would operate for the largest fraction of time are approximately the same as the locations with the largest amount of power available. However, if the speeds at a location are right around the chosen cut-in speed, adjusting the cut-in speed could significantly affect the turbine operation time.

*Capacity Factor*

The capacity factors throughout the domain at hub height are shown for three different rated speeds in Figure 6.17. When the capacity factor is calculated using a lower rated speed, as shown in Figure 6.17(a), the area just north of Point Wilson, which has the highest power density in Admiralty Inlet, has capacity factors of over 30%, which may be higher than economically viable. As the rated speed increases, the capacity factor north of Point Wilson decreases. Oppositely, in regions with lower power density, such as between Point Wilson and Admiralty Head, there is a desirable capacity factor of 30% with the lowest shown rated speed, but increasing the rated speed decreases the parameter to very low levels.

### *6.5.2 Resource Qualification and Turbine Survivability*

*Bi-directionality and Directional Deviation*

Figure 6.18 shows the bi-directionality metric $a$ for the idealized headland case. The flow is most asymmetric at the tip of the headland and to the sides. On each tide, the flow leaves the tip of the headland approximately parallel to the headland angle, such that near the headland tip, the flow is not bi-directional. Eddies lee of the headland also cause large asymmetry. Approximate directions are indicated in the plots with arrows for each tidal direction to help explain the size of the parameter around the domain.

The bi-directionality $a$ and directional deviation $\Theta$ parameters are shown in Figure 6.19 for model output at hub height; no adjustment has been made to the model output in these cases. Clearly the velocity fields are less bi-directional in areas near headlands where the eddy fields are most prominent, as was seen in the idealized headland case. However, the behavior around different headlands is quite variable. Around Admiralty Head and Point Wilson, there is less bi-directionality than in the middle of the channel, for example, but these areas are still much more bi-directional than around Marrowstone Island and in Admiralty Bay. North of Admiralty Head is an area that consistently has an active eddy field on ebb tide, but it has reasonably good bi-directionality and low directional deviation, whereas the area east of the northeast corner of Marrowstone Island is highly asymmetric

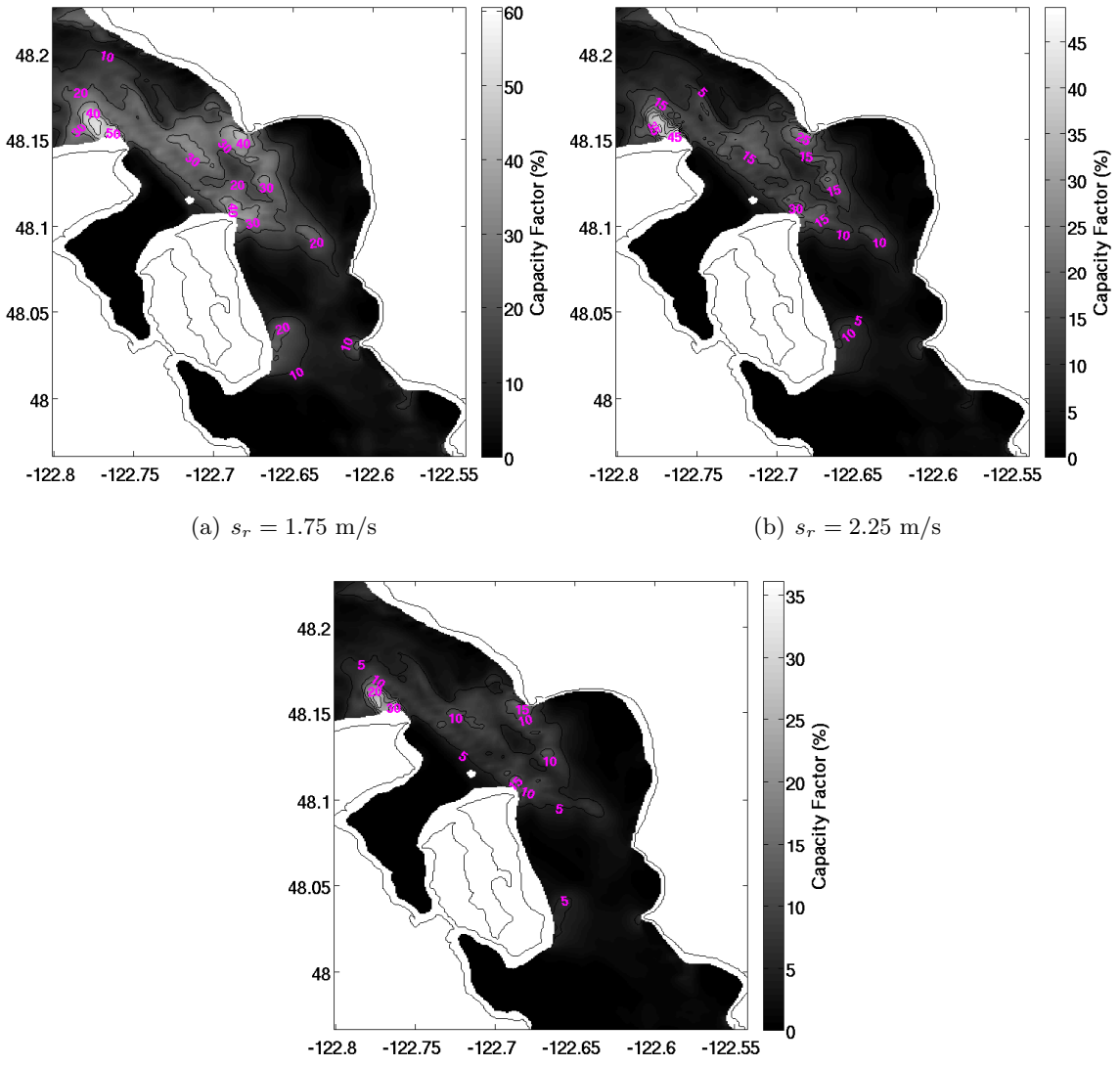


(a) $s_r = 1.75$ m/s

(b) $s_r = 2.25$ m/s

(c) $s_r = 2.75$ m/s

Figure 6.17: Capacity factor with varied rated speed at hub height from the model shown in both color and contours, adjusted by speed factor.

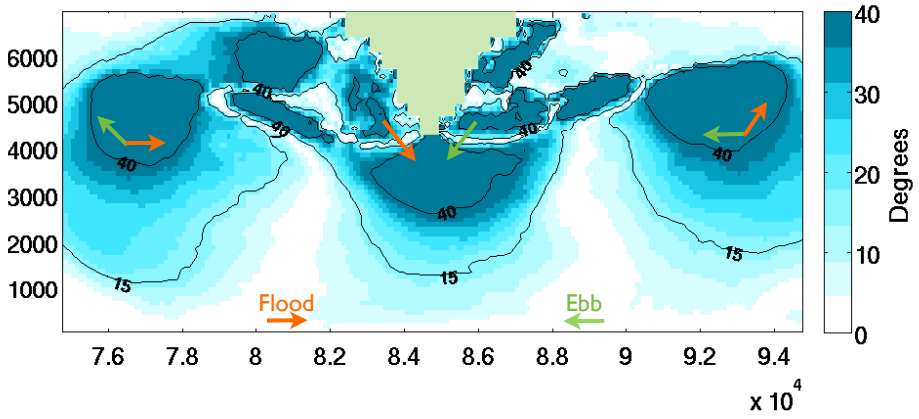


Figure 6.18: Mean bi-directionality at hub height from the idealized headland model shown in both color and contours. $x$- and $y$-axis units are meters. Arrows indicate approximate directionality at a few points on different tides: orange for flood and green for ebb. The headland is shown in white point south from the north side of the channel.

and increased directional deviation. Arrows on the plots show approximate directionality at several locations.

It appears that the vortices in and of themselves have a secondary impact on the directionality. This is particularly true with the calculation being weighted by cubic speed, since the recirculation in eddies in regions where there is significant change of direction often also has low speeds. This asymmetry depends most strongly on the channel geometry. North of Admiralty Head, for example, there is often a strong eddy on ebb tide. The strongest currents associated with the eddy are parallel to the channel: in the ebb direction in the main part of the channel and in the opposite direction nearer the coastline (Figure 6.20(a)). The eddy currents are approximately parallel to flood tide (Figure 6.20(b)), which leads to the flow in the area being highly bi-directional. While there are areas where the currents are turning in the eddy field, on the downstream side of an attached eddy, the speeds are relatively low and unimportant to power production considerations and thus do not significantly influence this metric. These areas may not matter significantly for turbine siting since they are low energy.

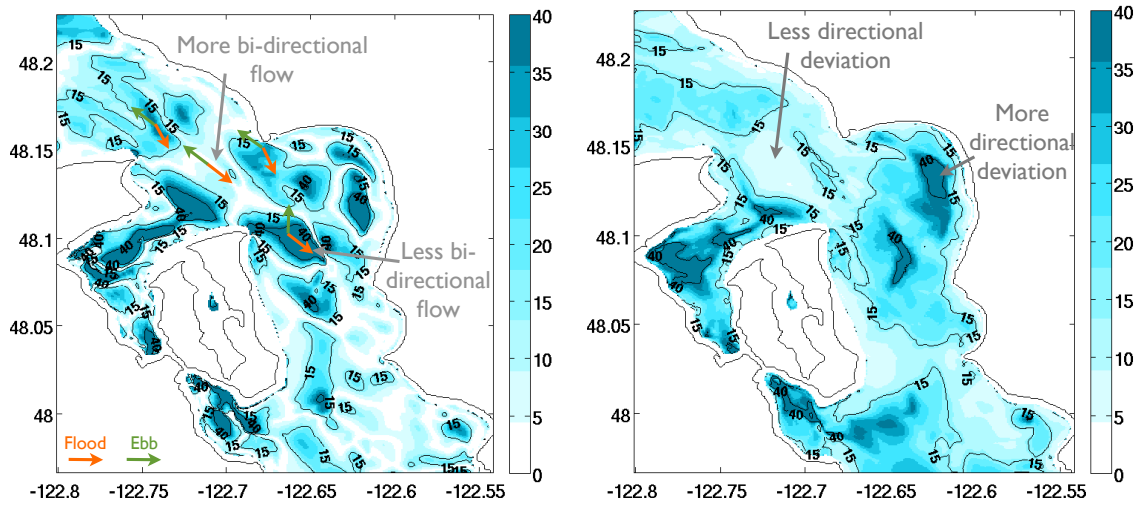


(a) Bi-directionality

(b) Directional Deviation

Figure 6.19: Asymmetry properties in degrees at hub height from the model shown in both color and contours. Arrows on bi-directionality plot indicate approximate directionality at a few points on different tides: orange for flood and green for ebb.

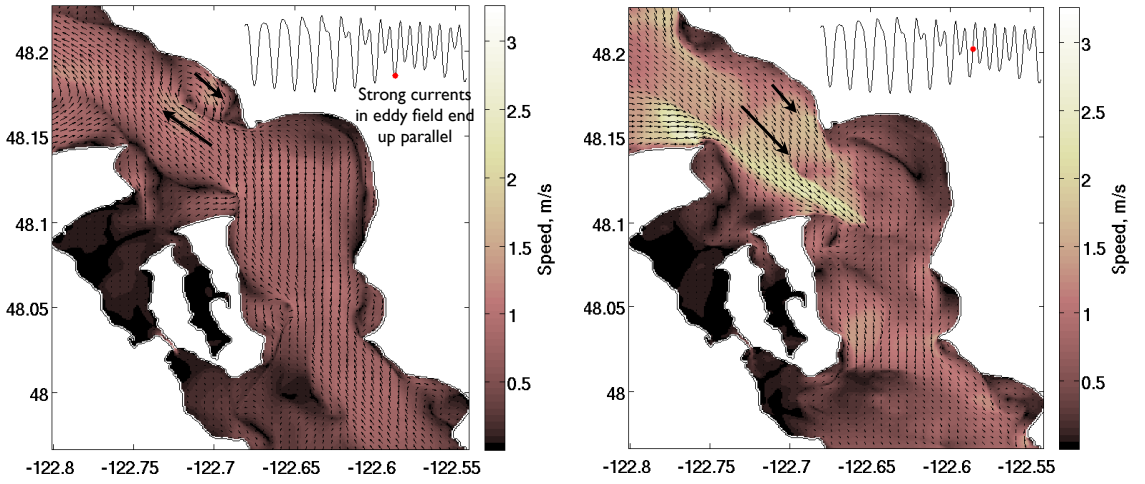


(a) End of flood tide.

(b) Flood tide.

Figure 6.20: Surface speed snapshots. In some eddy fields, the flow is not necessarily largely asymmetric if large eddy field currents are approximately parallel on flood and ebb tide.

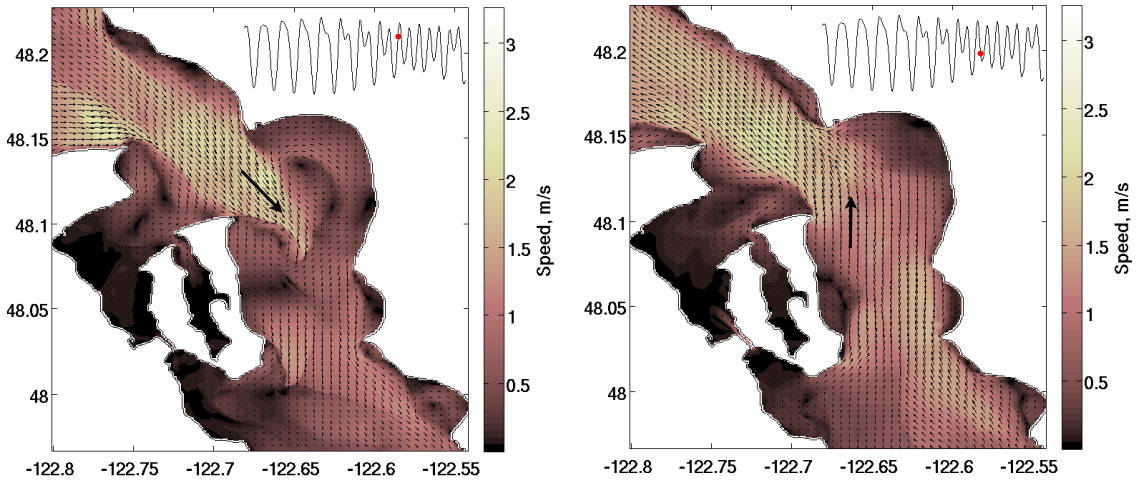


(a) Flood tide.

(b) Ebb tide.

Figure 6.21: Surface speed snapshots. A patch of highly asymmetric flow east of Marrowstone Island is largely caused by flow direction caused by the channel layout.

Opposite to this example are areas where the channel geometry causes the flow to be in significantly different directions on ebb and flood tide. One of the most noticeable patches of non-bi-directional flow is east of Marrowstone Island. This area is an active eddy field; however, a large part of the cause of the significantly non-bi-direcional angle is the fact that on flood tide, the channel pushes the flow to the southeast through the Inlet whereas on ebb tide in the same area it is pushed mainly north (Figure 6.21). The channel layout causes the most asymmetric areas, with bi-directionality of over 40 degrees. Eddy fields tend to cause the patches with values between 15 and 40 degrees. These areas of moderate values can be better understood using the in-depth analysis from Chapter 4. Given that the areas of highest resource are located near headland tips, the areas most affected by the eddy fields are potentially of the most importance for turbine siting, but it is important to understand the variety of values seen around the domain.

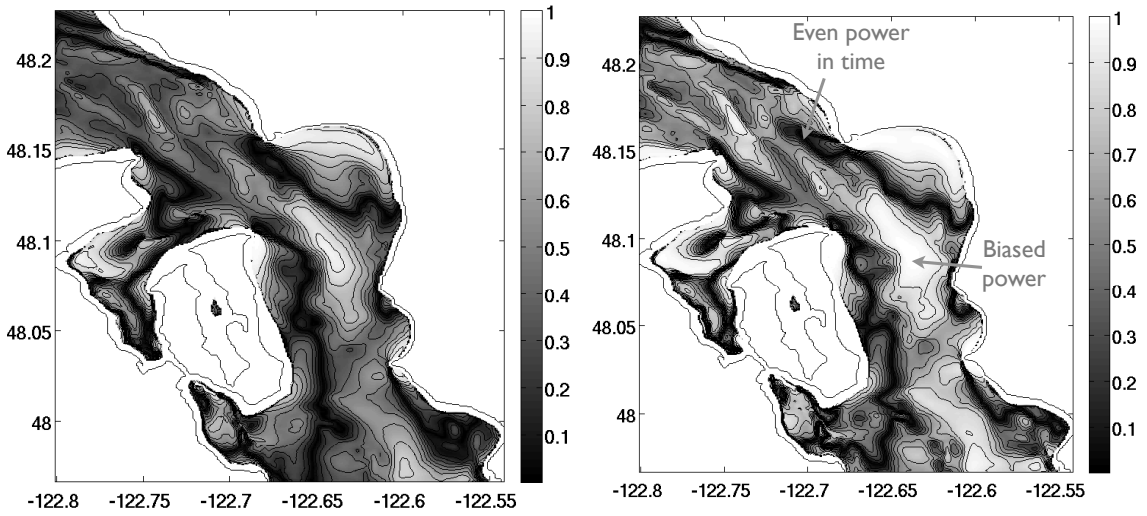


(a) Speed

(b) Power

Figure 6.22: Bias properties at hub height from the model shown in both color and contours. Lower values show areas with the most consistent property through tidal cycles and values closer to one are biased toward one flow direction.

*Mean Speed and Power Generation Bias*

Model output maps for bias comparisons are shown in Figure 6.22. The two maps are similar to each other, and they show that the areas with the most consistent power availability throughout the tidal cycle are near the tips of headlands, where there is an increase of tidal currents on each direction. Among the least consistent power areas is the north end of Admiralty Bay. In this area, currents are slow for most of flood and ebb tide, but are briefly stronger at the beginning of ebb tide as the recirculation area for the large Admiralty Bay eddy speeds up and pushes past Admiralty Head to start the tide.

### *6.5.3 Mean Vertical Velocity*

The vertical velocities in this hydrostatic simulation are not expected to be necessarily representative of the actual values of vertical velocities seen in Admiralty Inlet. Comparisons indicate that the difference between the data and model, particularly in highly dynamic

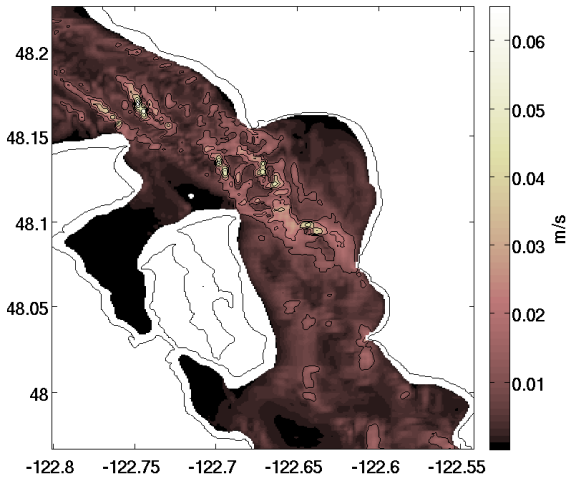


Figure 6.23: Mean vertical velocity at hub height

areas, may be as much as an order of magnitude (Section 3.3.2). However, the model does provide a means by which to see what areas may have significant vertical velocities and why. For example, a negative vertical velocity was found to be a common feature associated with convergence in the region and particularly near fronts in Chapter 3. Because of this, large vertical velocities may be found in areas of significance for turbine siting.

Despite the question of the realism of the absolute values of the vertical velocity output by the simulation, the location of the velocities in time and space may be important information for future development. The mean magnitude of vertical velocity is shown in Figure 6.23. The largest mean velocities are not near the coastlines but more toward the centers of the channels in the region. The largest values are in relatively small patches, and medium values are in much larger areas.

A method for splitting the vertical velocity into upsloping, or topographically-caused, and upwelling velocities was described in Section 4.2.6. Plots of mean and maximum/minimum vertical velocity split into upwelling and upsloping categories are shown in Section A.2.3. Those plots indicate that the largest values of mean vertical velocity are due to upsloping velocity in areas of steep bathymetry. This is in contrast with what was discussed in Section 4.2.6, in which upwelling velocities were larger than upsloping. In that case, the larger

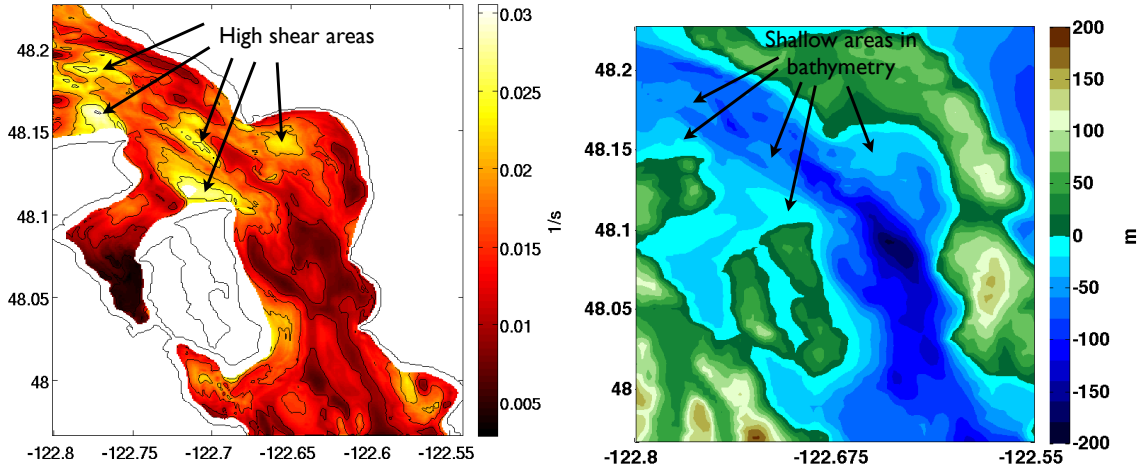


(a) Mean Shear

(b) Domain Bathymetry and Topography

Figure 6.24: Mean model shear at hub height compared with bathymetry from the model shown in both color and contours

upwelling velocities were higher in the water column, but nearer the seabed, as in these plots, the upsloping velocity is larger.

### *6.5.4 Shear and Turbulence*

The mean shear as output from the model at hub height is shown in Figure 6.24, along with the domain bathymetry. The highest mean shear areas correspond to areas where the bathymetry changes from deeper to shallower in the flow direction, drastically changing the speed profiles if the bathymetry gradient is steep enough.

In Chapter 5, turbulence intensity was found to compare well with data when using the inferred values for the turbulent kinetic energy. Turbulent kinetic energy was also compared in Chapter 5. Model turbulent kinetic energy was found to compare well with the classical turbulence data. This scale of turbulence has been found to be an important factor to consider for turbine siting due to a study finding that decreased turbulence length scales correlated with increased turbine load (Thomsen and Sørensen, 1999). Because of this, the mean turbulent kinetic energy from the model can be used to represent the energy contained

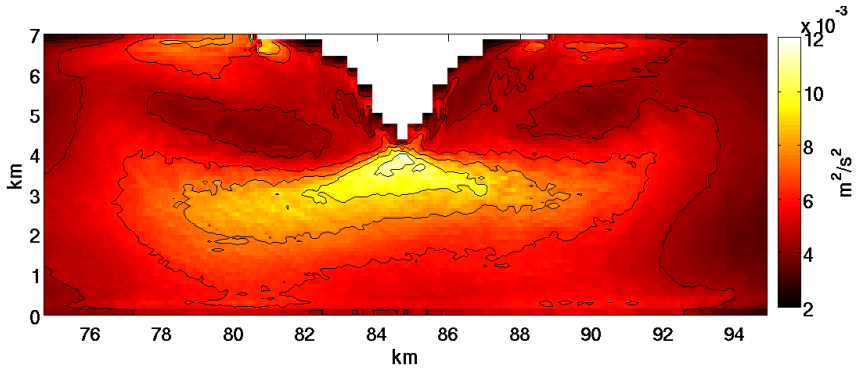


Figure 6.25: Mean turbulent kinetic energy at hub height from the idealized headland model shown in both color and contours.

in the mean small-scale turbulence in the domain. The turbulent dissipation rate was found to compare well between the model and data, often off by a factor of two; however the direct application to turbine siting is not as clear with the turbulent dissipation rate as with turbulence intensity and turbulent kinetic energy.

The mean turbulent kinetic energy for the idealized headland case is shown in Figure 6.25. The highest levels of turbulence are in the areas with the largest mean speeds (Figure 6.14) near the tip of the headland and to the sides. The area near the headland tip therefore has both the largest resource available and the highest levels of turbulence, on average.

Turbulence properties turbulent kinetic energy, $k$, and turbulent dissipation rate, $\varepsilon$, for the model simulations are shown in Figure 6.26. A comparison between these metrics and the turbulence intensity (Figure 6.27(a)) shows they each have different emphasis. The mean turbulent kinetic energy and turbulence dissipation rate are highest near the most energetic headlands where there are also often strong currents. This was also seen in the idealized headland case (Figure 6.25). An additional area of high $k$ and $\varepsilon$ is toward the southern end of the flood tide jet (Figure 4.3(b)) that is accompanied by eddies on either side and has complicated dynamics. On the other hand, the turbulence intensity is a relative measure and headland tips do not necessarily have large values since, while they have more turbulence, they also have higher speeds. The areas of largest turbulence intensity are locations that

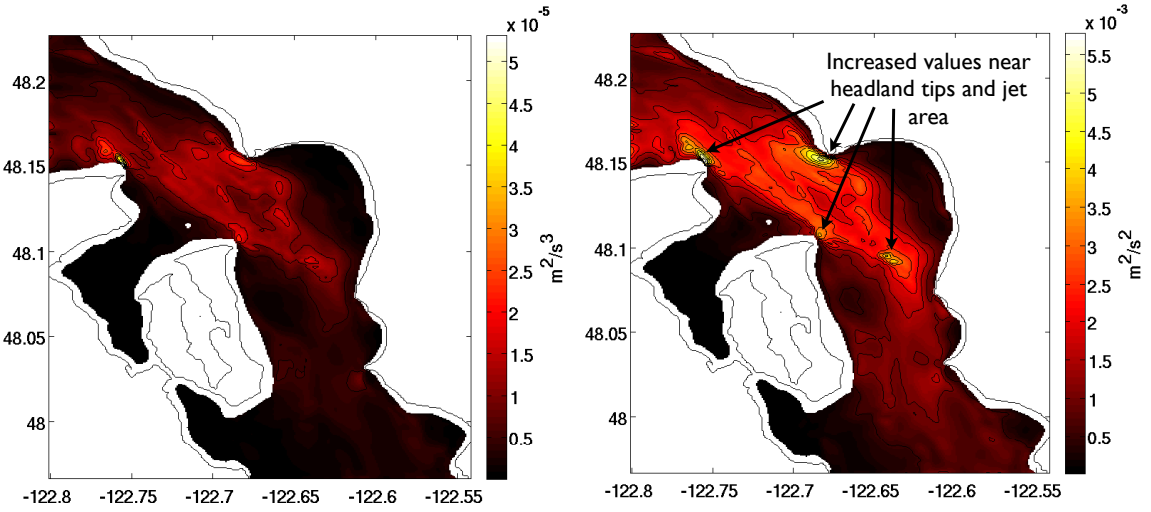


(a) Turbulence Dissipation Rate, $\varepsilon$

(b) Turbulent Kinetic Energy, $k$

Figure 6.26: Mean turbulence properties at hub height from the model shown in both color and contours

have relatively moderate to high mean $k$ but lower speeds. In the wind energy industry, 10% is a commonly-found turbulence intensity value (Thomson et al., 2011).

The mean turbulent kinetic energy, calculated using the "inferred" expression of turbulent kinetic energy as a function of turbulent dissipation rate and mean velocity (Section 5.3), is shown in Figure 6.27(b). The behavior is similar in this plot and in the directly output mean turbulent kinetic energy values shown in Figure 6.26(b). However, it was found in Section 5.3 that the inferred expression of mean turbulent kinetic energy compared better with data than the original model output. The inferred mean turbulent kinetic energy is shown in Figure 6.27(b).

## *6.6 Summary and Implications*

### *6.6.1 Summary*

Maps at hub height for the metrics have been shown throughout this chapter, along with detailed presentations of the metrics themselves. Metrics have been split into two categories:

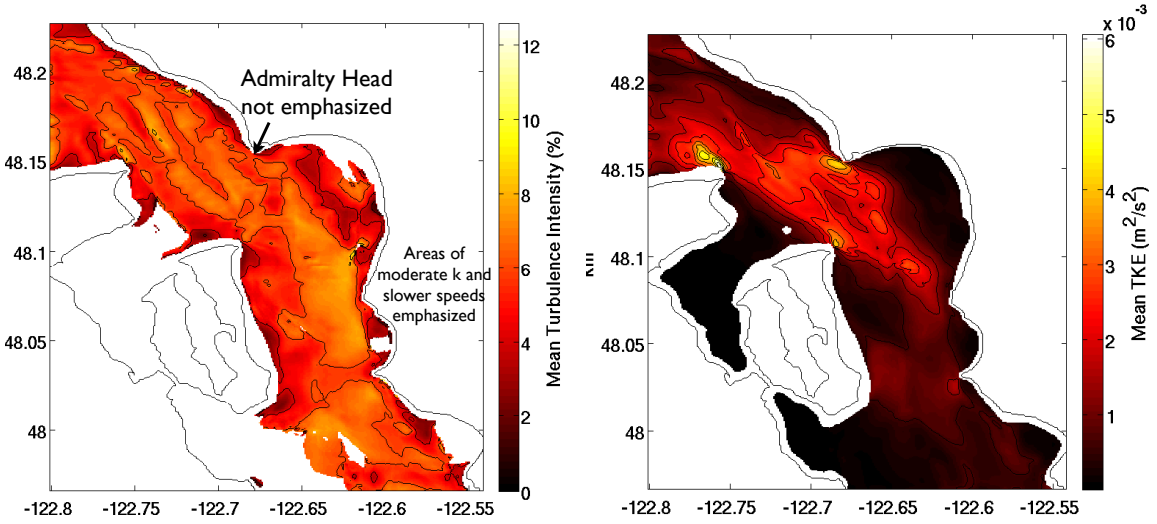


(a) Mean turbulence intensity

(b) Mean turbulent kinetic energy

Figure 6.27: Mean turbulence properties at hub height from the model using the inferred calculation for turbulent kinetic energy shown in both color and contours. White spaces inside the contours of the domain in Figure 6.27(a) indicate that the area is shallower than hub height and that the speed never exceeds the cut-in speed. This calculation of the mean turbulent kinetic energy has similar behavior as the mean turbulent kinetic energy output by the model itself (Figure 6.26(b)), but is a better representation of the values seen in the data.

resource quantification and resource qualification. Resource quantification metrics present the amount of resource available at a given location. Resource qualification metrics present the extractability of the resource, and are presented in conjunction with metrics that affect turbine survivability since these two categories are intertwined.

Due to a speed deficiency in the prediction of the numerical simulation, the model speeds used to calculate resource quantification metrics were adjusted by a factor calculated as the ratio of the average of data mean speed profiles to model mean speed profiles, and was found to be about 1.33. With this adjustment, the model metrics compared well with data at most locations, though typically the data and model output around Marrowstone Island behaved differently. Resource qualification metrics compared well between the data and model output without adjustment to the model output.

A turbine model implemented in ROMS is combined with a high resolution idealized headland simulation to study the effects of turbines on flow field quantities. This is presented in Appendix C.

### *6.6.2 Implications for Turbine Placement*

One of the next logical steps to this work is how a turbine developer might use this information to site a turbine array. The reality is that there is no one answer as to where to place a turbine, and it depends on a number of factors. The most important factors revolve around the turbine design specifics (yaw ability, cut-in speed, rated speed, diameter, resistance to various stressors), but other factors may include acceptable distance for transmission lines and depth for the turbines, end location for the transmission lines, how many turbines and therefore how much space is required, economic viability, and any zones where turbines are not allowed for recreational, environmental, political, or other reasons. In this study, the focus is on several possible factors based on turbine design to illustrate possible turbine placement strategies using this information.

For example, if the chosen turbine design is fixed-axis, the developer may want to place the turbine in flow that is largely bi-directional, say, with bi-directionality $a < 15$ degrees. If the turbine can yaw with the flow, then bi-directionality may not be a major concern;

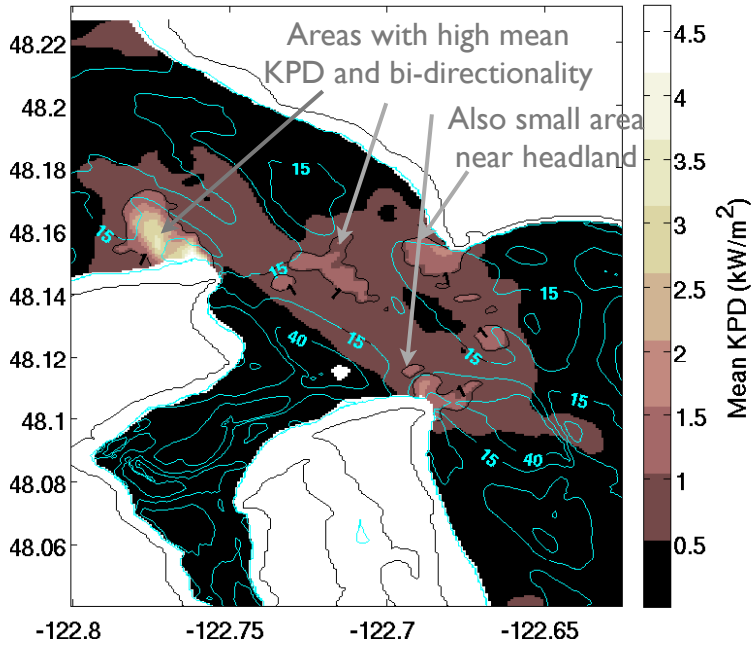


Figure 6.28: Map of mean kinetic power density as color with a black contour line at 1 kW/m$^2$ and bi-directionality as cyan contours at 15 and 40 degrees. Some areas with high power density and low asymmetry are indicated.

however, with the additional required moving parts for such a design, sensitivity to stresses in the flow field may be a more significant consideration than it would be to a fixed-axis turbine. In this case, choosing a region with low turbulence properties may be best. In both cases, a large resource would be a prerequisite.

Figure 6.28 shows a combined metric map of mean kinetic power density in color with a black contour indicating 1 kW/m$^2$, which is a possible cut-off for minimum resource to make a site worthwhile (Bedard et al., 2006). Also plotted are cyan contours of the bi-directionality at 15 and 40 degrees. A fixed axis turbine should possibly be sited in an area with bi-directionality less than 15 degrees. When bi-directionality limitations are combined with the areas of high resource, a few areas stand out as potential options. The headland areas are largely too asymmetric by this measure, though a few small areas near Admiralty Head and NE Marrowstone Island have large enough resource and low enough asymmetry

to fit this requirement. The larger areas of interest are in the middle of the channel between Point Wilson and Admiralty Head, and just north of Point Wilson. The area in the middle of the channel is far enough away from the headlands to be largely bi-directional and is located above a sill, which increases the resource. North of Point Wilson, the flow is fast-moving coming in from the Strait of Juan de Fuca and squeezed by the point, creating high velocities in the area. It is also shallow, causing more speed up, but this can cause problems for turbine siting as well. The area is up to around 40 meters of depth. With a turbine diameter up to 20 meters, this location may not be appropriate despite the large resource.

Turbulence properties are overlaid on the mean kinetic power density in Figure 6.29. A yaw turbine may be more sensitive to additional loads than a fixed-axis turbine due to additional necessary moving parts. Turbulence intensity contours, in Figure 6.29(a), are indicated at values of 7%. A turbulence intensity of 10% has been typically found in wind energy locations. Areas with large resource and low turbulence intensity are indicated. By this measure, many areas are available to turbine placement, including near each headland and in the middle of the channel. A possible problem with using turbulence intensity as a metric is that, while it is true that the turbulent kinetic energy in the system when normalized by the large speeds near the headlands is lower than other areas, that does not change the fact that there is still considerable turbulence there. Perhaps a better measure of turbulence would be the mean turbulent kinetic energy, as overlaid on mean kinetic power density in Figure 6.29(b). In this case, the areas around the headlands are generally collocated with high levels of turbulence. However, there are a few areas in which there is a large resource available and lower turbulence levels; these regions happen to align well with the bi-directionality case shown in Figure 6.28. It will be important for turbine developers to further identify the most relevant measure of turbulence at a site.

The two areas that have come up repeatedly in this section are the areas north of Point Wilson and in the channel between Point Wilson and Admiralty Head. The region north of Point Wilson may not be realistic for siting due to its shallow depths, though with a small diameter turbine, a successful power plant could potentially be developed given the magnitude of the resource. This could be better suited as a resource for the communities on the west side of the channel to minimize transmission cable lengths.

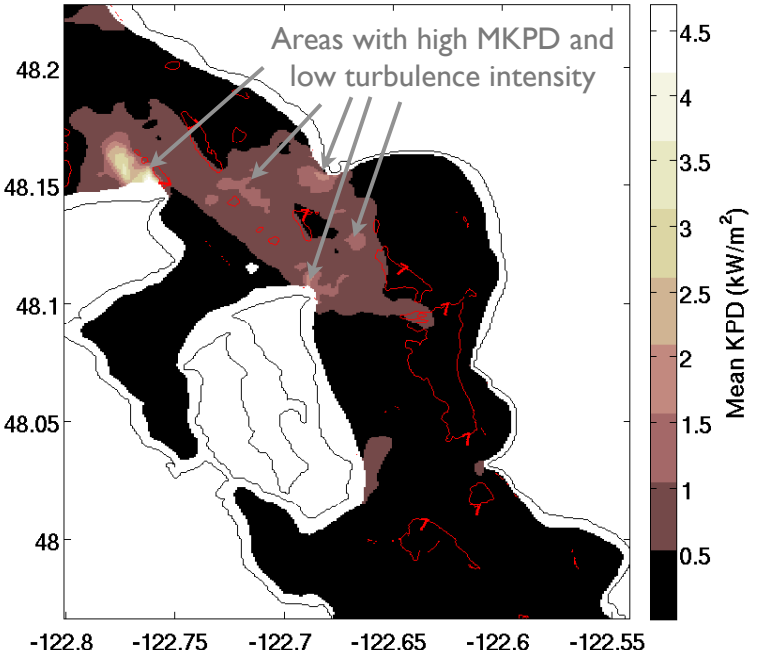


(a) Turbulence intensity contours at 8%

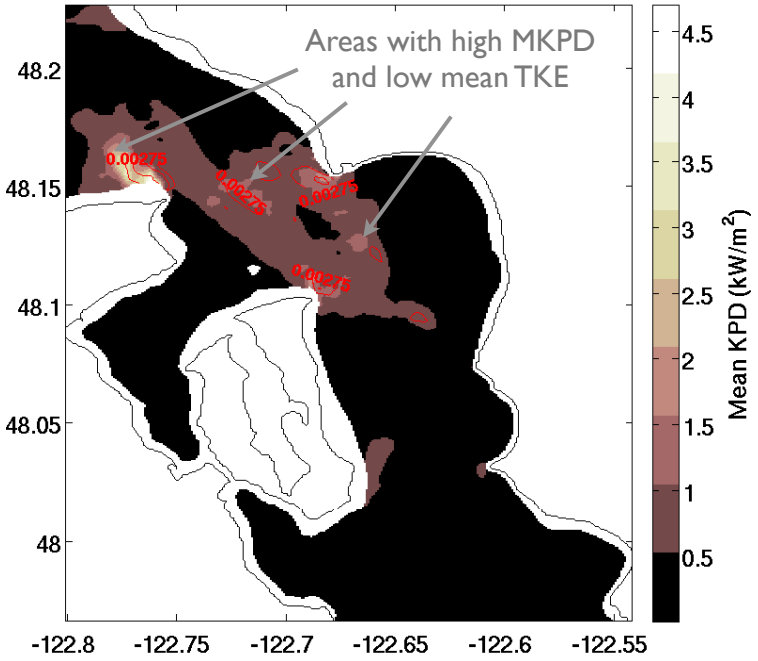


(b) Turbulent kinetic energy contours at $2.75 \times 10^{-3}$ and $4 \times 10^{-3}$ $m^2/s^2$

Figure 6.29: Map of mean kinetic power density as color and mean turbulence properties (both using the inferred calculation for turbulent kinetic energy) as red contours. Some areas with high power density and low turbulence are indicated.

The area in the middle of the channel avoids many of the issues that may be detrimental for turbines since it is away from the coastline and associated features. Turbines in the area would require longer underwater transmission lines, but the depths in the area are 50 to 60 meters, which may be a good balance between enough depth for large turbines but not too deep that the turbines are inaccessible. While the center of Admiralty Inlet is designated as the federal shipping channel, it has been previously determined that allowing a clearance depth of 15 to 25 meters is adequate to avoid contact between ships at the surface and turbines near the seabed (Polagye et al., 2010).

This kind of analysis can be improved with further understanding of turbine design considerations. Also, having functional relationships between each metric and its affect on both turbine lifetime and power production could lead to a map of the effective mean power density; this could be generated for a given turbine design with each metric already taken into account. For example, it was found that a fixed axis turbine would have a power reduction factor of between $\cos^2\theta$ and $\cos^3\theta$ due to horizontal tilting of the incoming flow to a turbine face, and this could be taken into account on a map combining mean kinetic power density and the effect of bi-directionality on mean kinetic power density. More information is needed, though, to know the degree to which different levels of turbulence intensity and other metrics reduce turbine efficiency. From a power utilization perspective, too, knowledge of how power production bias matters for a utility company could help with siting considerations. This information could be gathered in time from lab experiments and numerical models of turbines with various in-flow conditions to determine the effects on power production and turbine stresses.

# Chapter 7

# SUMMARY AND FUTURE WORK

There is potential for tidal hydrokinetic energy to play a role in a future of sustainable energy-independence. Admiralty Inlet, in the Puget Sound estuary in western Washington state, is a strong candidate for commercial-scale turbine placement based on its proximity to a sizable population and strong tidal currents over a large area. Given that there is limited underwater space with necessary conditions for turbine deployment, further understanding of the area and issues involved with turbine siting is needed in order to move forward with this technology. This research contributes to this need in multiple areas. First, a high resolution, realistic model of Admiralty Inlet was established to understand oceanographic issues that are pertinent to turbine siting. Second, vortex generation and travel around the region was studied, since vorticity has been identified as a potentially significant effect on turbine placement. Next, model output was compared with high quality turbulence data. This latter effort was intended to determine the regions with high turbulence levels, to investigate the accuracy of the turbulence closure scheme used in modeling the turbulence in the region, as well as to improve the modeling. Knowledge of the scheme's performance enables better use of the model output for siting purposes. Finally, metric maps of the region were generated for large-scale turbine siting.

## *7.1 Methodology*

A numerical model of Admiralty Inlet was developed using the ROMS code and was shown to perform satisfactorily according to many of the necessary measures. The model output reproduced sharp gradients and flow field changes seen in eddy fields. Turbulence fields were largely reproduced to within a factor of two (though turbulent kinetic energy was addressed separately; see summary in Section 7.3). Tidal free surface and velocity phases were consistent with data through Admiralty Inlet; however, amplitudes were low. This

deficiency in speed was inherited from the forcing regional model and resulted in model horizontal velocity magnitudes that were approximately 75% of the value of data speeds, on average. Model output and data metrics matched well when the deficiency was adjusted for in the quantitative metrics. Many of the relevant flow features were also present in the numerical simulation. Vortices were seen being generated with the tides off every headland in the region. Fronts were seen throughout the region, but in particular near Admiralty Head. The fronts were visible in the density and horizontal speed fields, which often displayed sharp horizontal gradients at the front of the flow when the tide changed directions.

Truncation error in the momentum advection scheme was investigated as possibly altering vorticity generation and energy dissipation mechanisms. Truncation error analysis was completed on the spatial terms of the upstream advection of momentum scheme that is the default choice for use in ROMS. In the previously-analyzed case of tracer advection in a uniform velocity field, the scheme is third-order accurate. However, this analysis found that for advection of momentum in a general velocity field, the scheme is first-order accurate. Calculations of the truncation error found minimal contributions to vorticity flux and energy dissipation.

### *7.2 Vorticity Dynamics*

Many of the flow features examined in connection with vorticity were present in the proposed pilot site location near Admiralty Head. These included fronts, vortices, and vertical velocity. The presence of persistent vortices affects the speed profile, which in turn would affect the power production for a turbine in the path of such a vortex.

The size and trajectory of vortices generated in Admiralty Inlet were seen to depend on the tidal cycle. For consecutive similar tidal cycles (*e.g.,* two higher high water tides), the time scale of substantial behavior change was found to be approximately one week. Eddies generated often persisted and affected the behavior near Admiralty Head on the following half-cycle. This behavior was most noticeable on flood tide, when large ebb eddies could significantly impact the speed profile and other flow fields, but was also seen on ebb tide. In one such example, when flood tide pushed southward through the channel, a large jet formed with oppositely-signed eddies on either side. These large eddies were located on one

side in shallow Admiralty Bay and on the other side lee of Marrowstone Island. Fronts were most commonly seen on ebb tide following the presence of a jet and associated large eddies on flood tide. These large flood eddies would entrain fresh water and move it northward. When the tide then slowed and switched to ebb tide, the fresh water was in position to travel with ebb tide, pushing past Admiralty Head as a front. The front would align with vortex generation, thus appearing in multiple fields (density, speed, and vorticity).

In-depth analysis was used to understand the mechanisms of vorticity governance in the region. Following the methodology in Dong et al. (2007), a modified version of the governing equation for vertical vorticity was volume-integrated and used to diagnostically solve for the boundary generation rate of vertical vorticity at within a small analysis domain around Admiralty Head. The dominant terms in the vorticity equation were boundary generation, advection into and out of the analysis domain, and stretching and tilting of the vertical vorticity. Boundary generation was found to be present during each half-cycle, starting out strong at the beginning of the tide. Advection was mostly out of the analysis domain of the generated vorticity, but the term enabled a detailed analysis of the presence or absence of persistent, old vorticity entering and/or exiting bounding walls. Generally, the vertical vorticity was increased due to stretching near the surface with a positive vertical gradient of convergent downwelling velocity (and some contracting near the seabed in a negative vertical gradient of vertical velocity), and decreased due to tilting of the vortex tube in regions of horizontal gradients on vertical velocity. Occasionally, in the presence of negative vertical gradients of upsloping vertical velocity, instead of the typical positive vertical gradients of upwelling vertical velocity, the signs of the stretching and tilting terms were switched, but this was not common. All of the terms changed sign with the direction of the half-cycle.

The most significant effect on the dynamics of the vorticity was the presence of old, persistent eddies from the previous half-cycle. In one flood tide, the persistent vortex from the previous ebb tide created a double peak in the speed and vorticity time series. All of the terms in the governing equation for vorticity also had a double peak, and similar behavior within each peak. During one ebb tide examined, multiple vortices from the previous flood tide (from in Admiralty Bay and the lee of Marrowstone Island) persisted with minor influence on the speed time series. This influx of oppositely-signed vorticity had

more noticeable effects on other terms in the governing equation, such as a change in sign of the tilting and stretching terms.

### *7.3 Turbulence Modeling*

Model output from the $k$-$\varepsilon$ turbulence closure scheme compared reasonably well (within a factor of two) with turbulence data for the Reynolds stress and turbulent dissipation rate. The deficiency seen in these two parameters is due to the known model speed deficiency. While the turbulent kinetic energy did not initially match well, limiting the frequency range of the turbulent kinetic energy to the classical turbulence range led to a much closer match. This indicates that the turbulence model performs reasonably well in the classical turbulence range for which the model was intended.

An approach was attempted to address the turbulent kinetic energy that is in the field data set but outside the classical range, and thus not captured directly in the numerical model. The frequency range for the inertial subrange in Kolmogorov's theory was extended to lower frequencies, based on spectral energy density data. With this extension, the turbulent kinetic energy could be calculated from the local mean speed and turbulent dissipation rate from the model output, and the match between the data and this calculation from model output was improved. As further discussed in Section 5.4, the field data could be approximated with other, more exact functions to improve the accuracy of the expression.

Given the comparisons made between the model output and the data, the turbulence parameters calculated from model output were found to be a reasonable representation of the data. This suggests that maps of turbulence intensity and mean turbulent kinetic energy can be confidently employed in turbine siting studies.

### *7.4 Metric Maps*

Flow metrics in a region of interest for turbine placement can be classified into two categories. The first, quantitative metrics, includes metrics that describe the size of the resource available. The second, qualitative and turbine survivability metrics, includes metrics that describe the extractability of the resource, as well as potential undue stresses on turbines.

Horizontal speeds from the model output were multiplied by a factor of 1.33 in order

to account for the known speed amplitude deficiency as compared with data. With this adjustment, quantitative metrics compared well between model output and data, and metric maps were generated for Admiralty Inlet at a nominal hub height of ten meters (mean speed, mean kinetic power density, mean power, turbine operation time, and capacity factor). It was not necessary to adjust model output for qualitative metrics. Metric maps of the region were made showing asymmetry properties (bi-directionality, directional deviation, and speed and power bias), mean shear, and mean turbulence properties (intensity, turbulent kinetic energy, and turbulent dissipation rate).

The best locations for turbine siting depends on many considerations. As determined by resource magnitude, lower flow asymmetry, and turbulence properties, the best locations in Admiralty Inlet were found to be just north of Point Wilson on the west side of the channel, and in the middle of the channel, over the sill between Point Wilson and Admiralty Head.

### *7.5 Future Work*

The deficiency in the $M_2$ tide leads to an underestimation of quantitative turbine siting metrics and of turbulence parameters. Several approaches could be followed in order to address the $M_2$ deficiency in the regional simulation which is inherited into the nested simulation. A straight-forward solution would be to artificially adjust the boundary forcing to roughly compensate for the $M_2$ deficiency. A more involved solution would be to improve the boundary forcing by improving the larger regional model, which is currently underway in the School of Oceanography at the University of Washington.

Though this model enables the in-depth spatial and temporal analysis of the flow field, it is important to remember its limitations. ROMS is a hydrostatic code, which limits the useful spatial resolution, and also limits the ability to model some dynamic features that are expected in the region. A future model of Admiralty Inlet should be at higher resolution and be made using a non-hydrostatic model. This would improve the veracity and numerical accuracy of the simulation results, especially at smaller length scales. The more resolved the numerical output, the better micro-siting of turbines for a commercial-scale array for tidal energy production.

An obvious but not necessarily straight-forward extension of the methodology in ideal-

ized or realistic systems would be the addition of turbines to the simulations. For example, if one turbine was added at the tip of the headland in the idealized headland case, would the mean kinetic power density plot change in appearance? Or if five or twenty turbines were added to the area? How would these turbines affect the directionality of the flows, which would then be seen in the resource qualification metric plots? With a turbine representation in place, a comparison could also be made between the power generated by an array of turbines arbitrarily placed in the domain, and turbines that have been intelligently placed by examining the metric maps of the domain. A collaboration is underway that introduces an advanced turbine model in ROMS in an idealized headland simulation to address such questions. Preliminary results from this collaboration are shown in Section C, and more work in this area is expected in the future.

n using model output from simulations and expect to continue having useful model output, the hydrostatic approximation that has been made at the core of the numerics must be kept in mind, particularly when increasing the grid resolution to a level that may begin to push against the approximation's limit. Another model consideration is one of timing in the year. Model results from the nested Admiralty Inlet model will not necessarily line up nicely in time with all of the various ADCP field data that has been collected. This means that while the data may not be directly comparable to the model output, it can still be used for quality control and to make sure that the same sorts of behavior are witnessed in each case.

# BIBLIOGRAPHY

Atlantic Kayak Tours (2010). `http://www.atlantickayaktours.com/pages/expertcenter/navigation/navigation-04.shtml`.

Babson, A., Kawase, M., and MacCready, P. (2006). Seasonal and interannual variability in the circulation of Puget Sound, Washington: A box model study. *Atmosphere-Ocean*, 44(1):29–45.

Barron, C. N., Kara, A. B., Martin, P. J., Rhodes, R. C., and Smedstad, L. F. (2006). Formulation, implementation and examination of vertical coordinate choices in the global navy coastal ocean model (NCOM). *Ocean Modell.*, 11:347–375.

Baston, S. (2012). Modelling tidal flow in the Pentland Firth. Environmental Interactions of Marine Renewable Energy Technologies, Orkney 1-3 May 2012.

Beckmann, A. and Haidvogel, D. B. (1993). Numerical simulation of flow around a tall, isolated seamont. Part I: Problem formulation and model accuracy. *J. Phys. Oceanogr.*, 23:1736–1753.

Bedard, R., Previsic, M., Polagye, B., Hagerman, G., and Casavant, A. (2006). North America tidal in-stream energy conversion technology feasibility study. Technical Report EPRI TP-008, EPRI technical report.

Black, K. P. and Gay, S. L. (1987). Eddy formation in unsteady flows. *Journal of Geophysical Research*, 92(C9):9514–9522.

Boon, J. D. (2004). *Secrets of the tide: Tide and tidal current analysis and applications, storm surges and sea level trends*. Horwood Publishing.

Burchard, H., Bolding, K., and Villarreal, M. R. (2004). Three-dimensional modelling of estuarine turbidity maxima in a tidal estuary. *Ocean Dynamics*, 54:250–265.

Canals, M., Pawlak, G., and MacCready, P. (2009). Tilted baroclinic tidal vortices. *Journal of Physical Oceanography*, 39:333–350.

Cannon, G. A. (1983). An overview of circulation in the Puget Sound estuarine system. Technical report, National Oceanic and Atmospheric Administration.

Chapman, D. C. (1985). Numerical treatment of cross-shelf open boundaries in a barotropic coastal ocean model. *J. Phys. Oceanogr.*, 15:1060–1075.

Chickadel, C., Talke, S. A., Horner-Devine, A. R., and Jessup, A. T. (2011). Infrared-based measurements of velocity, turbulent kinetic energy, and dissipation at the water surface in a tidal river. *IEEE Geoscience and Remote Sensing Letters*, 8(5):849–853.

City of Seattle (2010). The Greater Seattle datasheet. `http://www.seattle.gov/oir/datasheet/demographics.htm`.

Cushman-Roisin, B. and Beckers, J.-M. (2009). *Introduction to Geophysical Fluid Dynamics*. Academic Press.

Deleersnijder, E. L. (1989). Upwelling and upsloping in three-dimensional marine models. *Applied Mathematical Modelling*, 13(8):462–467.

Department of Defense (2007). *National Defense Authorization Act of 2007*.

Dong, C., McWilliams, J. C., and Shchepetkin, A. F. (2007). Island wakes in deep water. *Journal of Physical Oceanography*, 37(4):962–981.

Edwards, K. A., MacCready, P., Moum, J. N., Pawlak, G., Klymak, J. M., and Perlin, A. (2004). Form drag and mixing due to tidal flow past a sharp point. *Journal of Physical Oceanography*, 34(6):1297–1312.

Egbert, G. D. and Erofeeva, S. Y. (2002). Efficient inverse modeling of barotropic ocean tides. *J. Atmos. Oceanic Technol.*, 19:183–204.

Epler, J. (2010). Tidal resource characterization from acoustic Doppler current profilers. Master's thesis, University of Washington, Seattle.

Flather, R. A. (1976). A tidal model of the northwest European continental shelf. *Memoires de la Societe Royale de Sciences de Liege*, 6:141–164.

Fraenkel, P. (2009). The UK SeaGen project: Marine Current Turbines' experience. UK-Taiwan workshop on tidal current energy.

Frandsen, S. (2007). *Turbulence and turbulence-generated structural loading in wind turbine clusters*. PhD thesis, Risø National Laboratory.

Geyer, W. R. and Cannon, G. A. (1982). Sill processes related to deep water renewal. *J. Geophys. Res*, 87:7985–7996.

Geyer, W. R. and Signell, R. (1990). Measurements of tidal flow around a headland with a shipboard acoustic Doppler current profiler. *Journal of Geophysical Research*, 95(C3):3189–3197.

Godin, G. (1983). On the predictability of currents. *International Hydrographic Review*, 60:119–126.

Gooch, S., Thomson, J., Polagye, B., and Meggitt, D. (2009). Site characterization for tidal power. In *OCEANS 2009, Biloxi, MI*.

Greene, D. L., Hopson, J. L., and Li, J. (2003). Running out of and into oil: Analyzing global oil depletion and transition through 2050. Technical report, National Transportation Research Center.

Haas, K. A., Fritz, H. M., French, S. P., Smith, B. T., and Neary, V. (2011). Assessment of energy production potential from tidal streams in the United States. Technical report, Georgia Tech Research Corporation, NA.

Haidvogel, D. B., Arango, H., Budgell, W. P., Cornuelle, B. D., Curchitser, E., Lorenzo, E. D., Fennel, K., Geyer, W. R., Hermann, A. J., and Lanerolle, L. (2008). Ocean forecasting in terrain-following coordinates: Formulation and skill assessment of the Regional Ocean Modeling System. *Journal of Computational Physics*, 227(7):3595–3624.

Haney, R. L. (1991). On the pressure gradient force over steep topography in sigma coordinate ocean models. *J. Phys. Oceanogr.*, 21:610–619.

Hansen, A. C. and Butterfield, C. P. (1993). Aerodynamics of horizontal-axis wind turbines. *Annual Review of Fluid Mechanics*, 25:115–149.

Karl, T. R., Melillo, J. M., and Peterson, T. C. (2009). Global climate change impacts in the United States. Technical report, Cambridge University Press.

Karsten, R., Greenberg, D., and Tarbotton, M. (2010). Assessment of the potential of tidal power from Minas Passage and Minas Basin. *Currents*.

Kawase, M. and Beba, P. (2010). Depth optimization final report. Technical report, University of Washington.

Kelisi (2006). `http://en.wikipedia.org/wiki/File:PentlandFirthMap.png`.

Kundu, P. K. and Cohen, I. M. (2004). *Fluid Mechanics*. Elsevier Academic Press, third edition.

Lavelle, J. W., Mofjeld, H. O., Lempriere-Doggett, E., Cannon, G. A., Pashinski, D. J., Cokelet, E. D., Lytle, L., and Gill, S. (1988). A multiply-connected channel model of tides and tidal currents in Puget Sound, Washington and a comparison with updated observations. *NOAA Tech. Memo. ERL PMEL-84 (PB89-162515)*.

Legrand, C. (2009). Assessment of tidal energy resource. *EMEC*, pages 1–60.

Leonov, D. and Kawase, M. (2009). Sill dynamics and fjord deep water renewal: Idealized modeling study. *Continental Shelf Research*, 29(1):221–233.

Madsen, H. A. (2000). Yaw simulations using a 3D actuator disc model coupled to the aeroelastic code HAWC. *Proceedings of IEA Joint Action, Aerodynamics of Wind Turbines 13th Symposium, Stockholm*, pages 133–146.

Madsen, P. H. and Frandsen, S. (1984). Wind-induced failure of wind turbines. *Engineering Structures*, 6(4):281–287.

Maganga, F., Germain, G., King, J., Pinon, G., and Rivoalen, E. (2010). Experimental characterisation of flow effects on marine current turbine behaviour and on its wake properties. *Renewable Power Generation, IET*, 4(6):498–509.

Marine Current Turbines (2010). `http://www.marineturbines.com`.

Martin, V. (2011). Wind resource downstream of forested terrain. Master's thesis, University of Washington.

Mass, C. F. et al. (2003). Regional environmental prediction over the Pacific Northwest. *Bull. Amer. Meteor. Soc.*, 84:1353–1366.

McCabe, R. M., MacCready, P., and Pawlak, G. (2006). Form drag due to flow separation at a headland. *Journal of Physical Oceanography*, 36:2136–2152.

Mofjeld, H. O. and Larsen, L. H. (1984). Tides and tidal currents of the inland waters of western Washington. Technical report, National Oceanic and Atmospheric Administration.

NNMREC, University of Washington (2010). *Northwest National Marine Renewable Energy Center*.

Ocean Renewable Power Company (2010). `http://www.oceanrenewablepower.com/home.htm`.

O'Donnell, J., Marmorino, G. O., and Trump, C. L. (1998). Convergence and downwelling at a river plume front. *Journal of Physical Oceanography*, 28(7):1481–1495.

Open Hydro (2010). `http://www.openhydro.com`.

Panton, R. L. (2005). *Incompressible Flow*. John Wiley & Sons, Inc, third edition.

Pawlak, G. and MacCready, P. (2002). Oscillatory flow across an irregular boundary. *J. Geophys. Res*, 107:3036.

Pawlowicz, R., Beardsley, B., and Lentz, S. (2002). Classical tidal harmonic analysis including error estimates in matlab using T_TIDE. *Computers & Geosciences*, 28(8):929–937.

Polagye, B. (2010). Personal Communication.

Polagye, B., Bedard, R., and Previsic, M. (2007). Tidal in-stream energy conversion survey and characterization of SnoPUD project sites in Puget Sound. Technical Report EPRI-TP-003, EPRI technical report, WA.

Polagye, B., Copping, A., Kirkendall, K., Boehlert, G., Walker, S., Wainstein, M., and Cleve, B. V. (2010). *Environmental effects of tidal energy development: A scientific workshop*.

Polagye, B., Kawase, M., and Malte, P. (2009). In-stream tidal energy potential of Puget Sound, Washington. *Proceedings of the Institution of Mechanical Engineers, Part A: Journal of Power and Energy*, 223(5):571–587.

Polagye, B., Malte, P., Kawase, M., and Durran, D. (2008). Effect of large-scale kinetic power extraction on time-dependent estuaries. *Proceedings of the Institution of Mechanical Engineers, Part A: Journal of Power and Energy*, 222(5):471–484.

Polagye, B. and Thomson, J. (2011). Tidal energy resource characterization: Methodology and field study in Admiralty Inlet, Puget Sound, US. *Submitted*.

Polagye, B. L. (2009). *Hydrodynamic effects of kinetic power extraction by in-stream tidal turbines*. PhD thesis, University of Washington.

Pope, S. B. (2000). *Turbulent Flows*. Cambridge University Press.

Previsic, M., Bedard, R., and Polagye, B. (2008). System level design, performance, cost and economic assessment – Admiralty Inlet, Washington tidal in-stream power plant 2008 update. Technical Report EPRI-TP-006 SnoPUD Rev. 1, EPRI technical report, WA.

Public Utility District No. 1 of Snohomish County (2012). *Admiralty Inlet Pilot Tidal Project: Application for a New Pilot Project License (Minor Water Power Project)*.

Pugh, D. (2004). *Changing Sea Levels: Effect of Tides, Weather and Climate*. Cambridge University Press.

Rasch, P. J. (1994). Conservative shape-preserving two-dimensional transport on a spherical reduced grid. *Monthly Weather Review-USA*, 122:1337–1350.

Raymond, W. H. and Kuo, H. L. (1984). A radiation boundary condition for multi-dimensional flows. *Quarterly Journal of the Royal Meteorological Society*, 110:535–551.

Reed, S. (2006). Initiative 937. *Washington State*.

Roc, T., Thyng, K. M., and Conley, D. C. (2011). Applying a numerical decision-making tool for tidal current turbine (TCT) planning projects to the Puget Sound estuary - early results. *Proc. EWTEC*.

Secretary of State for Trade and Industry (2003). *Energy White Paper: Our energy future - Creating a low carbon economy*.

Seim, H. E. (1993). *Observations and Energetics of an Evolving Shear Instability in Admiralty Inlet*. PhD thesis, University of Washington.

Shchepetkin, A. F. and McWilliams, J. C. (1998). Quasi-monotone advection schemes based on explicit locally adaptive dissipation. *Monthly Weather Review*, 126(6):1541–1580.

Shchepetkin, A. F. and McWilliams, J. C. (2005). The Regional Ocean Modeling System (ROMS): A split-explicit, free-surface, topography-following coordinates ocean model. *Ocean Modelling*, 9(4):347–404.

Sheinman, Y. and Rosen, A. (1992). A dynamic model of the influence of turbulence on the power output of a wind turbine. *Journal of Wind Engineering and Industrial Aerodynamics*, 39(1-3):329–341.

Signell, R. P. and Geyer, W. R. (1991). Transient eddy formation around headlands. *Journal of Geophysical Research*, 96(C2):2561–2575.

Simpson, J. H., Burchard, H., Fisher, N. R., and Rippeth, T. P. (2002). The semi-diurnal cycle of dissipation in a ROFI: Model-measurement comparisons. *Continental Shelf Research*, 22:1615–1628.

Stips, A., Burchard, H., Bolding, K., and Eifler, W. (2002). Modelling of convective turbulence with a two-equation k-$var\epsilon$ turbulence closure scheme. *Ocean Dynamics*, 52(4):153–168.

Sutherland, D. A., MacCready, P., Banas, N. S., and Smedstad, L. F. (2011). A model study of the Salish Sea estuarine circulation. *Journal of Physical Oceanography*, 41(6):1125–1143.

Thomsen, K. and Sørensen, P. (1999). Fatigue loads for wind turbines operating in wakes. *Journal of Wind Engineering and Industrial Aerodynamics*, 80(1):121–136.

Thomson, J., Polagye, B., Durgesh, V., and Richmond, M. (2011). Measurements of turbulence at two tidal energy sites in Puget Sound, WA (USA). *Journal of Oceanic Engineering*, in press.

Umlauf, L. and Burchard, H. (2003). A generic length-scale equation for geophysical turbulence models. *Journal of Marine Research*, 61:235–265.

Verdant Power (2010). `http://verdantpower.com`.

Wagner, R., Courtney, M. S., Larsen, T. J., and Paulsen, U. S. (2010). Simulation of shear and turbulence impact on wind turbine performance. Technical report, Risø National Laboratory for Sustainable Energy Technical, University of Denmark.

Walter, R. K., Nidzieko, N. J., and Monismith, S. G. (2011). Similarity scaling of turbulence spectra and cospectra in a shallow tidal flow. *Journal of Geophysical Research*, 116(C10):C10019.

Wang, B., Giddings, S. N., Fringer, O. B., Gross, E. S., Fong, D. A., and Monismith, S. G. (2011). Modeling and understanding turbulent mixing in a macrotidal salt wedge estuary. *Journal of Geophysical Research*, 116(C2):C02036.

Warner, J. C., Geyer, W. R., and Lerczak, J. A. (2005a). Numerical modeling of an estuary: A comprehensive skill assessment. *darchive.mblwhoilibrary.org*, 110(C05001).

Warner, J. C., Sherwood, C. R., Arango, H. G., and Signell, R. P. (2005b). Performance of four turbulence closure models implemented using a generic length scale method. *Ocean Modelling*, 8(1-2):81–113.

Warner, S. J. and MacCready, P. (2009). Dissecting the pressure field in tidal flow past a headland: When is form drag "real"? *Journal of Physical Oceanography*, 39:2971–2984.

Washington State Department of Ecology (2011). Long-term marine water quality data. `http://www.ecy.wa.gov/apps/eap/marinewq/mwdataset.asp`.

White, L. and Wolanski, E. (2008). Flow separation and vertical motions in a tidal flow interacting with a shallow-water island. *Estuarine, Coastal and Shelf Science*, 77(3):457–466.

Worthington, M. (2011). Tidal energy technology and ORPC's projects in Cook Inlet. Presented to NOAA/AEA stakeholder meeting.

# Appendix A

# UPSLOPING VELOCITY DERIVATION

## *A.1 Separating Vertical Velocities into Components*

The vertical velocity can be split up as follows in order to better understand its underlying causes (Deleersnijder, 1989):

$$w = w_{us} + w_{uw}, \tag{A.1}$$

where $w$ is the vertical velocity, $w_{us}$ is vertical velocity due to topographic effects, called "upsloping velocity", and $w_{uw}$ is vertical velocity due to other effects, called "upwelling velocity." This is derived as follows, from Deleersnijder (1989).

We start with the coordinate transformation to $\sigma$ coordinates,

$$(\hat{t}, \hat{x}, \hat{y}, \hat{z}) = \left( t, x, y, L\frac{z+h}{\eta+h} = L\sigma \right), \tag{A.2}$$

where $z$ is the depth below a reference sea level, $\eta$ is the sea surface height, $h$ is the distance from the seabed to a reference sea level, and $L$ is the constant total depth in $\sigma$, or terrain-following, coordinates (*i.e.* $H = h + \eta$ in Cartesian coordinates, which changes in time, and $L$ is the constant equivalent in $\sigma$ space). See Figure A.1 for an illustration of the coordinate systems. The transformation is illustrated in Figure A.1. The relationship between the Cartesian vertical velocity and the $\sigma$ coordinate vertical velocity, $\omega$, is

$$w = \frac{H}{L}\omega + \sigma\frac{\partial \eta}{\partial t} - \underline{u} \cdot [(1-\sigma)\nabla h - \sigma \nabla \eta]. \tag{A.3}$$

We can find an expression for the upsloping velocity by deriving several vertical velocity terms individually. First, we follow a particle of water that is stationary with respect to the $\sigma$ coordinates, but oscillates up and down in Cartesian coordinates. In other words, the particle maintains a constant relative vertical relationship in the water column. This can be represented by $w_1 = \frac{\partial z}{\partial \hat{t}} = \frac{\partial z}{\partial t}$. Using Equation A.2, this can be shown as follows:

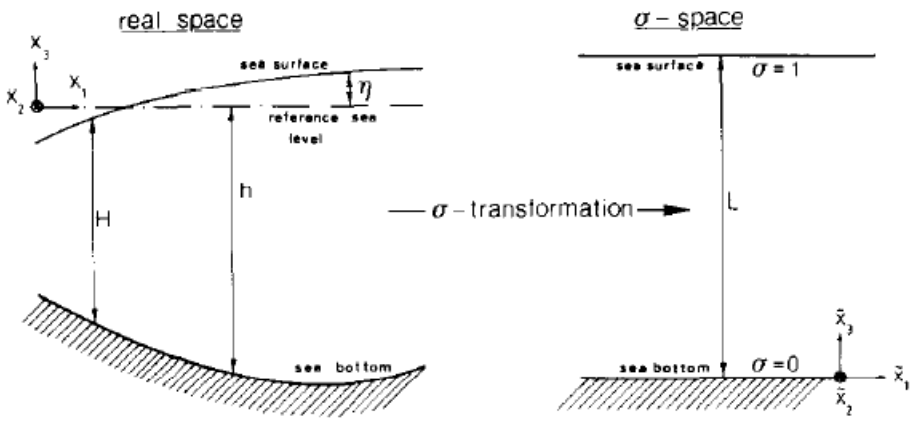


Figure A.1: Transformation to sigma coordinates (Deleersnijder, 1989)

$$\begin{aligned} \sigma &= \frac{z+h}{\eta+h} \\ z &= \sigma(\eta+h) - h \\ \frac{\partial z}{\partial t} &= \sigma\frac{\partial \eta}{\partial t} \\ \Rightarrow w_1 &= \sigma\frac{\partial \eta}{\partial t}. \end{aligned} \tag{A.4}$$

In the next situation, the $\sigma$ layers are at rest and we examine a particle moving along an iso-$\sigma$ surface with horizontal velocity $\underline{u}$. The particle does not cross the surfaces, so its velocity is orthogonal to a normal unit vector to the surface. In other words,

$$(\underline{u} + w_2\hat{k}) \cdot \hat{n} = 0,$$

for vertical velocity $w_2$ in this situation. A form for $\hat{n}$ can be derived geometrically to find an expression for this type of vertical velocity:

$$w_2 = -\underline{u} \cdot [(1-\sigma)\nabla h - \sigma\nabla\eta]. \tag{A.5}$$

Together, $w_1$ and $w_2$ give the velocity of a particle that moves without crossing an iso-$\sigma$ surface. Since the $\sigma$ layers are terrain-following and the sea surface and seabed are iso-$\sigma$

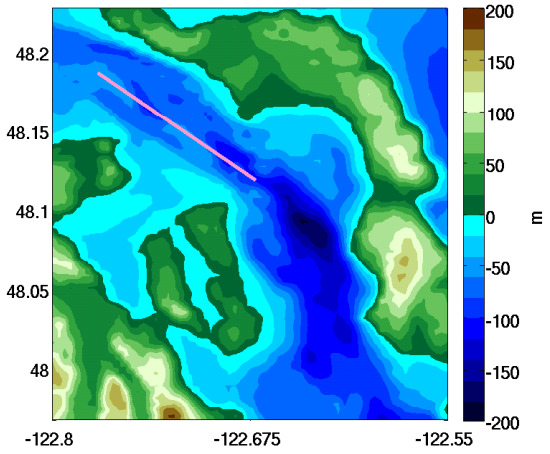


Figure A.2: Domain bathymetry with slice location indicated

surfaces, we can call $w_{us} = w_1 + w_2$ the vertical velocity that is due to the geometry of the basin.

Comparing Equations A.4 and A.5 with Equation A.3 and renaming the one remaining term as the upwelling velocity, as it is not directly induced by the top or bottom layers, returns Equation A.1.

An important note is that ROMS can directly output the upwelling velocity. It is called `omega` and in terms of the discussion here is given by

$$\text{omega} = w_{uw} = \frac{H}{L}\omega.$$

Note that this is assuming no vertical stretching, *i.e.*, a uniform vertical grid.

## *A.2 Example Plots*

### *A.2.1 Along-Channel*

Plots of mean vertical, upsloping, and upwelling velocity were shown in Figure 4.18 for the along-channel slice shown in Figure A.2. The maximum and minimum values of vertical velocities along the same slice are shown in Figure A.3 for $w$, upsloping, and upwelling velocities. The upsloping velocities are adjacent to the slopes in the bathymetry and largest

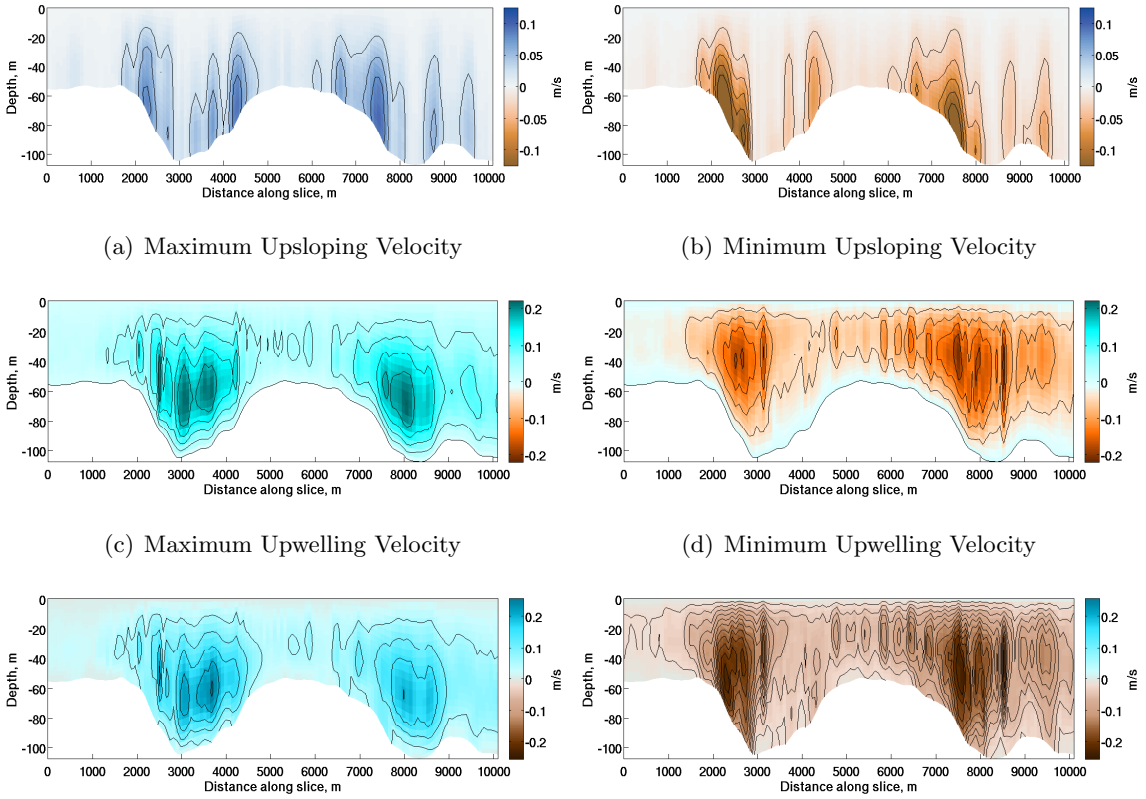


(a) Maximum Upsloping Velocity

(b) Minimum Upsloping Velocity

(c) Maximum Upwelling Velocity

(d) Minimum Upwelling Velocity

(e) Maximum Vertical Velocity

(f) Minimum Vertical Velocity

Figure A.3: Maximum and Minimum Vertical Velocities Over Time

moving downslopes, whereas the upwelling velocities are away from the bathymetry, mid-water column, particularly between hills. Interestingly, the maximum and minimum values are larger for the upwelling velocity than for the upsloping velocity, and thus these $w$ plots are most controlled by the upwelling plots. This is the opposite of the averaged plots shown in Figure 4.18. The shapes and locations of the high-valued regions are similar between the means and maximums/minimums.

### *A.2.2 Depth Slices*

The plot shown in Figure 4.20 of upwelling velocity near Admiralty Head at ebb tide is repeated in this section but shown for upsloping and full vertical velocity in order to help

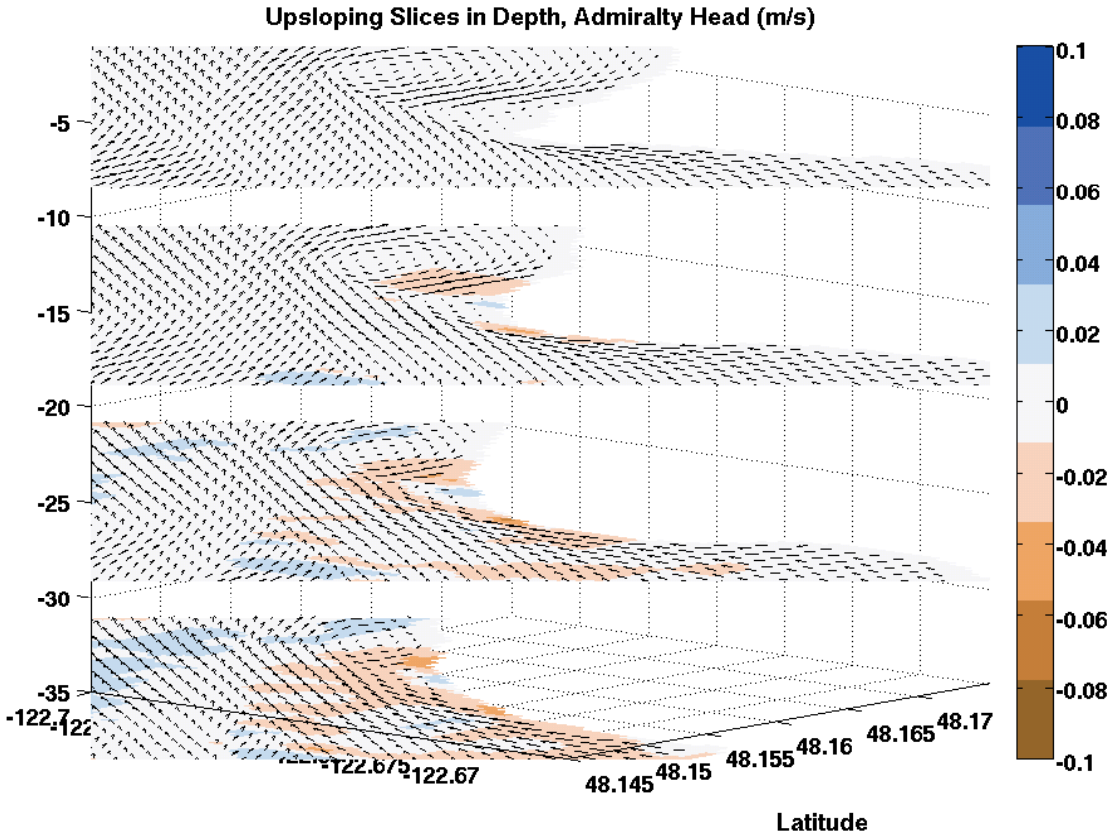


Figure A.4: Snapshot from an ebb tide on 9/5/06, showing slices in depth of upsloping velocity. Snapshot is at the same time as shown in Figures 4.6(c) and 4.15.

illustrate distinctions in the fields. Slices in depth of upsloping velocity are shown in Figure A.4 and in full vertical velocity are shown in Figure A.5. The magnitudes of the upsloping velocities (Figure A.4) are much smaller than the upwelling velocities. The full vertical velocity field looks very similar to the upwelling field shown in Figure 4.20 because the full vertical velocity is dominated by the large upwelling values.

### *A.2.3 Hub Height Plots*

The mean magnitude of vertical velocities at hub height are shown in Figure A.6. The full vertical velocity and upsloping velocity look very similar and are approximately the same

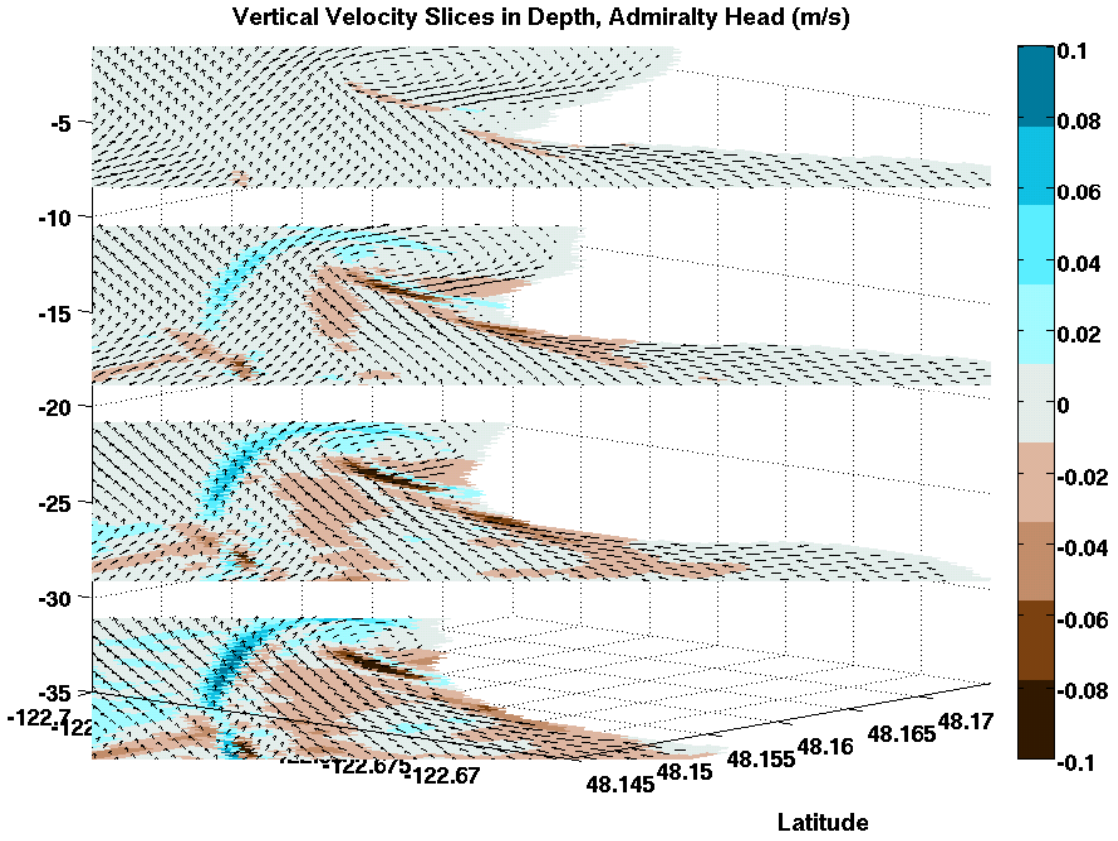


Figure A.5: Snapshot from an ebb tide on 9/5/06, showing slices in depth of vertical velocity. Snapshot is at the same time as shown in Figures A.4.

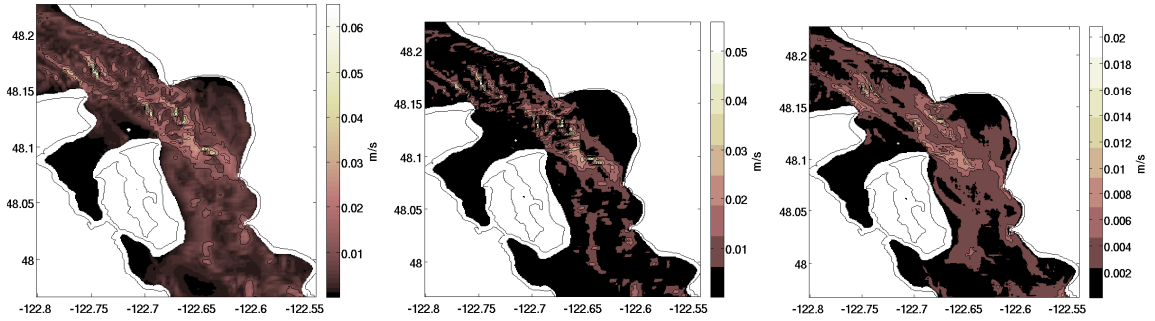


(a) Vertical Velocity (b) Upsloping Velocity (c) Upwelling Velocity

Figure A.6: Various mean vertical velocities

size whereas the upwelling velocity is 1/3 the size of $w$. The areas of strong magnitude are largely in the same place for all of the plots, indicating that the bathymetry directly or indirectly causes most of the vertical velocity in the system (this was also seen in Section A.2.1). The upsloping velocity tends to be more focused while the upwelling velocity tends to be more widespread.

Maximum and minimum values for each vertical velocity over time for each $(x, y)$ location at hub height are shown in Figures A.7, A.8, and A.9. The maximum and minimum upsloping velocity plots show that the strong currents occur near areas of sharp change in bathymetry in the presence of strong horizontal currents. While many of these areas overlap with with the strong areas in the upwelling plots, the shape of the highlighted areas for upwelling velocity is very different and much more spread out.

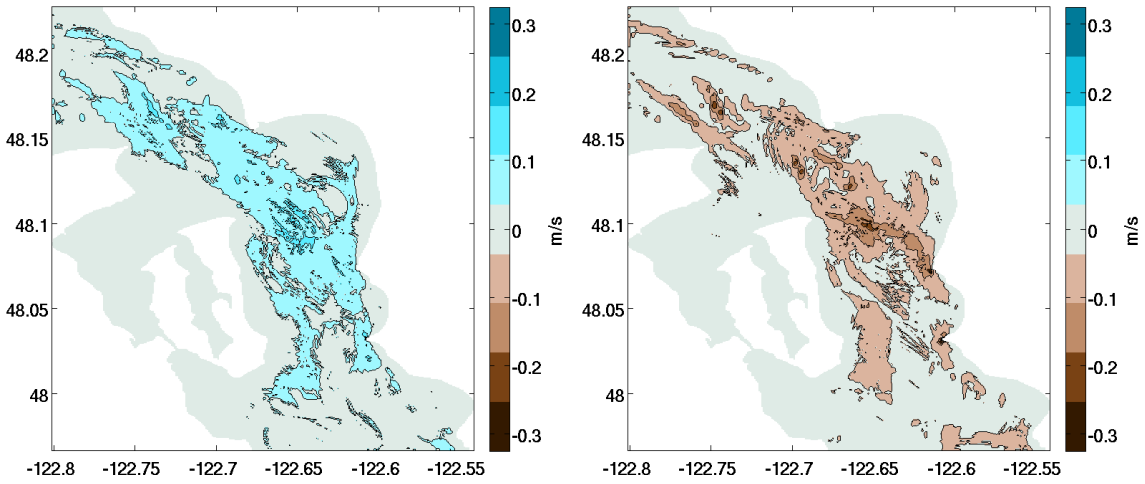


(a) Maximum (b) Minimum

Figure A.7: Maximum/minimum full vertical velocity in space over time at hub height

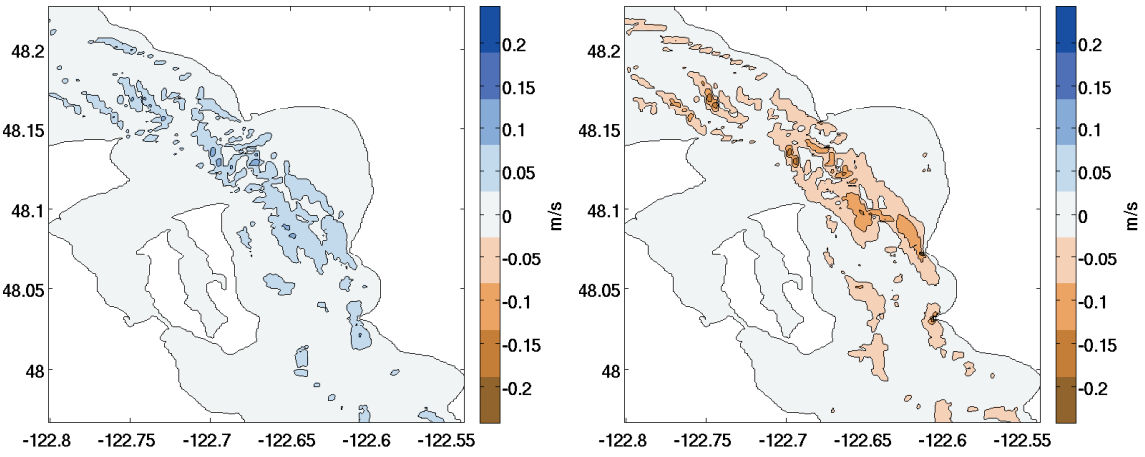


(a) Maximum (b) Minimum

Figure A.8: Maximum/minimum upsloping velocity in space over time at hub height

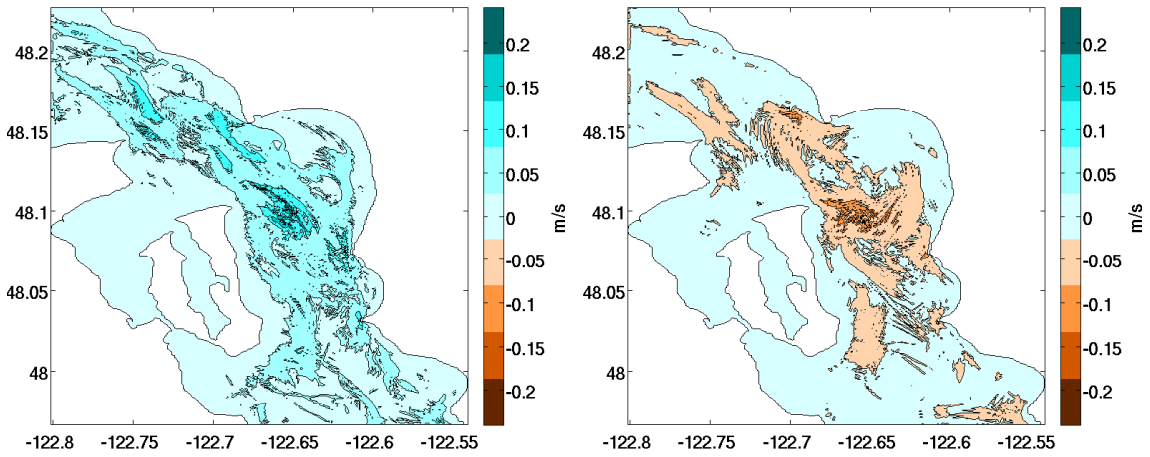


(a) Max Upwelling Velocity

(b) Min Upwelling Velocity

Figure A.9: Maximum/minimum upwelling velocity in space over time at hub height

Appendix B

# SITE CHARACTERIZATION METRICS: ADDITIONAL DETAILS

Alternative calculations to some of the existing tidal turbine siting metrics have been proposed in this work. Details on why they are proposed along with details on the effects of the changes are given in this appendix.

## *B.1 Directionality Details*

The proposed formulation for the directionality metrics involves weighting the angles of the horizontal velocity vectors based on the cube of their speed, so that the relationship between speed and power is used to maintain the ultimate goal of power production. This was found by trying combinations of two possible parts of the directionality calculations: utilization of a cut-in speed, and weights. A cut-in speed has been used in previous research to prevent erratic speeds around slack tide from having undue influence on metric calculations. However, when a cut-in speed is applied to the numerical simulation, which may have many points with consistently low speeds, much of the velocity information may be discarded. While the velocities at these points may be too low for utilization by a turbine, that will depend on the turbine design deployed. Also, other (quantitative) metrics, such as the mean kinetic power density, are intended to account for the size of the resource available, leaving directionality metrics to address directionality exclusively. An alternative or complement to the cut-in speed is to weight the speeds used in the directionality calculations.

The following sections show results from different methods for calculating the metrics for angles. In this first section, the mean angle and standard deviation of the angles are calculated based on the horizontal velocity vector angle for every point in time with no weighting, with and without a cut-in speed of $s_c = 0.7$ m/s. Next, the average and the standard deviation calculations are weighted linearly with speed, without the cut-in speed, and last, the metrics are weighted cubicly with speed, with and without a cut-in speed.

### *B.1.1 Results for Different Calculations*

When a cut-in speed is implemented in a calculation, no speeds below the cut-in are used. Weights may be used with or without a cut-in speed. A weight is calculated for each time step. In the linear weighting case, normalized weights $w_i$ for each $(u, v)$ pair are determined as follows:

$$w_i = \frac{|s_i|}{\sum_{i=1}^{N} |s_i|}, \tag{B.1}$$

where $s_i$ is the horizontal speed at time step $i$. In the case with cubic weighting, normalized weights are given by:

$$w_i = \frac{|s_i^3|}{\sum_{i=1}^{N} |s_i^3|}. \tag{B.2}$$

The case without weighting can be treated as having weights $w_i = 1/N$. The weighted average direction is found as

$$\theta_M = \sum_{i=1}^{N} w_i \theta_i, \tag{B.3}$$

for ebb and flood tide separately, where $\theta_i$ is the angle corresponding to the horizontal velocity at time step $i$. The standard deviation is also weighted and calculated separately for ebb and flood tides, and is given as

$$\sigma = \sqrt{\sum_{i=1}^{N} w_i (\theta_i - \theta_M)^2}. \tag{B.4}$$

The bidirectionality metric, represented by $a$, is calculated as

$$a = |\theta_{M,ebb} - \theta_{M,flood} - 180|, \tag{B.5}$$

where the calculation of $\theta_{M,ebb}$ and $\theta_{M,flood}$ includes corresponding weighting for each case. A value of 0 for $a$ implies perfect bi-directionality.

*No Weighting*

The bi-directionality $a$ and directional deviation $\Theta$ for the case with no weighting and no cut-in speed are shown in Figure B.1 at hub height. In the plot for $a$, a black contour is shown at a value of 10, and labelled red markers show the locations of example points to

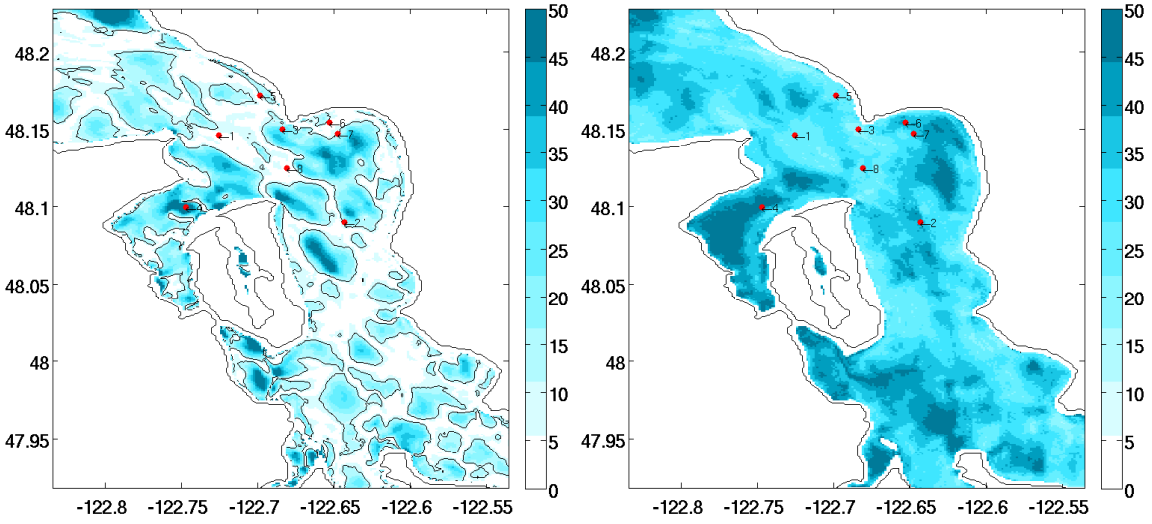


(a) Bi-directionality

(b) Directional Deviation

Figure B.1: Bi-directionality and directional deviation: no weighting, no cut-in speed

be examined later in this appendix. Dark colors indicate lower values, which is preferable for fixed-axis tidal turbines. The directional deviation is large throughout the domain.

In the next case, no weights are used, but the velocities used in the metrics are filtered ahead of time to eliminate $(u, v)$ pairs for which the speed is below 0.7 m/s. The bi-directionality and directional deviation are shown in Figure B.2. They are fairly similar to the non-weighted, no cut-in speed case shown above, except here locations whose speeds stay below the cut-in speed are not shown, leaving much of the maps empty. These empty points would not be good for generating power, though it leaves out a lot of available information.

*Linear Weighting*

In the case using linear weights and no cut-in speed, the weights used in the calculations are given in Equation B.1. The bidirectionality and directional deviation are shown in Figure B.3. The directional deviation is large throughout the domain, but the differences in the methods will be most easily seen in Section B.1.2.

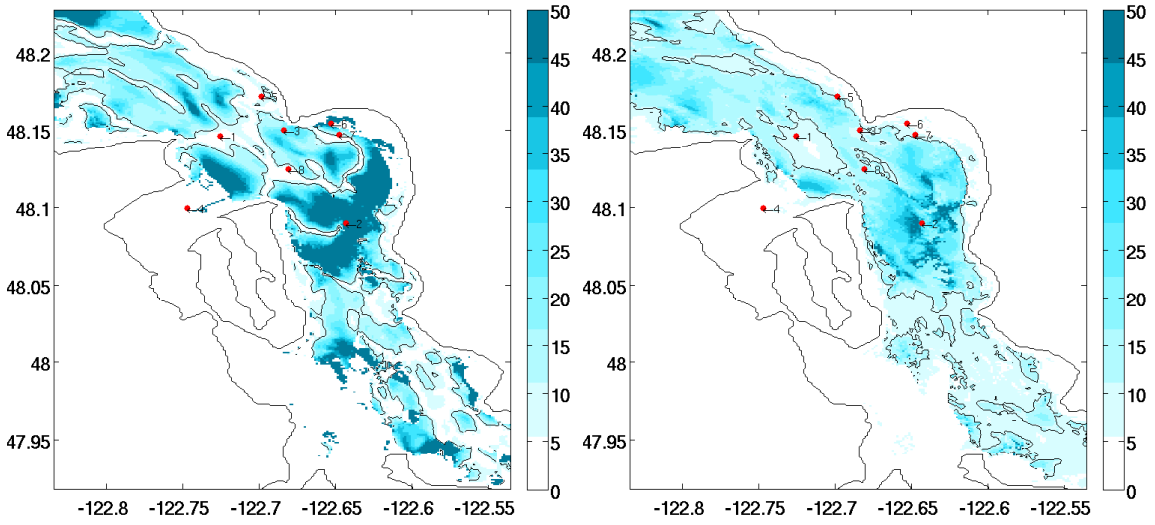


(a) Bidirectionality (b) Directional Deviation

Figure B.2: Bi-directionality and directional deviation: no weighting, cut-in speed of 0.7 m/s

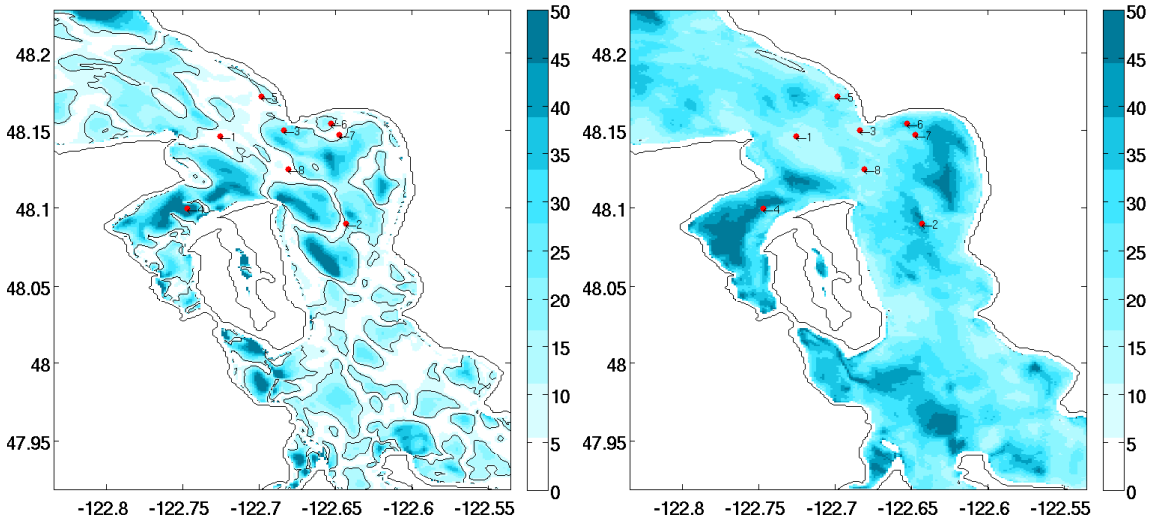


(a) Bidirectionality (b) Directional Deviation

Figure B.3: Bi-directionality and directional deviation: linear weighting, no cut-in speed

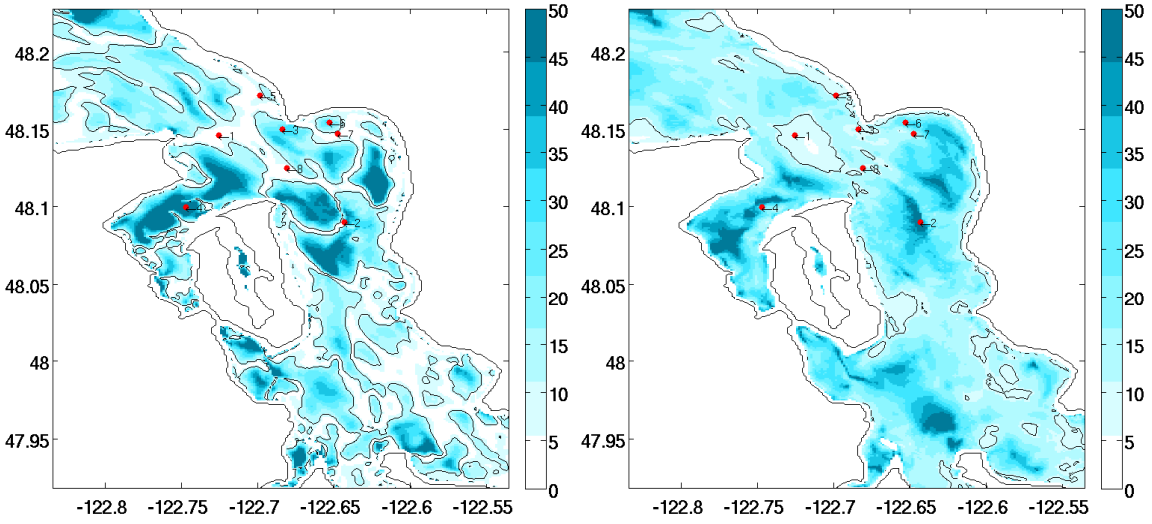


(a) Bidirectionality

(b) Directional Deviation

Figure B.4: Bi-directionality and directional deviation: cubic weighting, no cut-in speed

*Cubic Weighting*

For the case with cubic weights, the weights are given by Equations B.2. The bidirectionality and directional deviation for this case, with no cut-in speed, are shown in Figure B.4. In both of these metrics, the results have been refined relative to the previous methods. The directional deviation has decreased because the cubic weighting emphasizes the times with the strongest speeds.

The bidirectionality and directional deviation are shown in Figure B.5 for the case with cubic weighting and a cut-in speed of $s_c = 0.7$ m/s. These plots are similar to the cubic-weighted, no cut-in speed plots shown previously, but with empty locations where the speeds are below the cut-in speed.

### *B.1.2 Example Points*

Shown in this section are several example points to illustrate what $(u, v)$ pairs can look like in time from a specific location. This helps to interpret the metric maps, and to compare calculation methods. The points are labeled in all of the previous plots as numbered red dots

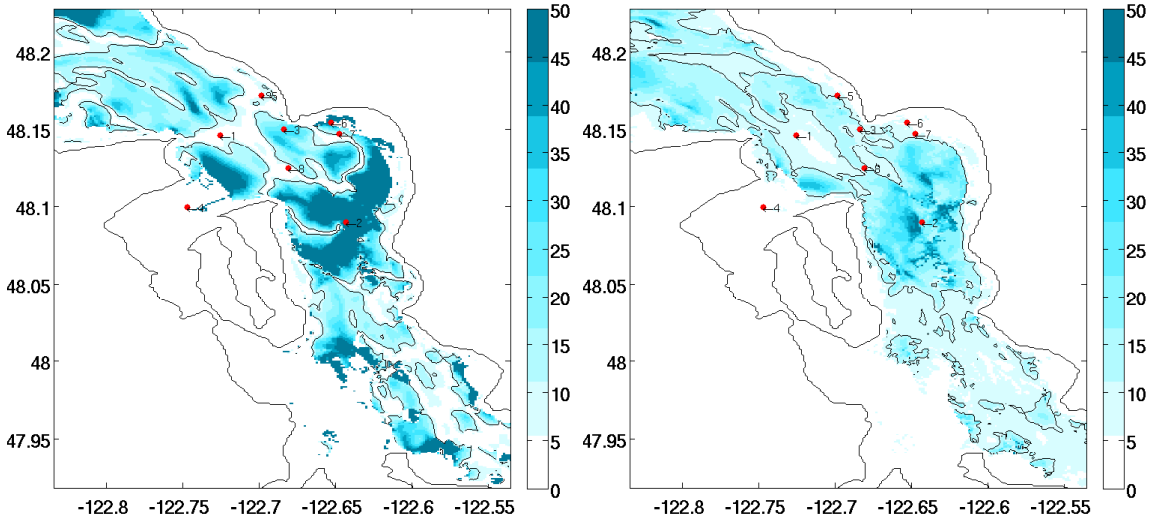


(a) Bidirectionality

(b) Directional Deviation

Figure B.5: Bi-directionality and directional deviation: cubic weighting, cut-in speed of 0.7 m/s

which correspond to the figures below. Each method of calculation has its own color/line type combination, as shown in the legends. The line represents the mean angle for that location and tide direction. Only three of the indicated points will be evaluated.

Example point 1, shown in Figure B.6, is in the middle of the channel between Point Wilson and Admiralty Head in an area that is bi-directional and has low directional deviation. This can be seen in the metric maps as well as the alignment and lack of scatter of the velocity points in each tidal direction in Figure B.6. Because of this, all of the methods give similar mean angles, though the two cubic-weighted methods are most tuned toward the strongest currents.

Example point 2 is located east of Marrowstone Island in the area affected by the large flood eddy. It is shown two ways in Figure B.7: first with ebb and flood chosen based on principal axis analysis with no cut-in speed, and the second principal axis analysis was done with a 0.7 m/s cut-in speed. This helps to illustrate the effect of the cut-in speed on the analysis. The cases without the cut-in speed have similar results, which are fairly

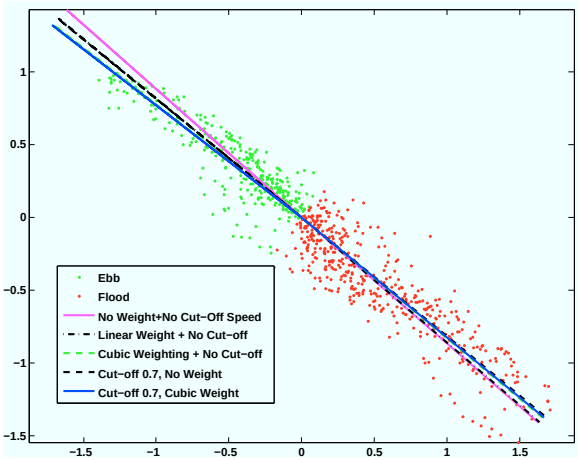


Figure B.6: Example point 1

bidirectional, but the cut-in speed cases are very asymmetric due the completely different principal axis identified, which heavily biases the metrics in these weaker current areas.

Example point 3 is located just off the tip of Admiralty Head in an area that is directly affected by the headland eddies. It is shown in Figure B.8 and is easily split into ebb and flood tide, resulting in a moderate asymmetry and directional spread.

## *B.2 Bias Details*

This metric is used to capture the bias of the strength of the speed or power to ebb or flood tide as a representation of potential asymmetry of power production throughout the day. Currently, researchers at the University of Washington (Gooch et al., 2009; Polagye and Thomson, 2011) calculate this metric as

$$\text{bias} = (\text{mean property on ebb})/(\text{mean property on flood}).$$

The problem with this calculation is that it does not give a linear relationship between various possible results. For example, if an ebb property is valued at 1 and a flood property is valued at 2, the bias calculation would give 1/2. However, if they were oppositely-valued, the bias calculation would give 2. The difference between these bias values is 3.5 even though the relationship between the two numbers is a factor of 2. A more proper way to

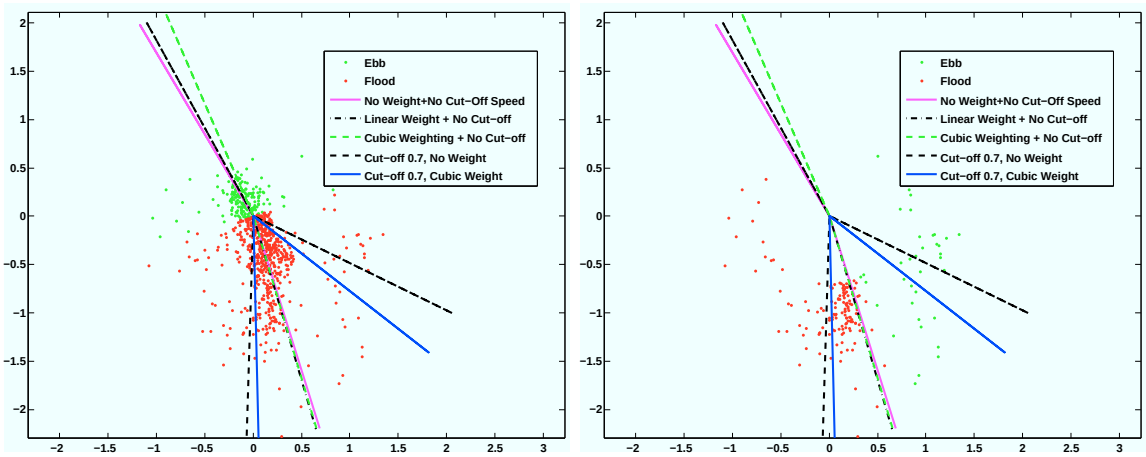


(a) Ebb/flood based on no cut-in speed

(b) Ebb/flood based on cut-in speed of 0.7 m/s

Figure B.7: Example point 2

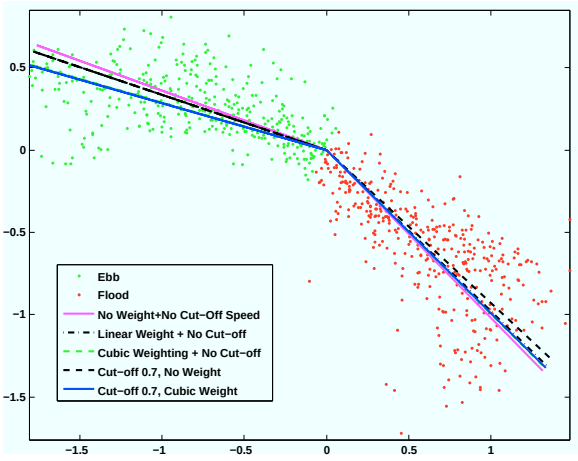


Figure B.8: Example point 3

represent their relationship may be that the bias is 1/2 when the flood is 2 and ebb is 1 and the bias is −1/2 when the flood is 1 and ebb is 2, giving an equivalent distance from zero for the same ratio of relationship, and with the sign showing which direction is dominating.

It is easy to differentiate between two tidal directions with pretty good accuracy, however, it is difficult to consistently determine which direction is flood and which is ebb specifically, especially for model output around headlands and other features that may have unexpected behavior. Because of this, it may be best to take the absolute value of the calculation described. This eliminates information of tidal direction if there is a bias, but also eliminates possible mistakes in directionality. From a siting perspective, knowledge about the deviation from roughly equivalent properties on ebb versus flood tide is important, but knowing which direction is dominant may not be. However, from an operational perspective, this would not be the case. In that case, further efforts can be made to determine flood versus ebb directionality for the specific turbine locations.

This new bias metric can be written as follows for speed bias and power bias

$$s_{bias} = 1 - \frac{\min(s_{M,one\ direction}, s_{M,other\ direction})}{\max(s_{M,one\ direction}, s_{M,other\ direction})}$$
$$p_{bias} = 1 - \frac{\min(p_{M,one\ direction}, p_{M,other\ direction})}{\max(p_{M,one\ direction}, p_{M,other\ direction})}$$

### *B.2.1 Examples and Results*

#### *x-y plane*

Figure B.9 illustrates the difference between including and not including direction information in the speed bias plot. In the plot with directionality, it was necessarily to guess the direction for flood everywhere ahead of time in order to categorize which direction the principal axis was pointing toward (ebb or flood). In general it is fairly easy to make this guess, but not in the more complicated flow areas of the domain. For example, the tides west of Marrowstone Island are difficult to categorize and some strange behavior is easy to see as the colors switch quickly between red and blue, due to some mis-categorization of directionality. Similar effects can be seen south of Marrowstone Island and at the southern end of the domain. While these instances of problems are relatively few and in areas that

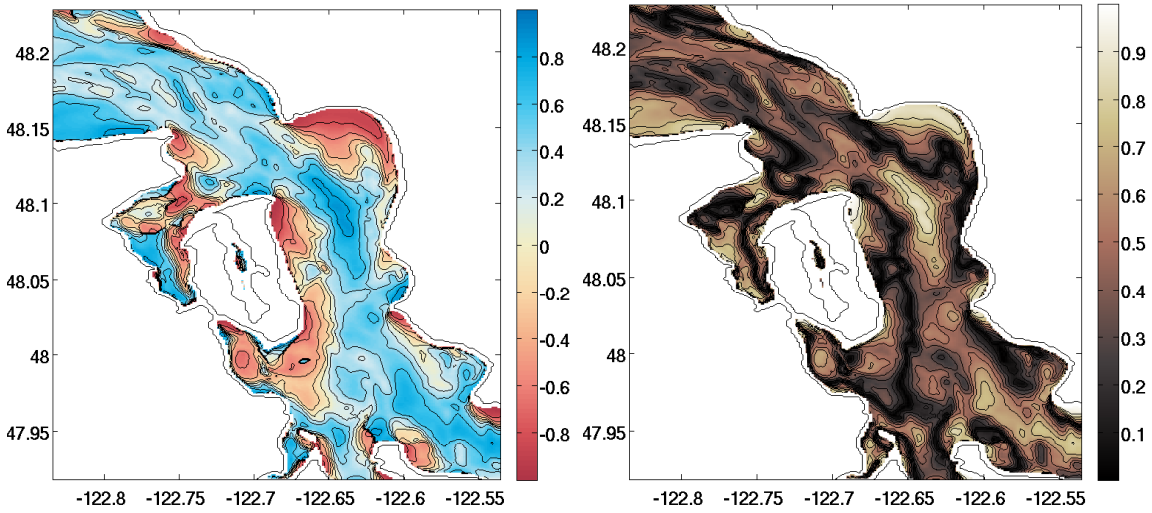


(a) With Directionality

(b) Without Directionality

Figure B.9: Speed bias at hub height

do not tend to matter as much for tidal energy, it is a problem with the metric that will be on-going, and the purpose of the metric is to present this specific bias information as correctly as possible, regardless of tidal energy potential at each specific location.

Taking the absolute value of the first plot gives the plot of speed bias without directionality. We get all of the important information in this plot: that is, the colors are dark where the tide is most balanced between flood and ebb speed strength, and the colors are lightest where the tide is most biased toward one direction.

There is relatively low bias between Point Wilson and Admiralty Head, with higher biases tending to be near headlands or in the large jet area east of Marrowstone Island.

Figure B.10 shows the kinetic power density bias without and without directionality. Everything is similar to the speed bias case, but all areas have been intensified due to the cubic relationship of power with speed.

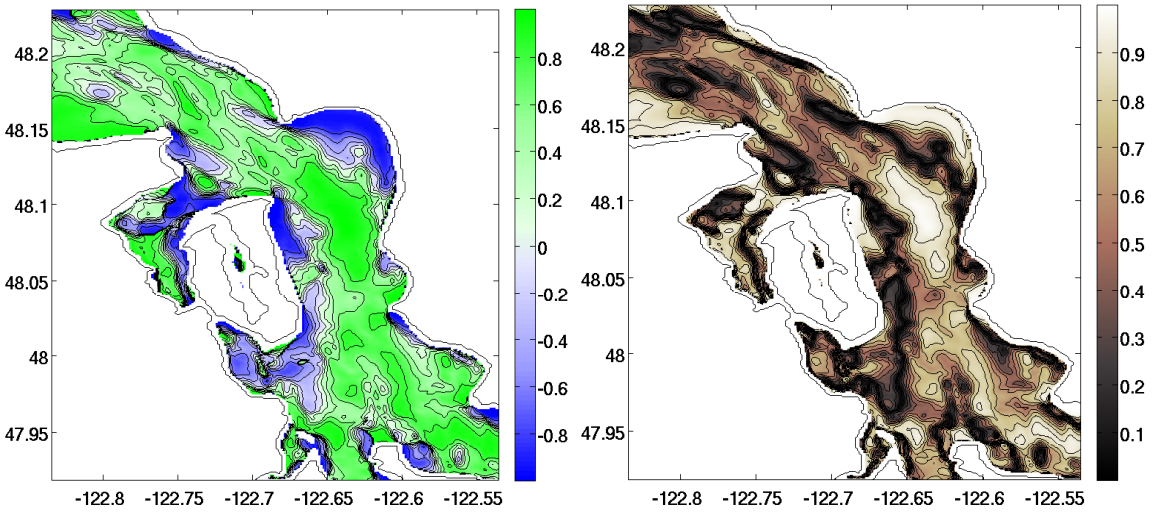


(a) With Directionality

(b) Without Directionality

Figure B.10: Power bias at hub height

Appendix C

# PRELIMINARY SIMULATIONS OF THE EFFECT OF TURBINES ON FLOW FIELDS AND METRIC MAPS

## *C.1 Introduction*

After working to understand the existing flow field characteristics of the area of interest, a logical next step is to understand the effects of turbines on the flow. To this end, a turbine model that is implemented in ROMS is used in several idealized headland channel flow simulations (Roc et al., 2011).

Flow fields will be compared between the initial, base case simulation with no turbines and two simulations with different array layouts near the headland tip. Plots will be examined at both hub height and the surface. In addition to examining the fields through a tidal cycle, mean plots and metrics will help display the differences created by the presence of turbines. Implications for the system and for turbine placement, along with future work in this rich area of research, will be discussed in the final section.

### *C.1.1 Turbine Model*

The turbine is modeled in ROMS by adding a force term to the momentum equations, representing the turbine in a grid cell (Roc et al., 2011). The form of this term is

$$\underline{F} = -\frac{1}{2}\rho A_d C |\underline{v}| \cdot \underline{v} \cdot \hat{n},$$

where $\rho$ is the fluid density, $A_d$ is the area of the turbine, $C$ is the drag coefficient, $\underline{v}$ is the velocity, and $\hat{n}$ is the unitary vector perpendicular to the rotor disc area.

Additionally, a term is added to each of the two $k$-$\omega$ turbulence closure scheme equations to simulate reduced turbulence length scales ($P_k$) and additional production of wake

turbulence due to the turbine's presence ($P_\omega$). The equations are as follows

$$\frac{Dk}{Dt} = \frac{\partial}{\partial z}\left(\frac{K_M}{\sigma_k}\frac{\partial k}{\partial z}\right) + P_s + P_B - \varepsilon + P_k$$
$$\frac{D\omega}{Dt} = \frac{\partial}{\partial z}\left(\frac{K_M}{\sigma_\omega}\frac{\partial \omega}{\partial z}\right) + \frac{\omega}{k}\left(c_1 P_s + c_2 P_B - c_3 \varepsilon F_{wall} + P_\omega\right),$$

where $D/Dt$ represents the material derivative, $k$ is the turbulent kinetic energy, $K_M$ is the vertical eddy viscosity, $P_s$ is the shear production, $P_B$ is the buoyancy production, $\varepsilon$ is the turbulent dissipation rate, $\omega$ is the turbulent frequency, and $F_{wall}$ is a wall function. Constants have the following values: $c_1 = 0.555$, $c_2 = 0.833$, $c_3 = -0.6$, $\sigma_k = 2.0$, and $\sigma_\omega = 2.0$. The added terms to represent the turbine are given by

$$P_k = -C_k \frac{uk}{L}$$
$$P_\omega = C_\omega \frac{P_s^2}{\varepsilon},$$

where $u$ is magnitude of the horizontal velocity, $L$ is the grid spacing of the porous disc, and parameters $C_\omega$ and $C_k$ are found empirically.

Turbines modeled this way are currently aligned with the $x$ or $y$ axis and have a fixed direction. More details on this turbine model as implemented in ROMS can be found in Roc et al. (2011).

### *C.1.2 Simulations*

The simulations examined here are similar to the idealized headland case discussed in Chapter 3. However, the grid has been refined due to the very high resolution used in these simulations. The turbine model requires one grid cell in thickness and three grid cells across. The turbines modeled are 30 meters in diameter and are modeled with three, 10 meter grid cells across, and one 30 meter cell in thickness. The resolution employed for these simulations is 30 meters in the $x$-direction, 10 meters in the $y$-direction, and 20 vertical layers. The domain is a flat-bottomed 40 km x 7 km x 100 meters deep channel with a smooth, symmetric headland at the center. This simulation is shallower than the previous headland simulation, and the $k - \omega$ turbulence closure scheme is used. Simulations are run for two $M_2$ tidal cycles with the same linear density initialization as in the previous headland case

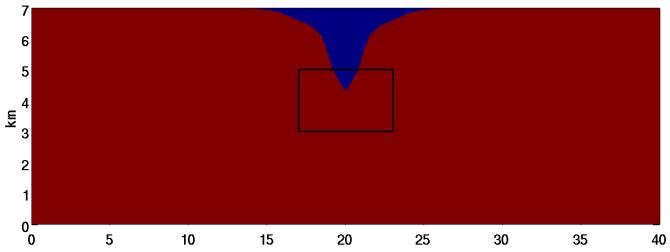


(a) Headland domain, zoom in box indicated

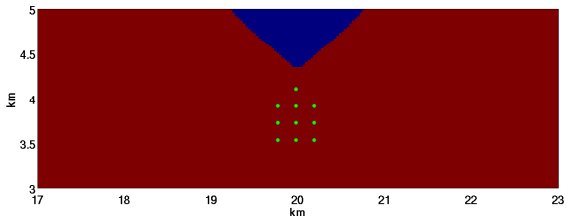


(b) Regular array, zoomed in

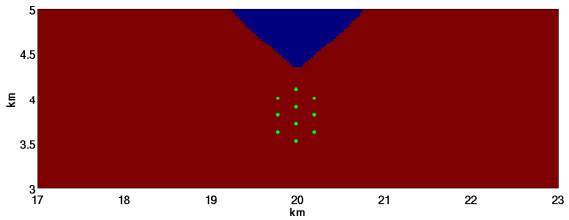


(c) Staggered array, zoomed in

Figure C.1: Turbine locations in the three simulation cases.

(Section 2.7.1). The first tidal cycle is considered ramp-up, and the second tidal cycle is used for analysis.

There are three simulation cases to examine: first, the initial case with no turbines; then two cases with 10 turbines each, in different configurations. Turbines are located at a hub height of 50 meters, mid way up the water column.

The three simulation cases are shown in Figure C.1. The initial case is shown in Figure C.1(a), which has no turbines modeled. Figure C.1(b) shows the "regular" array case, in which there is one turbine near the headland tip and the other nine are uniformly arranged behind, away from the tip. The "staggered" array case, shown in Figure C.1(c) has 3 columns of turbines, alternating with three then four then three turbines, which are staggered with respect to one another in columns.

## *C.2 Flow Fields*

The staggered turbine array layout appears to affect the flow field less than the regular turbine array. This is probably due to the fact that with the angle of the flow past the tip of the headland, the staggered array actually causes the turbine wakes to align, having less affect on the flow field, whereas in the regular layout, the wakes are staggered. See Figure C.1. Because of this, we will compare the base case with no turbines with the regular layout array to have the most extreme comparison, knowing that the results with the staggered array are somewhere between.

### *C.2.1 Hub Height*

Figure C.2 shows snapshots of a variety of model outputs from the base case with no turbines and the regular array. Generally, the presence of the turbines disrupts the flow features. In the speed, the sharp front in the base case is diffused and not noticeable in the regular array case. The turbines are visible as a decrease in speed at each turbine location along with a decrease in the wake. The dip in speed due to an eddy is in a slightly different location in the two cases, implying that the turbines' presence in the present locations alters the flow enough to change the eddy field patterns. The vorticity field appears to show that in the base case, the vorticity field is more cohesive, compared with the turbine case in which the vorticity patch is broken up by the turbines. The vertical velocity field in the base case shows a sharp front whereas the regular array again has a more diffuse frontal region, and there are a lot of small vertical velocity patches in the turbine array wake. The turbulent kinetic energy also has a cohesive patch in the base case, but this is disrupted and broken up by the turbines in the regular array case.

Another set of snapshots is shown in Figure C.3. This is in the middle of ebb tide in which a large eddy has developed lee of the headland, seen in the speed fields. The most noticeable feature is a flow feature from the headland tip that swirls downstream in the base case. It is easily seen in both the vertical velocity and turbulent kinetic energy. In the turbine case, the turbulence is too small-scale to be resolved explicitly on this grid and looks like streaks behind the turbines, and patches near the tip of the headland where the

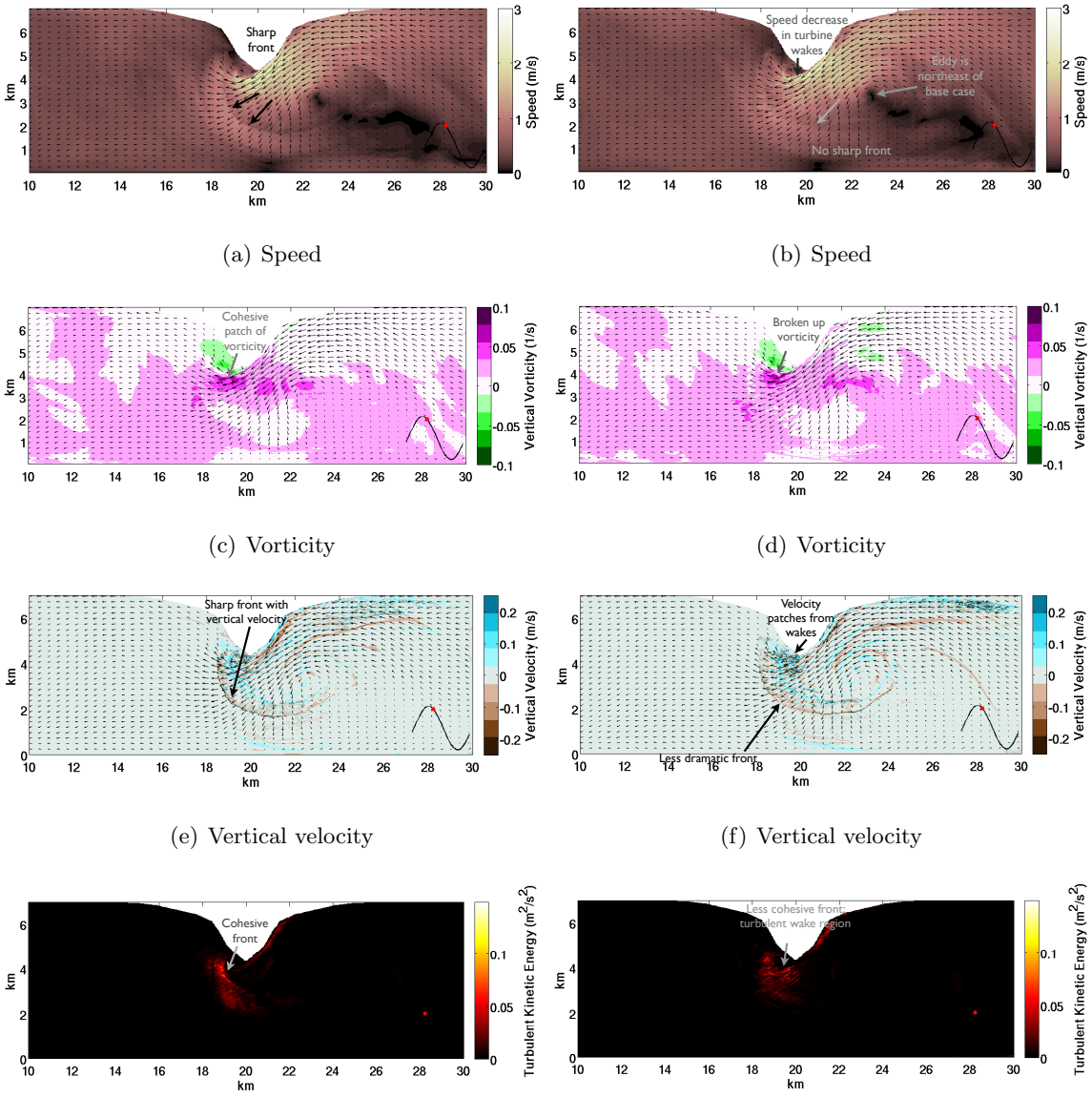


(a) Speed

(b) Speed

(c) Vorticity

(d) Vorticity

(e) Vertical velocity

(f) Vertical velocity

(g) Turbulent kinetic energy

(h) Turbulent kinetic energy

Figure C.2: Snapshots of speed, vorticity, vertical velocity, and turbulent kinetic energy are shown in color at hub height at the same time, with the $x$-axis the length along the channel and the $y$-axis the width across the channel. The left column is from the base case with no turbines and the right column is from the regular turbine array. Ebb tide is just starting.

swirl was in the other case.

In Figure C.4, snapshots are shown from a tide near the end of ebb tide. The speed in the base case shows some detailed behavior in the flow from the headland that is not seen in the turbine case. This is also seen in the vorticity field with additional patches of vorticity in the base case but not the turbine case. The dip in speed in the base case from the large eddy is again in a slightly different place than in the turbine case; in this case a little northeast of the dip in the turbine case. Accordingly, the speed up seen on the side of the eddy near the wall is a little smaller and less strong in the turbine case. The turbulent kinetic energy field in the base case shows a large swirl from the headland along with a large patch of increased turbulence along the wall. The turbine case shows increased turbulence persisting near the headland tip and a smaller, less strong patch along the wall.

Overall, these slight changes in behavior in the system can be seen in mean plots. The mean speed and vertical velocity plots for each simulation are shown in Figure C.5. The mean speed plots show the highest speeds near the headland tip, but the cases with turbines show a speed deficit at and in the wake of each turbine location. Since the flow is approximately parallel to the headland on each tide, the wake is also at an angle on each tide direction. There is a circular dip in speed to each side of the headland in the base case due to a large eddy that takes over the channel toward the end of each half-tide, as well as an increase in speed along the wall. These features are located in slightly different areas in each of the array cases, and have slightly different shapes and sizes.

The mean vertical velocity magnitude plots in Figure C.5 all show strong vertical velocities near the headland in the direction parallel to the flow past the headland, as well as smaller magnitudes, on average, throughout the eddy fields. The array cases show additional sharp increases in vertical velocity in the array area. The maximum mean value in the array cases is over double that of the base case.

### *C.2.2 Surface*

The extent to which the surface flow properties change with the presence of turbines helps show how much turbines may affect the rest of the water column away from hub height.

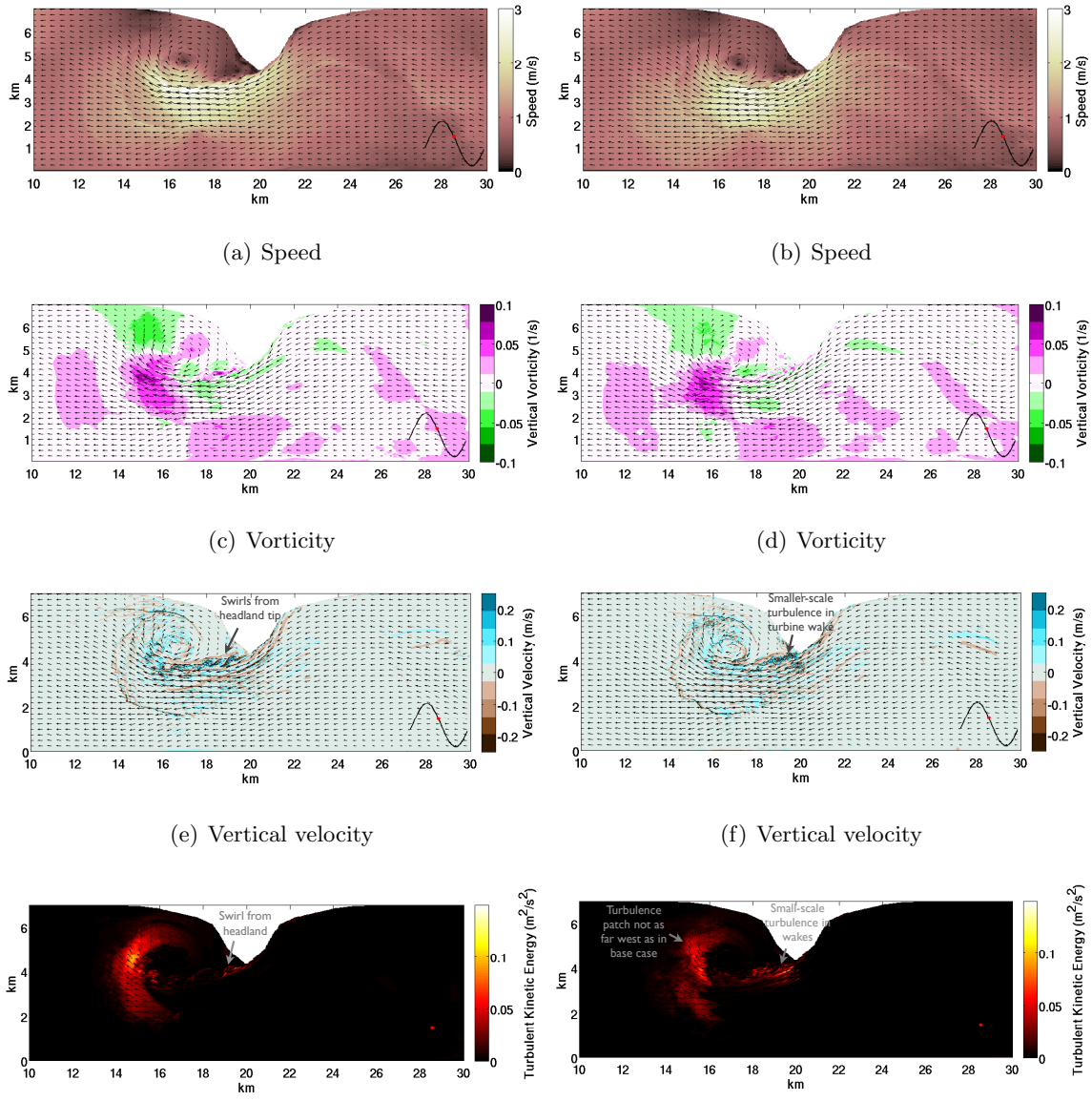


(a) Speed

(b) Speed

(c) Vorticity

(d) Vorticity

(e) Vertical velocity

(f) Vertical velocity

(g) Turbulent kinetic energy

(h) Turbulent kinetic energy

Figure C.3: Snapshots of speed, vorticity, vertical velocity, and turbulent kinetic energy are shown in color at hub height at the same time, with the $x$-axis the length along the channel and the $y$-axis the width across the channel. The left column is from the base case with no turbines and the right column is from the regular turbine array. This is at mid-ebb tide.

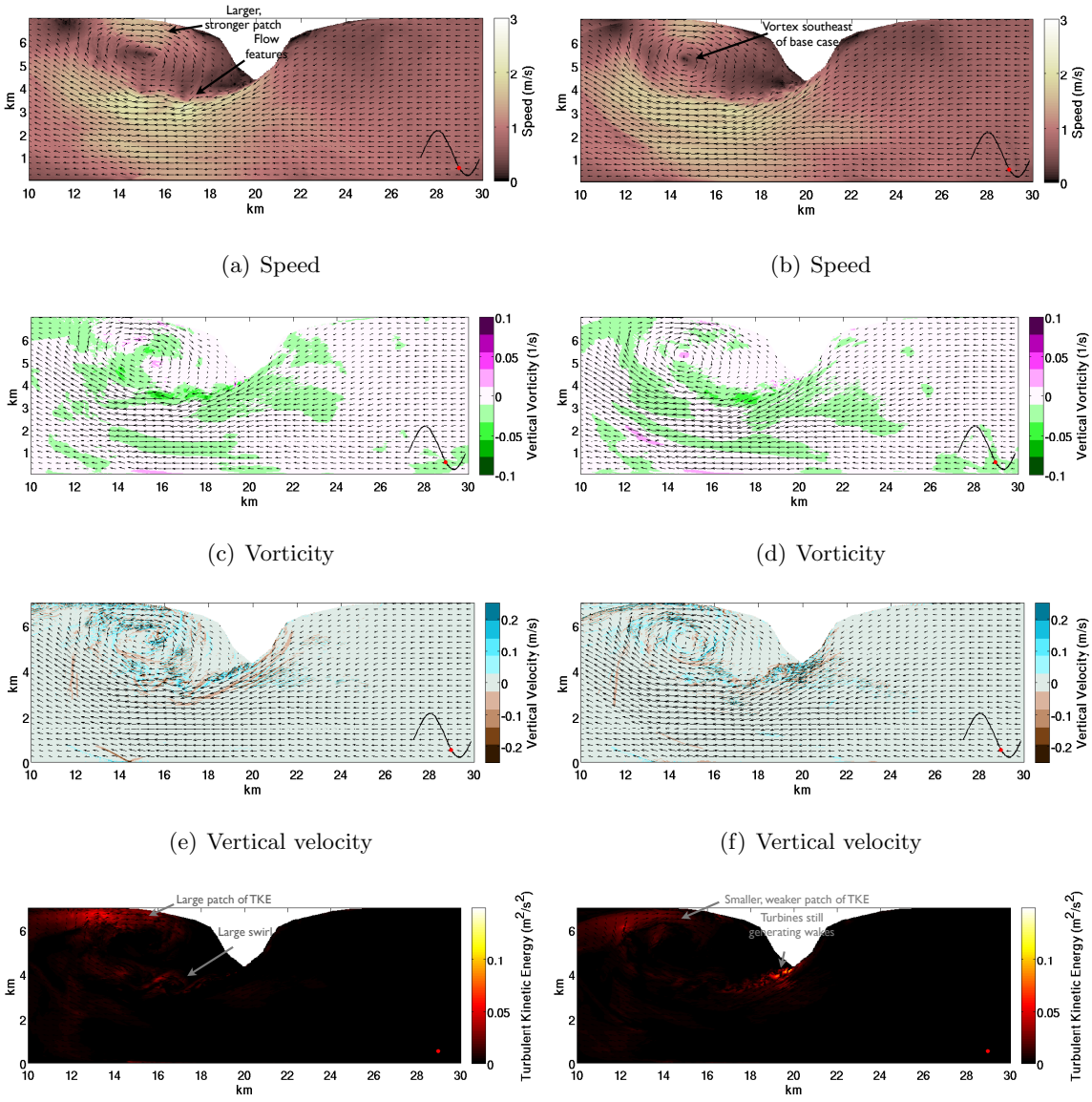


(a) Speed

(b) Speed

(c) Vorticity

(d) Vorticity

(e) Vertical velocity

(f) Vertical velocity

(g) Turbulent kinetic energy

(h) Turbulent kinetic energy

Figure C.4: Snapshots of speed, vorticity, vertical velocity, and turbulent kinetic energy are shown in color at hub height at the same time, with the $x$-axis the length along the channel and the $y$-axis the width across the channel. The left column is from the base case with no turbines and the right column is from the regular turbine array. This is toward the end of ebb tide.

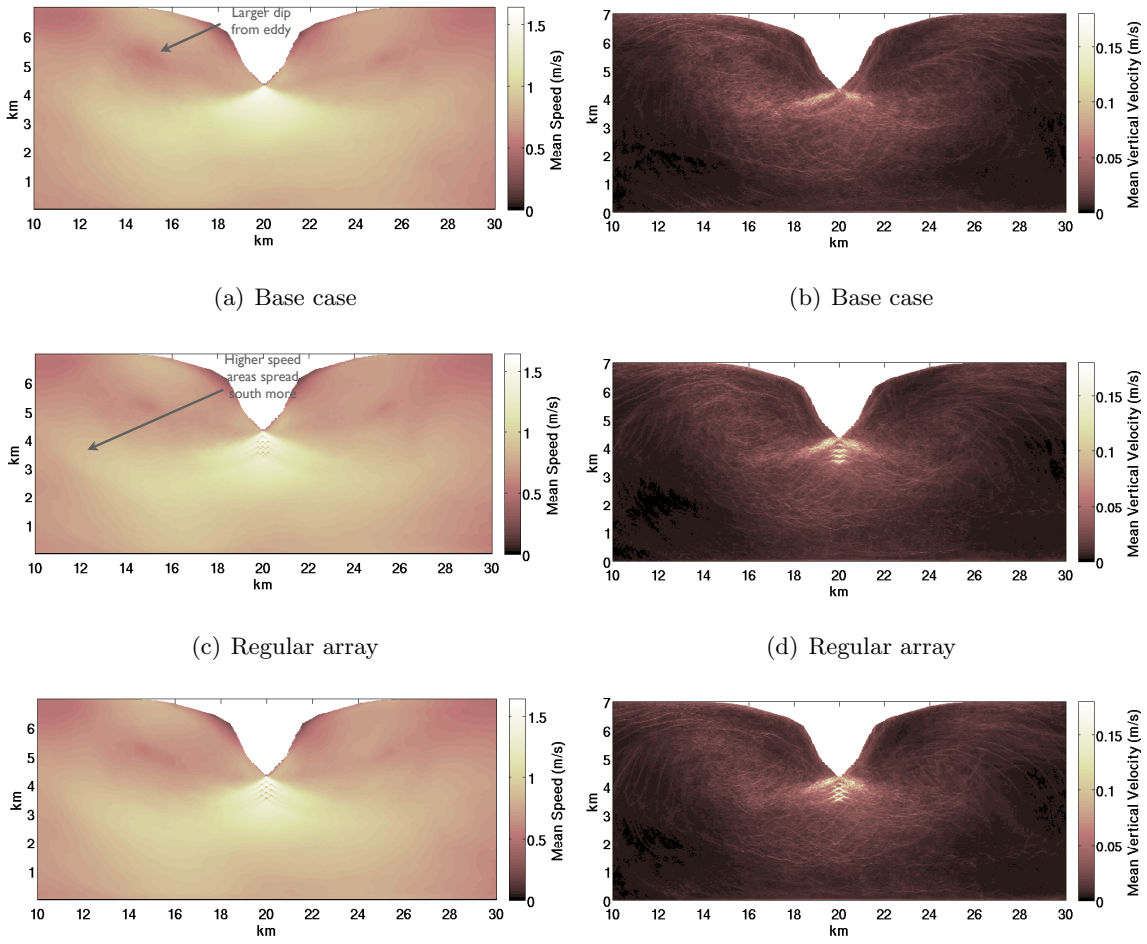


(a) Base case

(b) Base case

(c) Regular array

(d) Regular array

(e) Staggered array

(f) Staggered array

Figure C.5: Mean speed (left column) and mean vertical velocity magnitude (right column) at hub height.

Snapshots at the beginning of ebb tide in Figure C.6, the same time as shown in Section C.2.1, show differences between the base case and the regular turbine array case. In the initial case, the front of speed pushes further south and less west than in the array case, and the vortex is shifted. The vorticity field shows a cohesive patch beyond the headland in the base case, but a largely broken patch in the array case. As in the hub height case, the vertical velocity shows a stronger front in the no turbine case compared to the turbine case, and turbulence levels are increased with the presence of turbines even at the surface.

Plots are shown at the surface for mid-ebb tide in Figure C.7. Here again we find similar differences in behavior. Generally, the front of speed, vorticity, vertical velocity, and turbulent kinetic energy is sharp and further west in the base case. The array case has the flow slightly retarded by the turbines, shown in all flow fields.

Mean speed and vertical velocity magnitude are shown in Figure C.8. Even the mean surface properties are changed due to the turbines at mid-water column. The large eddy location is shifted in the array cases compared with the base case, and the mean speed is slightly higher in the array cases, probably due to increase in flow around the turbines. The turbines can be seen in the mean vertical velocity plot near the surface, and, like at hub height, the mean vertical velocity magnitude is much larger than in the initial case.

The turbines are even visible in the mean free surface plots, shown in Figure C.9. These plots are zoomed in very close to the headland tip. The array cases show that there are dips on the surface due to each turbine of 6-7 cm. The base case shows a dip on either side of the headland tip from vorticity shedding. While there is some decrease in the free surface near the headland tip in the turbine cases, there is not the same structure seen in the base case, perhaps showing another indication of the vorticity generation being disrupted by the turbines.

### *C.3 Metric Maps*

The mean kinetic power density and mean turbulent kinetic energy plots at hub height are shown in Figure C.10. The power density plots show that the areas of higher resource are shifted slightly south in the array cases, as was shown repeatedly in the previous plots. The turbines also deteriorate the contours of power density in their wake, as would be expected

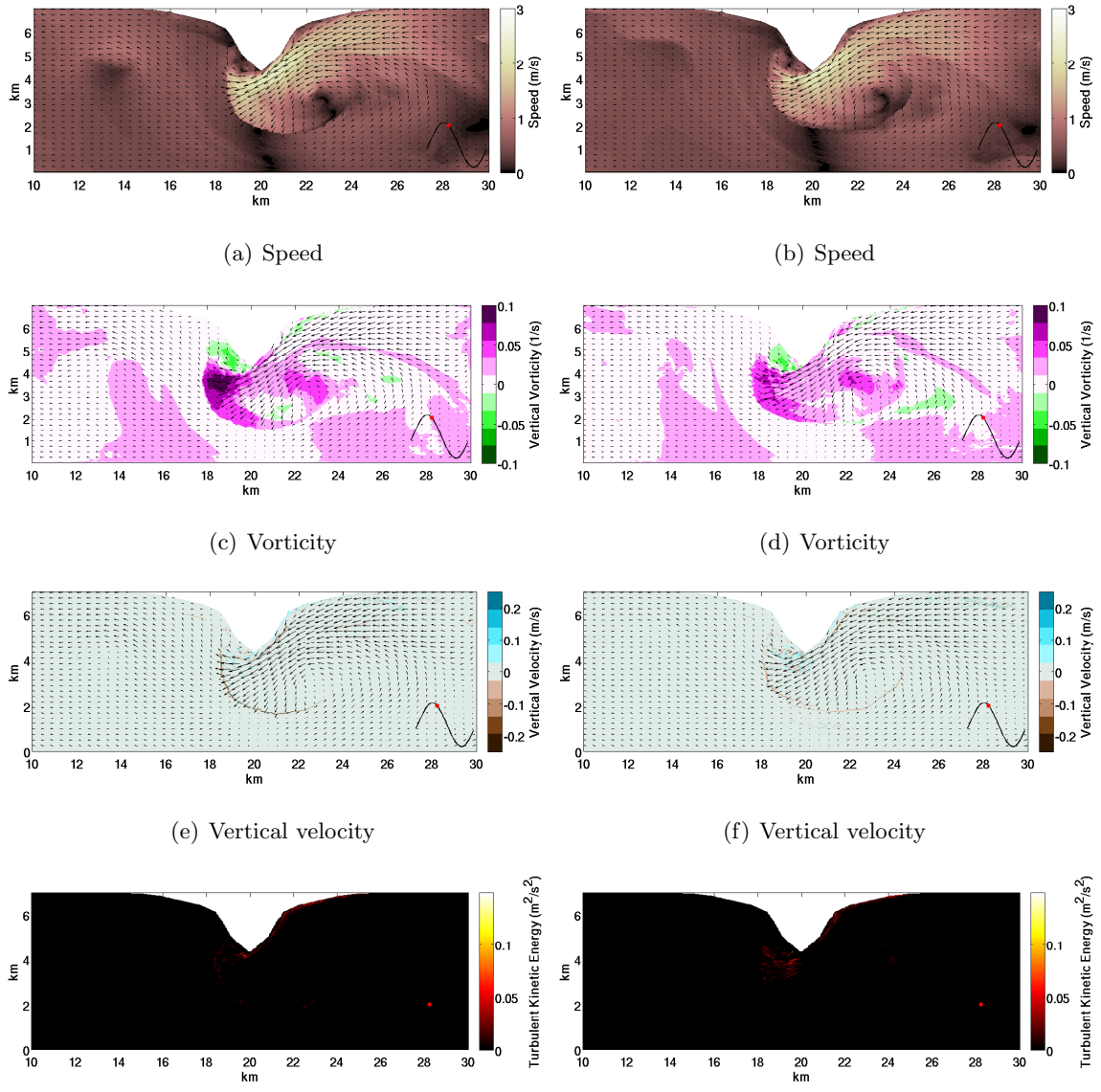


(a) Speed

(b) Speed

(c) Vorticity

(d) Vorticity

(e) Vertical velocity

(f) Vertical velocity

(g) Turbulent kinetic energy

(h) Turbulent kinetic energy

Figure C.6: Snapshots of speed, vorticity, vertical velocity, and turbulent kinetic energy are shown in color at the surface at the same time, with the $x$-axis the length along the channel and the $y$-axis the width across the channel. The left column is from the base case with no turbines and the right column is from the regular turbine array. Ebb tide is just starting.

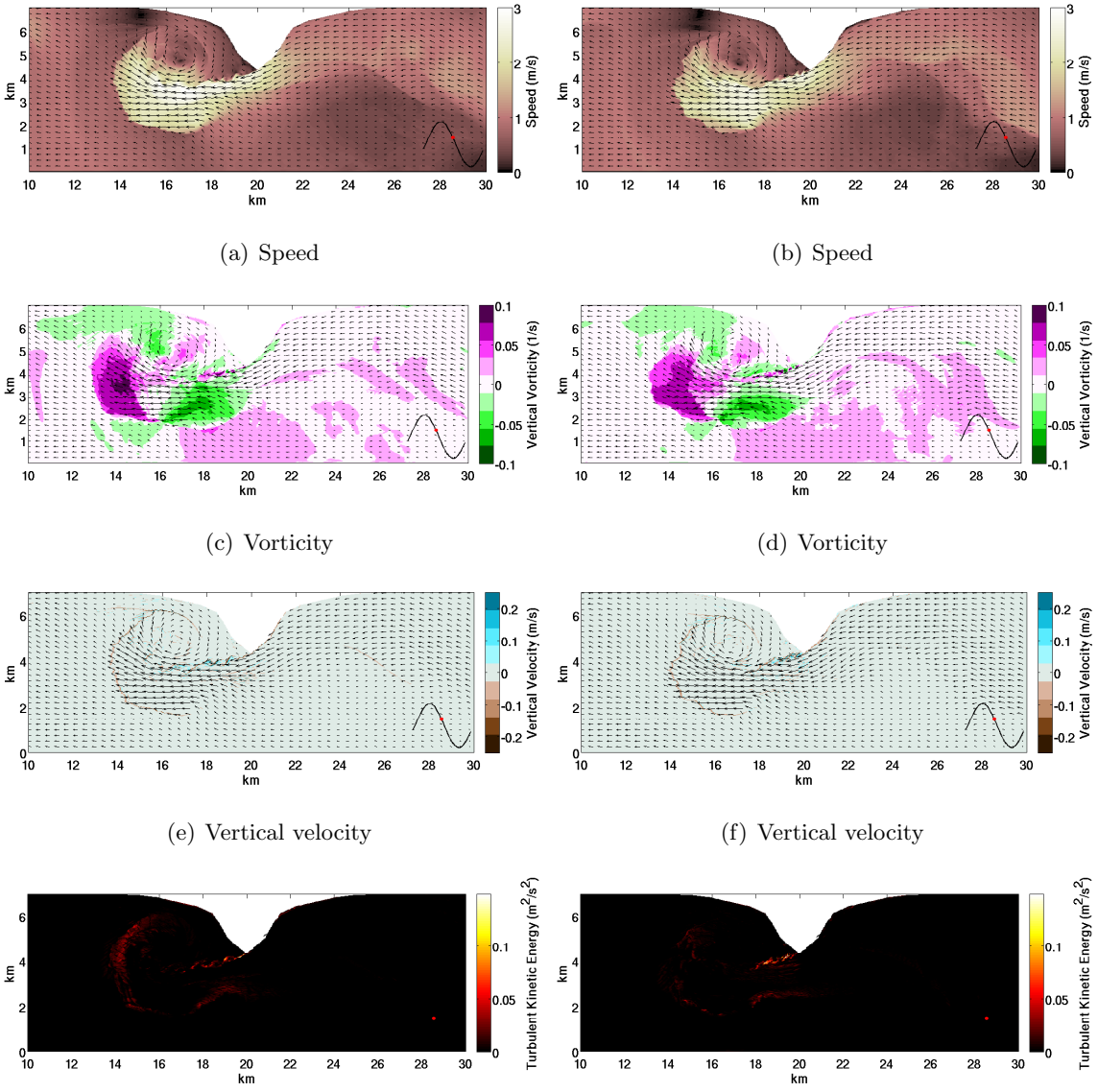


(a) Speed

(b) Speed

(c) Vorticity

(d) Vorticity

(e) Vertical velocity

(f) Vertical velocity

(g) Turbulent kinetic energy

(h) Turbulent kinetic energy

Figure C.7: Snapshots of speed, vorticity, vertical velocity, and turbulent kinetic energy are shown in color at the surface at the same time, with the $x$-axis the length along the channel and the $y$-axis the width across the channel. The left column is from the base case with no turbines and the right column is from the regular turbine array. This is at mid-ebb tide.

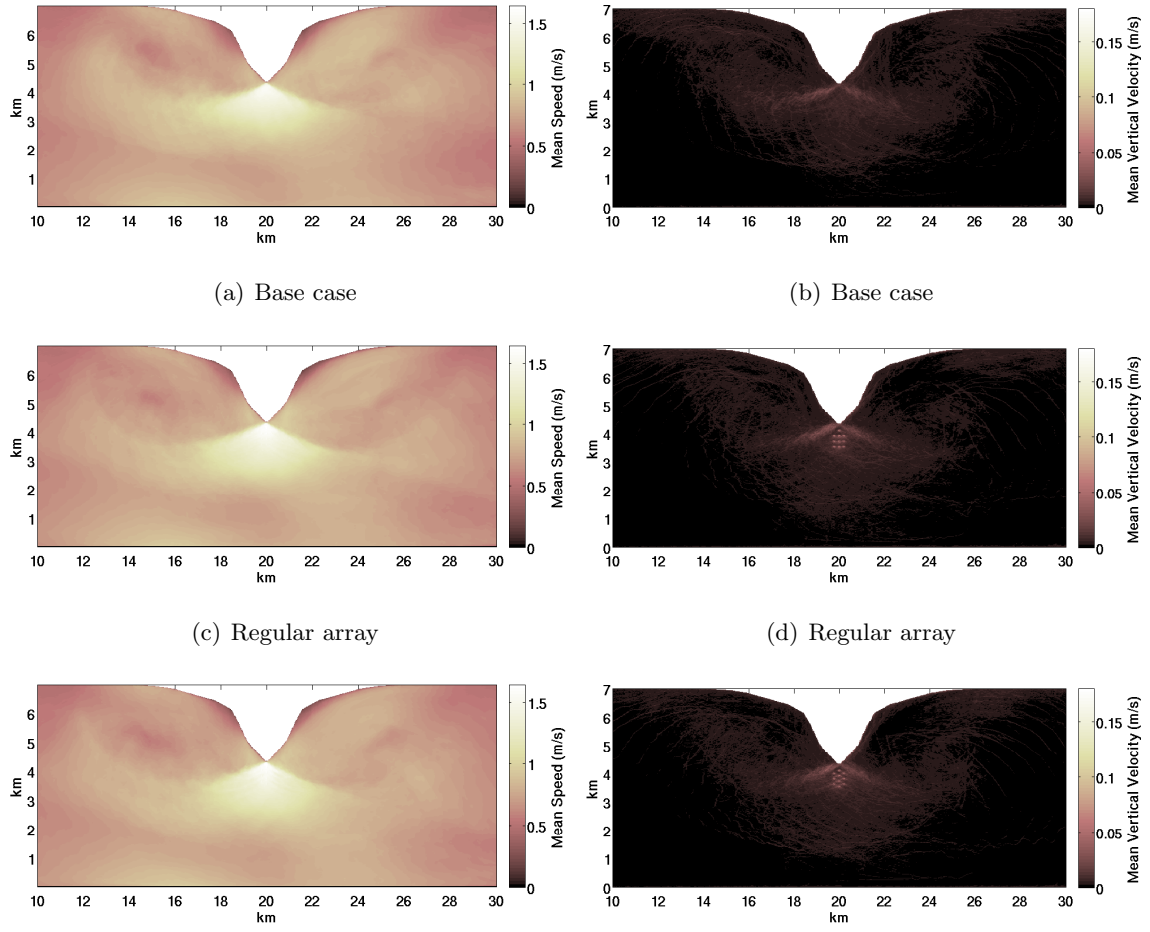


(a) Base case

(b) Base case

(c) Regular array

(d) Regular array

(e) Staggered array

(f) Staggered array

Figure C.8: Mean speed (left column) and mean vertical velocity magnitude (right column) at or near the surface.

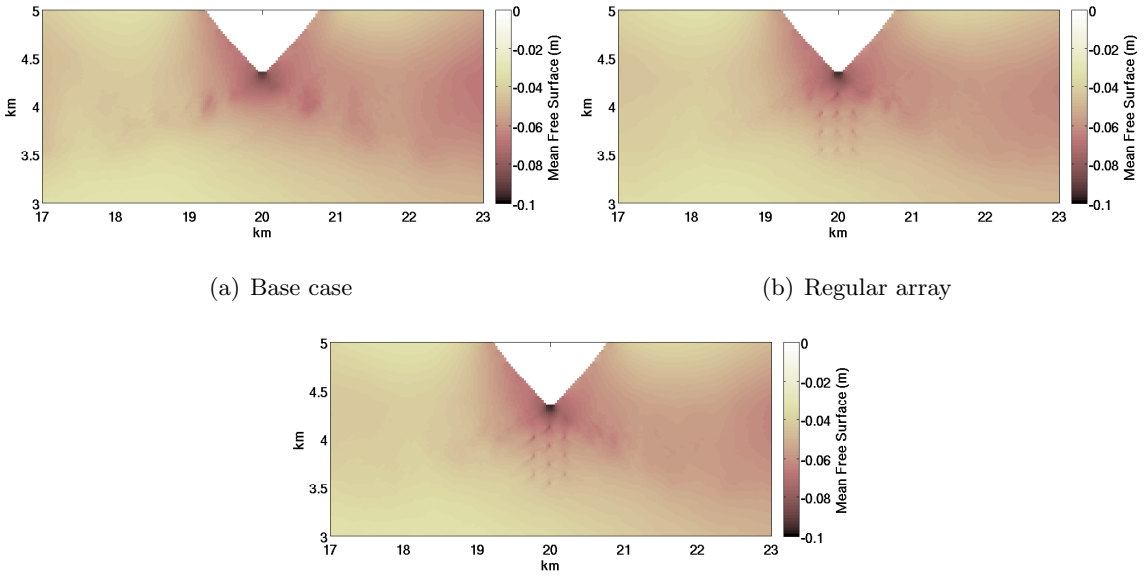


(a) Base case

(b) Regular array

(c) Staggered array

Figure C.9: Mean free surface near the headland tip. The turbine locations are just visible.

since they are taking energy from the system. The mean turbulent kinetic energy plots show a large increase in the magnitude and area of turbulence around the headland tip from the turbine wakes.

Asymmetry metrics are shown at hub height in Figure C.11. The presence of the turbines leads to larger areas of less bi-directionality near the headland tip. Directionality deviation patches are shifted in the different cases but not too different.

### *C.4 Summary and Discussion*

This chapter shows results from the first few simulations combining an idealized simulation of a realistic situation, baroclinic headland channel flow, with a validated turbine model. Results show potential flow field affects to the system. At hub height, the turbine array cases show differences in both mean flow and the details of the flow field. The flow shows a phase change due to the presence of the turbines, with the front in the array case typically just behind the front in the base case. The fronts are also more diffused in the array cases,

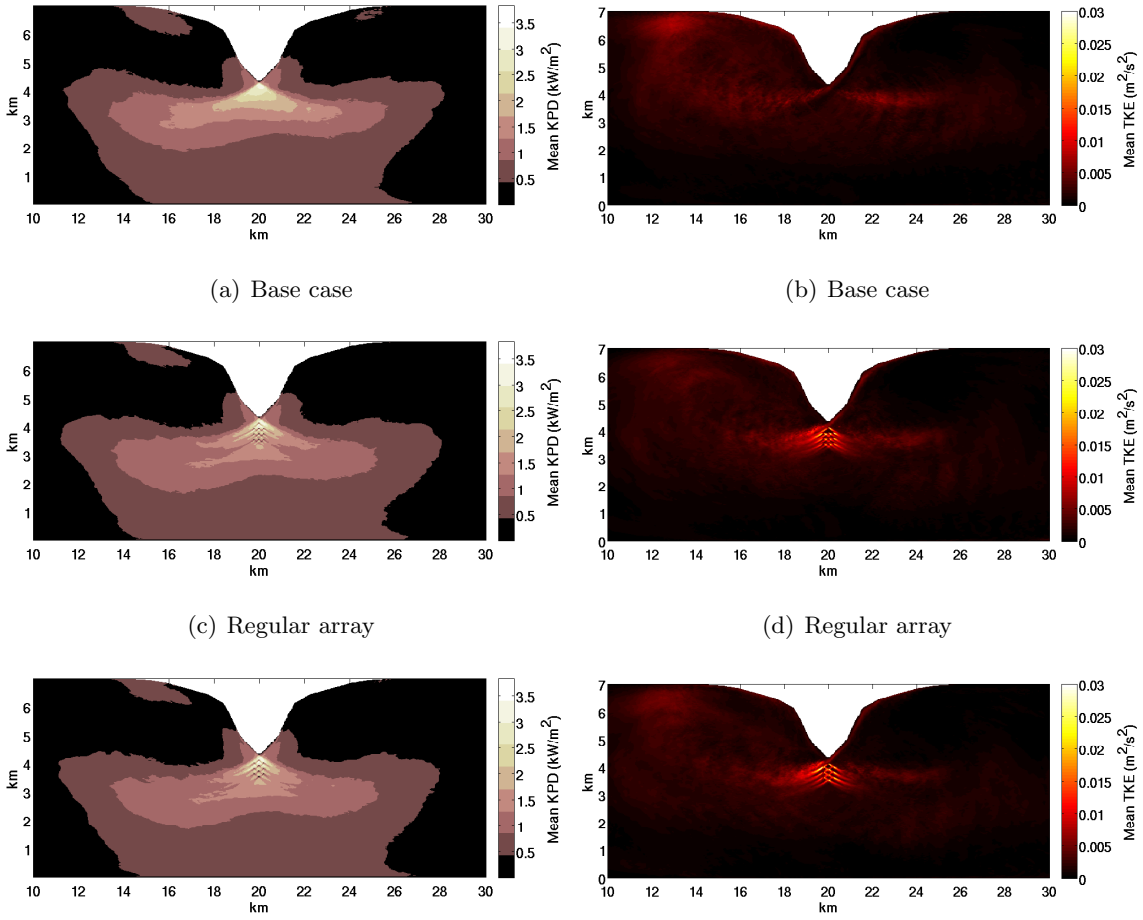


(a) Base case

(b) Base case

(c) Regular array

(d) Regular array

(e) Staggered array

(f) Staggered array

Figure C.10: Mean kinetic power density (left column) and turbulent kinetic energy (right column) at hub height.

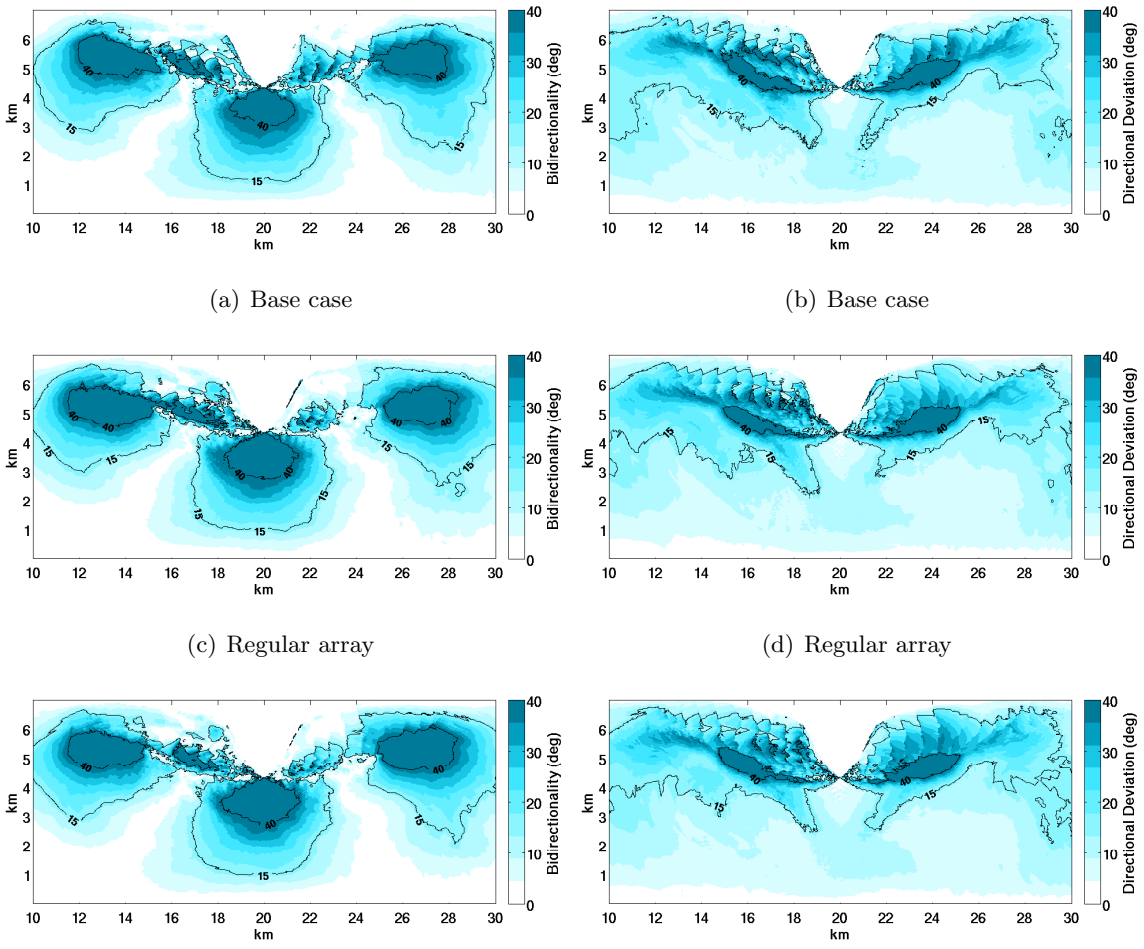


(a) Base case

(b) Base case

(c) Regular array

(d) Regular array

(e) Staggered array

(f) Staggered array

Figure C.11: Bi-directionality (left column) and directional deviation (right column) at hub height.

with less vertical velocity and a less sharp speed gradient marking the area as it moves around the system. The turbine arrays interrupt the formation of a resolved swirl from the headland tip, instead generating smaller-scale, unresolved streaks in the turbine wakes in the vertical velocity and turbulent kinetic energy fields. The eddies in the system are also located in slightly different areas when turbines are present, leading to a small difference in the areas of lower mean speed, among other effects. The effects of the turbines can be seen near the surface as well, even with just these ten turbines, in similar ways as at hub height but not as dramatic.

### *C.4.1 Implications for Estuary*

The changes in the system involved alteration to the timing and location of flow features in the system including vorticity generation, eddy location, turbulence scales, and fronts. Additional vertical velocities were seen near the turbines along with increased turbulence. Each of these changes could affect the location, timing, and rate of mixing and transport. The change in the eddy locations and rate could affect bottom sediment transport, which could affect the bathymetry in the area. The bathymetry was seen to correlate with the eddy field location in previous studies as well as possibly in Admiralty Inlet (see Figure C.12) (Geyer and Signell, 1990).

### *C.4.2 Implications for Turbine Siting*

The changes found in these simulations would not only affect the estuary system itself, but also any placement of additional turbines. For example, the mean kinetic power density plots shown in Figure C.10 illustrate how the turbine placement affects the power density available for other turbines to access. The same may be true in other aspects of the flow, such as bi-directionality and increased turbulence levels.

### *C.4.3 Future Work*

These simulations showed that ten turbines placed near the headland tip had an effect on the flow field of the simulation. This may be partially due to the turbine locations. Placement

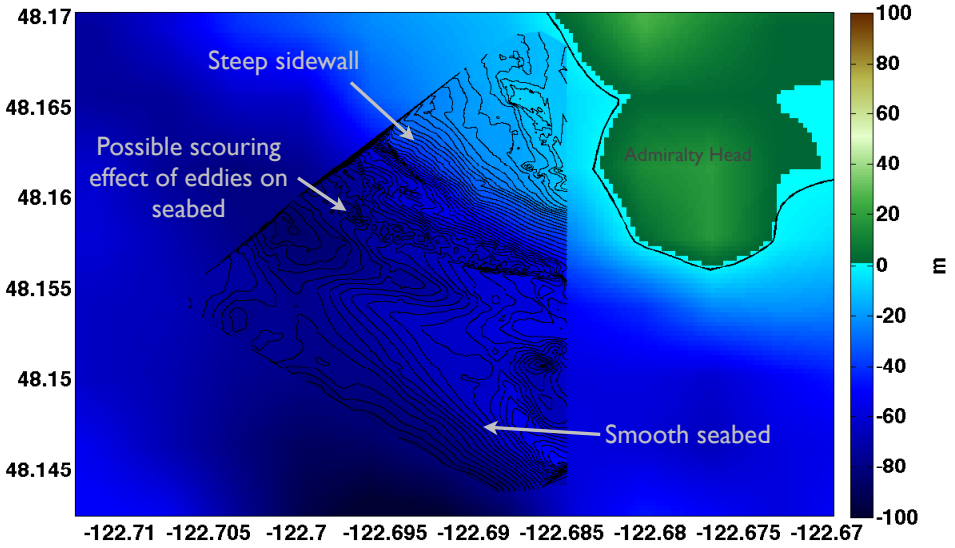


Figure C.12: High resolution bathymetry near Admiralty Head possibly showing effect of eddies on seabed

of turbines away from the headland may result in less effect on the system, which will be investigated in future simulations. Results may show that an additional consideration to be used for turbine siting is potential effect on the major local flow features, leading to the need to place turbines away from important flow features.

There are adjustments that could be made to future simulations to improve understanding and performance of results. For example, due to the high resolution needed in the simulations to model the turbines, only two tidal cycles were simulated here: one for spin-up time and one for analysis. Access to more tidal cycles would possibly alter model results. Implementing the turbine model in a non-hydrostatic ocean modeling code could lead to some distinct results. Additionally, turbines are currently located at a hub height in the middle of the water column. A more realistic hub height location for these thirty meter diameter turbines would be 25 meters rather than 50 meters above the seabed. Further, the turbine model itself is currently a fixed-axis turbine which must be aligned with the $x$-$y$ axes. In future work, a turbine that could yaw with the flow, or at least be tilted with the mean flow as a fixed-axis turbine, would be helpful to study. Incorporating cut-in and

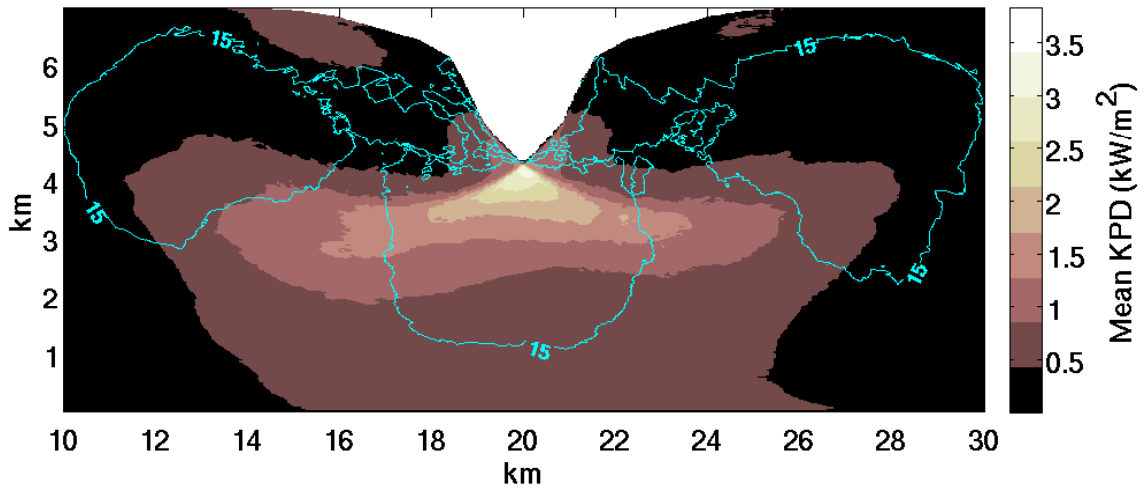


Figure C.13: Mean kinetic power density is shown in color at hub height in the base case with a cyan contour of bi-directionality overlaid at 15°.

rated speed parameters into the turbine model would allow for more realistic results.

More simulations are planned to continue this line of research. Looking at the results from the base case, we can choose a sample turbine distribution to attempt to optimize the array layout with metric maps of the simulation. For example, Figure C.13 shows the mean kinetic power density at hub height with contours showing the bi-directionality parameter. For this fixed-axis turbine, ideal locations may be due to a combination of these two metrics. A future simulation may look at the affects of turbines outside the high asymmetry areas (below 15° asymmetry) but within areas of high resource. An additional next simulation to examine is the extreme case with many turbines in the area to see the effect of an over-loaded channel.

Analysis on these results from a power production perspective is to be undertaken by Thomas Roc at the University of Plymouth.

# VITA

Kristen M. Thyng was born and raised in Seattle, WA. She earned a Bachelor of Arts degree in Physics with a minor in Mathematics at Whitman College in 2005. She earned a Master of Science degree in Applied Mathematics in 2007 and a Doctor of Philosophy in Mechanical Engineering in 2012 at the University of Washington.